University of Alberta

DIFFUSION TENSOR IMAGING OF THE HUMAN BRAIN

by

YUSUF ABU TAYEB BHAGAT

A thesis submitted to the Faculty of Graduate Studies and Research in partial fulfillment of the requirements for the degree of **DOCTOR OF PHILOSOPHY**

in

MEDICAL SCIENCES – BIOMEDICAL ENGINEERING

Edmonton, Alberta
Fall 2007

Library and Archives Canada

Published Heritage Branch

395 Wellington Street
Ottawa ON K1A 0N4
Canada

Bibliothèque et Archives Canada

Direction du Patrimoine de l'édition

395, rue Wellington
Ottawa ON K1A 0N4
Canada

Your file Votre référence
ISBN: 978-0-494-32919-1
Our file Notre référence
ISBN: 978-0-494-32919-1

NOTICE:
The author has granted a non-exclusive license allowing Library and Archives Canada to reproduce, publish, archive, preserve, conserve, communicate to the public by telecommunication or on the Internet, loan, distribute and sell theses worldwide, for commercial or non-commercial purposes, in microform, paper, electronic and/or any other formats.

The author retains copyright ownership and moral rights in this thesis. Neither the thesis nor substantial extracts from it may be printed or otherwise reproduced without the author's permission.

AVIS:
L'auteur a accordé une licence non exclusive permettant à la Bibliothèque et Archives Canada de reproduire, publier, archiver, sauvegarder, conserver, transmettre au public par télécommunication ou par l'Internet, prêter, distribuer et vendre des thèses partout dans le monde, à des fins commerciales ou autres, sur support microforme, papier, électronique et/ou autres formats.

L'auteur conserve la propriété du droit d'auteur et des droits moraux qui protège cette thèse. Ni la thèse ni des extraits substantiels de celle-ci ne doivent être imprimés ou autrement reproduits sans son autorisation.

In compliance with the Canadian Privacy Act some supporting forms may have been removed from this thesis.

While these forms may be included in the document page count, their removal does not represent any loss of content from the thesis.

Conformément à la loi canadienne sur la protection de la vie privée, quelques formulaires secondaires ont été enlevés de cette thèse.

Bien que ces formulaires aient inclus dans la pagination, il n'y aura aucun contenu manquant.

Canada

"He thought-while his hand moved rapidly-
what a power there was in words;
later, for those who heard them,
but first for the one who found them;
a healing power, a solution,
like the breaking of the barrier.
He thought, perhaps the basic secret
the scientists have never discovered,
the first fount of life,
is that which happens when a thought
takes shape in words."

Ayn Rand, The Fountainhead
Part 4- Howard Roark

ABSTRACT

Diffusion tensor magnetic resonance imaging (DTI) measures the diffusivity of water along different directions in the human brain on a voxel-by-voxel basis and yields information about tissue microstructure. The work in this thesis was conducted to address the objectives of improving DTI for generating good quality images and yielding more accurate and reproducible quantitative measures of mean diffusivity (Trace/3 ADC) and fractional anisotropy (FA) in studies of normal aging and acute ischemic stroke. The first set of objectives was achieved by incorporating cerebrospinal fluid (CSF) suppression by using the fluid-attenuated-inversion-recovery (FLAIR) method in DTI. This addressed issues of partial-volume-averaging of CSF with brain parenchyma and improved Trace/3 ADC and FA measures primarily in peripheral brain regions adjacent to CSF-filled spaces. The utility of CSF-suppression was further realized in characterizing diffusion anisotropy changes with age in the normal brain.

The second set of objectives dealt with improving the rapid single-shot echo planar imaging (EPI) method used to acquire DTI data by combining it with newer autocalibrating parallel imaging techniques. Although EPI provides a fast means of imaging in the time-sensitive clinical domain, it is fraught with detrimental image artifacts such as signal-dropouts, distortions and blurring due to its lengthy echo trains. The combination of EPI with parallel imaging lessened these artifacts by shortening the length of the echo train acquisition. The results were improved image quality and reproducible quantitative measures in the normal brain. This work was extended to studies of acute stroke patients where conventional diffusion-weighted imaging (DWI)

with single-shot EPI was compared to parallel imaging-based DWI for improved lesion conspicuity and diagnostic reliability in detecting acute ischemic lesions. The final objective was to monitor changes of diffusion anisotropy in discrete ischemic brain regions such as white matter fiber tracts and gray matter areas following an acute (≤34 hours of onset) stroke. This was studied in 2 separate cross-sectional groups and 1 group of serially scanned stroke patients. FA was elevated in many acute cases within 7 hours of stroke, but not beyond that time frame where it was more common to find small reductions of FA in the lesion.

786

الحمد الله رب العالمين .والصلوة والسلام على رسوله وعلى اهل بيتے واصحابه اجمعين

الداعي الاجل الفاطمي آقاسيدنا محمد برهاالدين (ط ع)

ني رزا مبارك انے دعاء مبارك ني بركة سي

PhD Thesis in Biomedical Engineering

تمام تهي چهے .

آ *Thesis* في الحضرة الامامية النورانية اشرق الله انوارها شكر ما ادبًا *Dedicate* گرون چهون

والحمد لله رب العالمين

Respectfully dedicated to the 52nd Dai al-Mutlaq,
*His Holiness, **Dr. Syedna Mohammed Burhanuddin (TUS)***

Acknowledgements

I thank my advisor, Dr. Christian Beaulieu, for his guidance, support and accessibility during the course of my Ph.D. studies. I appreciate his patience and the invaluable lessons obtained from his tutelage. I would also like to thank members of my advisory committee, Dr. Alan Wilman, Dr. Monica Gorassini, Dr. Derek Emery and Dr. Ashfaq Shuaib for their efforts and time spent on discussing several aspects of my work and evaluating my thesis. I'm grateful to Dr. Ken Butcher for reading my thesis and serving as an examiner during the defense. I thank Dr. Richard Thompson and Dr. Don Gross for being members of the candidacy exam committee. I thank Dr. Kelvin Jones and Dr. Wilman for chairing my candidacy and defense exams, respectively. It was a pleasure to have Dr. Richard Frayne as my external examiner for the defense. I greatly admired the breadth of his knowledge in MRI and the probing questions he posed during the exam.

I am indebted to Dr. Edward Kendall for introducing me to magnetic resonance in medicine during my MSc. studies at the University of Saskatchewan. His influence and guidance have helped shape the course of my career.

I wish to thank Dr. Richard Snyder, Dr. Peter Allen, Dr. Zoltan Koles, Dr. Wilman and Dr. Beaulieu for their lectures in exciting courses such as biophysical instrumentation, fundamentals of NMR, MRI, image processing and imaging methods in medicine. This coursework provided the foundational knowledge for several of my projects. I thank Dr. Vivian Mushahwar for taking the time to evaluate student presentations during the monthly biomedical engineering (BME) dept. seminars. I am grateful to Dr. Chris Hanstock, Dr. Changho Choi, Dan Gheorghiu, Karim Damji and Peter Seres for serving as resources in the NMR center and for maintaining the magnets. Patient recruitment for the stroke studies was accomplished through the efforts of several members from Neurology (A.H. Owen Stroke Prevention Clinic) and Radiology. In this regard, I wish to offer my profound thanks to Dr. Shazam Hussain, Dr. Muzaffar Siddiqui, Dr. Shuaib, Dr. Butcher, Dr. Fawaz Al-Hussain, Dr. Nasir Rizvi, Dr. Perkash Maheshwari, Dr. Dulka Munawadu, Dr. Faiz Sher, Dr. Naveed Akhtar, Dr. Abdul Mateer, Dr. Emery, Dr. Sandeep Naik, Beulah Fitzpatrick, Yvette Ludwig, Tracy Clare and Tammy Leatherdale.

I am grateful to Maisie Goh for solving my scholarship woes, assistance with administrative matters and for caring about student welfare. I thank Beau 'the Beef' Sapach for help with computing matters, and for being an excellent spotter and fun workout partner. I have always appreciated his friendship and being able to share interests such as motorcycles, traveling, music and football with him. Also thanks to Carol Hartle, Gritchi Castro and former BME staff member, Brenda Carrier for their help in organizing committee meetings, seminars and official paperwork.

I acknowledge the Heart and Stroke Foundation, the Canadian Institutes of Health Research, the Canadian Stroke Network (CSN) and AstraZeneca for granting me the 'Focus on Stroke' doctoral research scholarship. Moreover, I appreciate the support of the CSN in flying me out to 4 national conferences and 1 workshop across the breadth of Canada and putting me up in ritzy hotels. I'm not ashamed to admit I was spoilt rotten by

their generosity and got accustomed to it. On a more serious note, it was a great experience to meet nice people, network with the MVPs of stroke research in Canada, and see parts of the country I had never imagined I would see before. I also thank the faculties of Graduate Studies and Medicine and Dentistry for the Walter H. Johns fellowships, graduate research awards and the 75th anniversary award. I would be remiss not to acknowledge the University of Alberta for the numerous books and journal articles I received through inter-library loans over the years, for maintaining a well stacked gym in the Butterdome and for providing an unlimited bandwidth (initially) to download music and movies for my relaxation when I wasn't working or studying. In this regard, the NFL network should also be acknowledged (Long live the Green Bay Packers!).

I acknowledge the numerous graduate students from BME who have helped me by enhancing my understanding of NMR fundamentals, providing friendship and solidarity, accompanying me to conferences, serving as precious 'magnet water' for scans and empathizing from time to time. This list first includes past BME students and some very close friends such as Atiyah Yahya, Hyeonjin Kim, Sherif El Basiouny, Aisha Yahya, Anthony Tessier, Steven Thomas, Jason Mendes, Alexander Holden, Isidro Bonilla, Lindsay Snook and Alison Campbell. The current students who I thank for the same above reasons are Amir Eissa, Franaz Khosrow-Khavar, Jeff Snyder, Luis Concha, Jacob Ellegood, Rob Stobbe, Gaolang Gong and Marc and Catherine Lebel.

I also wish to thank Sheikh Saifuddin Amravatiwala and Dr. Sheikh Juzer Tyebkhan from the Anjuman-E-Saifee jamaat of Edmonton for their elegant sermons, spiritual guidance, and kind words. Also deserving my gratitude are other community members such as Ali Akbar and Tasneem Ali, Tassaduq and Naz Adamjee, Zuher Karimjee, and Dr. Huseni and Shabana Rangwala. Friends whose company and support I have greatly valued are Shazam and Ruby Hussain, Taha and Amly Taher, Amer and Sabaa Hussain, Mustufa Pardawala, Hussain Zeerapurwala, Asif Ali, Garson Law, Saravanan Subramanian, Allison Falconer, Sathish Ankamuthu, Jay Srinivasan and Naren Narendranath.

The love of my parents and sister has been a constant blessing in my life. My father has always been my hero. I strive to follow his examples everyday and be like him, by being religious, opening my heart and maintaining a strong mind. My mother has made me who I am today. She continues to give me strength and always teaches me to be humble and forgiving. My sister, Yakuta never shies from sharing my burdens, making time to listen to me and giving me precious advice. I pray for her success and know she'll excel in her Ph.D. studies. I thank my mother-in-law and brother-in-law, Taha for opening their hearts and lives to me and loving me unconditionally. I'm so proud to be a part of their family.

Lastly and very specially, I thank my wife and best friend, ***Sarah*** who can be defined as my spotter in life's brutal gym. Her love, support, sacrifices and unwavering belief in my abilities enabled me to make that final push, complete writing my thesis and successfully defend it. She is the sweetest person and has the biggest heart of anyone I know, not to mention a plethora of delicious recipes that kept me fueled and working hard towards the end of studies. I adore her and I am in awe of her accomplishments and abilities. Through her actions, I strive to become a better person, at work and at home.

Table of Contents

Page

Chapter 1 INTRODUCTION 1

1.1 Objectives....1
1.2 Outline of Contents....2

Chapter 2 CONCEPTS OF MAGNETIC RESONANCE IMAGING 4

2.1 Magnetic Field Interactions of Nuclei....4
2.2 Bulk Magnetization....7
2.3 Resonance Condition....10
2.4 Radiofrequency Pulse Characteristics....11
2.5 The Rotating Frame of Reference....13
2.6 Relaxation....15
2.6.1 T1 Relaxation....15
2.6.1.1 Inversion Recovery....16
2.6.2 T_2 Relaxation....17
2.6.2.1 T2* and T2'....18
2.7 Free Induction Decay....19
2.8 Spin Echoes....20
2.9 Spatial Localization....21
2.9.1 Frequency Encoding....22
2.9.2 Phase Encoding....23
2.9.3 Notes on K-space....25
2.9.4 Slice Selection....28
2.10 Concluding Remarks....29

Chapter 3 THE HUMAN BRAIN: FOCUS ON AGING AND STROKE 30

3.1 Microscopic Organization of the Brain....31
3.2 Macroscopic Organization of the Brain....32
3.3 White Matter Organization....32
3.3.1 Structural and Functional Characteristics of White Matter....33
3.4 Blood Supply of the Brain....34
3.4.1 Anterior Cerebral Artery Territory....34
3.4.2 Middle Cerebral Artery Territory....34

4.3.2.3 Utility of the Quantitative Measures in Diseases.....66
4.3.3 Advanced Applications: Fiber Tracking.....69
4.3.4 Strategies for Optimizing DTI data Acquisition.....70
4.3.4.1 Optimizing the b value.....72
4.3.4.2 Optimizing Arrangement of Sampling Vectors.....72
4.3.5 Underlying Assumptions in DTI.....73
4.3.6 Limitations of the Diffusion Tensor Model.....74
4.4 Methods of Analysis for DTI data.....74
4.5 Concluding Remarks.....75

Chapter 5 ECHO-PLANAR IMAGING 76

5.1 The Need to Speed up Acquisition.....76
5.2 Background.....77
5.3 EPI Pulse Sequence.....79
5.3.1 Burden on the Gradient System.....80
5.3.2 Extent of Sampling.....81
5.3.3 Image Contrast.....81
5.3.3.1 GRE EPI.....81
5.3.3.2 SE EPI.....82
5.3.4 Signal-to-noise Ratio in EPI.....82
5.4 Artifacts in EPI.....83
5.4.1 N/2 Ghosting.....84
5.4.1.1 Phase Errors.....84
5.4.1.2 Eddy Currents.....86
5.4.2 Artifacts Arising from Low Bandwidth.....87
5.4.2.1 Chemical Shift Effects from Fat-Water Shift..... 88
5.4.2.2 Geometric Distortions and Susceptibility..... 89
5.5 Shortening the EPI Readout Interval.....90
5.5.1 The Conjugate Symmetry of K-space.....91
5.5.2 Partial Fourier Single Shot EPI.....92
5.6 EPI Sequences for Diffusion Studies.....93
5.6.1 SE EPI.....93
5.6.2 Twice Refocused SE EPI.....94
5.7 Concluding Remarks.....96

Chapter 6 PARALLEL IMAGING 97

6.1 Limits of Speed in Conventional Imaging.....98
6.2 Undersampling K-Space: A Time Savings Approach.....99
6.3 Features of Parallel Imaging.....101
6.3.1 Utility of Phased Array of Receiver Coils.....103
6.3.2 Coil Sensitivity Profiles.....104
6.4 Parallel Imaging Methodology.....106

3.4.3 Vertebral Arteries....35
3.4.4 Posterior Cerebral Artery Territory....36
3.4.5 Collateral Blood Supply to Brain....36
3.4.5.1 Circle of Willis....36
3.4.5.2 Opthalmic Artery....37
3.4.5.3 Leptomeningeal Collaterals....37
3.5 Aging of the Human Brain....37
3.5.1 Structural Changes with Aging....37
3.5.2 Functional Consequences of White Matter Loss in Aging....38
3.6 Stroke....39
3.6.1 Risk Factors and Epidemiology of Stroke....40
3.6.2 Pathology of Ischemic Infarction....40
3.6.3 White Matter Injury....40
3.6.3.1 Role of the Ca^{2+} ion in Ischemia....41
3.6.3.2 Wallerian Degeneration....42
3.6.4 Ischemic Penumbra and Therapeutic Time Window....43
3.6.4.1 Thrombolytic Therapy....43
3.6.5 Classification of Stroke: Stroke Syndromes....44
3.6.5.1 Infarction in the MCA Territory....44
3.6.5.2 Infarction in the ACA Territory....45
3.6.5.3 Infarction in the PCA Territory....45
3.6.5.4 Occlusion of the Carotid Artery....45
3.6.5.5 Brainstem Infarction....45
3.6.5.6 Infarction in the Cerebellum....45
3.6.6 Quantification of the Neurologic Deficit....46
3.7 Imaging in Stroke....46
3.7.1 X-ray Computed Tomography....47
3.7.2 Positron Emission Tomography....47
3.7.3 Single Photon Emission Computed Tomography....48
3.7.4 Conventional MRI Techniques....48
3.7.5 Diffusion and Perfusion Weighted MRI....49
3.8 Concluding Remarks....51

Chapter 4 DIFFUSION TENSOR MRI 52

4.1 Diffusion: Physical Background....52
4.2 NMR and Diffusion....54
4.2.1 The b Factor....55
4.2.2 T2-shine Through....58
4.2.3 Diffusion Anisotropy....59
4.3 The Diffusion Tensor....60
4.3.1 Estimating the Diffusion Tensor....62
4.3.2 Quantitative Measures from DTI....63
4.3.2.1 Trace/3 ADC....63
4.3.2.2 Index of Diffusion Anisotropy....64

6.4.1 K-Space Based Methods....106
6.4.1.1 Summary of K-Spaced Based Approach....110
6.4.1.2 Autocalibrating K-Space Methods: An Introduction to GRAPPA....110
6.4.2 Image Domain Based Methods....113
6.4.2.1 Autocalibrating Image Domain Methods: An Introduction to mSENSE....116
6.4.3 Practical Issues in Parallel Imaging....116
6.4.3.1 Image Reconstruction through Ease of Implementation....117
6.4.3.2 Reconstruction Related Artifacts....117
6.4.3.3 SNR in Parallel Imaging....118
6.5 Combining Parallel Imaging with Echo Planar Imaging....119
6.5.1 Improved Spatial Resolution....119
6.5.2 Reduced Susceptibility Effects....120
6.6 Concluding Remarks....121

Chapter 7 DIFFUSION ANISOTROPY IN SUBCORTICAL WHITE MATTER AND CORTICAL GRAY MATTER: CHANGES WITH AGING AND THE ROLE OF CSF-SUPPRESSION 122

7.1 Partial Volume Averaging in Diffusion MRI....123
7.1.1 Role of CSF-Suppression and Aging....124
7.1.2 Goals of the Study....124
7.2 Methods....124
7.2.1 Regions-of-Interest Analysis....125
7.3 Results....126
7.3.1 Effect of CSF-Suppression and Fractional Anisotropy....129
7.3.2 Diffusion Changes Associated with Aging....135
7.4 Discussion....139
7.4.1 Effect of CSF-Suppression on Quantitative Measurements....139
7.4.2 Age-Related Diffusion Changes....141
7.5 Synopsis of Recent DTI Based CSF-Suppression/Aging Studies....144
7.6 Concluding Remarks....145

Chapter 8 THE RELATIONSHIP BETWEEN DIFFUSION ANISOTROPY AND TIME OF ONSET AFTER STROKE 146

8.1 Introduction....147
8.1.1 DTI Based Studies of Stroke....147
8.1.2 Goal of the Study....148

8.2 Methods....148
8.2.1 MRI Acquisition and Post-processing....150
8.2.2 Regions-of-Interest Analysis....150
8.2.3 Statistical Analysis....151
8.3 Results....151
8.3.1 Diffusion Anisotropy in Major WM Tracts....154
8.3.2 Diffusion Anisotropy in Subcortical WM (in the Gyri)....160
8.4 Discussion....160
8.4.1 Comparison with Previous DTI based Stroke Studies....161
8.4.2 Limitations of the Study....162
8.4.3 Re-evaluation of Statistics for Multiple Group Comparisons....163
8.5 Concluding Remarks....163

Chapter 9 COMPARISON OF GRAPPA AND mSENSE FOR DIFFUSION TENSOR IMAGING 165

9.1 Background....166
9.1.2 Parallel Imaging Based DTI Studies....166
9.1.3 Parallel Acquisition Techniques- Methodology....166
9.1.4 Non-DTI Based mSENSE and GRAPPA Studies....167
9.1.5 Goals of the Study....167
9.2 Methods....167
9.2.1 SNR Calculations....169
9.2.2 Regions-of-Interest Analysis....169
9.3 Results and Discussion....170
9.3.1 Higher 'R' Factors....173
9.3.2 Quantitative Findings....174
9.3.3 Re-evaluation of Statistics for Multiple Group Comparisons....177
9.4 Concluding Remarks....178

Chapter 10 SERIAL DIFFUSION TENSOR IMAGING OF ACUTE STROKE 179

10.1 Serial Studies of Diffusion Anisotropy....179
10.1.2 Purpose....180
10.2 Methods....180
10.2.1 MRI Acquisition and Post-processing....181
10.2.2 Regions-of-Interest Analysis....183
10.2.3 Statistical Analysis....184
10.3 Results....184
10.3.1 Longitudinal Changes of Diffusion Anisotropy in White Matter....191
10.3.2 Longitudinal Changes of Diffusion Anisotropy in Gray Matter....198

10.4 Discussion.....205
10.4.1 Trace/3 ADC Changes in White and Gray Matter.....205
10.4.2 Comparison with Previous Serial DTI Reports of Ischemic Stroke.....206
10.4.3 Limitations of the Study.....208
10.5 Concluding Remarks on Serial Study of Diffusion Anisotropy.....210
10.6 Supplementary Data from a Cross-Sectional Study of Diffusion Anisotropy Changes in Gray Matter.....210
10.6.1 Methods.....211
10.6.2 Results.....212
10.6.3 Concluding Remarks on Cross-Section of Stroke Patients with Gray Matter Lesions.....216

Chapter 11 EVALUATION OF PARALLEL ACQUISITION TECHNIQUES mSENSE and GRAPPA IN DIFFUSION-WEIGHTED IMAGING OF ACUTE STROKE 217

11.1 Introduction.....218
11.2 Methods.....219
11.2.1 MRI Acquisition and Post-processing.....219
11.3 Results and Discussion.....220
11.4 Conclusions and Future Directions.....222

Chapter 12 CONCLUSIONS 223

12.1 Cerebrospinal Fluid –Suppression and Aging.....223
12.2 Diffusion Anisotropy in Acute Stroke.....224
12.3 The Role of Parallel Acquisition Methods in Diffusion Imaging.....225
12.4 Summary.....226

BIBLIOGRAPHY 227

Appendix 1 MRVISION IMAGE PROCESSING COMMANDS 251

A1.1 To Generate Diffusion Tensor Indices.....251
A1.2 To Generate Apparent Diffusion Coefficient Maps.....254

List of Tables

Page

Chapter 2 CONCEPTS OF MAGNETIC RESONANCE IMAGING

2-1 Typical values of relaxation parameters T1 and T2 (ms) for Hydrogen components of different body tissues at 1.5T.....19

Chapter 4 DIFFUSION TENSOR MRI

4-1 Typical values of the apparent diffusion coefficient (ADC, mean ± SD) in free water (N=4) and in the normal (21-25 years) human brain (N=5).....58

4-2 Common measures of the eigenvalues and Trace/3 ADC (mean ± SD) in a WM tract and a gray matter area in the normal (21-25 years) human brain (N=5).....64

4-3 Common FA values (mean ± SD) computed from different brain regions of normal human subjects (N=5, 21-25 years).....68

Chapter 7 DIFFUSION ANISOTROPY IN SUBCORTICAL WHITE MATTER AND CORTICAL GRAY MATTER: CHANGES WITH AGING AND THE ROLE OF CSF-SUPPRESSION

7-1 Standard DTI and FLAIR DTI derived diffusion measures for a Ni-doped water phantom.....127

7-2 Standard and FLAIR FA values (mean ± SD) of major brain regions from the young (21-25 years) and old (61-74 years) age groups.....131

7-3 FLAIR DTI-derived diffusion measures (mean ± SD) of major brain regions from the young age group (21-25 years).....133

7-4 FLAIR DTI-derived diffusion measures (mean ± SD) of major brain regions from the old age group (61-74 years).....134

Chapter 8 THE RELATIONSHIP BETWEEN DIFFUSION ANISOTROPY AND TIME OF ONSET AFTER STROKE

8-1 Characteristics of Patient Population.....149

8-2 Mean (±SD) ipsilateral and contralateral eigenvalues (λ_1, λ_2 and λ_3) in select patients from 2-7 hours after stroke.....154

Chapter 9 COMPARISON OF GRAPPA AND mSENSE FOR DIFFUSION TENSOR IMAGING

9-1 Acquisition times (min) and echo times (TE, ms) for conventional DTI with and without phase partial Fourier (PPF) and mSENSE or GRAPPA based DTI sequences with varying acceleration factors (R).....168

Chapter 10 SERIAL IMAGING STRENGTHENS THE RELATIONSHIP BETWEEN DIFFUSION ANISOTROPY AND TIME OF ONSET AFTER STROKE

10-1 Characteristics of Serial Patient Population.....183

10-2 Lesion Volumes of Serial Patient Population.....186

10-3 Mean (±SD) relative (r) Trace/3 ADC, FA and T2-weighted signal intensity values in 13 patients with major and subcortical WM tract lesions.....196

10-4 Mean (±SD) ipsilateral and contralateral eigenvalues (λ_1, λ_2 and λ_3 ($x10^{-3}$ mm^2/s)) in 4 patients with subcortical WM lesions.....198

10-5 Mean (±SD) relative (r) Trace/3 ADC, FA and T2-weighted signal intensity values in 10 patients with deep and cortical GM lesions.....199

10-6 Characteristics of a Cross Section of Patients Demonstrating Gray Matter Lesions.....212

List of Figures

Page

Chapter 2 CONCEPTS OF MAGNETIC RESONANCE IMAGING

2-1 Nuclei possessing nonzero $\vec{\mu}$ shown as microscopic magnets.....6
2-2 Magnetic moment vectors are (A) aligned randomly and (B) aligned parallel to the external magnetic field.....7
2-3 An example of Zeeman splitting for a spin -1/2 system.....9
2-4 Individual magnetic moments align to create a macroscopic magnetization that points along the *Bo* axis.....10
2-5 A linearly polarized field shown as two counter-rotating circularly polarized fields.....13
2-6 Motion of the bulk magnetization vector in the presence of a rotating RF field as seen in (a) the RF-rotating frame and (b) the laboratory frame....14
2-7 T1 recovery where at t = T1 after the excitation pulse, 63% of the magnetization has recovered alignment with B_0.....16
2-8 T2 decay, signifying the 63% reduction of the magnitude of transverse magnetization at t = T2 from an initial value.....18
2-9 Spin echo formation.....21
2-10 Linear magnetic field gradient along direction x.....22
2-11 Basic sequence of events in an imaging experiment.....23
2-12 Pulse sequence diagrams for A) Gradient echo and B) Spin echo sequences.....26
2-13 A) Line by line data acquisition scheme (K-space trajectory) employed in conventional gradient echo or spin echo imaging. B) K-space trajectory used in EPI, where all lines are acquired following a single excitation....27

Chapter 3 THE HUMAN BRAIN: FOCUS ON AGING AND STROKE

3-1 An illustration of the human brain with several labeled regions.....31
3-2 Simple diagram of a neuron.....32
3-3 A schematic of the major arteries of the brain.....35

Chapter 4 DIFFUSION TENSOR MRI

4-1 A schematic of the Stejskal-Tanner pulsed gradient experiment (top) and its effect on a system of diffusing spins (bottom).....55
4-2 Calculation of the apparent diffusion coefficient (ADC) map.....57
4-3 An example of the confounding effects of T2-shine through.....59
4-4 The effects of changing the direction of diffusion-sensitizing gradients on the signal intensity in diffusion-weighted images (a, b, c) and the computed ADC maps (e, f, g) in a normal subject.....60
4-5 Pictorial representation of raw DTI data from a normal 24 year old male subject.....62
4-6 Images of the 3 eigenvalues (λ_1, λ_2, λ_3) and Trace/3 ADC map (top).....64
4-7 Four Axial (A), Coronal (B) and Sagittal (C) FA maps from a healthy 22 year old male subject.....69
4-8 Axial FA maps of eight slices from one young subject (25 yrs).....70
4-9 The DTI Pyramid.....71

Chapter 5 ECHO-PLANAR IMAGING

5-1 Conventional K-space encoding.....78
5-2 K-space trajectory for the most common form of EPI.....79
5-3 EPI Pulse sequence (Gradient echo type) used for outlining the K-space trajectory shown in Figure 5-2.....80
5-4 Pulse sequence diagram for a single shot SE EPI sequence.....82
5-5 Phase profile in the presence of a static background gradient for even and odd echoes in an EPI sequence.....85
5-6 Example phantom image of N/2 ghosting.....85
5-7 Delays between the gradient field and the analog-to-digital converter (ADC) timings result in N/2 ghosting.....87
5-8 Examples of chemical shift artifacts in diffusion weighted single shot echo planar axial images.....89
5-9 Examples of distortions and susceptibility artifacts along the PE direction.....90
5-10 A depiction of conjugate synthesis.....92
5-11 The K-space profile of an EPI sequence with the Partial Fourier technique.....93
5-12 Diffusion-weighted SE EPI pulse sequence.....94
5-13 TRSE pulse sequence timing diagram.....96

Chapter 6 PARALLEL IMAGING

6-1 Sequential filling of K-space in conventional MRI.....98
6-2 Effects of partial sampling of K-space data.....100
6-3 Undersampling K-space data.....101

6-4 Examples of phased array coil formats.....102
6-5 Surface coil images.....104
6-6 Example of sensitivity profiles.....105
6-7 A K-space diagram depicting the spatial modulations from phase encoding gradients.....107
6-8 An overview of the several spatial harmonic profiles derived by linear combination of coil sensitivities in an 8-channel array.....108
6-9 Diagram of the K-space trajectory for a partially parallel acquisition using five spatial harmonics.....109
6-10 Schematic of the GRAPPA algorithm.....112
6-11 An example of the image domain based SENSE relation with an accelerated image acquisition with $N_c = 4$ channels or coils.....114

Chapter 7 DIFFUSION ANISOTROPY IN SUBCORTICAL WHITE MATTER AND CORTICAL GRAY MATTER: CHANGES WITH AGING AND THE ROLE OF CSF-SUPPRESSION

7-1 A set of standard (above) and FLAIR-DTI (below) derived T_2-weighted (T2W; b = 0 s/mm^2), diffusion-weighted images (DWI; b = 1000 s/mm^2), Trace/3 ADC maps, and FA maps from an elderly subject (age = 70 years).....128
7-2 Representative sets of FA maps of four slices acquired on a young age group volunteer (22 years) using standard (above) and FLAIR (below) DTI sequences.....129
7-3 Representative sets of FA maps of four slices acquired on an old age group volunteer (71 years) using standard (above) and FLAIR (below) DTI sequences.....130
7-4 Comparisons of standard (black bars) and FLAIR (gray bars) DTI derived (a) Trace/3 ADC and (b, c, d) eigenvalues in the young (21-25 years) and old (61-74 years) age groups for the subcortical white matter in the gyri and cortical gray matter.....132
7-5 Comparisons of fractional anisotropy between the young (black bars, n = 8, 21-25 years old) and the older (gray, n = 10, 61-74 years old) age groups for (a) major white matter and deep gray matter regions, and (b) subcortical white matter in the gyri and cortical gray matter regions.....136
7-6 Comparisons of (a) Trace/3 ADC, (b) λ_1, (c) λ_2, and (d) λ_3 between the young (black bars; n = 8, 21-25 years old) and the older (gray; n = 10, 61-74 years old) age groups in the genu of the corpus callosum, external capsule, and subcortical white matter (superior frontal gyrus SFG, superior temporal gyrus STG and middle occipital gyrus MOG).....138

Chapter 8 THE RELATIONSHIP BETWEEN DIFFUSION ANISOTROPY AND TIME OF ONSET AFTER STROKE

8-1 Representative set of T_2-weighted images (T2W; b = 0 s/mm^2), isotropic diffusion-weighted images (DWI; b = 1000 s/mm^2), Trace/3 ADC maps, and FA maps from 2 patients depicting hyperacute (Patient 1; 2 hours post symptom onset) and acute (Patient 18; 14 hours post symptom onset) infarcts in the MCA distribution involving major WM tracts and subcortical WM regions.....152

8-2 Representative sets of Trace/3 ADC and FA maps from 4 patients with elevated relative (r) FA values in major white matter tracts ≤7 hours post symptom onset.....153

8-3 Time course of relative (r) FA (A) and Trace/3 ADC (B) changes in major WM tracts in 21 patients following ischemic stroke onset.....155

8-4 Time course of relative (r) FA (A) and Trace/3 ADC (B) changes in subcortical WM (in the Gyri) in 19 patients after ischemic stroke.....156

8-5 Comparisons of the mean ± SD values (all ROIs measured in 26 patients) for relative (r) Trace/3 ADC, FA and T2-weighted signal intensity in (A) ischemic major WM tracts and (B) subcortical WM (in the gyri).....157

8-6 Percentage of (A) major and (B) subcortical WM (in the gyri) tracts with either increase, decrease, or no change of rFA in 26 patients.....158

8-7 Trends of rT2-weighted signal intensity versus rFA in major WM tracts (A) and subcortical WM (in the Gyri) (B) from 2-34 hours following stroke in 26 patients.....159

Chapter 9 COMPARISON OF GRAPPA AND mSENSE FOR DIFFUSION TENSOR IMAGING

9-1 Representative sets of b0 (T2-weighted), b1000 (isotropic diffusion weighted) images and Trace/3 ADC and FA maps of one inferior slice (level of pons) from one subject with conventional (R=1), and mSENSE and GRAPPA R=2 based DTI.....171

9-2 Image sets (b0, b1000) and Trace/3 ADC and FA maps of a middle slice (level of corpus callosum) from one subject with conventional (R=1), and mSENSE and GRAPPA R=2 based DTI.....172

9-3 Poor quality Trace/3 ADC and FA maps of one middle slice (level of corpus callosum) from one subject using mSENSE and GRAPPA R=3 and 4 based DTI.....173

9-4 Fractional anisotropy (a) and Trace/3 ADC (b) values (mean ± SD) for three brain regions in 5 normal subjects using conventional DTI R1-PPF, R1-no PPF and mSENSE and GRAPPA R=2 DTI methods.....175

9-5 Relative (Parallel Acquisition Technique (PAT R=2) / R1-PPF) signal-to-noise ratio (SNR) measurements (mean ± SD) of mSENSE or GRAPPA R=2 for three brain regions in 5 normal subjects.....176

Chapter 10 SERIAL DIFFUSION TENSOR IMAGING OF ACUTE STROKE

10-1 T2-weighted images (T2W; b = 0 s/mm^2), isotropic diffusion-weighted images (DWI; b = 1000 s/mm^2), Trace/3 ADC and FA maps of one slice from 2 patients (patient 10 (A) and patient 1 (B); Table 10-1) during the initial and follow-up scanning phases post stroke onset.....187

10-2 Trace/3 ADC and FA maps of one slice from the initial and follow-up scanning phases of patients 1 to 4 (Refer to Table 10-1 for patient details) post stroke onset.....188

10-3 Trace/3 ADC and FA maps of one slice from the initial and follow-up scanning phases of patients 5 to 8 (Refer to Table 10-1 for patient details) after stroke.....189

10-4 Trace/3 ADC and FA maps of one slice from the initial and follow-up scanning phases of patients 9 to 13 (Refer to Table 10-1 for patient details) following stroke onset.....190

10-5 Initial (≤7 hours) and follow-up (21.5–29 hours) time course of relative (r) fractional anisotropy (FA) changes in A) major WM tracts (N=10) and B) subcortical WM (in the Gyri, N=11).....192

10-6 Initial (≤7 hours) and follow-up (21.5–29 hours) time course of relative (r) Trace/3 ADC and T2-weighted signal intensity changes in A) major WM tracts (N=10) and B) subcortical WM (in the Gyri, N=11).....193

10-7 Time course of Relative FA in (A) major WM tracts (N=10) and (B) subcortical WM (N=11) following stroke onset.....194

10-8 Trends of rT2-weighted signal intensity (on b = 0 s/mm^2 EPI images) versus rFA during the (A) initial (56 ROIs) and (B) follow-up (77 ROIs) phases post stroke in 10 patients with major WM tract lesions 195

10-9 Trends of rT2-weighted signal intensity (on b = 0 s/mm^2 EPI images) versus rFA during the (A) initial (108 ROIs) and (B) follow-up (149 ROIs) phases post stroke in 11 patients with subcortical WM lesions.....197

10-10 Initial (≤7 hours) and follow-up (22–29 hours) time course of relative (r) fractional anisotropy (FA) changes in A) deep GM (N=4) and B) cortical GM (N=8) after ischemic stroke onset.....200

10-11 Initial (≤7 hours) and follow-up (22–29 hours) time course of relative (r) Trace/3 ADC and T2-weighted signal intensity changes in A) deep GM (N=4) and B) cortical GM (N=8) after ischemic stroke onset.....201

10-12 Time course of Relative FA in deep GM (N=4), cortical GM (N=8) following stroke onset.....202

10-13 Trends of rT2-weighted signal intensity (on b = 0 s/mm^2 EPI images) versus rFA during the (A) initial (18 ROIs) and (B) follow-up (19 ROIs) phases post stroke.....203

10-14 Trends of rT2-weighted signal intensity (on b = 0 s/mm^2 EPI images) versus rFA during the (A) initial (45 ROIs) and (B) follow-up (53 ROIs) phases post stroke.....204
10-15 Example diffusion-weighted images (DWI; b = 1000 s/mm^2) and time-to-peak (TTP) maps of 3 matching consecutive slices from 6 patients during the initial phase (2.5-5h) of stroke onset.....209
10-16 T2-weighted images (T2W, b=0 s/mm^2), isotropic diffusion-weighted images (DWI, b=1000 s/mm^2), Trace/3 ADC and FA maps from 2 patients.....213
10-17 Time course of relative (r) (A) fractional anisotropy (FA), and (B) Trace/3 apparent diffusion coefficient (ADC) and T2-weighted signal intensity (on b=0 s/mm^2 images) changes in deep GM in 6 patients after ischemic stroke onset.....214
10-18 Time course of relative (r) (A) fractional anisotropy (FA), and (B) Trace/3 apparent diffusion coefficient (ADC) and T2-weighted signal intensity changes in cortical GM in 7 patients after ischemic stroke....215

Chapter 11 EVALUATION OF PARALLEL ACQUISITION TECHNIQUES mSENSE and GRAPPA IN DIFFUSION-WEIGHTED IMAGING OF ACUTE STROKE

11-1 An axial DWI (b=1000 s/mm^2) section of a 79-year old female hyperacute stroke patient within 5 hours of symptom onset for the conventional (R=1) and mSENSE and GRAPPA (R=2) DWI methods.....220
11-2 Two axial DWI (b=1000 s/mm^2) sections and corresponding Trace/3 ADC maps of a 55-year old acute stroke patient within 13 hours of symptom onset for the conventional (R=1) and mSENSE and GRAPPA (R=2) DWI methods.....221
11-3 Two axial DWI (b=1000 s/mm^2) sections and corresponding Trace/3 ADC maps of an 85-year old subacute stroke patient within 26.5 hours of symptom onset for the conventional (R=1) and mSENSE and GRAPPA (R=2) DWI methods.....222

List of Symbols and Abbreviations

ACA	Anterior cerebral artery
ACS	Autocalibration signal
ADC	Apparent diffusion coefficient
ALIAS	Albumin therapy in acute stroke
A/P	Anterior-posterior phase encoding
ATP	Adenosine triphosphate
b	Scalar quantity that characterizes diffusion sensitization
B_0	Static magnetic field
$B_1^e(t)$	Pulse envelope function
$\vec{B}_1(t)$	Radiofrequency magnetic field
BW	Acquisition bandwidth
BW_{RO}	Bandwidth of the readout gradient
BW_{PE}	Bandwidth of the phase encoding gradient
∇C	Concentration gradient
C_j	Coil sensitivity function
C^{tot}	Composite sensitivity profiles
Ca^{2+}	Calcium
CBF	Cerebral blood flow
CNS	Central nervous system
CSF	Cerebrospinal fluid
CT	X-ray computed tomography
D	Diffusion coefficient, proportionality constant
d_{csp}	Chemical shift in pixels
D_{xx}, D_{yy}, D_{zz}	Diagonal elements of the tensor (**D**)
DTI	Diffusion Tensor Imaging
DWI	Diffusion-weighted imaging
ECA	External carotid artery
EPI	Echo planar imaging

FA	Fractional anisotropy
FID	Free induction decay
FLAIR	Fluid attenuated inversion recovery
FOV	Field of view
FT	Fourier transform
g	Geometry factor of a phased array of coils
G_x	Amplitude of the linear gradient (varying along direction x)
GM	Gray matter
GRAPPA	Generalized autocalibrating partially parallel acquisitions
GRE	Gradient recalled echo
^1H	Hydrogen
I	Spin quantum number
I^{full}	Full image
I^{fold}	Aliased image
ICA	Internal carotid artery
IFT	Inverse Fourier transform
$\vec{J}$	Angular momentum of the nucleus
J	Macroscopic flux density
K	Boltzmann constant (1.38×10^{-23} J/K)
m_I	Magnetic quantum number
$\vec{M}$	Magnetization
$\vec{M}_z$	Longitudinal magnetization
M_{xy}	Transverse magnetization
MCA	Middle cerebral artery
MRI	Magnetic Resonance Imaging
mSENSE	Modified sensitivity encoding
N↑	Number of spins parallel to the static field
N↓	Number of spins anti-parallel to the static field
n_j	Complex coil weight factors
N_s	Total number of spins in the object being imaged
N_x, N_y	Number of frequency encoding and phase encoding points

Na^+	Sodium
NEX	Number of excitations averaged
NIHSSS	National institutes of health stroke scale score
PAT	Parallel acquisition technique
PCA	Posterior cerebral artery
PET	Positron emission tomography
PICA	Posterior inferior cerebellar artery
PPF	Phase partial Fourier
PRoFESS	Prevention regimen for avoiding second strokes
PSF	Point spread function
PWI	Perfusion-weighted imaging
r	distance or relative value (ipsilateral/contralateral)
R	Acceleration factor
R2	Transverse relaxation rate
RF	Radiofrequency
R/L	Right-left phase encoding
ROI	Region-of-interest
S	Signal intensity in the presence of diffusion gradients
S_0	Signal intensity in the absence of diffusion gradients
SE	Spin echo
SENSE	Sensitivity encoding
SMASH	Simultaneous acquisition of spatial harmonics
SNR	Signal-to-noise ratio
SPECT	Single photon emission computed tomography
STEAM	Stimulated echo acquisition mode
T	Tesla
T1	Longitudinal relaxation time
T2	Transverse relaxation time (irreversible)
T2'	Transverse relaxation time (reversible)
T2*	Apparent transverse relaxation time (reversible + irreversible)
T_{acq}	Total acquisition time

T_s	Absolute temperature of a spin system
TE	Echo time
t-PA	Recombinant tissue plasminogen activator
TR	Repetition time
Trace ADC	Trace apparent diffusion coefficient
Trace/3 ADC	Mean diffusivity
TSE	Turbo spin echo
TTX	Tetrodotoxin
WM	White matter
Δ	Time elapsed between the diffusion gradients
ΔB	Field inhomogeneity across a voxel
ΔE	Energy difference
γ	Gyromagnetic ratio (42.58 KHz/mT)
δ	Duration of the diffusion gradients
$\varepsilon_1, \varepsilon_2, \varepsilon_3$	Principal, secondary and tertiary eigenvectors
$\lambda_1, \lambda_2, \lambda_3$	Eigenvalues of **D**
$\vec{\mu}$	Magnetic moment
ρ	Spin density
τ	Time
φ	Phase angle
χ	Magnetic susceptibility factor
ω_0	Larmor frequency
ω_{rf}	Excitation carrier frequency
$\hbar$	Planck's constant ($h = 6.6 \times 10^{-34}$ J.s) divided by 2π

1

INTRODUCTION

Magnetic resonance imaging (MRI) is a powerful tool for evaluating brain structure and function. Progress in MRI research during the past 30 years has made it possible to better understand human brain function in normal and disease conditions. Several MRI techniques are routinely used in research and clinical settings to answer questions related to brain anatomy, physiology and pathology at acute and chronic stages. The noninvasive and nondestructive properties of MRI make it ideal for use in longitudinal studies also.

Diffusion tensor MRI (DTI) (Basser *et al* 1994a; Pierpaoli *et al* 1996) is one MRI technique used for studying brain microstructure. DTI can highlight white matter tracts to yield a better understanding of the early metabolic changes and the subsequent structural degradation in white matter after stroke (Sotak 2002). The advantage of DTI lies in its ability to probe brain microstructure. DTI is based on the principle that water diffuses faster along the length of an axon than across or perpendicular to it. Using this principle, the micro-structural integrity (given by diffusion anisotropy) and coherence of white matter tracts can be assessed *in vivo*.

1.1 Objectives

The objectives of this thesis were to improve the DTI technique to generate good quality images to provide more accurate and reproducible quantitative parameters in studies of normal aging and acute ischemic stroke. Image quality is mainly determined by factors such as distortions, blurring, artifacts, noise and contrast. These factors, when sufficiently addressed for a given MR image can aid in visualizing fine anatomical details, improving lesion conspicuity in disease and yielding accurate and highly reproducible quantitative measures in normal or diseased tissues. The following hypotheses were evaluated in this thesis:

1) Incorporating cerebrospinal-fluid (CSF) suppression by means of the fluid-attenuated-inversion-recovery (FLAIR) method in DTI would lead to a more accurate estimation of diffusion anisotropy (measured using fractional anisotropy (FA)) values in well-localized regions of the normal brain. The improvements in FLAIR-DTI FA values would permit a better characterization of the changes in FA with age in two distinct populations.

2) Combining the rapid echo planar imaging (EPI) method used to acquire DTI data with parallel imaging techniques would improve the conspicuity of detailed image features and generate more reliable quantitative diffusion measurements in brain regions compromised by the EPI-related artifacts. In the clinical domain, these imaging improvements would translate to better lesion conspicuity and diagnostic reliability in detecting acute ischemic lesions in stroke patients.

3) Evaluating diffusion anisotropy changes (using FA as a metric) in discrete ischemic brain regions divided into white matter (WM) and gray matter (GM) areas in well-defined time intervals would demonstrate that measurements of FA, unlike mean diffusivity, differ with time of onset after stroke within 34 hours of symptom development.

1.2 Outline of contents

The five chapters (chapters 2-6) following the first chapter of the thesis deal with the background and theoretical framework related to the development and application of DTI to studies of aging and acute stroke. It begins with an introduction to the concepts of magnetic resonance imaging (MRI) (Chapter 2). The chapter covers topics related to the nuclear magnetic resonance (NMR) signal formation, relaxation mechanisms, image contrast, spatial encoding and slice selection.

Chapter 3 aims to convey a brief background of the general organization of the human brain on microscopic and macroscopic levels. Furthermore, it details the structural and functional aspects of WM, and the effects of aging on the human brain with a focus on WM. Other topics treated in some detail include the onset, pathophysiology, classification, the clinical evaluation and imaging of stroke. Also, issues relating to axonal injury and Wallerian degeneration are highlighted.

Chapter 4 outlines DTI theory starting with an introduction to diffusion theory. Other topics covered pertain to diffusion in NMR, introduction to the diffusion tensor, its measures, assumptions made in the use of DTI and limitations of the tensor model. Furthermore, topics on analytical methods in DTI such as regions-of-interest analysis are included.

Chapter 5 presents fundamentals of the EPI method used to acquire DTI data. The main topics of this chapter are the theory of EPI, a review of common EPI pulse sequences used and the detrimental artifacts observed from its implementations have been detailed.

Chapter 6 reviews the theory of parallel imaging with a focus on the K-space based and image domain based methods. Examples of the SMASH (Simultaneous acquisitions of Spatial Harmonics) and SENSE (Sensitivity Encoding) techniques have been covered. Also the detailed workings of the self calibrating methods associated with SMASH, such as GRAPPA (Generalized Autocalibrating Partially Parallel Acquisitions) and mSENSE

(Modified SENSE) have been reviewed. The practical issues of implementing parallel imaging and the advantages of using these methods with EPI have been added.

The main objectives of this thesis were to improve DTI for generating good quality images and yielding more accurate and reproducible quantitative measures for incisive studies of tissue microstructure in normal human aging and ischemic stroke at 1.5T. Chapters 7-11 detail results from the developmental and applications aspects of the research work in this thesis.

Chapter 7 highlights our experience with implementing CSF suppressed FLAIR-DTI to address partial volume averaging of CSF with brain parenchyma and gives an account of the improvements in diffusion anisotropy measures of the human brain for a young and an elderly age group when compared to conventional DTI. In this study we further compared the FLAIR based measures of diffusion anisotropy between these two age groups to get an idea of changes with aging in the normal human brain. Chapter 8 presents our findings on the changes in diffusion anisotropy within 34 hours of ischemic stroke onset in a cross-section of acute stroke patients demonstrating white matter infarcts.

Chapter 9 presents our work on the comparison of the self-calibrating methods, mSENSE and GRAPPA for DTI in terms of image quality and quantitative diffusion metrics. Chapter 10 details our results on changes in diffusion anisotropy in a group of 13 patients scanned longitudinally with a mSENSE based DTI sequence at two time points (≤7 hours and from 21.5-29 hours) post ischemic stroke onset. For this work, we also studied the changes in diffusion anisotropy of deep GM and cortical GM ischemic regions in a cross-section of patients scanned from 2-26.5 hours post symptom onset. In chapter 11, which is an extension of our work on parallel imaging for diffusion studies, the results from our comparisons of mSENSE and GRAPPA to conventional diffusion-weighted imaging in acute stroke patients have been shown. Lastly, the conclusions from these studies and implications for future work are presented in chapter 12.

2

CONCEPTS OF MAGNETIC RESONANCE IMAGING

Our treatment of nuclear magnetic resonance (NMR) originates from the independent efforts of Bloch and coworkers (Bloch 1946) and Purcell and colleagues (Bloembergen *et al* 1948; Purcell *et al* 1946) to detect the magnetic moment of various nuclei using electromagnetic effects in water samples and paraffin samples, respectively. However, the discovery of the chemical shift, a small displacement of the resonance frequency of a nucleus in different chemical environments, paved the way for magnetic resonance to secure its place as an important non-destructive analytical method in modern science (Liddel and Ramsey 1951). NMR was progressively extended to analytical studies of humans and animals after the generation of one- and two-dimensional distributions of MR signals from animals. The stage for using NMR to generate images was set by Mansfield, who considered the use of magnetic field gradients for a spatial separation of NMR signals, in essence suggesting the use of gradients for spatial encoding (Mansfield and Grannell 1973). The first two-dimensional proton image of a water phantom was produced by Lauterbur and mentioned in a report (Lauterbur 1973), which predicted the application of this scanning technique to studying *in vivo* disease processes based on alterations in chemical compositions and diffusion coefficients within biological tissues.

2.1 Magnetic Field Interactions of Nuclei

The principle of NMR involves the nuclei of an object to be imaged, magnetic fields (from the scanner) and the resonance phenomenon. The resonance phenomenon is a result of the interactions of nuclei with magnetic fields. In general MRI deals with the collective behavior of a large number of nuclei present in a macroscopic object. Therefore an object being imaged can be viewed as a linearly magnetized nuclear spin system, and the signal detected arises from the system by an input radio-frequency (RF) excitation that drives the system to the state of resonance. A biological sample or a physical object can be separated into its fundamental molecules, further to its atoms and then to nuclei, which possess a finite radius ($\sim 10^{-14}$ m), a finite mass ($\sim 10^{-27}$ Kg) and a net electric charge ($\sim 10^{-19}$ coulomb). Nuclei with odd atomic weights or odd atomic numbers such as in the case of hydrogen have an angular momentum $\vec{J}$, referred to as spin ($\vec{J} \neq 0$ for angular spin). Therefore in MRI, a collection of nuclei in an object being imaged is referred to as a nuclear spin system (Liang and Lauterbur 2000). An important property

of this spin system is the inducted nuclear magnetism caused by placing the system in an external magnetic field.

The nuclear magnetism of a spin system originates from the microscopic magnetic field associated with a nuclear spin. The existence of this field is dependent on the basis that a proton (a specific nucleus) has electrical charges and that it rotates around its own axis if it possesses a non-zero spin. A nucleus with a non-zero spin creates a magnetic field around it, analogous to the one surrounding a microscopic bar magnet (Figure 2-1). A vector, $\vec{\mu}$ referred to as the nuclear magnetic moment, or simply the magnetic moment, represents this quantity. The spin angular momentum and the magnetic moment vector are related to one another by

$$\vec{\mu} = \gamma \vec{J} \qquad (2.1)$$

where γ is a proportionality constant between $\vec{\mu}$ and $\vec{J}$ known as the gyromagnetic ratio. Since magnetic moment is a vector, its magnitude and orientation need to be stated to enable an appropriate definition. The magnitude of μ is then given by,

$$\mu = \gamma \hbar \sqrt{I(I+1)} \qquad (2.2)$$

where $\hbar$ is $h/2\pi$ ($h = 6.6 \times 10^{-34}$ J.s) and I is the nuclear spin quantum number. It should be mentioned that the gyromagnetic ratio for the ^{1}H nucleus is 42.58 MHz/T, where T is Tesla, the unit of a given magnetic field. The gyromagnetic ratios for other NMR-active nuclei are 10.71 MHz/T for ^{13}C, 40.05 MHz/T for ^{19}F, 11.27 MHz/T for ^{23}Na and 17.25 MHz/T for ^{31}P (Haacke *et al* 1999; Liang and Lauterbur 2000).

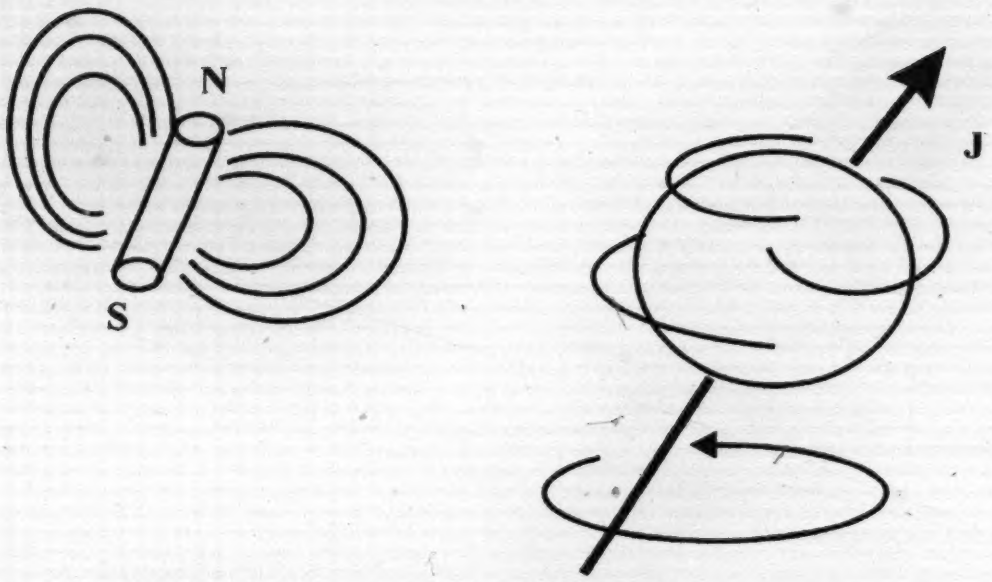

Figure 2-1: Nuclei possessing nonzero $\vec{\mu}$ shown as microscopic magnets

The nuclear spin quantum number I, assumes integer or half integer values for a given nucleus based on, 1) nuclei possessing an odd mass number have half-integral spin, 2) nuclei with an even mass number and an even charge number yield a zero spin and 3) nuclei having an even mass number but an odd charge number have integral spin. For the proton, ^{1}H, I = ½ designating a spin system called a spin-1/2 system. Therefore a nucleus can be rendered NMR active only if the $I \neq 0$. Macroscopic magnetization is achieved by exposing the object to a given magnetic field of strength *Bo*. Assuming *Bo* is applied in the z-direction, the z-component of the magnetic moment, $\vec{\mu}$ due to *Bo* is given by

$$\mu_z = \gamma m_I \hbar \qquad (2.3)$$

where m_I is the magnetic quantum number assuming 2I+1 different states for a nucleus with a non-zero spin. With 2I+1 orientations possible for $\vec{\mu}$ with respect to the *Bo*, the angle θ between $\vec{\mu}$ and *Bo* is calculated from

$$\cos\theta = \frac{\mu_z}{\mu} = \frac{m_I}{\sqrt{I(I+1)}} \qquad (2.4)$$

Based on equation 2.4, for a spin-1/2 system, θ = ±55°, which implies that in a spin-1/2 system, any magnetic moment vector takes one of the two possible orientations with parallel, or spin up, and anti-parallel, or spin down, corresponding to m_I = +1/2 and -1/2 (Figure 2-2) (Haacke *et al* 1999; Liang and Lauterbur 2000).

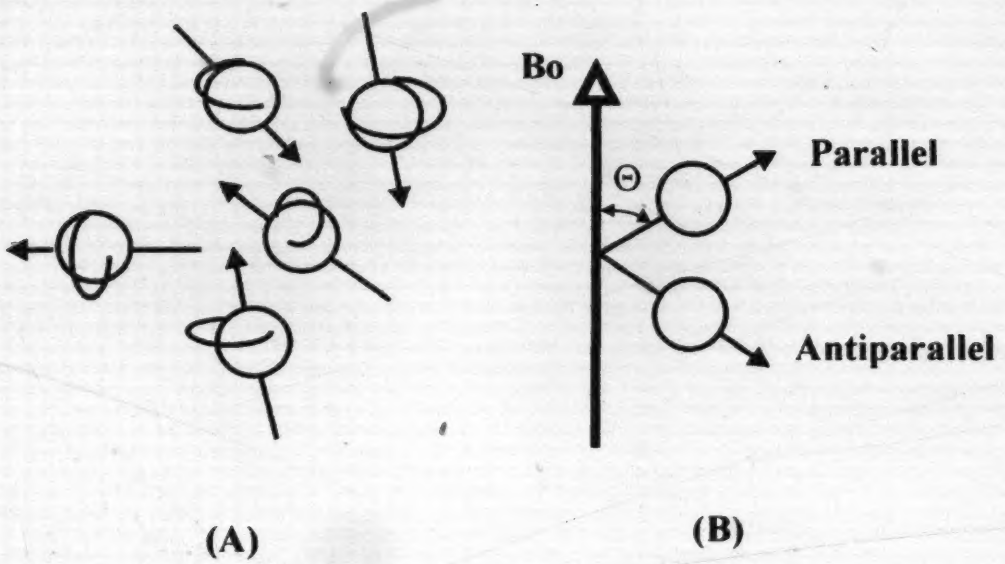

Figure 2-2: Magnetic moment vectors are (A) aligned randomly and (B) aligned parallel to the external magnetic field

The spin (or magnetic moment) vectors experience a torque in the presence of a magnetic field, which is analogous to a top that spins about the gravitational axis. The result is a nuclear precession around the axis of the magnetic field or a precession of $\vec{\mu}$ about the z-axis of *Bo*, given by the Larmor equation as

$$\omega o = \gamma Bo \qquad (2.5)$$

where ωo is the angular frequency in radians per second also given by 2πf, f, representing the resonant frequency in Hz.

2.2 Bulk Magnetization

The collective behavior of a spin system depends on a macroscopic magnetization vector, $\vec{M}$, which is the vector sum of all microscopic magnetic moments within the object. If $\vec{\mu}_n$ is the magnetic moment assigned to the nth nuclear spin, then

$$\vec{M} = \sum_{n=1}^{N_s} \vec{\mu}_n \qquad (2.6)$$

where N_s is the total number of spins in the object being imaged. Here $\vec{M}$ is defined for a spin-1/2 system, adhering to the tenet that $\vec{M} = 0$ in the absence of an external magnetic field. Upon placing the object in the external magnetic field, $\vec{Bo}$, $\vec{\mu}_n$ assumes one of two possible orientations with respect to the z-axis at any given time. Spins in different orientations have different energy of interaction with $\vec{Bo}$. In this case from quantum theory,

$$E = -\vec{\mu} . \vec{Bo} = -\mu_z Bo = -\gamma \hbar m_I Bo \qquad (2.7)$$

For spins aligned parallel to Bo ($m_I = ½$), $E\uparrow = -1/2\gamma \hbar Bo$, and for spins aligned anti-parallel to Bo ($m_I = ½$), $E\downarrow = 1/2\gamma \hbar Bo$. It becomes evident that the spin up state is the lower energy state and the spin down state is the higher energy state. The energy difference is denoted by

$$\Delta E = E\downarrow - E\uparrow = \gamma \hbar Bo \qquad (2.8)$$

This non-zero difference in energy level between the two spin states is known as the "Zeeman splitting" phenomenon (Liang and Lauterbur 2000) (Figure 2-3). The spin population difference in the two states is related to their energy difference and can be expressed using the Boltzmann relationship as

$$\frac{N\uparrow}{N\downarrow} = \exp\left(\frac{\Delta E}{KT_s}\right) \qquad (2.9)$$

where $N\uparrow$ is the number of spins in the spin-up state, $N\downarrow$ is the number of spins in the spin-down state, Ts, the absolute temperature of a spin system and K, the Boltzmann constant (expressed as 1.38×10^{-23} J/K). In practice, $\Delta E << KT_s$. Consequently, through first order approximation,

$$\exp\left(\frac{\Delta E}{KT_s}\right) \approx 1 + \frac{\gamma \hbar B_0}{KT_s} \qquad (2.10)$$

This also implies that,

$$\frac{N\uparrow}{N\downarrow} \approx 1 + \frac{\gamma \hbar B_0}{KT_s} \qquad (2.11)$$

and,

$$N\uparrow - N\downarrow \approx N_s \frac{\gamma \hbar B_0}{2KT_s} \qquad (2.12)$$

Equation 2.12 shows that there is an excess of a very small fraction ($\gamma\hbar B_o/2KT_s$) of spins in the lower energy state. This uneven spin distribution between the two states occurs because a spin is more likely to assume a lower energy state (more stabilized) than a higher one.

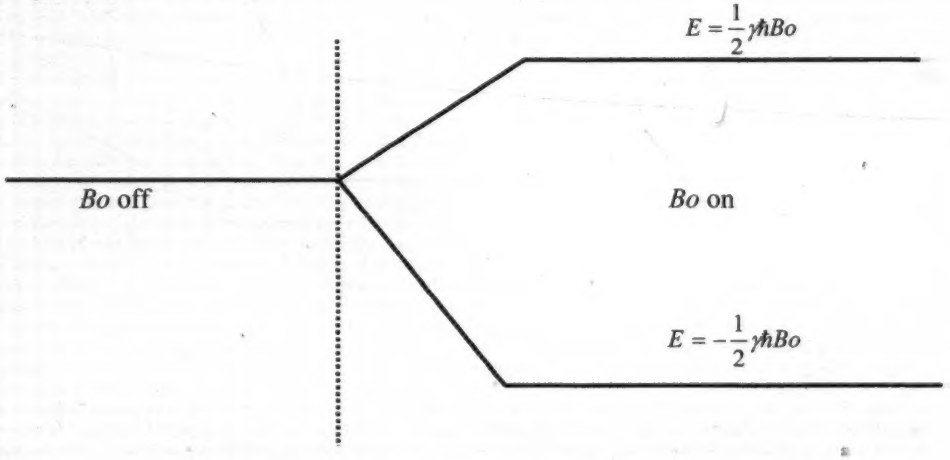

Figure 2-3: An example of Zeeman splitting for a spin -1/2 system

The population difference between the two states, albeit small, generates an observable macroscopic magnetization vector $\vec{M}$ from a spin system, which is now magnetized. The resultant bulk magnetization is

$$\begin{aligned}\vec{M} &= \mathrm{M_x}\,\vec{i} + \mathrm{M_y}\,\vec{j} + \mathrm{M_z}\,\vec{k} \\ &= \left(\sum_{n=1}^{N_s}\mu_{x,n}\right)\vec{i} + \left(\sum_{n=1}^{N_s}\mu_{y,n}\right)\vec{j} + \left(\sum_{n=1}^{N_s}\mu_{z,n}\right)\vec{k}\end{aligned} \qquad (2.13)$$

where $\mu_{x,n}$, $\mu_{y,n}$, $\mu_{z,n}$ are projections of $\vec{\mu}_n$ along x, y and z axes and $\vec{i}$, $\vec{j}$, $\vec{k}$ are the unit vectors of the three axes. The first two terms in Equation 2.13 assume zero values, since the projection of $\vec{\mu}_n$ on the transverse or xy plane has a random phase while it precesses about the z axis; $\mu_{z,n}$ (according to equation 2.3) assumes values of $+1/2\,\gamma\,\hbar$ and $-1/2\,\gamma\,\hbar$ for spins aligned parallel and anti-parallel to *Bo*, respectively. By substituting the values of $\mu_{z,n}$ into equation 2.13, we obtain

$$\vec{M} = \left(\sum_{n=1}^{N\uparrow}\tfrac{1}{2}\gamma\hbar - \sum_{n=1}^{N\downarrow}\tfrac{1}{2}\gamma\hbar\right)\vec{k} = \tfrac{1}{2}(N\uparrow - N\downarrow)\gamma\hbar\vec{k} \qquad (2.14)$$

The difference between these states yields a bulk magnetization vector along the positive direction of the z axis at equilibrium and its magnitude is given by

$$M_z^0 = \left|\vec{M}\right| = \frac{\gamma^2 \hbar^2 BoN_s}{4KT_s} \qquad (2.15)$$

which being valid for a spin-1/2 system, means that the magnitude of $\vec{M}$ is directly proportional to the strength of the external field *Bo* and the total number of spins in the system *Ns*. The only two parameters that can be altered are *Bo* and *Ts* (Liang and Lauterbur 2000). Increasing *Bo* or decreasing *Ts* can increase the magnitude of $\vec{M}$ (Figure 2-4).

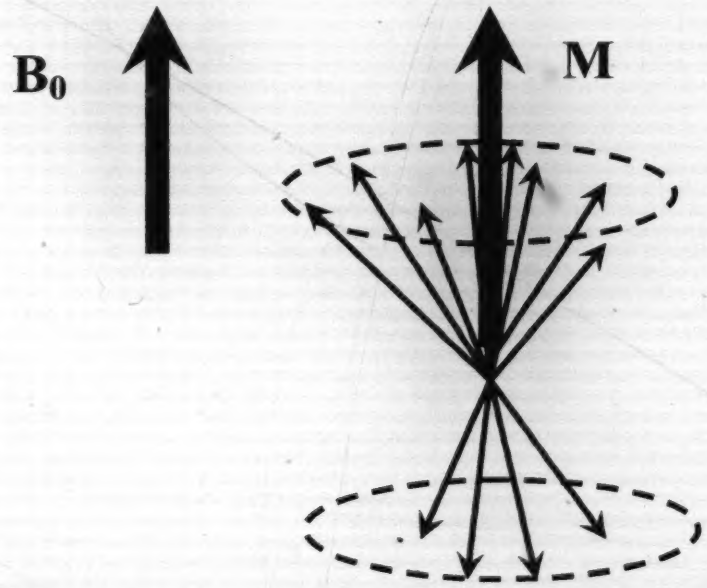

Figure 2-4: Individual magnetic moments align to create a macroscopic magnetization that points along the *Bo* axis. Due to random phases, transverse components of individual spins cancel out.

2.3 Resonance Condition

Prior to discussing the resonance condition, in an effort to better understand the application of an external force on a magnetized spin system, the popular swing analogy is examined. Let us suppose that a row of swings at a children's playground have the same length, implying that each swing-child complex has the same natural frequency. If the children do not start swinging at the same instance in time, a random phase relationship exists among the swings, i.e. at a given time the children are at different

points of the swinging arc. In order for the swings to attain phase coherence, external forces must be applied at the natural frequency of the swings. So if all the swings are pushed in unison at the natural frequency of the swing by someone positioned behind each swing, the children will soon swing in phase, exerting a coherent force on the suspension bar.

For the case of a magnetized spin system, the source of the external force is an oscillating magnetic field denoted as $\vec{B}_1(t)$, which is distinct from the static $\vec{B}o$ field. The resonance condition from classical physics is that $\vec{B}_1(t)$ rotates in the same manner as the precessing spins. However, using the quantum model as the basis for a more rigorous argument, electromagnetic radiation of frequency ω_{rf} bears energy (Planck's law),

$$E_{rf} = \hbar\omega_{rf} \qquad (2.16)$$

In order to induce a coherent transition of spins from one energy state to another, the radiation energy must equal the energy difference ΔE between the adjacent spin states. This is shown by the relationship,

$$\hbar\omega_{rf} = \Delta E = \gamma\, \hbar Bo \qquad (2.17)$$

or

$$\omega_{rf} = \omega_o \qquad (2.18)$$

This last equation is known as resonance condition where ω_0 is defined as the Larmor frequency.

2.4 Radiofrequency Pulse Characteristics

The B_1 field is short-lived and oscillates in the radiofrequency (RF) field, thereby referred to simply as the RF pulse. This B_1 field is also turned on only for a few microseconds or milliseconds and contrasting to the $\vec{B}_o$ field, is much weaker. The B_1 field can be expressed as

$$\vec{B}_1(t) = 2B_1^e(t)\cos(\omega_{rf}t + \varphi)\vec{i} \qquad (2.19)$$

where B_1^e(t) is the pulse envelope function, ω_{rf} is the excitation carrier frequency and φ is the initial phase angle. This field is termed linearly polarized due to its oscillation along the x-axis. It can be decomposed into two circularly polarized fields rotating in opposite directions,

$$\vec{B}_1(t) = B_1^e(t)[\cos(\omega_{rf}t + \varphi)\vec{i} - \sin(\omega_{rf}t + \varphi)\vec{j}]$$

$$+ B_1^e(t)[\cos(\omega_{rf}t + \varphi)\vec{i} + \sin(\omega_{rf}t + \varphi)\vec{j}] \qquad (2.20)$$

The first term in brackets rotates clockwise whereas the second term rotates counterclockwise as in Figure 2-5. Because the counterclockwise component rotates in a direction opposite to that of the precessing spins, its effects on the spin system will be negligible, if ω_{rf} is near the Larmor frequency (Liang and Lauterbur 2000). The effective $\vec{B}_1(t)$ field then is

$$\vec{B}_1(t) = B_1^e(t)[\cos(\omega_{rf}t + \varphi)\vec{i} - \sin(\omega_{rf}t + \varphi)\vec{j}] \qquad (2.21)$$

This is further decomposed into x and y components as

$$B_{1,x} = B_1^e(t)\cos(\omega_{rf}t + \varphi) \quad (2.22) \text{ and } B_{1,y} = -B_1^e(t)\sin(\omega_{rf}t + \varphi) \quad (2.23)$$

Some NMR systems use "quadrature" RF transmitter coils to generate a circularly polarized field in order to reduce RF power deposition. In summation an RF pulse generates an oscillating $\vec{B}_1(t)$ field perpendicular to the $\vec{B}_o$ field. The parameters that characterize an RF pulse include i) the envelope function B_1^e(t), ii) the excitation carrier frequency ω_{rf} determined by the resonance condition and iii) the initial phase angle, φ. The envelope function B_1^e(t) uniquely specifies the shape and duration of an RF pulse and therefore its excitation property.

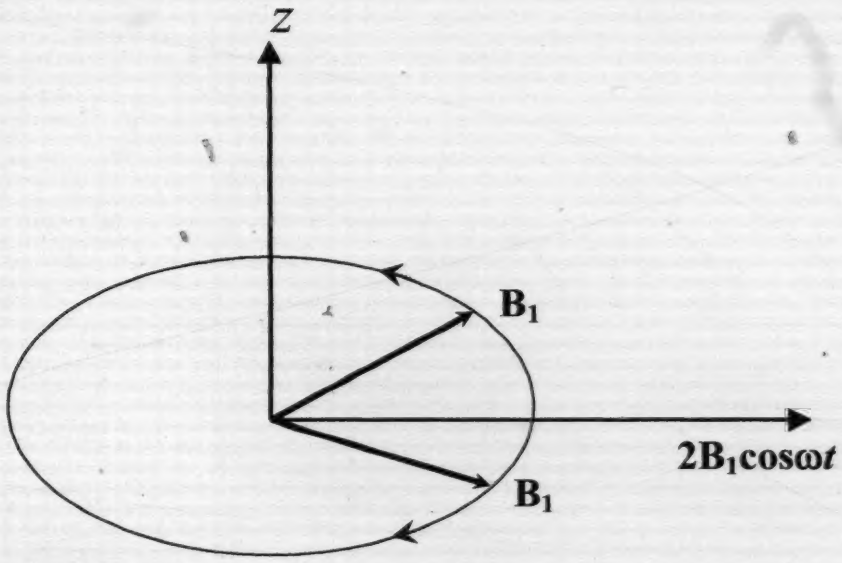

Figure 2-5: A linearly polarized field shown as two counter-rotating circularly polarized fields

2.5 The Rotating Frame of Reference

The rotating frame is a coordinate system whose transverse plane is rotated at an angular frequency ω. To generate a distinction from the conventional stationary frame, x', y' and z' are used to denote the three orthogonal directions of this frame and correspondingly i', j' and k' are their unit directional vectors. The two rotating frames in this case correspond to $\omega = \omega_o$ and $\omega = \omega_{rf}$. The first case is where the (x', y')- plane precesses at the Larmor frequency of the spin system and it can be called the Larmor-rotating frame. The second case is where the (x', y') - plane rotates as the $\vec{B}_1(t)$ field and it can be termed the RF-rotating frame. In the case where $\omega_{rf} = \gamma Bo$, both rotating frames are similar (Liang and Lauterbur 2000).

The time dependent behavior of $\vec{M}$ in the presence of an applied magnetic field $\vec{B}_1(t)$ has been described quantitatively by Bloch (1946), which in a more general form is given by Torrey (1956) as

$$\frac{d\vec{M}}{dt} = \gamma \vec{M} \times \vec{B} - \frac{M_x\vec{i} + M_y\vec{j}}{T_2} - \frac{(M_z - M_z^o)\vec{k}}{T_1} \qquad (2.24)$$

where M_z^o is the thermal equilibrium value for $\vec{M}$ which can be calculated from equation 2.15 (Bloch 1946; Torrey 1956). T1 and T2 are time constants denoting relaxation processes of a spin system after it has been disturbed from its thermal equilibrium state. These topics will be addressed in detail in upcoming sections. Currently, the interest reflects the behavior of $\vec{M}$ in the presence of the RF excitation period, provided the duration of the RF excitation pulse is short compared to T1 and T2 as is mostly practiced. With that characteristic assumed, the Bloch equation takes the form,

$$\frac{d\vec{M}}{dt} = \gamma \vec{M} \times \vec{B} \qquad (2.25)$$

The effects of an RF pulse on a spin system can be described by examining the time-dependent behavior of $\vec{M}$ during the excitation period. Observed in the RF-rotating frame, the effect of the excitation $\vec{B}_1$ field is a precession of the bulk magnetization about the x' axis as shown in Figure 2-6. This precession of $\vec{M}$ about the $\vec{B}_1$ field is called 'forced precession'. The forced precession results in the bulk magnetization being tipped away from the z' axis creating a transverse component, $\vec{M}_{x,y}$. The angle between $\vec{M}$ and the z axis is defined by α, known as the flip angle. This flip angle depends on both the magnitude of the $\vec{B}_1(t)$ field and the duration of exposure.

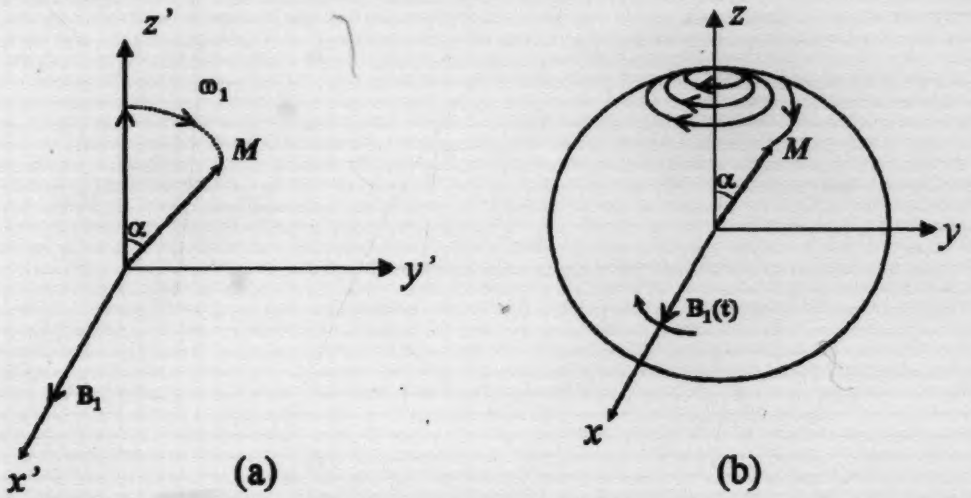

Figure 2-6: Motion of the bulk magnetization vector in the presence of a rotating RF field as seen in (a) the RF-rotating frame and (b) the laboratory frame.

2.6 Relaxation

Spins are not isolated but instead interact with each other and their environment. This interaction of the spins with the surroundings gives rise to important modifications in their behavior. The spin-lattice relaxation time, T1, characterizes how quickly the longitudinal magnetization can grow back to its maximum value along the magnetic field direction. In contrast, T2 and T2* are characteristic times that describe the disappearing rate of the transverse magnetization. The T2 decay of the signal is time-dependent and cannot be recovered, whereas part of the time-independent T2* effect can be reversed by way of spin echo experiments.

2.6.1 T1 Relaxation

Let us suppose that the equilibrium magnetization of a body is disturbed from its equilibrium value by the temporary application of an RF pulse. As a result of the continued presence of the static magnetic field, the magnetization returns to its equilibrium magnetization vector, $M_0\hat{z}$. A constant interaction growth rate from the proton interacting with the lattice suggests that the rate of change of longitudinal magnetization, $dM_z(t)/dt$, is proportional to the difference $M_0 - M_z$. The proportionality constant represents the inverse of the time scale of the growth rate. The first order rate equation describing longitudinal magnetization is,

$$\frac{d}{dt}M_z(t) = k(M_0 - M_z(t)) = -\frac{(M_0 - M_z(t))}{T1} \qquad (2.26)$$

where T1 = -1/k is termed the spin-lattice relaxation time. T1 has been used to characterize how fast the longitudinal magnetization can re-grow to its equilibrium value. The term spin-lattice is used to signify the fact that this relaxation takes place due to quantum mechanical actions between the lattice of molecules and their enclosed spins (Haacke *et al* 1999). For the initial condition where $M_z(0) = 0$ (90° pulse application), the solution of the differential equation is,

$$M_z(t) = M_o(1 - e^{\frac{-t}{T1}}) \qquad (2.27)$$

T1 ranges from tens to thousands of milliseconds for protons in human tissues over the B_0 field of interest. Typical T1 values for various tissues are shown in Table 2-1. An illustration of the exponential re-growth for an initial T1 value of 950 ms is shown in Figure 2-7.

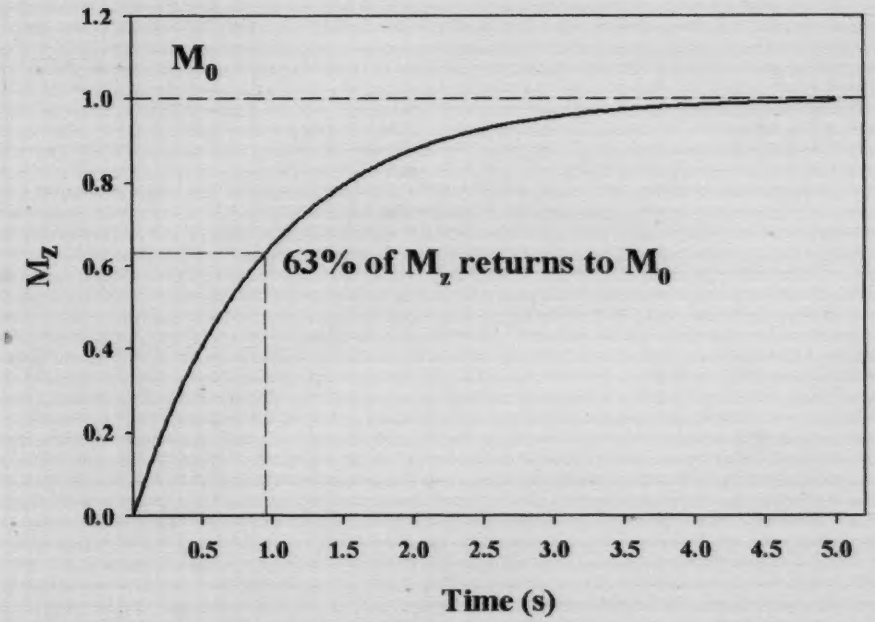

Figure 2-7: T1 recovery where at t = T1 after the excitation pulse, 63% of the magnetization has recovered alignment with B_0.

2.6.1.1 Inversion Recovery

The recovery of the signal following the application of an inversion pulse (180°) is given as

$$M_z = M_o(1-2e^{\frac{-t}{T1}}) \qquad (2.28)$$

if $Mz(t=0) = -M_0$

Different tissues exhibit different T1 values. When this property is exploited, it enables an alternative method of generating contrast in images. In the case of two separate tissues with different T1 values, if their respective magnetizations are inverted, they tend to recover at the rate of their T1s. However, based on T1-discriminating properties, the shorter T1 spins from one tissue will reach equilibrium faster than the longer T1 spins from the other. If, at the moment that the magnetization of tissue bearing a longer T1 crosses zero (referred to as the null point), a 90° pulse is applied, then signal from longer T1 tissue is suppressed and only signal from the shorter T1 tissue is observed. This T1-based property of tissues is very useful for suppressing signals from cerebrospinal fluid

(CSF) in fluid attenuated inversion recovery (FLAIR) imaging (Hajnal *et al* 1992). FLAIR allows the visualization of signal from brain only and effectively addresses partial volume averaging of CSF with brain tissue.

2.6.2 T2 Relaxation

The mechanism for the decay of transverse magnetization is reviewed in this section. Spins experience local fields which are combinations of the applied field and the fields of their neighbors. Because the variations in the local fields lead to different local precession frequencies, each spin tends to spread out or fan out in time, thereby decreasing the net magnetization vector. The spreading out or fanning out process is referred to as dephasing. The total transverse magnetization is the vector sum of all the individual transverse components.

If we are to assume the absence of any field inhomogeneities, the characterized time of the overall rate of reduction in transverse magnetization is described by the spin-spin relaxation time, T2. The transverse relaxation rate R2 is given by R2 = 1/T2. A first order approximation describing transverse relaxation is given as,

$$\frac{d}{dt}M_{xy}(t) = k'[0 - M_{xy}(t)] = \frac{-M_{xy}(t)}{T2} \qquad (2.29)$$

where T2 = -1/k'. Solving this we arrive at,

$$M_{xy}(t) = M_{xy}(0)\ e^{\frac{-t}{T2}} \qquad (2.30)$$

Once a transverse magnetization is established, it starts to quickly disappear. This is due to the local microscopic field inhomogeneities that cause the spins to become out of phase with each other, resulting in signal loss. There are several physical factors responsible for the reduction of transverse magnetization. One example is the motion of molecules whose electrons produce local fields (that vary as a function of time) with respect to the spin of interest. In one voxel, spins that experience different local time-dependent microscopic fields will be out of phase with each other, resulting in signal loss. This signal loss is irreversible (Haacke *et al* 1999). A curve representing this signal decay is shown in Figure 2-8. T2 is on the order of tens of milliseconds for protons in most human tissues (Table 2-1).

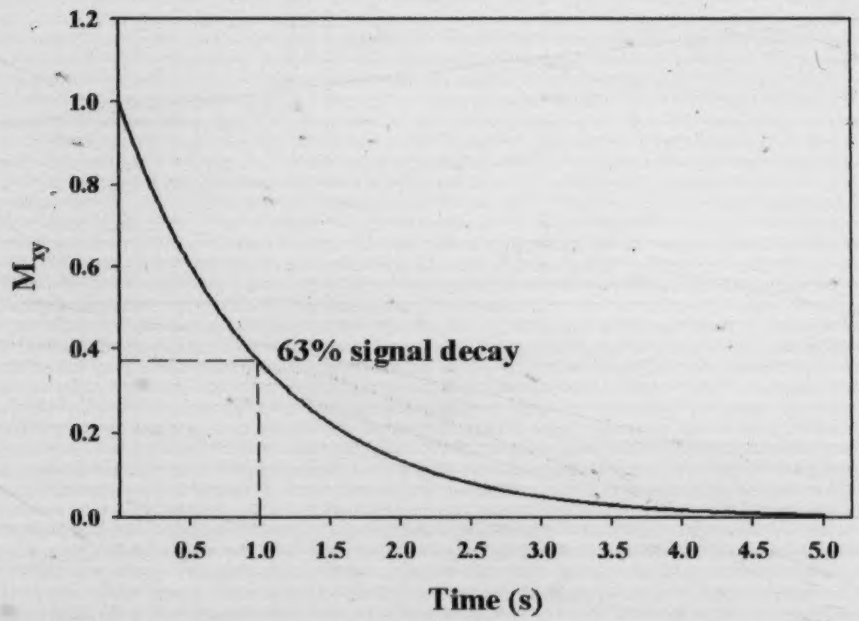

Figure 2-8: T2 decay, signifying the 63% reduction of the magnitude of transverse magnetization at t = T2 from an initial value.

2.6.2.1 T2* and T2'

In reality, static magnetic field inhomogeneities result in time-independent field variations in a gradient echo experiment, further leading to greater phase dispersion across a voxel and signal loss. This effect is determined by the field distribution and the geometries of the source of the field inhomogeneities. The signal behavior is complex, but for many instances can be approximated by a single exponential decay as,

$$M_{xy}(TE) = M_{xy}(0)\ e^{\frac{-TE}{T2^*}} \qquad (2.31)$$

where,

$$1/T2^* = 1/T2 + 1/T2' \qquad (2.32)$$

$$1/T2' = |\gamma \Delta B| \qquad (2.33)$$

where ΔB is the field inhomogeneity across a voxel. To better understand dephasing, we must examine the dispersion of phase over time. The phase is given by,

$$\phi(r) = \gamma \Delta B(r) t \qquad (2.34)$$

Phase dispersion is also examined in section 2.9.2 (Phase encoding). Since this local field variation is time-independent, the signal loss can be reversed by applying a 180° pulse after the 90° pulse to refocus the spins (see section 2.8). Local inhomogeneities occur near the air/tissue interfaces, metal implants etc. The rate of the signal decay adjacent to these structures depends on their susceptibility differences with the surrounding tissue. The higher the susceptibility difference, the larger ΔB and consequently the more rapid the signal decay (Haacke *et al* 1999).

Table 2-1: Typical values of relaxation parameters T1 and T2 (ms) for Hydrogen components of different body tissues at 1.5T (Haacke *et al* 1999)

Tissue	T1 (ms)	T2 (ms)
White matter	600	80
Gray Matter	950	100
Cerebrospinal Fluid	4500	2200
Muscle	900	50
Fat	250	60
Blood	1200	100-200*

*For T2 values of blood, the higher value applies to arterial blood and the lower values applied to venous blood

2.7 Free Induction Decay

Free induction decays (FID) occur due to the action of a single pulse on a nuclear spin system (Liang and Lauterbur 2000). The term can be broken down to "free" referring to the fact that the signal is generated by the free precession of the bulk magnetization vector about the B_0 field; "induction" pointing to the fact that the signal was produced based on Faraday's law of electromagnetic induction; and "decay" symbolizing the characteristic decrease of the signal amplitude with time. FID signals are transitory signals from a spin system following pulse excitations (from a pulse with a flip angle, α), which mathematically take form as

$$S(t) = \sin\alpha \int_{-\infty}^{+\infty} \rho(\omega) e^{-t/T_2(\omega)} e^{-i\omega t} d\omega \qquad t \geq 0 \qquad (2.35)$$

where $\rho(\omega)$ establishes the characteristics of an FID signal. The FID of a spin system with a single spectral component resonating at frequency ω_o can be stated as

$$S(t) = M_z^o \sin\alpha \; e^{-t/T_2} e^{-i\omega_o t} \qquad t \geq 0 \qquad (2.36)$$

FID signals are moderated in terms of their amplitudes and decay rates. Independent of the spectral distribution of a spin system, the FID reaches its maximum signal amplitude at t = 0, given by

$$A_f = \sin\alpha \int_{-\infty}^{\infty} \rho(\omega) d\omega = M_z^o \sin\alpha \qquad (2.37)$$

The flip angle and the thermal equilibrium of the bulk magnetization are factors that regulate the maximum amplitude of the FID signal. The FID bears a characteristic T2 decay given by equation 2.36 when the sample and the magnetic field are both homogeneous. $T2^*$ is used to characterize the signal decay in the presence of field inhomogeneities (section 2.6.2.1).

In summary, an FID signal is the transient response of a spin system following a pulse excitation. The magnitude of the signal is dependent on the flip angle, total number of spins in the sample and the magnetic field strength. The duration of an FID signal depends mainly on the degree of the field inhomogeneity, characterized by the T2* decay.

2.8 Spin Echoes

Spin echoes are formed when after the 90° pulse, a second RF pulse is applied at a time τ later to refocus the spins (Hahn 1950; Hahn 1953). These RF pulses are called 180° pulses or refocusing pulses. Upon the application of a 180° pulse at a time, τ after the 90° excitation pulse, a spin echo develops τ ms later, therefore being at $t = 2\tau$ after the 90° pulse. A 180° pulse inverts the plane of the transverse magnetization. This reverses time-independent field variations (T2* effects), should they continue identically before and after the 180° pulse. The rationale being that magnetic field inhomogeneities cause the same dephasing before and after the 180° pulse (Figure 2-9).

Natural transverse relaxation occurs randomly hence its contribution to de-phasing is not reversed in a spin echo. The period between the initial 90° pulse and the echo is referred to as the *echo delay* or *echo time* (TE). The amplitude of the echo is proportional to $e^{\frac{TE}{T2}}$. Due to this greater amplitude as compared to the alternate 'gradient echoes', spin echoes are known to compensate for many types of dephasing, granting them higher signal to noise ratios.

In contrast to the spin-echo, gradient echoes are formed through the application of a specially designed gradient rather than the application of a rephasing RF pulse; therefore only one excitation pulse is required without the need to apply the 180° pulse. Although local susceptibility effects are refocused in the case of the spin echo, a signal reduction is observed for the gradient echo due to the unrecoverable dephasing induced by the local susceptibility. These images have a T2* contrast and can be rapidly acquired.

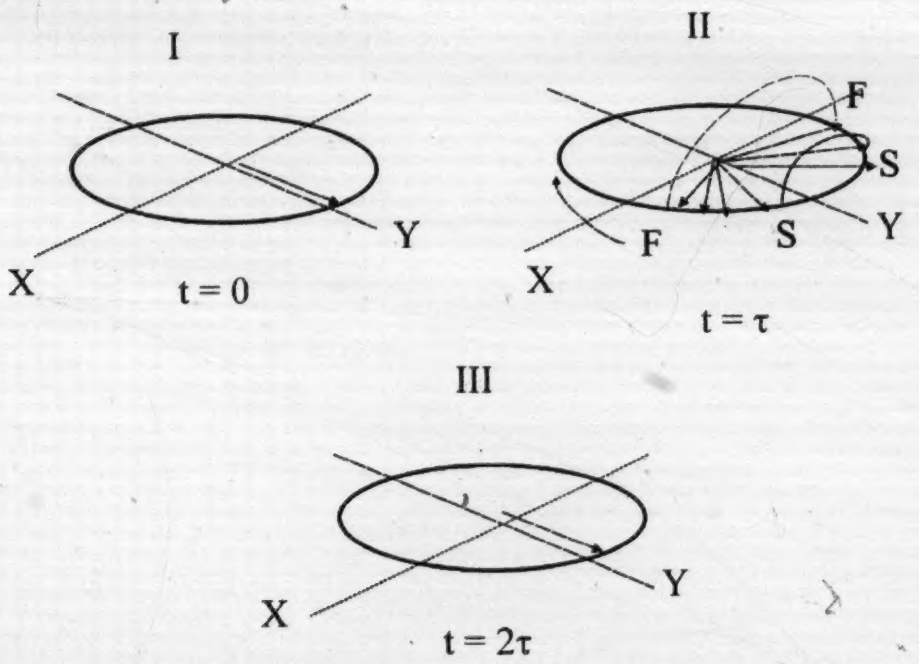

Figure 2-9: Spin echo formation. **I.** At time t = 0, spins are in phase. **II.** At time t = τ after a 90° pulse, the partly dephased transverse magnetization is switched into mirror image positions by a 180° RF pulse around y. **III.** The fast precessing spins, **F**, eventually catch up with slow ones, **S**, resulting in complete refocusing at t = 2τ.

2.9 Spatial Localization

Magnetic field gradients are fields that vary as a function of position in a particular direction. These gradients are formed by inducing electric currents in specially shaped coils constructed around a tube nested within the bore of the magnet. The three sets of orthogonal gradients in MRI equipment are termed the G_x, G_y and G_z gradients according to the x, y and z directions along which the magnetic field changes strength. The term, 'linear' is applied to these gradients because they change the strength of the magnetic field linearly as a function of distance. The role of RF pulses and gradient fields is elucidated by the describing the concepts of slice-selective excitation and spatial information encoding given later in this section.

2.9.1 Frequency encoding

In NMR, spatial localization information is encoded into the precession frequency through the application of linear magnetic field gradients. A linear magnetic field gradient is a field aligned with B_0, but whose amplitude changes linearly with position (Figure 2-10). Thus the net field, frequency and phase, all rely on position.

$$B = B_0 + G_r \cdot r \qquad (2.38)$$

$$\omega = \gamma (B_0 + G_r \cdot r) \qquad (2.39)$$

$$\theta = \gamma (B_0 + G_r \cdot r)\, t \qquad (2.40)$$

Where G_r is the amplitude of the linear gradient (varying along direction, r)
r is the position of spin
t is the duration of the gradient

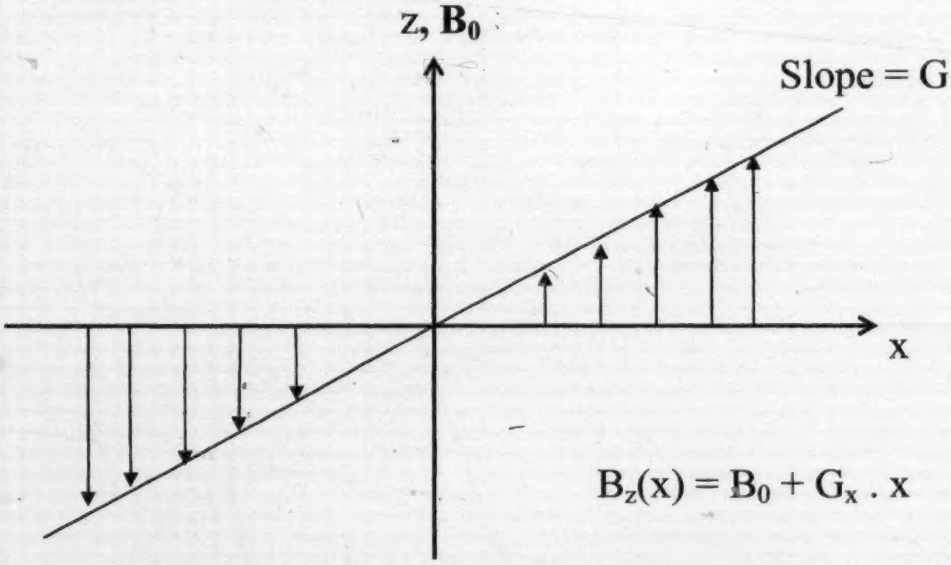

Figure 2-10: Linear magnetic field gradient along direction x

Formation of a 2D image requires spatial encoding in 2 orthogonal directions. This cannot be achieved by frequency encoding through simultaneous application of two orthogonal gradients along 2 axes, x and y, since it only results in 1D encoding along the direction of the vectorial sum of the two gradients. This is where phase encoding needs to be considered.

2.9.2 Phase encoding

The most common approach for generating 2D images is to perform frequency encoding in one axis with phase encoding being performed along another axis. If a gradient is applied for a time, τ, the spins dephase according to,

$$\phi(r) = \omega(r)\,\tau = \gamma G\, r\, \tau \qquad (2.41)$$

Now, phase information that is a function of spatial location is encoded into the spins.

If after excitation, the phase encoding gradient is applied along the y axis and data acquired while applying an orthogonal frequency encoding gradient along x, then the sampled time series data points are frequency encoded along x (given that spins will precess at a frequency proportional to their locations on the x axis) and have been imparted identical phase offsets by phase encoding. However to complete phase encoding along the y axis, this sequence of events must be performed several times, each with a different phase (Figure 2-11).

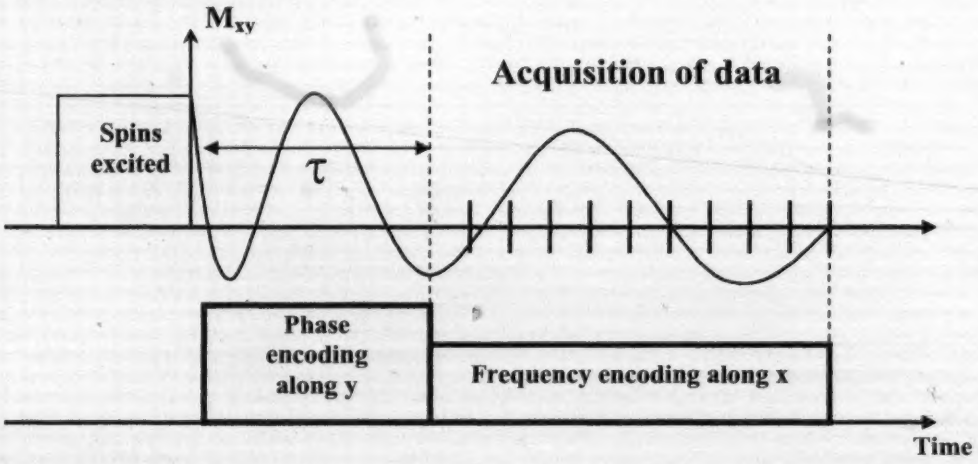

Figure 2-11: Basic sequence of events in an imaging experiment. This sequence is repeated several times, each time with the gradient (G) amplitude varied along the phase encoding axis.

In frequency encoding, data are sampled in the presence of the frequency encoding gradient. Hence, each subsequent point will accrue an additional phase offset in time given as,

$$\Delta\phi(x) = \omega(x)\,\Delta t = \gamma G x \Delta t \qquad (2.42)$$

This phase offset is also a function of the x position, where t advances from one data point to the next. For an experiment employing 64 x 64 resolution, this means that 64 samples are acquired with increasing phase angle at each point and additionally, the phase at each specific instant in time is a function of location along the x axis.

In phase encoding, the gradient is applied for a constant time period (Edelstein *et al* 1980). To add a different phase value to the spins with each repetition of the above sequence of events, the gradient amplitude is varied. Hence,

$$\Delta\phi(y) = \Delta\omega(y)\,\tau = \gamma\,\Delta G y\,\tau \qquad (2.43)$$

From the point of view of the rotating frame, frequency encoding divides the spins such that those experiencing the most positive gradient amplitude spin the fastest, whereas those with the most negative amplitude spin more slowly. This difference in precession rates of the spins permits frequency encoding. Phase encoding is similar in that although it begins in an identical manner to frequency encoding (a gradient is applied that induces a temporary separation in precessional frequencies), it does not remain applied. Because of this, the spins revert to a common precessional frequency along a given x position, but now exhibit unique phases.

A Fourier transform analysis of the recorded time domain signal can help recover the magnetization at each frequency or position during the application of gradients. In spatial encoding an x and a y gradient (G_x, G_y) are applied to a spin system in order to perform frequency and phase encoding. The receiver coil spans the extent of the sample and the detected signal S(t) is given by integrating the magnetization M_{xy} over the range of x and y positions as,

$$S(t) = e^{(-i\gamma B_0 t)} \iint M_{xy}(x,y) e^{(-i\gamma G_x x t)} e^{(-i\gamma G_y y t)} dx dy \qquad (2.44)$$

The above relationship is expressed in the rotating frame as,

$$S(t) = \iint M_{xy}(x,y) e^{(-i\gamma G_x x t)} e^{(-i\gamma G_y y t)} dx dy \qquad (2.45)$$

Keeping in mind that the Fourier transform (FT) is,

$$F(\omega) = \int_{-\infty}^{\infty} f(t) e^{-i\omega t} dt \qquad (2.46)$$

The substitution of $\omega = \gamma G t$, and extension in 2 dimensions demonstrates that equation 2.45 can be a 2D FT. But K is used instead of ω and is given as,

$$K = \gamma G t \quad \text{(for rectangular gradients) or}$$
$$\gamma \int G(t) dt \quad \text{(for arbitrary shaped gradients)} \qquad (2.47)$$

Hence the NMR Fourier space is called K-space given by,

$$K_x = \gamma G_x t \tag{2.48}$$

$$K_y = \gamma G_y t \tag{2.49}$$

Combining equations 2.48 and 2.49 with equation 2.45, we get,

$$S(K_x, K_y) = \iint M_{xy}(x, y) e^{(-iK_x x)} e^{(-iK_y y)} dx dy \tag{2.50}$$

$$= FT \{M_{xy}(x, y)\}$$

The inverse Fourier transform (IFT) of the detected signal recovers the spatial distribution of the transverse magnetization (magnetization content at each x-y location).

$$M_{xy}(x, y) = IFT \{S(K_x, K_y)\} \tag{2.51}$$

2.9.3 Notes on K-space

Knowledge of K-space can aid in understanding how data are acquired with different pulse sequences. Based on equation 2.50, the FT relates spatial position and K-space. Hence, K-space is like frequency space, but more insightfully is a net gradient area space. The distance ΔK, that separates adjacent sampled data points in the phase and frequency axes is denoted by,

$$\Delta K_{phase} = \gamma \Delta G \tau \tag{2.52}$$

$$\Delta K_{frequency} = \gamma G \Delta t \tag{2.53}$$

The method by which data are acquired to form an image can be visualized by virtue of K-space diagrams or trajectories. Different MRI sequences sample K-space in different formats. For conventional sequences (typical spin echo or gradient echo (Figure 2-12)), one K_x line is acquired with each RF pulse, however fast imaging methods such as echo planar imaging (EPI) sample K-space entirely (all lines) after a single excitation pulse (Figure 2-13).

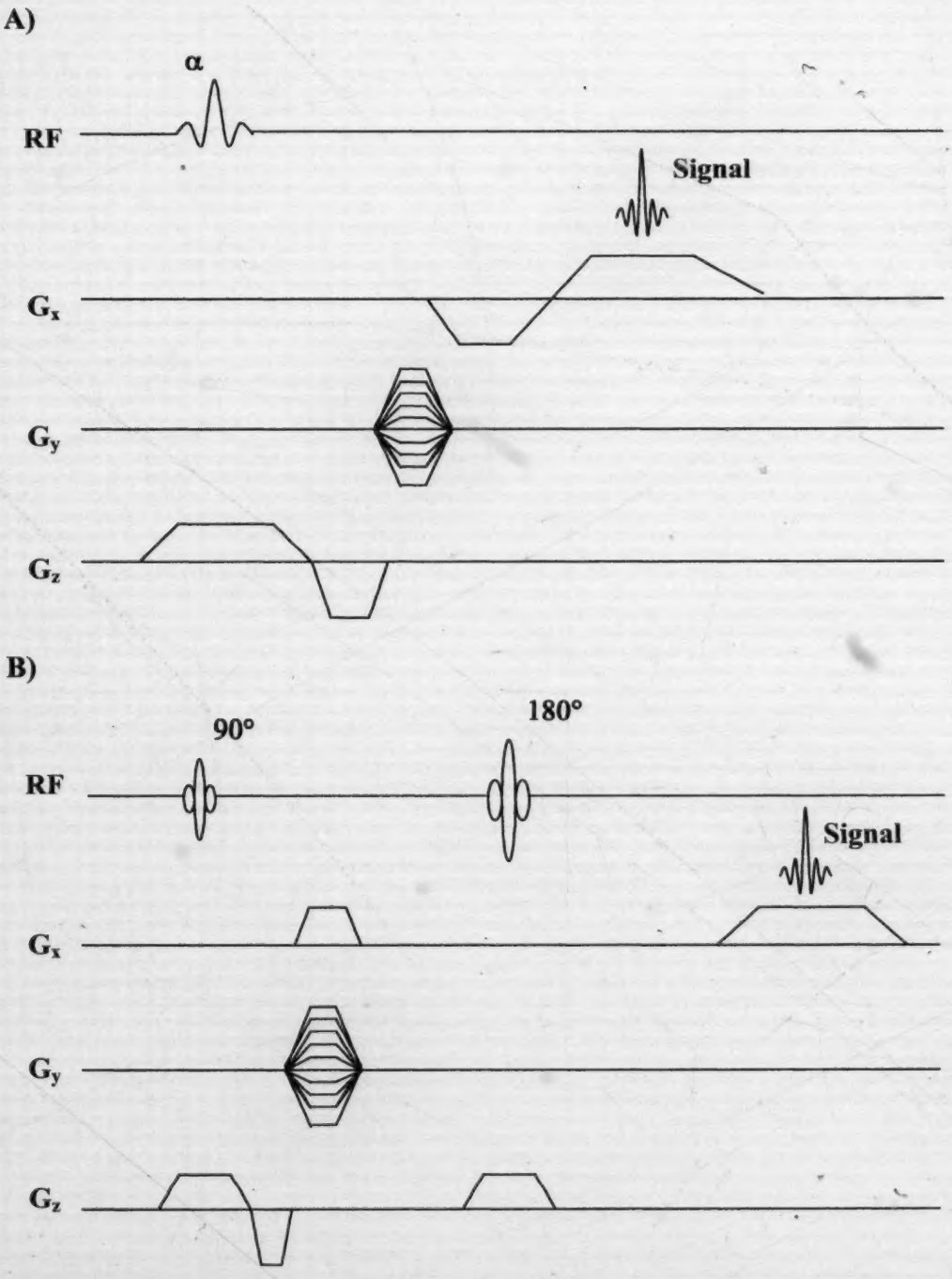

Figure 2-12: Pulse sequence diagrams for A) Gradient echo and B) Spin echo sequences (Gz refers to the slice select gradient reviewed in section 2.9.4).

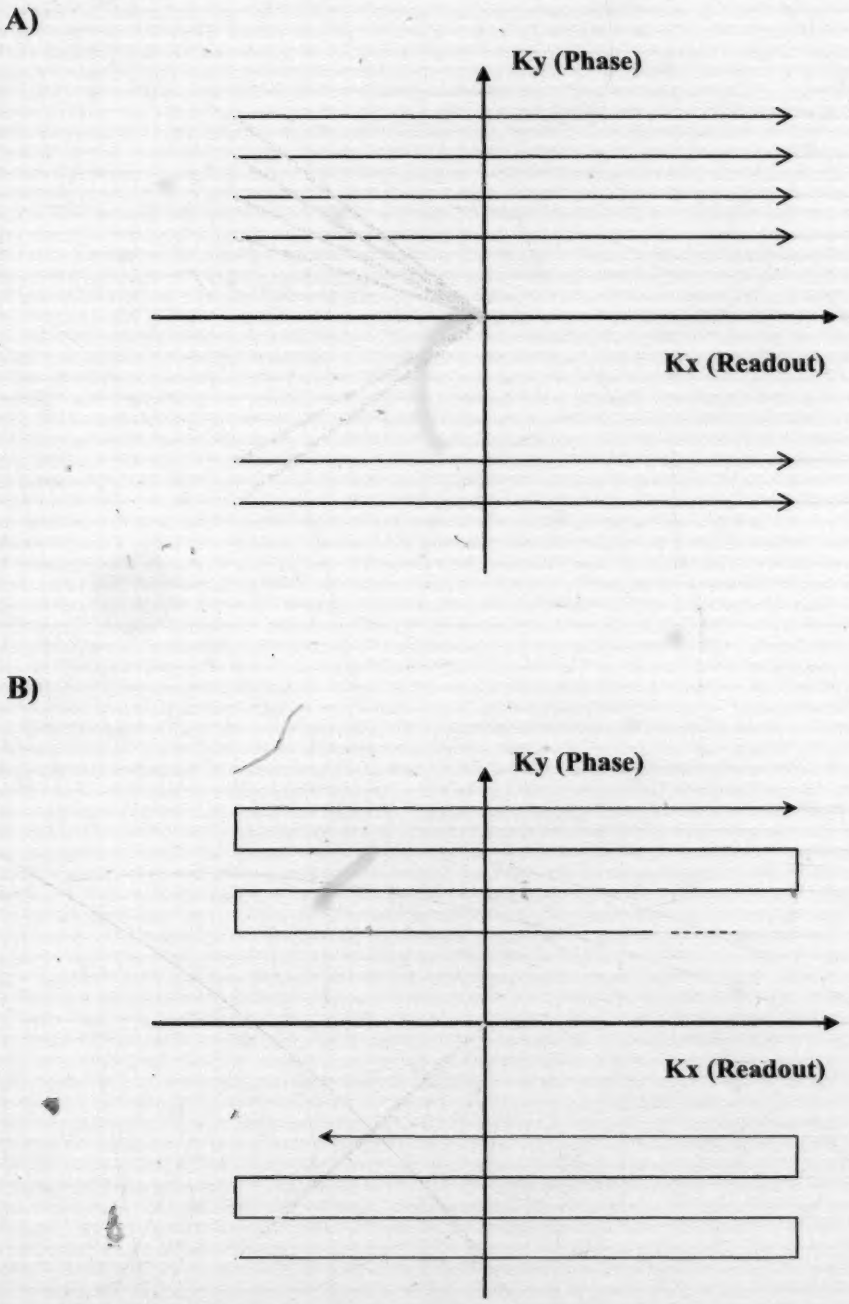

Figure 2-13: A) Line by line data acquisition scheme (K-space trajectory) employed in conventional gradient echo or spin echo imaging. B) K-space trajectory used in EPI, where all lines are acquired following a single excitation.

2.9.4 Slice Selection

Spins within a specific slice can be excited by the process of spatially selective excitation, leaving spins in other areas unaffected. In slice selection, a slice selective gradient and a spatially selective pulse are introduced. During RF excitation, a gradient is applied perpendicular to the imaging plane in order to differentiate spins in a given direction z (slice selective direction). By creating a spectrum of precessional frequencies along z, a segment of these spins (within a slice) can be preferentially excited by modulating the B_1 RF carrier envelope such that the excitation bandwidth of the RF pulse is matched to the frequency band occupied by the spins.

Assume a slice with thickness, Δz is centered at $z = z_0$. By applying a z gradient, the precessional frequency of bandwidth (BW) of the slice will be,

$$\begin{aligned}\Delta\omega &= \omega_{top} - \omega_{bottom} \\ &= \gamma [B0 + G_z(z_0 + \Delta z/2)] - \gamma [B_0 + Gz(z_0 - \Delta z/2)] \\ &= BW_{rf}\end{aligned} \qquad (2.54)$$

The approximate relationship between the slice profile and the excitation pulse envelope, $B_1(t)$, called the small tip angle approximation. This dictates that for flip angles $\leq \pi/2$, the slice excitation profile is the FT of the RF envelope. To achieve uniform selective excitation across a rectangular slice, a boxcar frequency excitation profile is required. Under the small tip angle approximation, this calls for the use of a sinc shaped RF pulse envelope in the time domain.

By applying the slice select gradient, the fanning of precession frequencies also results in a detrimental dephasing related signal loss in the slice select direction. In order to compensate for this dephasing, consider that at time t=0 (corresponding to the center of the RF pulse in the slice select axis), the spins in a given slice are instantly excited. For a height, z, the transverse magnetization acquires a phase (in the rotating frame) given by,

$$\phi(z, t) = -\gamma G_{\text{slice select}}\, z\, t \qquad (2.55)$$

If this slice is assumed to be a slab consisting of smaller slices at different z positions, then according to equation 2.55, this results in dephasing and in the end, signal loss. The solution is to reverse the gradient, where an opposite polarity gradient field will revert the accrual such that all excited spins have zero initial phase. The dephasing starts at excitation, t=0, and stops when the slice select gradient is turned off. The total phase acquired is denoted by,

$$\phi = -\gamma z \int_0^T G_{slice\ select}\, dt \qquad (2.56)$$

where $\int_0^T G_{slice\ select}\,dt$ is the area under the gradient

The reversal of phase effects is conducted by the following relationship,

$$\frac{\left|\int G_{refocus}\,dt\right|}{\left|\int G_{slice\ select}\,dt\right|} = 0.5 \qquad (2.57)$$

To implement a refocusing gradient, a negative polarity and any combination of gradient amplitude and duration in accordance with equation 2.57 should be applied.

2.10 Concluding Remarks

This chapter has outlined the fundamental principles required for an imaging experiment. This sufficient background will enable the reader to move on to chapter 4- Diffusion Tensor MRI. Further details of advanced sequences such as the echo planar imaging method with more underlying theory can be found in chapter 5.

3

THE HUMAN BRAIN: FOCUS ON AGING AND STROKE

The interaction of humans with their environment is controlled by the nervous system, a complex communication network. Human reaction is determined by the central nervous system (CNS) based on the information relayed from the environment. The central nervous system is bilateral and symmetrical and can be divided into the cerebral hemispheres, brainstem, cerebellum and the spinal cord (Figure 3-1). The idea that the various regions are specialized for different functions is the cornerstone of modern neural science (Kandel *et al* 2000). The brain functions as an ensemble of different processing centers that are linked through neural pathways formed by white matter (WM) tracts.

Each brain hemisphere is concerned primarily with sensory and motor processes on the contralateral side of the body. The ventricles in the brain contain cerebrospinal fluid (CSF). Brain functions responsible for our cognitive abilities occur primarily in the cerebral cortex, which overlies the cerebral hemispheres. The two hemispheres consist of the frontal, parietal, occipital and temporal lobes. These lobes consist of the cortical regions as well as the underlying white matter. The frontal lobe is involved in executive functions, planning for future action, behavior, sequencing of tasks, motor planning and judgment of insight. The parietal lobe regulates somatic sensation and body image and the occipital lobe regulates vision. Functions such as hearing, learning, memory and emotion are controlled by the temporal lobe. Each lobe has convolutions, the crests of these convolutions called *gyri* and intervening grooves referred to as *sulci* (Kandel *et al* 2000).

All information related from the body to the cerebrum and cerebellum, and vice versa traverses the brainstem, which comprises the medulla oblongata, pons and midbrain. Several cranial nerves also emerge from the brainstem, and it is involved in cardiovascular control, respiratory control, and regulation of pain sensitivity, alertness and consciousness. The cerebellum lies behind the pons and plays a crucial role in the integration of sensory perception and motor output. Several neural pathways link the cerebellum with the motor cortex, which conveys information to the muscles causing them to move. Other neural pathways link the cerebellum to the spinocerebellar tract, which provides feedback on the position of the body in space. The cerebellum integrates these pathways and utilizes the constant feedback on body position to fine-tune motor movements (Kandel *et al* 2000).

This chapter aims to review brain organization at the microscopic and macroscopic levels and involves a discussion on the structural and organizational aspects of white matter as pertains to diffusion tensor imaging (DTI). The main focus of this chapter is to tie in the fundamental background of human neuroanatomy and function to vital processes such as aging and stroke, two of the studies that form a part of this thesis.

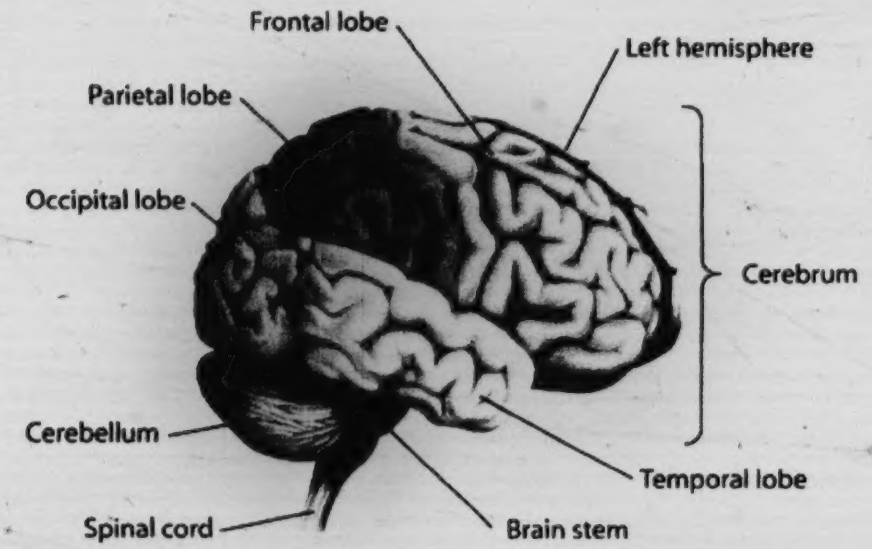

Figure 3-1: An illustration of the human brain with several regions labeled. (Source: Heart and Stroke Foundation of Canada)

3.1 Microscopic Organization of the Brain

The brain is made up of individual units- neurons (or nerve cells) and glial cells. Neurons are highly specialized in receiving, processing, integrating and transmitting information. This information is relayed through chemical and electrical signaling. The human brain contains approximately 10^{11} neurons with anywhere from 10^{13}-10^{14} connections (or synapses) between these neurons (Beatty 2001).

The neuron is composed of a cell body or soma, dendrites and an axon. The cell gives rise to dendrites and axons. The axon is the transmitting component of the neuron. Axons can differ in length (up to 1.0 m) and are usually thin (0.2 – 20 μm) relative to the diameter of the cell body (up to 50 μm or more). The region of the cell body from where the axon emerges is termed axon hillock. Axons are insulated by a fatty myelin sheath, which is interrupted at regular intervals by regions called the nodes of Ranvier (figure 3-2). Branches of the axon from one neuron (pre-synaptic neuron) form synaptic

connections with the dendrites or cell body of another neuron (post-synaptic neuron). The branches of the axon may synapse with as many as 1000 other neurons. Synaptically connected groups of neurons of the same type form ensembles referred to as neural centers that perform specific functions.

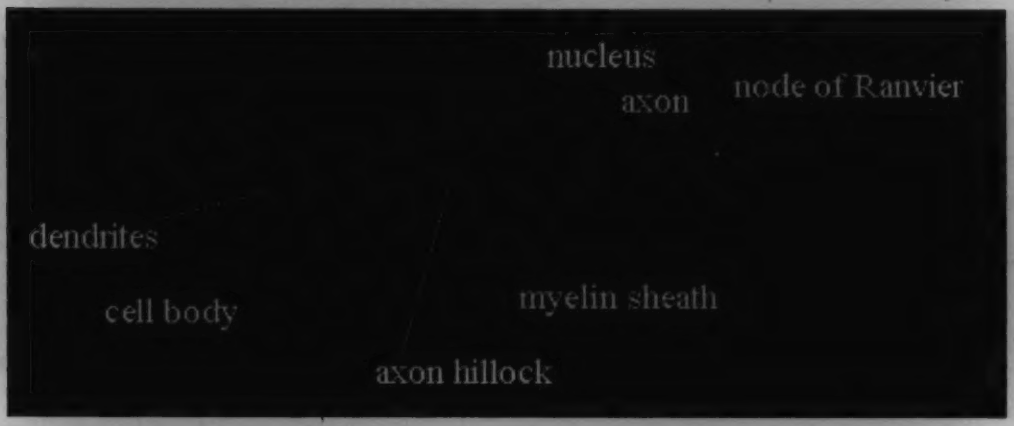

Figure 3-2: Simple diagram of a neuron. The axons from the cell body form white matter (WM). Several axons combine together to form a WM fiber tract.

3.2 Macroscopic Organization of the Brain

Macroscopically, the brain comprises three main categories- the two tissues, gray matter (GM) and white matter (WM), and CSF. GM is formed by the aggregation of neuronal cell bodies, dendrites, terminal arborizations of the axons and glial cells. WM is composed of groups of axons (nerve bundles or fasciculi) that connect different GM regions. GM is distributed at the exterior of the brain, forming its cortex, in the cerebellum, in the brainstem, and also at the center of the brain in the basal ganglia (comprising the globus pallidus, putamen and caudate nucleus), hippocampus, amygdala and central nuclei of the thalamus and hypothalamus (Warner 2001). The WM tracts constitute a large part of the subcortical tissue of the two hemispheres. The role of GM is to process information and generate signals that are communicated by WM pathways.

3.3 White Matter Organization

WM fibers range from 1 mm to 1 m in length. Information within and between neurons is conveyed by electrical and chemical signals. Transient electrical signals can transfer information rapidly and over long distances. These signals, in the form of receptor potentials, synaptic potentials and action potentials are all produced by temporary changes in the current flow into and out of the cell that drives the electrical potential across the cell membrane away from its resting value (Kandel *et al* 2000). The intraaxonal environment contains microtubules, neurofilaments and microfilaments.

Myelin is composed of multiple lipid bilayers. This composition allows myelin to envelop tightly around axons, speeding communication throughout the brain by insulating these neural wire connections. Myelin is formed by oligodendrocytes, which are small cells with many processes. A single oligodendrocyte forms myelin sheaths around many axons by wrapping its plasma membrane around the axons. Although myelin comprises ~50-60% of the weight of WM (Hildebrand *et al* 1993), unmyelinated axons are not uncommon in the brain (Aboitiz *et al* 1992).

The terms generally used to characterize WM are tracts and fasciculi. A tract may consist of several nerve fibers with a common origin and destination. However, a distinct group of nerve fibers is referred to as a fasciculus or peduncle. The merging, splitting and criss-crossing of different nerve bundles, or different tracts result in complex fascicular structures.

3.3.1 Structural and Functional Characteristics of White Matter

WM comprises 50% of the adult human brain by volume (Zhang and Sejnowski 2000). WM fiber tracts are organized into 3 main categories of projection, commissural and association fibers. The *association fibers* link one portion of the cortex with another in the same hemisphere. Some association pathways are very short, joining adjacent cortical regions, whereas others are much longer, connecting cells in different cortical lobes. The two types of association fibers are the short arcuate fibers (U fibers) and the long fibers. The short fibers connect adjacent gyri whereas the long fibers link cortical areas that are spread apart. Fibers that link the two hemispheres are termed *commissural fibers*. The most massive system of commissural fibers is the corpus callosum. In humans, the anterior commissure forms a second much smaller pathway between the right and left cerebral hemispheres. The remaining portion of the white matter connects the cortex with the brain stem. These are the *projection fibers* and may be either ascending or descending. Many of the projection fibers link the thalamus and the cortex. Other projection fibers connect the cortex with more caudal regions of the brain stem and spinal cord (Beatty 2001).

Of all WM tracts, the corpus callosum is the largest. Belonging to the class of commissural fibers, this tract runs left-right connecting homologous cortices of the left and right hemispheres. It consists of approximately 200 million transcallosal fibers and is involved in communication among sensory, motor and association areas thus serving as an important inter-hemispheric brain structure (Demeter *et al* 1988; Tomasch 1954). Other fibers deserving mention are those of the internal and external capsules included in the group of projection fibers. The internal capsule, through which almost all information to and from the cerebral cortex passes, is divided into two segments- the anterior and posterior limbs. The anterior limb is related to sensory pathways. The posterior limb of the internal capsule is related to motor and somatosensory pathways (Filley 2001).

Above the internal capsule is a collection of fan shaped fibers called corona radiata. Superior to this structure is found the white matter region called centrum semiovale, which is located below the cortical mantle. WM tracts are also classified based on their location. Examples are *periventricular WM* referring to fiber tracts that lie adjacent to the lateral ventricles and *subcortical WM* that refer to WM tracts in the gyri just below the cortex (Filley 2001).

3.4 Blood Supply of the Brain

The human brain forms 2% of total body weight, receives 15% of the cardiac output and takes up 20% of the oxygen used by the body. This level of blood supply and oxygen is needed by the brain to sustain its high metabolic requirements. The total blood flow to the brain ranges from 750 to 1000 ml/min and about 350 ml/min of this amount flows only through the vertebrobasilar system. The flow per unit mass of GM is 4 times that of WM and increases with activity (Kandel *et al* 2000).

The aorta is the main artery of the body. It supplies blood to all parts of the body with the exception of the lungs. The aorta ascends from the heart and forms an arch, the aortic arch, which divides into the brachiocephalic artery, the left common carotid artery and the left subclavian artery. The brachiocephalic artery further divides into the right subclavian and the right common carotid artery. Each subclavian artery branches off into a vertebral artery on each side. Each common carotid divides into an external carotid artery (ECA), which supplies blood to the face, scalp, skull and meninges and an internal carotid which supplies the brain with blood (Kandel *et al* 2000).

Each internal carotid artery (ICA) ascends along one side of the neck. The ICA enters the cranium through the carotid foramen (a small opening), further penetrating the dura (membrane that envelops the brain and spinal cord) and branches into the anterior and middle cerebral arteries (Kandel *et al* 2000) (Figure 3-3). This section aims to briefly review the arterial territories of the brain.

3.4.1 Anterior Cerebral Artery Territory

Large branches of the anterior cerebral artery (ACA) supply the cortex and WM of the inferior frontal lobe, the medial surface of the frontal and parietal lobes and the anterior portion of the corpus callosum. Smaller penetrating branches supply the deeper cerebrum, including limbic structures (hippocampus and amygdala), head of the caudate nucleus and the anterior limb of the internal capsule (Kandel *et al* 2000).

3.4.2 Middle Cerebral Artery Territory

The branches of the middle cerebral artery (MCA) supply most of the cortex and WM tracts in the frontal, parietal and temporal lobes. Smaller lenticulostriate arteries supply

the deep WM and diencephalic (posterior subdivision of the forebrain) structures such as the posterior limb of the internal capsule, the putamen, the outer globus pallidus and body of the caudate (Kandel *et al* 2000).

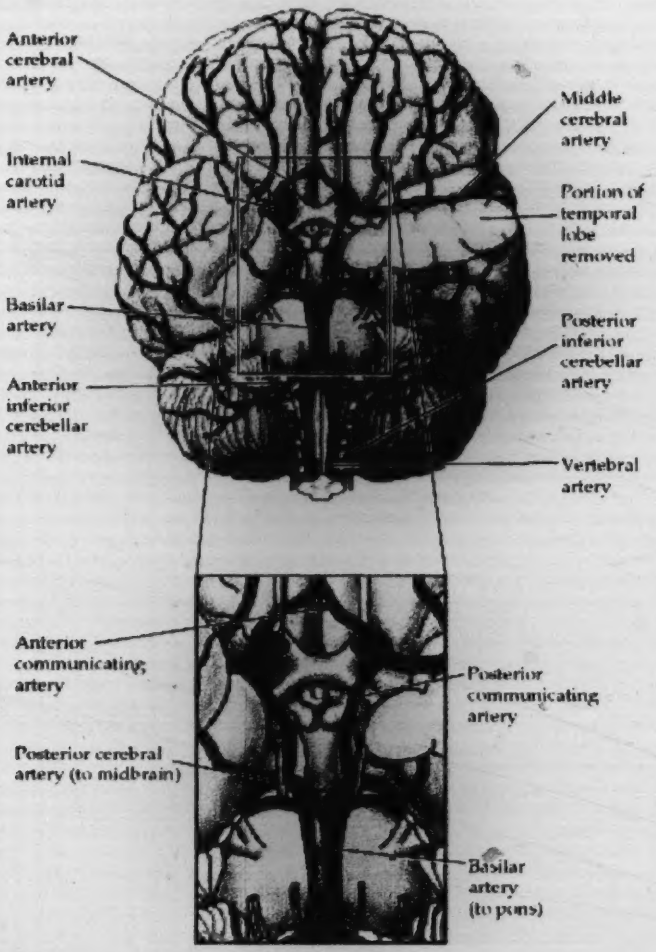

Figure 3-3: A schematic of the major arteries of the brain. The enlargement of the boxed area displays the circle of Willis (Source: http://www.ncbi.nlm.nih.gov/books (Purves *et al* 2001)).

3.4.3 Vertebral Arteries

The left and right branches of the vertebral arteries arise from the subclavian arteries and enter the cranium through the foramen magnum. Each artery gives off an anterior spinal

artery and a posterior inferior cerebellar artery. The vertebral arteries join together at the ponto-medullary junction of the pons to form the basilar artery. At the level of the pons, the basilar artery gives off the anterior inferior cerebellar artery and the internal auditory artery. The penetrating arteries coming off the basilar artery supply brainstem WM. At midbrain level, the basilar artery gives off the superior cerebellar artery which supplies cerebellar WM (Filley 2001; Kandel *et al* 2000).

3.4.4 Posterior Cerebral Artery Territory

The basilar artery branches into two posterior cerebral arteries (PCA) supplying the inferior temporal and medial occipital lobes and the posterior portion of the corpus callosum. Smaller penetrating branches of these vessels supply the thalamus and subthalamic nuclei and parts of the midbrain (Kandel *et al* 2000).

3.4.5 Collateral Blood Supply to Brain

Cerebral collateral circulation is important in the brain for maintaining a nominal level of blood flow in case of obstructive diseases or when the principal channels fail (Liebeskind 2003). The arterial network comprises the extracranial and intracranial routes. The intracranial collateral vessels are made up of the *primary collaterals* consisting of the arterial segments of the circle of Willis used in cases of acute need, and the secondary collaterals such as the ophthalmic artery and the leptomeningeal vessels, which develop due to an ischemic stimulus when primary collateral flow is insufficient (Liebeskind 2003). The leptomeningeal vessels are present or develop between the ACA, MCA and PCA. They can also serve as an important connection between the ICA and the vertebrobasilar system (Liebeskind 2005).

3.4.5.1 Circle of Willis

The two ACAs are connected by the anterior communicating artery. The PCAs are connected to the ICAs by the posterior communicating arteries. The circle of Willis is therefore made up of the proximal PCAs, the posterior communicating arteries, the ICAs prior to their bifurcations, the proximal ACAs and the anterior communicating artery (Figure 3-3). The circle of Willis provides an overlapping blood supply. Such interconnections between the blood vessels (anastomoses) help support the brain when part of its blood supply is blocked (Liebeskind 2005).

Collateral support in the anterior portion of the circle of Willis is provided through the anterior communicating artery and by the reversal of flow in the proximal ACA. The posterior communicating arteries may provide collateral blood flow support in either direction between the anterior and posterior circulations. The proximal PCAs at the posterior end of the circle of Willis make up for an alternative source of collateral blood flow support (Liebeskind 2003).

3.4.5.2 Ophthalmic Artery

Collateral flow can also be established by the reversal of flow (retrograde flow) through the branches of the ophthalmic artery between the ECA and the ICA. This type of flow through the ophthalmic artery is a mark of reduced cerebral perfusion pressure (Liebeskind 2005).

3.4.5.3 Leptomeningeal Collaterals

Leptomeningeal arteries are pial arteries that serve as connecting branches between two major cerebral arteries supplying two different cortical territories. The direction of blood flow in these vessels is dependent on the hemodynamic and metabolic circumstances of the two connected territories (Liebeskind 2005). Leptomeningeal anastomoses between the distal segments of the major cerebral arteries provide supplementary collateral blood flow. The number and size of these anastomotic vessels is greatest between the anterior and middle cerebral arteries, and diminishes with connections between the middle and posterior cerebral arteries, further decreasing between the posterior and anterior cerebral arteries. Similar collateral connections are also found between the vertebral and basilar segments of the posterior circulation through the major cerebellar arteries. Other collateral routes comprise the link between the external carotid artery and the vertebrobasilar system through the branches of the occipital artery (Liebeskind 2003).

There is considerable inter-individual variability of leptomeningeal vessels. The presence of flow in these vessels is associated with poor hemodynamic status where collateral blood flow through the circle of Willis was insufficient (Liebeskind 2005).

3.5 Aging of the Human Brain

To understand the complex process of aging of the brain, one must have a firm grasp on the developmental aspects of the CNS. WM and GM differ significantly in their patterns of development. Nerve cells begin to develop early in gestation with the entire complement of CNS neurons formed prior to birth. In contrast WM does not begin to form until the second trimester of gestation. The process is only partially completed at birth and is only 90% complete by age 2. The remaining period of myelination is prolonged with recent studies indicating that it may well continue throughout the end of the 6th decade of life. Of the major WM tracts, the association and commissural fibers are known to be the last to myelinate (Filley 2001).

3.5.1 Structural Changes with Aging

Age-related decreases in brain weight, gyral atrophy, and an increase in the volume of the lateral ventricles have been reported previously (Kemper 1994). Brain volume appears to

remain constant until age 50, after which a 2% decrease per decade was observed. One factor influencing brain volume has been identified as atrophy of the gyri in the frontal, temporal and parietal lobes and parasagittal brain regions, which starts at age 40 and strongly correlates with increasing age. A second factor resulting in an age-related brain volume decline is an increase in volumes of the lateral ventricles and subarachnoid spaces beginning during the sixth decade of life (Kemper 1994). In a quantitative MRI study, Courchesne *et al.* reported a 25% increase in the intracranial CSF volumes in older adults (>60 years) from 14% increases in young and middle adulthood (Courchesne *et al* 2000). Pfefferbaum *et al.* showed an increase in CSF volumes of 25% and 33% for cortical and ventricular fractions from young and middle (20-50 years) to late adulthood (50-75 years) (Pfefferbaum *et al* 1994).

Age-related progressive losses (34-53%) in nerve cells of small (~12-19 μm) and large (>19 μm) diameter were observed in gyral regions of the superior frontal, superior temporal, postcentral, precentral and inferior temporal gyri (Kemper 1994). In the putamen, cell declines of 27-30% were noted in individuals between ages of 55 and 65 years. Previously, the loss of myelin has been implicated in the decline of brain volumes resulting in increased GM/WM ratios (Kemper 1994). A study by Miller *et al.* reported GM/WM ratios of 1.3, 1.1 and 1.5 at 20, 50 and 100 years of age, respectively, reflecting the deficiency of WM in early and very late adulthood with relative parity between the two tissues in midlife (Miller *et al* 1980). Marked age-related losses of myelin staining were found in the anterior frontal, temporal and superior parietal WM regions (Kemper 1994). In a postmortem study of aged human brains, Meier-Ruge *et al.* reported 10-15% fewer myelinated nerve fibers of >1 μm in diameter, and an increase in extracellular space in the corpus callosum, gyrus rectus and precentral gyrus (Meier-Ruge *et al* 1992). Tang *et al.* have reported a 27% decrease in the length of myelinated fibers in WM brain regions of older (>60 years) individuals (Tang *et al* 1997). These studies reflect the extent of the various structural changes impacting GM and WM tissues in the aging human brain.

3.5.2 Functional Consequences of White Matter Loss in Aging

There are several functional consequences to cerebral WM changes in aging. Although WM loss is confirmed in the course of aging, in the presence of Alzheimer's disease (occurring mainly in late adulthood) GM losses can further accentuate the reduction in brain volume (Filley 2001). However increases in sulcal CSF fluid volume have been associated with mainly a loss of WM, not GM. Stereoscopic methods reveal that 10% of neocortical cells are lost during normal life span. But there is no evidence of a correlation between the number of neurons in the aging human brain and any cognitive test measures.

Animal studies of aging point to a slowing of conduction velocity between the basal forebrain and the neocortex, suggestive of age-related decreases in subcortical myelin (Aston-Jones *et al* 1985). Some reports have linked WM loss in aging to subcortical myelin decline (Malone and Szoke 1985). Other reports point to the free radical mediated

attacks on myelin that increase with aging thereby leading to a gradual myelin breakdown (Weber 1994).

Conventional T2-weighted MRI scans reveal widespread WM hyperintensities reflective of WM instability or decline in normal elderly subjects. In most elderly patients, WM lesions are strongly correlated with cardiovascular disease and are likely the result of cerebral ischemia. Age-related WM lesions may also be linked to diffuse areas demyelination that represents the histologic correlate of periventricular T2-weighted WM hyperintensities commonly seen in elderly patients at risk for cerebrovascular disease (Pugh and Lipsitz 2002). To that effect, other imaging studies indicate that cerebral WM abnormalities are related to attenuated performance on tasks requiring processing speed, immediate and delayed memory, executive functions and indices of global cognition. Although the changes in myelinated systems would be expected to affect all cognitive functions in aging, the impact would logically be more apparent in the frontal lobes in the form of poor frontally mediated tasks due to the abundance of WM tracts in that area (Filley 2001).

3.6 Stroke

The perfusion state of a tissue in which the blood supply does not match the demand is called *ischemia* (Hochachka *et al* 1996). Depending on the severity of this condition, after a certain time period, any tissue will succumb to ischemia. The brain, and in particular neurons, are very susceptible to inadequacies in blood supply. Metabolically active cells like neurons rely on the oxidation of glucose and subsequent mitochondrial ATP production for their functioning and survival. Neurons, in contrast to other metabolically active cells contain larger glucose stores, where anaerobic inhibition of mitochondrial oxidative phosphorylation will rapidly result in dysfunction and cell death (Fiskum *et al* 1999). WM is highly susceptible to cerebral ischemia, where its pathology is manifested by damage to oligodendrocytes, myelinated axons and glial cells (Dewar *et al* 2003; Pantoni *et al* 1996; Petty and Wettstein 1999; Stys 2004). Severance of the central axonal pathways causes disruption of signal transmission (Stys 2004) and can lead to sensory and motor impairments, and neurocognitive decline (Filley 2001; Leys *et al* 1999).

Stroke is the direct result of prolonged cerebral ischemia. In ~20% of human stroke cases, the main cause of circulatory disturbance is not the occlusion, but a rupture of a vessel, resulting in intracerebral or subarachnoid hemorrhage. These cases are aptly termed hemorrhagic strokes. The remaining 80% of strokes are ischemic in origin and termed, 'ischemic strokes'. Ischemic strokes can also be classified in terms of mechanism into embolic and thrombotic strokes. Embolic strokes are characterized by the blockage of a blood vessel by a blood clot or an embolus that travels through the bloodstream into cerebral circulation. Thrombotic stroke is the result of blood clot (thrombus) formation in situ. The onset of stroke is evident from the dysfunction of specific brain regions resulting in sudden focal neurological deficits such as vision and speech impairment, loss of balance, or numbness or weakness of the face, arm or leg.

3.6.1 Risk factors and epidemiology of stroke

The main risk factors for stroke are age, presence of diabetes, smoking, and hypertension. Stroke symptoms consist of focal symptoms of weakness or speech impairment, trouble seeing in one or both eyes, and loss of balance or coordination (Broderick *et al* 2007).

In Canada, between 40,000 to 50,000 people suffer from strokes each year, which is a prevalence of ~0.16%. Currently, 300,000 Canadians are living with the effects of stroke. Of the 100 people who are afflicted with stroke, 15% die, only 10% recover completely, 25% recover with a minor impairment or disability, 40% remain with moderate or severe impairment and 10% are severely impaired to point of requiring long term care (Statistics & Background Information - Stroke Statistics 2006). Eight to twelve percent of ischemic strokes and 37% to 38% of hemorrhagic strokes result in death within 30 days (Heart disease and stroke statistics- 2007 update 2007). As a result stroke, which ranks 3rd among natural causes of death behind heart disease and cancer, represents a progressive disease entity despite the major advances in science. In 2002, the estimated cost of stroke was $2.7 billion, reflecting grave social and economic consequences.

3.6.2 Pathology of Ischemic Infarction

The loss of oxygen supply to neurons due to an embolus, thrombosis or prolonged hypotension leads initially to malfunction within a few seconds. If the ischemic insult is prolonged, the high energy dependent sodium (Na^+)-potassium (K^+) pump begins to fail. This pump functions in maintaining a tenfold difference in extracellular to intracellular Na^+ concentration. Failure of the pump results in an inflow of Na^+, water and calcium (Ca^{2+}) ions from the extracellular to the intracellular space (Auer and Siesjo 1988). The cell swells, producing cytotoxic edema thereby diminishing the area of the extracellular space (Klatzo 1987). In the presence of reduced oxygen supply, the endothelial cells begin to lose their function and their resultant integrity. Intravascular fluid leaks into the extravascular space producing vasogenic edema that spreads easily through WM owing to its low cellular density and ample extravascular space (Heo *et al* 2005; Klatzo 1987).

Cytotoxic edema predominates during the first 6 hours post ischemia, and is gradually replaced by vasogenic edema which is responsible for an increase in brain volume in the first few days following infarction (Heo *et al* 2005).

3.6.3 White Matter Injury

Reduction of the energy supply leads to a cascade of events including depolarization, influx of Na^+ and the subsequent reverse operation of the membrane protein, the Na^+/Ca^{2+} exchanger which ends in an intracellular Ca^{2+} overload and irreversible axonal injury (Petty and Wettstein 1999; Stys *et al* 1992). The class of clinical strokes restricted to WM areas (25%) associated with ischemia induced WM injury also include axonal

injury, which occurs at the margins of gray matter ischemic zones and spinal cord injury in which post-traumatic ischemia plays an important role in tissue injury. Chronic ischemia may also be responsible for the subcortical WM lesions seen in elderly patients in which oligodendrocytes and the myelin sheath are preferentially destroyed (Petty and Wettstein 1999).

3.6.3.1 Role of the Ca^{2+} ion in Ischemia

The inadequate blood supply to white matter results in an attenuation of the Na^+/K^+ ATPase activity. A direct result of this decline in ATP levels is failure of the Na^+ pump with a subsequent elevation in intracellular Na^+, reduction in intracellular K^+, and a massive membrane depolarization that causes the macroscopic 'anoxic depolarization' (Lipton 1999). The influx of Na^+ occurs mainly through a class of Na^+ gated channels referred to as tetrodotoxin (TTX) voltage gated Na^+ channels. Membrane depolarization also triggers the opening of voltage gated Ca^{2+} channels and relieves the block of the N-methyl-D-Aspartate (NMDA) receptor resulting in a large increase in intracellular Ca^{2+} concentrations. In addition the breakdown of the Na^+ gradient disrupts transport processes that depend on this gradient, most importantly the uptake of glutamate from the synaptic cleft. This leads to a disturbance in the operation of the Na^+/Ca^{2+} exchanger, a membrane protein that normally acts to remove intracellular Ca^{2+}, further increasing intracellular Ca^{2+} levels. Two classes of voltage gated Ca^{2+} channels (L-type and N-type) have also been implicated as another source for Ca^{2+} entry in anoxic and traumatic axonal injury. The Ca^{2+} overloading of the intracellular compartment produces permanent injury and loss of function (Petty and Wettstein 1999; Stys 2004).

Increases in intracellular Ca^{2+} concentration are conceivably the cause of axonal damage due to ischemia, which would trigger a cascade of events. These include disintegration of axonal transport and cytoskeletal damage including microtubular disruption and neurofilament sidearm loss resulting from the aberrant activity of Ca^{2+}-dependent enzymatic pathways that initiate protein breakdown or ATP alterations. The involvement of cytoskeleton breakdown in the evolution of ischemic damage in myelinated axons has been shown by the loss of microtubules and neurofilaments from isolated optic nerves under anoxic conditions (Petty and Wettstein 1999).

Despite similarities in structure, central and peripheral WM fibers vary in their response to hypoxia. Central axons are far more sensitive to prolonged periods (>30 min) of hypoxia compared to peripheral axons. Longer periods of exposure to hypoxia result in an ionic deregulation including Ca^{2+} accumulation in the axoplasm (cytoplasmic axon environment). Reoxygenation promotes recovery in peripheral fibers whereas central axons continue to deteriorate in the face of resumed oxygenation (Stys 2004). Astrocytes, a class of star shaped glial cells, are far more resistant to oxygen deprivation than their associated myelinated axons. Oligodendrocytes may be more affected by ischemia due to susceptibility of cells to free radical damage, sensitivity to glutamate toxicity and a greater dependence on oxidative phosphorylation. Like astrocytes, oligodendrocytes can

be damaged by Ca^{2+} influx to the point of structural degradation (Petty and Wettstein 1999).

3.6.3.2 Wallerian Degeneration

The secondary degeneration of WM is divided into retrograde and anterograde or Wallerian degeneration. From the site of the primary lesion, retrograde degeneration proceeds proximally toward the cell body whereas anterograde degeneration moves distally towards the terminals of the axon. Alternatively, Wallerian degeneration is defined as degradation of the distal parts of nerves following injury of the proximal axon or cell body (Koeppen 2004; Luo and O'Leary 2005). This phenomenon is observed in a wide variety of demyelinative, vascular, degenerative, toxic and metabolic diseases (Filley 2001). A WM lesion that injures axons at the site of the lesion is capable of producing damage in others regions of the tract also, the time course lasting from months to years. Wallerian degeneration is characterized by disintegration of axonal structures (microfilaments) within days after injury, followed by myelin breakdown from macrophage infiltration and lastly, atrophy of the tracts.

Studies of experimental models of cerebral ischemia in the first stage have shown degeneration of descending axons in the brain stem detected as early as 2-7 days post onset, with the second stage (2 weeks post injury) reflecting myelin degradation and astrocyte infiltration (Iizuka *et al* 1989; Johnson *et al* 1950; Lexa *et al* 1994). Studies from light and electron micrographs demonstrate buildup of cellular debris and loss of myelinated fibers of injured nerves.

The morphological changes in axons undergoing Wallerian degeneration can be extrapolated from studies focused on diffuse axonal injury, a condition where widespread damage to the axons within WM of the injured brain arises from a traumatic injury (Povlishock and Christman 1995) or ischemic event (Yam *et al* 1998). In the early stages (1-2 days) of diffuse axonal injury, axonal damage is linked to large reactive axonal swellings called retraction balls, whereas in later stages (weeks to months) axonal injury is associated with microglial clusters and Wallerian degeneration. Some of the hallmarks of early axonal damage from diffuse axonal injury as a result of a traumatic episode are impaired anterograde axoplasmic transport from intra-axonal neurofilament misalignment, leading to axonal swelling and disconnection (delayed axotomy) (Povlishock and Christman 1995; Yam *et al* 1998). Furthermore, the disturbances impacting the neurofilament could be due to an imbalance in the plasma membrane of the axon (axolemma) from the entry of Ca^{2+} in the intra-axonal compartment. The resulting ultrastructural changes have been outlined in the previous section (3.6.3.1).

Further insights into axonal changes in Wallerian degeneration can also be obtained from studies of axonal transections in multiple sclerosis (Trapp *et al* 1998). Multiple sclerosis is a demyelinating disease marked by patches of hardened tissue in the brain or the spinal cord. It is interesting to note the ongoing axonal changes in areas of active and chronic cases of demyelination and inflammation of this disease. Active multiple sclerosis lesions

are characterized by loss of myelin and presence of myelin debris within the demyelinated area. Another characteristic of the active lesions is the presence of small-diameter axons and large ovoids (egg shaped terminal axons). However chronic lesions demonstrate scant amounts of small ovoids. Other axons in active lesion zones have constrictions, dilatations or large swellings surrounded by macrophages and microglia (Trapp *et al* 1998).

3.6.4 Ischemic Penumbra and Therapeutic Time Window

The ischemic penumbra constitutes underperfused tissue suffering from ischemia that surrounds the infarcted core, and is at risk of dying, but in contrast to the infarcted core has not been irreversibly damaged (Astrup *et al* 1981). Here, essential energy requiring processes such as the Na^+-K^+ ATPase pump are still able to maintain ionic gradients and hence membrane neuronal integrity. The penumbra was defined in a primate model of MCA occlusion by outlining the thresholds for cerebral ischemia (Jones *et al* 1981). Jones *et al.* showed that when local cerebral blood flow (CBF) as measured using a hydrogen gas clearance method fell below 23 ml/100 g/min, reversible paralysis occurred; although profound ischemia even for brief durations was irreversible. When local CBF fell below 10 ml/100 g/min for 2 hours or below 18 ml/100 g/min during permanent occlusion, irreversible infarction occurred (Jones *et al* 1981). Although Jones *et al.* measured CBF in distinct GM and WM regions such as the insular cortex, caudate nucleus, thalamus, putamen, the internal capsule and centrum semiovale, they did not outline separate thresholds for infraction for the two tissues based on CBF (Jones *et al* 1981). In humans, MRI and positron emission tomography based studies have demonstrated that GM has a higher infarction threshold for CBF and cerebral blood volume (CBV) than WM in patients within 24 hours of ischemic stroke onset suggesting that WM is more resistant to ischemia than GM (Arakawa *et al* 2006; Bristow *et al* 2005; Butcher *et al* 2005; Falcao *et al* 2004; Koga *et al* 2005).

The importance of the ischemic penumbra is the recognition that ischemic processes may be reversible. Theoretically, this zone of inactive but structurally intact tissue is potentially salvageable and can be restored to functional normality if perfusion can be reestablished, or if this zone can be afforded neuroprotection until reperfusion occurs spontaneously (Donnan *et al* 2003). Since penumbral tissue can be identified very early after stroke with the aid of various neuroimaging modalities, particularly MRI (discussed in Section 3.7.5), there is great interest in selecting patients for therapy. Common strategies focus on rapid reperfusion with thrombolytic agents or neuroprotection from the damaging neurotoxic cascade following ischemia.

3.6.4.1 Thrombolytic therapy

Thrombolysis consists of pharmacological dissolution of a blood clot by administration of thrombolytic agents that target the breakdown of fibrin, an insoluble fibrous protein formed from fibrinogen during the clotting of blood. Thrombolytic agents are

plasminogen activators, which convert the proenzyme, plasminogen into an active enzyme, plasmin that digests fibrin to soluble degradation products. Tissue plasminogen activator (t-PA) is routinely used in treatment of patients with thromboembolic disease (Collen and Lijnen 2005).

Evidence based on large randomized clinical trials has demonstrated that intravenous administration of t-PA within 3 hours post onset of acute ischemic stroke is safe (Tissue plasminogen activator for acute ischemic stroke. The National Institute of Neurological Disorders and Stroke rt-PA Stroke Study Group 1995). After the 3 hour time window, there is a greater risk of developing hemorrhage and also the benefit of intravenous thrombolysis decreases. Between 3 and 6 hours post ischemic stroke onset, some centers consider treatment with intra-arterial thrombolysis, although there is no wide scale consensus as it is unproven and results from ongoing stroke trials are being awaited (Hjort *et al* 2005; Schellinger *et al* 2004). Intra-arterial thrombolysis is more beneficial in cases of proximal large artery occlusion (Schellinger *et al* 2001). Beyond 6 hours and up to 24 hours post onset, there are a variety of diagnostic and therapeutic practices currently in testing, some involving administration of neuroprotective agents to target the neuropathological cascade of ischemia.

3.6.5 Classification of Stroke: Stroke Syndromes

Clinical classification of stroke is especially important for ischemic stroke due to potentially different etiologic reasons. The clinical examination is vital in the subclassification of ischemic stroke because it serves as a link between researchers who require pathophysiologic information to develop and evaluate new therapies, and clinicians who are required to make rational decisions affecting patient management. Due to an overlap in the presentation of ischemic and hemorrhagic stroke, neuroimaging is required to provide a definitive diagnosis. This section briefly discusses the primary symptoms, vascular territories (outlined in section 3.4) and common etiologies of stroke.

3.6.5.1 Infarction in the MCA territory

Infarction in the MCA territory (cortex and WM) results in the most frequently encountered stroke syndrome with contralateral weakness, sensory loss and visual field impairment. Depending on the hemisphere involved, there can be language disturbances or impaired spatial perception. If weakness is severe (plegia), muscle tone is decreased initially only to recover over days or weeks (Kandel *et al* 2000).

In more than 95% of right handed individuals and in the majority of left handed people, the left hemisphere is dominant for language (Kandel *et al* 2000). Destruction of the left opercular cortex in left-dominant individuals causes disturbance of speech, aphasia. Disturbance of learned motor acts, apraxia, may also occur. The lack of awareness of space and patient's own body contralateral to the lesion, termed hemineglect, may also occur. This is seen more often in the case of non-dominant parietal stroke.

3.6.5.2 Infarction in the ACA territory

Infarction in the ACA territory also causes weakness and sensory loss similar to the convexity lesions, but here the distal contralateral leg is mainly affected. Urinary incontinence may also occur. Aphasia may result from damage to the supplementary motor area (Kandel *et al* 2000).

3.6.5.3 Infarction in the PCA territory

Infarction in the PCA territory results in contralateral homonymous hemianopsia by damaging the calcarine cortex. The inability to read, alexia, may occur if the posterior corpus callosum is involved. If the PCA occlusion is proximal, the resulting lesion may affect - the thalamus causing hemisensory loss and sometimes spontaneous pain, or the midbrain with ipsilateral occulomotor palsy (paralysis) or the corticospinal tract or superior cerebellar peduncle resulting in an inability to coordinate voluntary muscular movements, ataxia (Kandel *et al* 2000).

3.6.5.4 Occlusion of the Carotid artery

Atherothrombotic vessel occlusion commonly occurs in the ICA rather than the intracranial vessels. In a patient with an incomplete circle of Willis, infarction may include territories of both, the MCA and ACA with arm and leg weakness and sensory loss. An alternative cause of leg weakness and sensory loss is the occlusion of the MCA at its proximal stem (Kandel *et al* 2000).

3.6.5.5 Brainstem infarction

Infarction of the brainstem follows occlusion of the vertebral or basilar arteries mainly rather than their medial or lateral branches. Lesions of the posterior fossa are indicated by: 1) bilateral long tract signs (motor or sensory), 2) contralateral motor or sensory signs, 3) cerebellar signs, 4) stupor or coma, 5) nystagmus or disconjugate eye movements and 6) involvement of ipsilateral cranial nerves (Kandel *et al* 2000).

3.6.5.6 Infarction of the cerebellum

Infarcts of the inferior cerebellum with its extensive vestibular connections can result in vertigo, nausea, and nystagmus without other symptoms suggesting disease of the inner ear or vestibular nerve. Superior cerebellar hemispheric infarcts result in gait and ipsilateral limb ataxia (Kandel *et al* 2000).

3.6.6 Quantification of the neurologic deficit

The clinical assessment and quantification of deficits after stroke onset are required for proper patient management. A need to determine the level of impairment is an important factor for the use of several scales to assess patients. Several different impairment scales and scores have been developed to assess the neurologic status at various stages in the course of stroke. In general terms, these scales measure motor function, speech, consciousness and sensation. One such scoring method is the National Institutes of Health stroke scale score (NIHSSS), a widely used scoring system from the American Heart Association. This score will be reviewed briefly since it was used to quantify neurologic deficits of the stroke patients whose MRI data were used in this thesis.

The aim of the scoring systems is to quantify various symptoms and output a final score to grade patient outcome using a numerical approach. The advantage of these scoring systems is that they can be used universally to direct appropriate therapeutic interventions, compare data, recruit patients in various clinical trials, and in clinical studies for making statistical comparisons (Onal *et al* 2001).

The NIHSSS (range, 0 to 42, 0 being normal and 42 implying death) evaluates a variety of neurologic deficits, including motor, sensory, language and visual impairments. It is reproducible, can be quickly performed and correlates with infarct volume and functional outcome 3 months following stroke. It contains 11 items, some of which are not found in other scales (Brott *et al* 1989; Kelly-Hayes *et al* 1998).

3.7 Imaging of Stroke

Brain imaging has been central to the expansion of knowledge in the acute ischemic stroke process. In particular, functional neuroimaging generates maps of brain physiology such as tissue perfusion and metabolism. Imaging of these variables in acute stroke has allowed pathophysiological insights into the understanding of cerebral ischemia thereby providing the justification for clinical trials of thrombolysis and support for animal studies. Imaging techniques are also considered of significant importance in patient management due to their ability to classify patients in the context of pathophysiology rather than solely by clinical or anatomical data (Guadagno *et al* 2004). Neuroimaging offers critical information for proper management of acute stroke patients in terms of accurate identification of ischemic stroke, identification of arterial stenoses and occlusions, prediction of stroke severity, assessment of persistent abnormal perfusion and occlusion, and insights into possible mechanisms of stroke (Sa de Camargo and Koroshetz 2005).

This section aims to briefly discuss the potential advantages and disadvantages of current neuroimaging modalities used to scan stroke patients. The techniques discussed are x-ray computed tomography, positron emission tomography, single photon emission computed

tomography, MRI focusing on conventional MR techniques, and advanced imaging methods such as diffusion and perfusion weighted imaging.

3.7.1 X-ray Computed Tomography

The principle behind x-ray computed tomography (CT) is the same as conventional X-ray imaging. Radiation is passed through tissue from multiple directions. The detectors measure the degree of attenuation of the existing radiation and images are reconstructed in cross section. CT scanning of the brain requires exposure to radiation with the average dose equivalent to the background radiation received in 1 year (Semelka *et al* 2007). Early CT changes are marked by parenchymal hypodensity where an increase in intracellular water components leads to loss of GM-WM differentiation. Also evident, is the phenomenon of cerebral swelling due to an increase in the extracellular water observed as cortical sulci flattening, asymmetry between the sylvian fissures and ventricular compression. CT has 58% sensitivity in stroke detection within 5 hours of onset (Barber and Davis 2003).

The main advantages of CT in stroke are its wide availability and the fact that it is relatively inexpensive. Furthermore, CT is sensitive to hemorrhage and useful for detecting subarachnoid hemorrhage. Also its rapidity is a useful feature when scanning restless stroke patients. The downsides of CT scanning are exposure to radiation, its low sensitivity to infarction in the hyperacute stage (≤ 6 hours post onset), and difficulties in distinguishing acute from chronic infarction. Another limitation includes the poor imaging of posterior fossa structures and lacunar strokes (Barber and Davis 2003).

3.7.2 Positron Emission Tomography

Positron emission tomography (PET) measures regional cerebral blood flow (CBF), consumption of oxygen with the cerebral metabolic rate of oxygen ($CMRO_2$), the consumption of glucose with the cerebral metabolic rate of glucose (CMR_{glc}) and the oxygen extraction fraction. These measures allow the delineation of CBF thresholds for electrical and structural failure and as such PET has enabled a characterization of the ischemic penumbra (Barber and Davis 2003; Bockisch *et al* 2004). In PET, patients are given radionuclide isotopes that are radioisotope labeled biological molecules such as ^{18}F-Fluorodeoxyglucose. As these tracer isotopes decay, a positron (subatomic particle with the same mass as an electron but with positive charge) is emitted. The positron interacts with an electron resulting in the annihilation of both particles and release of 2 Gamma rays that are detected by one of a large number of external detectors configured in one or more rings. Subsequently images are reconstructed.

PET allows the quantification of cerebral blood flow, demonstration of cerebral metabolism and enables mapping of neuroreceptors. It also demonstrates the ischemic penumbra. The disadvantages of PET are that it is costly due to the radioisotopes used, exposure to ionizing radiation, and the technical and logistical issues surrounding the

short half-life of the radioisotopes used. This modality has been limited to research at large tertiary institutions and thus far no standardized image acquisition or analysis protocols for stroke imaging have been outlined, thereby reducing the role of PET in clinical stroke (Barber and Davis 2003; Bockisch *et al* 2004; Wintermark *et al* 2005).

3.7.3 Single Photon Emission Computed Tomography

Single photon emission computed tomography or SPECT can be used to study changes in CBF, to assess the degree and extent of ischemia, yield an understanding of likely pathogenesis and demonstrate collateral flow. In SPECT, radiotracers are distributed in the brain according to the rate of CBF. The emitted photons are then detected using Gamma cameras or Gamma detector systems. High resolution images can be obtained within 20-30 minutes. Images can be reconstructed in any orientation with the matrix of the pixels reflecting the number of counts emitted by the Gamma rays. In areas of reduced perfusion, less radiotracer is emitted and the regions appear less bright. SPECT can give a semi-quantitative and qualitative assessment of blood flow (Barber and Davis 2003).

The main advantages of SPECT are its ability to give perfusion information, demonstration of collateral flow and reveal ischemic tissue in the presence of normal CT and conventional MRI results. Its main limitations are that like PET, SPECT is technically and logistically complex to implement requiring the involvement of operators and nuclear medicine physicians. Additionally, one is exposed to ionizing radiation. To date, there are no standard protocols for SPECT imaging in the realm of acute clinical stroke (Barber and Davis 2003; Wintermark *et al* 2005).

3.7.4 Conventional MRI Techniques

Conventional MRI methods such as T1-weighted or T2-weighted imaging provide alternatives to CT scans, but are less used as screening methods. The advantages of these techniques are the lack of bone artifacts and their superior imaging of the brainstem. However, they are more expensive than CT and are relatively insensitive to ischemic stroke within 6 hours of onset since cytotoxic edema predominates during that time frame. By 12 hours post stroke onset, T2-weighted images show hyperintense signals due to a significant portion of the induced edema being vasogenic in origin (Barber and Davis 2003). Reduced signal intensity on T1-weighted scans is more likely a subacute time frame phenomenon, indicative of prolonged T1 relaxation such as in CSF.

Fluid attenuated inversion recovery (FLAIR) sequences are used in conjunction with other T2-weighted sequences because of the relative conspicuity of any given lesion with a prolonged T2. This method is good for detecting supratentorial lesions, although it is relatively insensitive to brainstem and cerebellar lesions. In some cases, FLAIR demonstrates hyperintense signals within 6-8 hours of stroke onset in the presence of

normal T2-weighted images (Tress 2003). FLAIR is also used in detecting subarachnoid hemorrhage between 12 hours to 7 days post onset (Schellinger *et al* 2003).

Hyperacute parenchymal hemorrhage can also be detected by conventional MRI methods by utilizing one of the T2-weighted magnetic susceptibility sensitive sequences such as T2*-weighted gradient echo. Evidence of intracranial hemorrhage can be seen in hyperacute stages in the form of hypointense regions and also at time points greater than 3 months on T2*-weighted images. The key substrate for the visualization of hemorrhage is the paramagnetic deoxyhemoglobin, which changes the local magnetic field gradient leading to a dephasing of stationary or passing protons inside and in close proximity of the intracranial hemorrhage (Schellinger *et al* 2003).

Conventional MRI techniques are widely available, rapid and non-invasive providing high soft tissue resolution in any orientation. One can also 'weight' images to augment tissue contrast and multiple sequences can be obtained providing more information than from one sequence alone (Barber and Davis 2003). The downsides are that these methods are expensive and are contraindicated in patients with metal fragments, pacemakers and other electronically or magnetically implanted devices. Furthermore, they offer poor sensitivity for infarction in the hyperacute stage and are limited in scope to help stratify patients in acute stroke trials (Barber and Davis 2003).

3.7.5 Diffusion and Perfusion Weighted MRI

One of the important sources of contrast in MRI is the signal loss caused by proton dephasing in the present of coherent and incoherent flow. Random diffusion of protons into areas of varying magnetic field strengths leads to random phase shifts. There is a resultant loss of signal from these protons due to these phase shifts. Protons diffuse greater distances in pure water rather than in tissue water in the span of a 40 ms imaging time. Thus the process of diffusion, comprising the rate and direction of diffusion reflect the hindered motion of water molecules in a given medium. The apparent diffusion coefficient (ADC) quantifies diffusion and proton displacement. The details surrounding diffusion weighted imaging (DWI) have been discussed in great depth in chapter 4 and will not be undertaken in this section except to highlight its role in clinical stroke and outline any associated disadvantages.

The role of DWI in clinical practice became clear when it was noted that the ADC of water was significantly slower in regions of ischemia compared with normally perfused regions of the brain. The ADC was noted to decrease by 30-60% relative to the contralateral region following stroke onset (Moseley *et al* 1990b). Presently, DWI is increasingly used in combination with echo planar imaging (EPI, chapter 5) to detect stroke onset in the clinical realm. The sensitivity of DWI ranges from 57-86% within 2 to 3 hours of stroke onset compared with that of CT (14-43%) within the same time frame (Lansberg *et al* 2000). Furthermore, DWI is more sensitive than CT for picking up changes involving the MCA territory. Also DWI is a more efficient early predictor of the volume of tissue ultimately infarcted compared to CT. Conventional MRI is known to

correctly identify acute cerebral ischemia in 71-80% of the cases and with the addition of DWI, that figure increases to 94%. Inter-observer agreement is better in DWI than in conventional MRI (Tress 2003).

Perfusion weighted imaging (PWI) detects miscroscopic flow at the capillary level and therefore is useful to study changes occurring at the cellular level. The two types of perfusion imaging techniques are: 1) signal monitoring using exogenous contrast agent (e.g. Gadolinium) referred to as dynamic susceptibility-weighted bolus tracking (DSC) MRI and 2) endogenous contrast dependent methods such as arterial spin labeling (Copen and Sorensen 2003). We will focus on the first method as it was primarily used to perform perfusion imaging in stroke patients whose Diffusion Tensor data are used in this thesis.

PWI by DSC MRI is useful and robust for monitoring the underlying hemodynamics in stroke patients. T2*-weighted single-shot echo planar images are acquired sequentially every few seconds (~12 slices every 2 seconds) in order to observe the first pass of an intravenous injection of a bolus of magnetic susceptibility inducing contrast agent through a capillary bed. The reason for using T2*-weighted imaging is because signal decay due to magnetic field inhomogeneities is not refocused as in T2-weighted imaging. A decrease in signal intensity in perfused regions is the result of a decrease in T2* and is dependent on the volume and transit of the contrast agent that perfuses through a given slice. Ischemic areas are identified by either a lesser degree of signal loss, by delays in the arrival of the bolus or by an increase in the transit time of the bolus if the arterial input function can be assessed from bolus dynamics with an artery. Typical maps of relative mean transit time, relative cerebral blood volume, relative cerebral blood flow and relative time to peak are generated from the bolus dynamics to demonstrate regional abnormalities in tissue perfusion (Copen and Sorensen 2003; Wu *et al* 2005).

The presence of the ischemic penumbra (Section 3.6.4) is based on the mismatch between the perfusion rim on perfusion-weighted images (PWI) and the ischemic core outlined from the diffusion-weighted image (DWI) (Karonen *et al* 1999; Schlaug *et al* 1999). The penumbra would be the hypoperfused tissue on PWI that is not yet abnormal on the DWI. The presence of PWI/DWI mismatch is suggestive of a major vessel occlusion, although exceptions can occur. Identification of penumbral zones may be valuable in selection of patients for thrombolytic therapy (up to 6 hours post onset in some cases) which can reperfuse and rescue penumbral tissue and reduce the final infarct size (Hjort *et al* 2005).

Diffusion and Perfusion weighted imaging with EPI are subject to the same contraindications as conventional MRI methods and are bounded by the same challenges of implementing EPI as outlined in chapter 5. These are sensitivity to chemical shift artifacts, susceptibility artifacts that induce image distortions and potential for generating electric currents which can result in muscle contractions and twitching (Barber and Davis 2003).

3.8 Concluding Remarks

This chapter gives an overview of the anatomical and functional aspects of the human brain with a focus on white matter characteristics. The role of white matter in normal human aging and ischemic stroke were elaborated upon since these two conditions have been investigated in detail in this thesis. A discussion of imaging in stroke including MRI and other imaging modalities was also undertaken. Subsequent chapters will give the background of methods used for imaging the white matter areas of the brain with some detailed practical examples.

4

DIFFUSION TENSOR IMAGING

Diffusion MRI generates images representing the spatial distribution of the diffusion coefficient of a molecular species (usually water) on a quantitative level (Le Bihan *et al* 1986). Measurements with this method are based on the NMR signal attenuation phenomenon from the molecular diffusion of water molecules. Diffusion driven water molecular displacements are on the order of micrometers during typical measurement times, thus making diffusion MRI a very powerful tool for probing tissue microstructure. From its early beginnings, diffusion-weighted imaging (DWI) has generated a high level of enthusiasm due to its advanced sensitivity for detecting acute ischemic events (Moseley *et al* 1990b; Moseley *et al* 1990c). At present, the manifold applications of DWI stem from its enhanced sensitivity to the microstructural properties of the brain.

Diffusion tensor imaging (DTI) (Basser *et al* 1994a; Basser *et al* 1994b), an advanced version of DWI is better suited for a more comprehensive evaluation of diffusion changes in complex tissue such as white matter. This heightened sensitivity to the diffusion directionality of water within the tissue microstructure is based on the finding that water diffuses faster along the length of an axon than across or perpendicular to it. The structural and organizational information obtained from a DTI scan serve to complement conventional anatomical exams. In a period of ~13 years, DTI has been applied to a wide spectrum of clinically important areas such as ischemia (Mukherjee 2005; Sotak 2002), neuropsychiatric disorders (Lim and Helpern 2002; Pfefferbaum and Sullivan 2005), aging (Minati *et al* 2007; Moseley 2002), and fiber tracking (Mori and van Zijl 2005).

This chapter reviews the basic physics of diffusion, effects of diffusion on the MR signal, and the design of DWI and DTI techniques with a focus on their respective capabilities and limitations. In addition, various methods of analyzing data derived from DTI are also explored.

4.1 Diffusion: Physical Background

Molecular diffusion refers to the random translational movement of molecules (Brownian motion) resulting from the thermal energy carried by them. Classically, diffusion relates

the macroscopic flux density, J to an established concentration gradient, ∇C by Fick's law (Crank 1975) given as,

$$J = D\nabla C \qquad (4.1)$$

where, D is the proportionality constant referred to as the diffusion coefficient in units of mm^2/s.

The time dependent form of this equation allows one to determine D from the measured concentration profile of a tracer. In this approach, the microscopic displacements are on the order of millimeters and the measurement time is on the order of minutes. The NMR method is different from this method in that it directly monitors the net molecular displacements of an ensemble of spins. The dependence of this displacement on the measurement time was given by Einstein (Einstein 1956) as,

$$\langle r^2 \rangle = 2Dt \qquad (4.2)$$
(or 6Dt, when considering 3-dimensional displacements)

where t is the diffusion time

$\langle r^2 \rangle$ is the mean squared displacement of the spin ensemble and corresponds to the variance of the displacement distribution

D, the diffusion coefficient acts as the proportionality constant

From the above equation, one can obtain order of magnitude estimates of the length scales probed during the diffusion time, t. In the case of brain parenchyma, where the diffusivity of water is estimated at 0.85×10^{-3} mm^2/s (Pierpaoli *et al* 1996), and considering t = 40 ms, which is the norm for diffusion times in clinical experiments, a root mean square displacement of 8 μm is computed. This value approximates the diameter of the axon in brain white matter.

The occurrence of the mean displacement due to the random thermal motion of molecules is best observed in the almost linear dependence of diffusion on temperature (Le Bihan *et al* 1989). From equation 4.2, the diffusion coefficient can be incorporated into the conditional probability distribution that characterizes molecular displacement. The distribution, denoted by $P(r_2, r_1, \tau_D)$ is the conditional Gaussian probability of finding a spin first at point r_1 and then between positions r_2 and $r_2 + dr_2$ after a time interval, τ_D (Einstein 1956). For free diffusion in 3 dimensions, the distribution is,

$$P(r_1 r_2 \tau_D) = \frac{1}{\sqrt{(4\pi D\tau_D)^3}} e\left(\frac{-(r_1 - r_2)^2}{4D\tau_D}\right) \qquad (4.3)$$

This term assumes the role of the diffusion propagator and its Gaussian nature helps quantify the diffusion coefficient with NMR.

4.2 NMR and Diffusion

The effect of diffusion on an ensemble of spins can be understood in terms of the phase, ϕ of the magnetization in the transverse plane of the rotating reference frame and its behavior in an applied magnetic field gradient with amplitude, G. A gradient pulse encodes the static spins in each voxel with a spatially varying resonant frequency and therefore with a characteristic phase dispersion. This phase dispersion tends to get more complicated and incoherent as the spins randomly translate with varying velocity levels in the direction of the applied gradient. The variance of the distribution of intravoxel phase dispersion is magnified in a similar way to the conditional displacement distribution given by equation 4.3 (Le Bihan 1995).

Diffusion-weighting can be explained by considering the phase changes during a simple bipolar pulsed gradient spin echo experiment (Stejskal and Tanner 1965). The general expression for the phase evolution of a spin at position x_1 in the z-axis after a time,τ is given as

$$\phi = \gamma \int G x_1 dt = \gamma G x_1 \tau \qquad (4.4)$$

In the pulsed gradient spin echo sequence or the Stejskal-Tanner sequence, the diffusion gradient is applied in two matched pulses, one on either side of a 180° RF refocusing pulse (Figure 4-1). After the initial 90° RF pulse, the transverse spins experience the first pulsed gradient. During this gradient pulse, the spins undergo a magnetic field dependence on their spatial position. As such, an ensemble of spins rapidly gets out of phase. Following the 180° pulse, the dephased spin ensemble experiences the second matching pulsed magnetic field gradient. If the spin spatial positions remain identical between the two pulsed gradients, the effect of the 2nd pulse is to induce a similar spatially dependent precession rate variation and thus refocusing of the ensemble. In this case, the net phase change will be zero and the ensemble maintains most of its signal. However, if the spins have moved in the time interval between the pulses, refocusing is imperfect. The end result of such a gradient pair is that faster moving molecules give rise to more signal loss owing to incomplete rephasing (Le Bihan 1995).

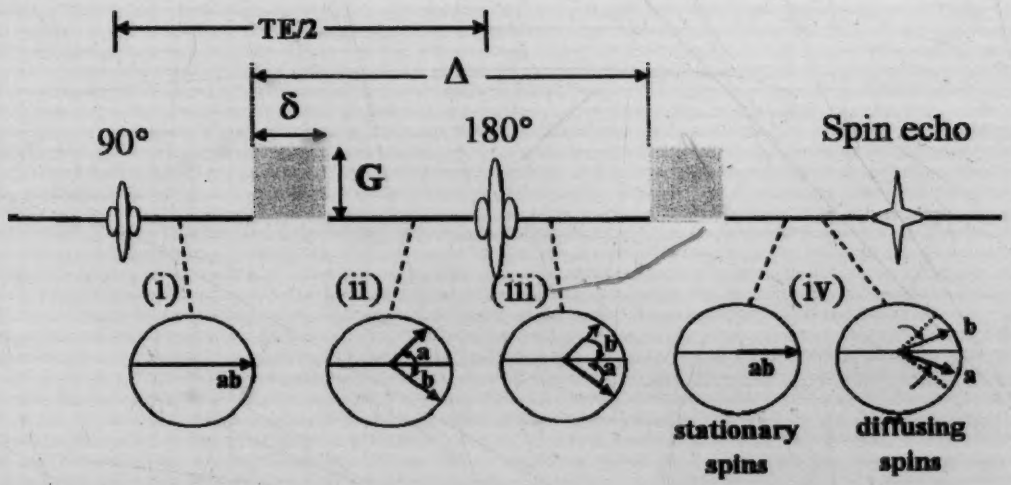

Figure 4-1: A schematic of the Stejskal-Tanner pulsed gradient experiment (top) and its effect on a system of diffusing spins (bottom). The pulse sequence with its timings and gradient variables is shown above. G, gradient amplitude; δ, duration of the gradients; Δ, separation between the gradient pulses; TE, echo time. The state of the transverse magnetization in the rotating frame at 4 different stages (i to iv) during the diffusion experiment in the case of a two-spin system (a and b) is shown below. The spin echo forms at time t = TE from the onset of the 90° pulse and has an amplitude that depends on the phase coherence remaining between the two spins. In (iv), for the case of stationary spins, the diffusion gradients have no effect on the echo amplitude, whereas diffusing spins experience different levels of gradient fields resulting in echo attenuation.

4.2.1 The *b* factor

In the case of fixed diffusion weighting, and considering a single species with diffusivity, D, it can be shown that the signal in a diffusion-weighted experiment is given by:

$$S = S_0 e^{-TE/T_2} e^{-bD} \qquad (4.5)$$

where S_0 is the signal intensity in the absence of diffusion gradients
b is the b factor or b value, a single scalar quantity that characterizes diffusion sensitization

In equation 4.5, the first exponential term is from the weighting due to T2 relaxation. The second term demonstrates that signal attenuation from diffusion is exponential for a non-restricted homogeneous medium. The b factor depends on the magnitude, duration and separation of the pulsed gradient pair and ignoring the contribution from cross-terms and background gradient effects is given by,

$$b = \gamma^2 G^2 \delta^2 (\Delta - \frac{\delta}{3}) \qquad (4.6)$$

where γ is the gyromagnetic ratio (42.58 MHz/T for protons)

The b factor describes the degree to which an image signal is further attenuated by diffusion, above and beyond existing T1 and T2 weighting. The diffusion time is denoted by (Δ - δ/3), where the second term reflects the finite duration of the pulsed field gradients (Stejskal and Tanner 1965). The units for the b factor are s/mm^2 and values in the realm of clinical imaging range from 800-1500 s/mm^2. The b factor can be increased by either varying the gradient amplitude, G, the separation between the gradients, Δ or their duration, δ. However, increasing Δ or δ lengthens the diffusion time and leads to extended echo times for spin-echo diffusion sequences, which yields poor signal-to-noise ratio in the resulting images (Jones 2005).

The diffusion coefficient, D, is referred to as the apparent diffusion coefficient (ADC), and can be obtained from the slope of the plot of $\ln(S/S_0)$ versus gradient sensitivity, b (Figure 4-2). The term *apparent* had been linked to D due to the heterogeneity of diffusion in different systems. In pure liquid, the factors that determine the mobility of molecules are weight, inter-molecular interactions and temperature. However, in neural tissues for instance, molecular mobility is hindered by cellular structures such as axonal membranes and myelin sheaths and may no longer be random. The additional interactions decrease the measured diffusion coefficient by an amount depending on the permeability of the structures (barriers) as well as their spacing. Furthermore, molecules in different intra- and extracellular compartments may undergo diffusion at differing rates. An imaging voxel may also be influenced by the contribution of incoherent motions from blood in the capillary network. Due to these interactions with the tissue microstructure, the measured diffusion coefficient is deemed *apparent* (Le Bihan *et al* 1986; Le Bihan 1988). Some measurements of ADC in free water and the human brain are given in Table 4-1.

With short diffusion times, molecules experience fewer boundaries and display diffusion behavior closer to free diffusion providing diffusion time is kept short enough. However, with increased diffusion times, more barriers hindering diffusion are encountered, and the ADC decreases (diffusion decay curves drop off less rapidly) and reaches an asymptotic value. Typical diffusion time in spin echo sequences are ~20-40 ms for gradient amplitudes (G) of 3 Gauss/cm.

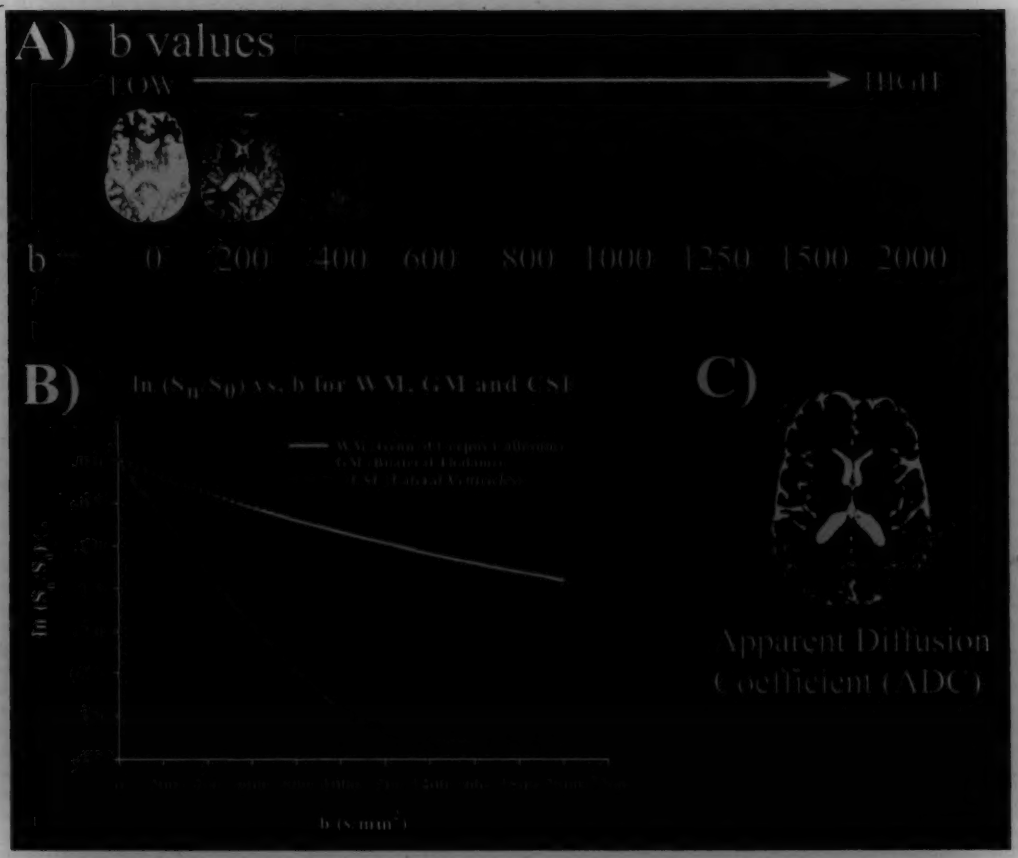

Figure 4-2: Calculation of the apparent diffusion coefficient (ADC) map. An ADC map is computed from a minimum of two images with different b values, where b (s/mm^2) is the magnitude of diffusion weighting within an image. (A) Higher b values impart more diffusion weighting to an image. The ADC map is calculated by performing a pixel by pixel fitting of the signal intensity vs. b value. (B) A plot of the natural log of the signal intensities versus b value yields a straight line with the slope equal to the ADC. This parameter reflects the average speed of water diffusion for each voxel in the image. The plot above (B) demonstrates the signal attenuation curves for a range of b values from 0 to 2000 for a white matter (WM) tract, the genu of the corpus callosum, a gray matter (GM) area, bilateral thalami, and cerebrospinal fluid (CSF) in a normal 26 year old subject. At b=1000 s/mm^2, we observed signal intensity decreases of 57% and 53% in WM and GM areas, respectively, relative to their initial values (at b=0 s/mm^2) whereas the signal from CSF in the ventricles was reduced by 95% relative to its initial value. (C) The ADC map here was calculated from one image without (b=0 or T2-weighted image) and one with (b=1000 s/mm^2) diffusion weighting.

Table 4-1: Typical values of the apparent diffusion coefficient (ADC, mean ± SD) in free water (N=4) and in the normal (21-25 years) human brain (N=5)

Substance/Tissue	ADC (x 10^{-3} mm^2/s)
Water (19° C)	2.03 ± 0.01
Cerebrospinal Fluid	2.40 ± 0.20
White Matter Tracts	
Genu of Corpus Callosum	0.84 ± 0.04
External Capsule	0.71 ± 0.02
Gray Matter	
Thalamus	0.72 ± 0.03
Cortical Gray Matter	0.86 ± 0.05

4.2.2 T2-shine through

A DWI image is greatly influenced by T2 relaxation, made necessary due to the relatively long TE employed. This T2 contribution is in part due to the fact that the level of sensitivity to diffusion increases with the time separation between the pulse gradient pair resulting in long TEs. The combined T2 and diffusion sensitivity makes the diffusion-weighted image ambiguous when considered alone and can lead to wrongful interpretations. A DWI may show hyperintensity, potentially misdiagnosed as acute stroke even in the case of more rapid diffusion, if T2 elevation dominates. This phenomenon is called the T2-shine through effect (Figure 4-3) and manifests as a hindrance when viewing diffusion-weighted images in isolation (Burdette *et al* 1999). The degree of T2-weighting is constant and does not depend on the b value, such that the computed ADC maps are independent of T2. The ADC maps serve as a definitive means of confirming the presence of acute stroke lesions (reduced ADC) without the encumbering effects of T2-shine through.

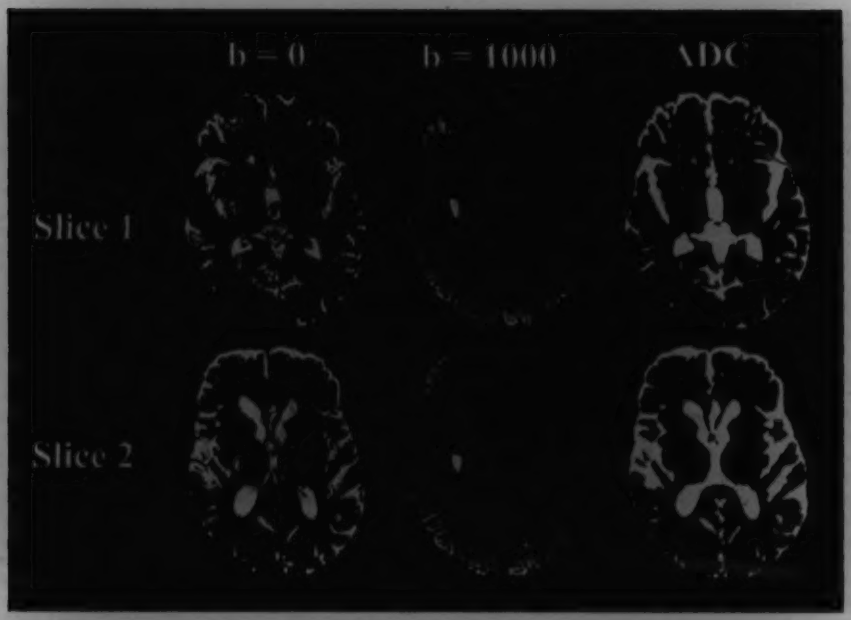

Figure 4-3: An example of the confounding effects of T2-shine through. Here, the b=0 (T2-weighted images), b=1000 (diffusion-weighted images) and ADC maps from two 5-mm thick slices of a 75 year old male stroke patient are shown 26 hours post symptom onset. The infarct in the right middle cerebral artery territory is visible on the T2-weighted (subtly) and diffusion-weighted (quite conspicuous) images at the level of the basal ganglia and external capsule. However, there is no evidence of reduced ADC on the ADC maps for these two slices, which would have confirmed the presence of an acute infarct. The hyperintensities on the diffusion-weighted images can be attributed to the hyperintensity in the T2-weighted images, or due to T2-shine through.

4.2.3 Diffusion Anisotropy

In early reports of the clinical utility of DWI in acute stroke, it became apparent that the ADC in certain regions of the mammalian brain was directionally dependent on the diffusion encoding gradient (Moseley *et al* 1990a; Moseley *et al* 1990b), an observation that was later confirmed in human brain white matter (WM) (Chenevert *et al* 1990; Doran *et al* 1990) (Figure 4-4). In samples like cerebrospinal fluid (CSF) that lack coherently oriented boundaries, diffusion is similar in all directions and is referred to as *isotropic* diffusion. However, in WM tracts, diffusion along the axons is relatively unimpeded whereas diffusion perpendicular to the axons may be limited by interactions with the axonal membranes and myelin sheath. In other words, diffusion in this medium is characterized as being *anisotropic* in nature (Beaulieu and Allen 1994; Beaulieu 2002). Although the presence of myelin was initially implicated as a determinant of diffusion anisotropy, recent experiments have shown that diffusion is still anisotropic in neural tissue devoid of myelin (Gulani *et al* 2001; Prayer *et al* 1997; Wimberger *et al* 1995).

Others have shown that diffusion is anisotropic due to the presence of intact cell membranes and myelin only serves to modulate anisotropy (Beaulieu and Allen 1994; Beaulieu *et al* 1996; Beaulieu 2002).

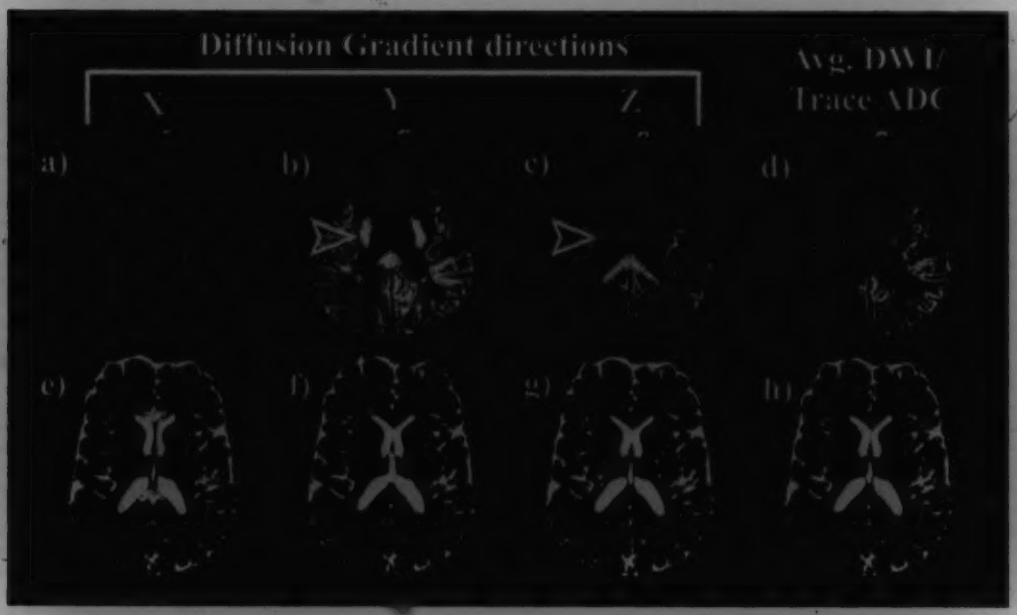

Figure 4-4: The effects of changing the direction of diffusion-sensitizing gradients on the signal intensity in diffusion-weighted images (a, b, c) and the computed ADC maps (e, f, g) in a normal subject. The arrowheads point to the right posterior limb of the internal capsule. When diffusion gradients are applied parallel to a fiber tract (c) (along Z, superior-inferior), regions appear hypo-intense suggestive of rapid water diffusion. In cases where the gradients are oriented perpendicular to a white matter tract (b) (along Y, anterior-posterior), regions appear hyper-intense indicating slower diffusion in those directions. To avoid confounding effects of anisotropy, an average diffusion-weighted image (Avg. DWI, d) or Trace ADC map (h) is generated from the mean of the 3 directional DWIs (a, b, c) or directional ADC maps (e, f, g), respectively.

4.3 The Diffusion Tensor

The characterization of diffusion anisotropy requires the correlation of water mobility along different directions and a consideration of the interactions between diffusion gradients in orthogonal directions. Accurate ADC measurements can be made when all gradients- background, imaging or diffusion in all directions are considered. Hence diffusion cannot be expressed as a vector quantity, but requires characterization in terms of 9 diffusion coefficients grouped in an effective rank 2 tensor (3 x 3 matrix), **D**, given as

$$\mathbf{D} = \begin{bmatrix} D_{xx} & D_{xy} & D_{xz} \\ D_{xy} & D_{yy} & D_{yz} \\ D_{xz} & D_{yz} & D_{zz} \end{bmatrix} \qquad (4.7)$$

The diagonal elements (D_{xx}, D_{yy}, D_{zz}) correspond to diffusivities in the direction of the 3 orthogonal axes. The off-diagonal elements relate diffusivities along those orthogonal axes. The off-diagonal elements do not convey diffusivities, meaning D_{xy} does not refer to diffusion in the x-y direction. But these elements reflect the correlation between molecular displacements in orthogonal directions, meaning D_{xy} correlates diffusion along the x and y axes (Basser *et al* 1994b). The off-diagonal elements also reflect the symmetry of the diffusion tensor (equation 4.7).

The alignment of the tensor with the principal axes of the anisotropic medium (e.g. WM tract) is denoted by a zero value for the 3 off-diagonal elements. Now the tensor is diagonalized and its diagonal elements correspond to its eigenvalues, given by,

$$\mathbf{D} = \begin{bmatrix} \lambda_1 & 0 & 0 \\ 0 & \lambda_2 & 0 \\ 0 & 0 & \lambda_3 \end{bmatrix} \qquad (4.8)$$

The 3 eigenvalues (λ_1, λ_2, λ_3) match the three diffusivities along the principal axes of the tensor. The orientation of these principal axes is given by 3 mutually orthogonal eigenvectors (ε_1, ε_2, ε_3). The orientation of the tensor is assumed to be parallel to the principal eigenvector, the one associated with the largest eigenvalue. The principal eigenvector is considered as being collinear with the dominant fiber orientation within the voxel (Basser *et al* 1994a).

The displacement profile of diffusion in an isotropic medium can be classified as a sphere since diffusion is equal in all directions. In anisotropic mediums, since diffusing particles will diffuse faster along the principal axis of the medium, rather than in a perpendicular orientation, the displacement profile is characterized by an ellipsoid rather than a sphere. The diffusion tensor can be characterized by this ellipsoid. The orientations of the axes of this ellipsoid are denoted by the eigenvectors, and the lengths are given by the diffusion distance in time, t. According to equation 4.2, since the displacement in a given time is proportional to the square root of the diffusivity, therefore the ellipsoids' axes are scaled to coincide with the square root of the eigenvalues ($\sqrt{\lambda_1}$, $\sqrt{\lambda_2}$, $\sqrt{\lambda_3}$). For WM tracts, the largest eigenvalue (λ_1) is assumed to lie along the axon, rendering some information as to the directionality of a tract. The other eigenvalues (λ_2, λ_3) are smaller in scale and are considered to be perpendicular to the axon. In WM fiber tract imaging, fiber tract directions and mean diffusion distances can be represented by the ellipsoids (Basser *et al* 1994a; Basser and Pierpaoli 1996).

4.3.1 Estimating the Diffusion Tensor

The symmetry of the tensor ($D_{xy} = D_{yx}$, $D_{xz} = D_{zx}$ and $D_{yz} = D_{zy}$) allows us to determine only 6 unknown elements. In DTI, these elements are estimated from a series of diffusion weighted images where gradients are applied in non-collinear and non-coplanar directions. The minimum number of diffusion images required for estimating the tensor is 6 with the addition of a non-diffusion weighted image (b=0) (Basser *et al* 1994b) (Figure 4-5). According to equation 4.5, by taking the logarithm of the diffusion weighted signal intensities, a set of simultaneous linear equations is established which can be solved using linear algebra to yield estimates of the tensor. However, here the b value is now the b matrix (Basser *et al* 1994b; Mattiello *et al* 1997), whose elements, b_{ij}, measure the signal attenuation by the corresponding diffusion tensor element, D_{ij}. Equation 4.5 can now be observed as,

$$\ln(\frac{S}{S_0}) = -(b_{xx}D_{xx} + 2b_{xy}D_{xy} + 2b_{xz}D_{xz} + b_{yy}D_{yy} + 2b_{yz}D_{yz} + b_{zz}D_{zz}) \qquad (4.9)$$

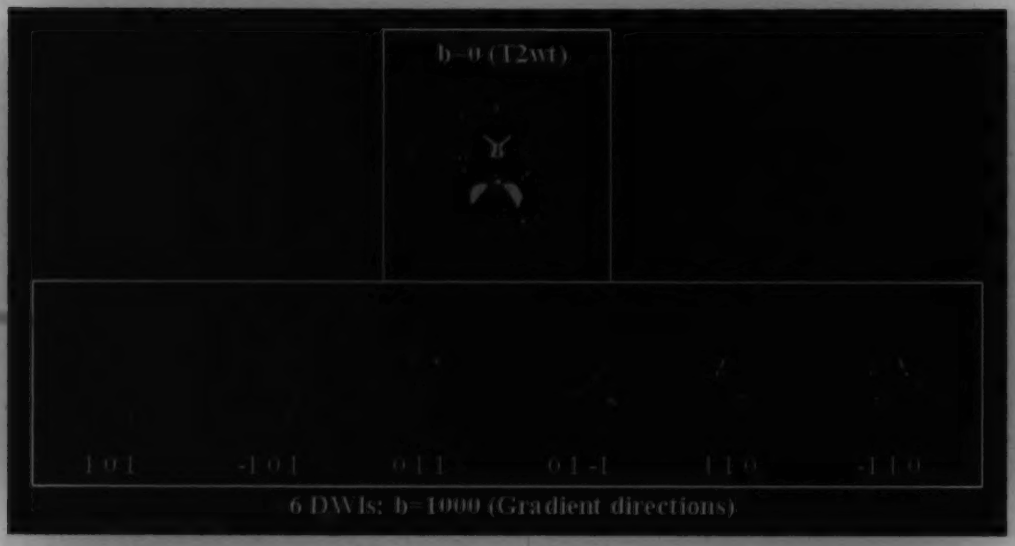

Figure 4-5: Pictorial representation of raw DTI data from a normal 24 year old male subject. One b=0 (or T2-weighted) image (above) and 6 diffusion-weighted images with gradient directions (referring to X, Y and Z; Siemens 1.5 T Sonata scanner) marked below are shown.

4.3.2 Quantitative measures from DTI

Diffusion tensor measures are rotationally invariant, i.e. they assume values independent of the sample's orientation with respect to the laboratory frame, and thereby provide a useful means of comparing data between subjects or even within the same subject (Jones 2005).

4.3.2.1 Trace/3 ADC

The Trace ADC is the sum of the 3 diagonal elements of the tensor and is by far the most common measure listed in DTI studies. It is given as,

$$\text{Trace}(\mathbf{D}) = D_{xx} + D_{yy} + D_{zz} = \lambda_1 + \lambda_2 + \lambda_3 \qquad (4.10)$$

Trace/3 (**D**) or Trace /3 ADC is equal to the geometrically averaged mean diffusivity. Examples of images of the eigenvalues (λ_1, λ_2, λ_3) and Trace/3 ADC are shown in Figure 4-6. The most remarkable property of Trace/3 ADC is that it lies within a narrow range of values in the human brain ($0.70 - 0.95 \times 10^{-3}$ mm^2/s) and appears to be quite similar across a range of normal mammalian brains including mice, rats, cats, monkeys and humans (Basser and Jones 2002). Furthermore, the homogeneity of the Trace/3 ADC maps in human adult subjects confers an advantage in the detection of acute ischemic lesions since the effects of anisotropy are averaged out. Some common estimates for the 3 eigenvalues and the Trace/3 ADC in a white matter and gray matter structure of the human brain are given in Table 4-2.

Figure 4-6: Images of the 3 eigenvalues (λ_1, λ_2, λ_3) and Trace/3 ADC map (top). The eigenvalue maps display uniform signal intensity for areas undergoing isotropic water diffusion (e.g. CSF), whereas anisotropic structures like white matter tracts display considerable differences in signal intensity from λ_1 to λ_3. The uniform Trace/3 ADC map allows the reliable detection of acute ischemic lesions in clinical stroke. Below, a simulated cross section of a neural fiber with orientations of the eigenvalues along (λ_1) and across (λ_2, λ_3) the fiber tract is shown.

Table 4-2: Common measures of the eigenvalues and Trace/3 ADC (mean ± SD) in a WM tract and a gray matter area in the normal (21-25 years) human brain (N=5)

Tissue	λ_1	λ_2	λ_3	Trace/3 ADC
White Matter Tract				
Genu of Corpus Callosum	1.64 ± 0.08	0.57 ± 0.06	0.32 ± 0.05	0.84 ± 0.04
Gray Matter				
Cortical Gray Matter	1.06 ± 0.07	0.85 ± 0.05	0.68 ± 0.05	0.86 ± 0.05

Units are in $x10^{-3}$ mm^2/s

4.3.2.2 Index of Diffusion Anisotropy

Prior to the use of DTI, the ratio of the ADCs obtained in two orthogonal directions was taken as an index of diffusion anisotropy. However, this approach was viewed as

inaccurate since a prior estimate of the fiber orientation was not available thereby rendering such an index as rotationally variant (Jones 2005). The simplest measure of the anisotropy can be obtained from the ratio of the largest to the mean of the two smallest eigenvalues [$\lambda_1/((\lambda_2 + \lambda_3)/2)$]. However, to avoid introducing a bias in measurements from sorting of eigenvalues especially at low SNR values (Pierpaoli and Basser 1996), the more robust measures of volume ratio (VR), fractional anisotropy (FA) and relative anisotropy (RA) were introduced. These anisotropy indices possess two favorable properties: 1) they are rotationally invariant and objective estimates of diffusion anisotropy, which show no bias due to fiber orientation and 2) they are symmetric functions of the three principal diffusivities (eigenvalues) and are less sensitive to extraneous noise compared to the asymmetric functions of the principal diffusivities, e.g. measures such as the ratio of the largest to the smallest principal diffusivity (Papadakis *et* 1999). Since the bulk of the work in this thesis is based on FA measurements, FA will be discussed below in detail.

$$FA = \sqrt{\frac{3}{2}} \frac{\sqrt{(\lambda_1 - \langle\lambda\rangle)^2 + (\lambda_2 - \langle\lambda\rangle)^2 + (\lambda_3 - \langle\lambda\rangle)^2}}{\sqrt{\lambda_1^2 + \lambda_2^2 + \lambda_3^2}} \qquad (4.11)$$

where $\langle\lambda\rangle = \frac{1}{3}(\lambda_1 + \lambda_2 + \lambda_3)$

The numerator is related to the variance of the 3 eigenvalues about their mean. FA normalizes this measure by the magnitude of the tensor as a whole. Similar to the magnitude of a vector being derived from the sum of the squares of its individual components, the magnitude of a tensor can be obtained from the sum of the squares of its eigenvalues. Therefore, FA measures the fraction of the tensor that can be ascribed to anisotropic diffusion. FA is normalized so that it varies from 0 (signifying a fully isotropic medium) to 1 (when diffusion is restricted to one direction only). A measure such as FA can be very sensitive to noise particularly at low SNR values where anisotropy is overestimated (Kingsley and Monahan 2005; Pierpaoli and Basser 1996). Therefore care should be exercised when comparing anisotropy indices from different studies where different imaging parameters may have been employed.

Although the other indices of anisotropy such as VR and RA were introduced at the same time as FA, FA has been more popular due to its well-defined range (0 for isotropic diffusion to 1 for highly anisotropic diffusion) and for affording a better sense of the expected anisotropy values for a given brain region. VR describes the ratio of the volume of an ellipsoid to the volume of a sphere, whose radius is the averaged diffusivity and ranges from 1 (signifying complete isotropic diffusion) to 0 (reflecting highest anisotropic diffusion). RA, defined as the ratio of the variance of the eigenvalues to their mean has an identical range to FA with similar implications (Kingsley 2006). In a numerical comparison of these three anisotropy measures, FA, VR and RA, Papadakis *et al.* showed that FA mapped diffusion anisotropy with the greatest detail and exhibited better noise immunity characteristics (high SNR) relative to VR and RA (Papadakis *et al* 1999). Others have used either numerical or regions-of-interest analysis methods and

concluded that FA provides higher SNR and the highest contrast-to-noise ratio between GM and WM when compared to RA (Alexander *et al* 2000; Hasan *et al* 2004; Kingsley and Monahan 2005; Sorensen *et al* 1999).

Common FA measures for different WM and gray matter regions in the elderly human brain are given in Table 4-3. Cortical GM also demonstrates anisotropy presumably due to the arrangement and ordering of its various layers (layers 1 to 6), which give rise to directionality. Figure 4-7 shows FA maps for the brain in axial, sagittal and coronal planes. Figure 4-8 displays axial FA maps with labeled brain regions.

4.3.2.3 Utility of the Quantitative Measures in Diseases

There has been great interest in using the quantitative measures of DTI to provide insights into the nature and degree of the pathology that occurs in diseases of the central nervous system when cellular structures are damaged or disrupted as a result of the pathological process. In highly ordered structural systems, such as in the axonal fibers of WM, the directional nature of the diffusion-sensitizing gradients of DTI can encode properties that vary with direction.

In the context of cerebral ischemia, the mean diffusivity given by Trace/3 ADC is reduced by 30-60% of its control values within 30 minutes of onset ((Moseley *et al* 1990b), remains low for the first few days (unless reperfusion has occurred) (Marks *et al* 1999), pseudonormalizes within 1 week and is elevated at chronic time points (Beaulieu *et al* 1999; Schlaug *et al* 1997). The reduction of Trace/3 ADC is associated with cellular change in energy metabolism that finally results in decreased activity and subsequent failure of the Na^+/K^+ pumps, which in turn leads to cytotoxic edema (Sotak 2002). Current hypotheses point to possible decreases in the extracellular and intracellular water mobility and the shift of water from extracellular to intracellular spaces, an increase in restriction of intracellular diffusion due to changes in membrane permeability, or increased tortuosity in the extracellular space arising from cell swelling (Sotak 2002). Cellular swelling within the first 24 hours following ischemia is suggested as a possible mechanism for increases (up to 45% increases) in diffusion anisotropy (given by FA) observed during this time frame in humans (Green *et al* 2002; Ozsunar *et al* 2004a; Schaefer *et al* 2003; Yang *et al* 1999) and animal models (Carano *et al* 2000; Does and Gore 2000; Liu *et al* 2007).

The renormalization and subsequent elevation (~150% increases) of the Trace/3 ADC at chronic time points (90 days to 1 year) following cerebral ischemia is suggestive of losses of cell membrane integrity (Sotak 2002). The breakdown of restrictive barriers allows a larger net displacement of the water molecules for the same diffusion duration, resulting in an elevated Trace/3 ADC. Furthermore, the disruption of the cytoarchitecture leads to loss of tissue anisotropic structures detected as a reduction (~40% to 70% decreases) in FA values in chronic stroke patients within the lesion and in regions remote from the primary lesion (due to retrograde and Wallerian degeneration) (Pierpaoli *et al* 2001; Thomalla *et al* 2004; Werring *et al* 2000). This pattern of elevated Trace/3 ADC and

reduced diffusion anisotropy in ischemic lesions within the chronic phase was also observed in animal models (Carano *et al* 2000; Liu *et al* 2007; Song *et al* 2003; Sun *et al* 2006).

Song *et al.* (2003) have proposed that the eigenvalues (λ_1, λ_2 and λ_3) of the diffusion tensor can be used as specific markers of axonal and myelin injury during chronic ischemia. In their serial studies of retinal ischemia in mice, they attributed the earlier (3 day) decreases (~15% drops) in diffusion anisotropy to reductions in parallel diffusivity (given by λ_1) with unchanged perpendicular diffusion (given by $((\lambda_2+\lambda_3)/2)$), which was consistent with histological findings of axonal degeneration. However, the steeper decreases (~40%) in diffusion anisotropy at later time points (5-14 days) were attributed to increases in perpendicular diffusivities indicative of demyelination (Song *et al* 2003; Sun *et al* 2006). Human studies of ischemic stroke (Sorensen *et al* 1999) within 24 hours and corpus callosotomy (Concha *et al* 2006) at 1-week after surgery have also noted reductions in anisotropy which were tied to more precipitous declines in λ_1, relative to λ_2 and λ_3 in WM.

Increases in mean diffusivity (or Trace/3 ADC) and reductions in diffusion anisotropy have also been observed in other diseases such as multiple sclerosis (Lin *et al* 2007; Lowe *et al* 2006), epilepsy (Assaf *et al* 2003; Concha *et al* 2005a), ischemic leuokoaraiosis (Jones *et al* 1999a; O'Sullivan *et al* 2004) and Alzheimer's disease (Medina *et al* 2006; Zhang *et al* 2007), to name a few neurological disorders.

Table 4-3: Common FA values (mean ± SD) computed from different brain regions of normal human subjects (N=5, 21-25 years)

Region	FA
Combined Subcortical White Matter tracts[a]	0.45 ± 0.05
Combined Cortical Gray Matter[b]	0.22 ± 0.01
Major White Matter Tracts	
Genu of Corpus Callosum	0.68 ± 0.04
Splenium of Corpus Callosum	0.75 ± 0.04
Anterior limb - Internal Capsule	0.64 ± 0.04
Posterior limb - Internal Capsule	0.66 ± 0.02
External Capsule	0.48 ± 0.03
Corona Radiata	0.56 ± 0.01
Centrum Semiovale	0.46 ± 0.04
Deep Gray Matter	
Thalamus	0.40 ± 0.03
Putamen	0.20 ± 0.01
Globus Pallidus	0.34 ± 0.01
CSF	0.14 ± 0.03

[a]The combined FA values reflect means (± SD) from five subcortical white matter gyri
[b]The combined FA values reflect means (± SD) from eleven cortical gray matter regions

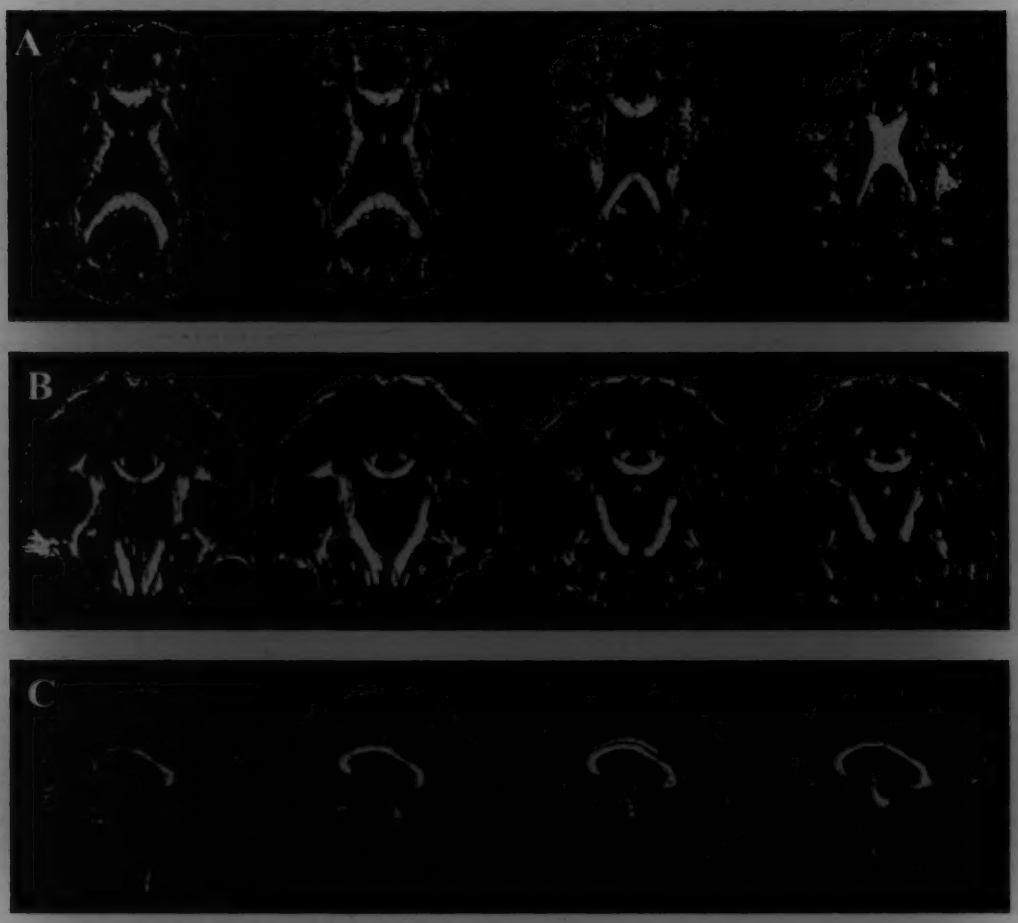

Figure 4-7: Four Axial (A), Coronal (B) and Sagittal (C) FA maps from a healthy 22 year old male subject. The intensity of the images is directly proportional to anisotropy. Gray matter and CSF-filled regions (ventricles and sulci) appear darker due to their lower FA values (Table 4-3). White matter tracts appear brighter reflecting their higher FA values. Voxel sizes are ~1.7 x 1.7 x 3.0 mm^3.

4.3.3 Advanced Applications: Fiber Tracking

Robust and readily interpretable fiber orientation maps can also be derived from the information contained within the diffusion tensor, i.e. the eigenvector associated with the largest eigenvalue (Pajevic and Pierpaoli 1999). The key element here is that components of the orientation of the fiber are represented by different primary colors, a practice termed, *Color mapping* (Colormap example in Figure 4-9). The principal direction of diffusion in each voxel is represented by a color scheme where a set color is assigned to each major direction (anterior-posterior, superior-inferior and left-right). With the fiber

orientation realized in one voxel, a path of smooth transition from voxel to voxel can be conceptualized to form the trajectory of WM pathways *in vivo*. In fiber tracking, algorithms to perform this aforementioned task are put to test to follow smooth pathways in the fiber orientation field to reconstruct WM tracts in an automated manner (Basser *et al* 2000; Jones *et al* 1999c; Mori and van Zijl 2002).

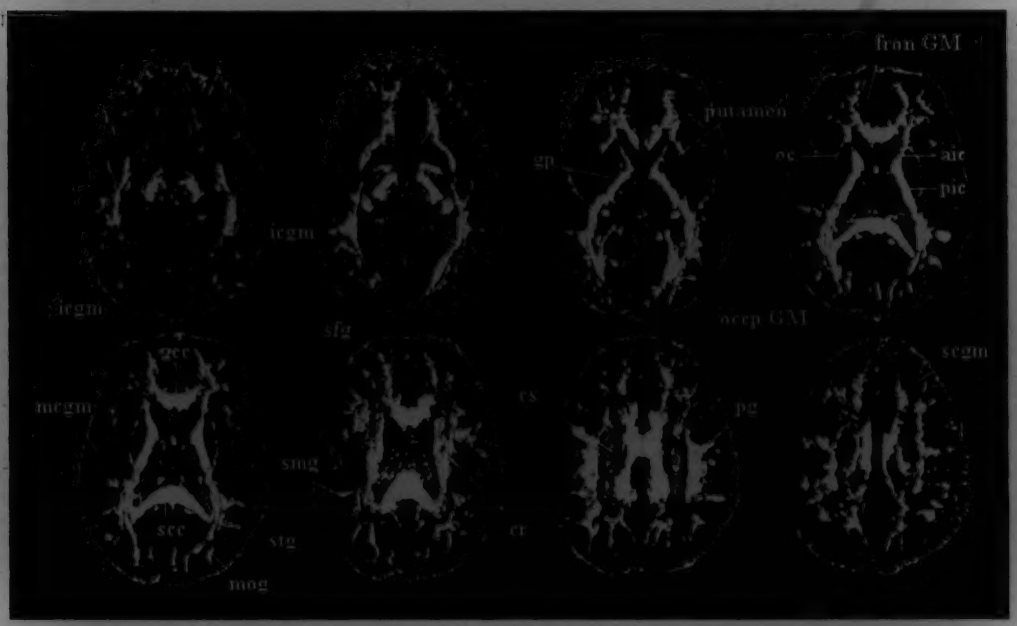

Figure 4-8: Axial FA maps of eight slices from one young subject (25 yrs). Recognizable white matter and gray matter structures are labeled. The contrast has been made extreme in order to better visualize the background cortical gray matter. **icgm**, inferior cortical GM; **gp**, globus pallidus; **fron GM**, frontal GM; **ec**, external capsule; **aic**, anterior limb of internal capsule (IC); **pic**, posterior limb of IC; **temp GM**, temporal GM; **occp GM**, occipital GM; **gcc**, genu of the corpus callosum (CC); **scc**, splenium of the CC; **mcgm**, middle cortical GM; **stg**, superior temporal gyrus; **mog**, middle occipital gyrus; **smg**, supra marginal gyrus; **sfg**, superior frontal gyrus; **cr**, corona radiata; **cs**, centrum semiovale; **pg**, postcentral gyrus; **scgm**, superior cortical GM.

4.3.4 Strategies for Optimizing DTI data Acquisition

Single shot techniques for signal acquisition have become the gold standard for acquiring DTI data due to improved SNR per unit time and the elimination of gross motion artifacts. Echo-Planar Imaging (EPI) is the most common technique used for systems with appropriate hardware (Turner 1998). The Stejskal-Tanner sequence is used in combination with an EPI readout to enable fast scan times, thus making DTI clinically feasible. Rapid gradient switching enables attainment of acquisition times of <100 ms.

However, EPI images are vulnerable to susceptibility artifacts, chemical shift artifacts, distortions and blurring due to T2* decay during the EPI readout. The use of EPI for Diffusion imaging and DTI has been explored in great detail in Chapter 5 along with possible solutions to address the common artifacts that arise from implementing EPI.

This section gives an overview of some parameters that can be optimized during DTI to yield the most reliable results.

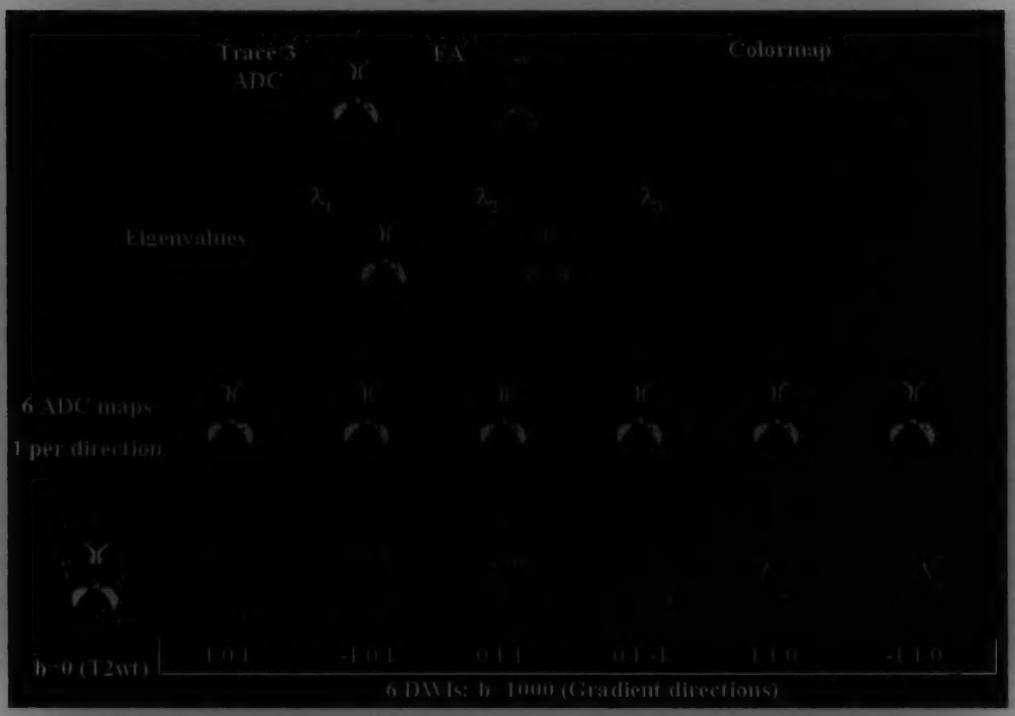

Figure 4-9: The DTI Pyramid. A pictorial depiction of the full complement of images required to obtain quantitative measures from DTI. Shown below are one b=0 (or T2-weighted) image (bottom) and 6 diffusion-weighted images with gradient directions (referring to X, Y and Z; Siemens 1.5 T Sonata scanner). The next row above shows 6 ADC maps computed, 1 per direction. The by-products of the tensor, the eigenvalues (3rd row from bottom) are useful to measure diffusivities along (λ_1) or across (λ_2, λ_3) the fiber tracts. The homogeneous Trace/3 ADC maps are derived from the mean of the eigenvalues. The FA map shown is also obtained from the eigenvalues and highlights WM tracts. The colormap aids in visualizing the direction of the axons by viewing the direction of water flow within the WM tracts on the FA map (Red represents water flowing left to right, green indicates water flow anterior to posterior and blue, superior to inferior or into the plane of the image).

4.3.4.1 Optimizing b value

Xing *et al.* showed that to minimize the variance in the estimated ADC, the optimal diffusion weighting should be calculated according to (Xing *et al* 1997),

$$b \approx \frac{1.1}{ADC} \qquad (4.12)$$

According to their theoretical and experimental data, the sensitivity of diffusion-weighting is maximum when ADC (b_2 - b_1) = 1.1, which corresponds to a greater signal attenuation (b_2 and b_1 are diffusion sensitization factors for two point diffusion-weighting). With ADC values ranging from 0.69-1.0 x 10^{-3} mm^2/s in the normal human brain, according to equation 4.12, the b value should range from 1100 to 1594 s/mm^2. To achieve higher b values, in cases where the gradient power is limited, the duration of the diffusion encoding gradients must be increased, leading to an increase in TE and T2 relaxation. Also, at higher b values, diffusion decay is non-linear and ADC cannot be estimated accurately. Eis and Hoehn-Berlage have shown that the most precise estimate of ADC is achieved from two diffusion weighting amplitudes or b values (Eis and Hoehn-Berlage 1995) in contrast to using more than two equally spaced amplitudes. Although optimal b values currently in use range from 700 to 1000 s/mm^2 (Le Bihan *et al* 2001), others have found that higher b values (~1500 s/mm^2) lead to increased contrast between infarcted tissue and normal background tissue in acute clinical stroke settings (Pereira *et al* 2002).

Another important recommendation for estimating the ADC after accounting for the effects of T2-weighting is that the optimal ratio of the number of measurements made at the higher b value to the number made at the lower b value, $N_{high}/N_{low} \cong 8.7 : 1$ (Jones *et al* 1999b).

4.3.4.2 Optimizing Arrangement of Sampling Vectors

Although the tensor can be effectively estimated from only 7 images- 6 diffusion-weighted and 1 non-diffusion weighted image, acquiring more images helps to augment the precision of the experiment. Commonly, with acquisition of 7 images (6 diffusion weighted), the scheme involves placing gradients at full amplitude on two axes simultaneously. According to equation 4.6, increasing the gradient amplitude for a given b value, results in a reduction of the required duration of the diffusion encoding gradients, a drop in TE and hence greater SNR per unit time. Several studies have demonstrated that it is better to acquire as many unique sampling orientations as possible, with the limit reaching 30 unique orientations (Batchelor *et al* 2003; Jones *et al* 1999b).

The remaining acquisition strategies in DTI mainly deal with the EPI method. These have been treated separately in a detailed manner in Chapter 5.

4.3.5 Underlying Assumptions in DTI

There are several underlying assumptions made in the use of DWI and DTI that must be satisfied to be able to use these methods with confidence. The main assumption of a Gaussian form for the probability distribution (tied to the theoretical description of diffusion, section 4.2) does not hold much weight when one considers the impeding cellular architecture of the sample being investigated, which for our case is neural tissue. Diffusion is impeded not only by the structural arrangement of specific fiber tracts and ordering of cortical layers, but is further modulated by structures such as the axonal membranes, myelin sheaths and intracellular organelles (Beaulieu 2002). The deviation of the Gaussian form of the probability distribution is obtained from experimental evidence from non-monoexponential signal attenuation plots. This type of data may reflect complications such as restriction, background gradients, exchanges or anisotropy, and requires a comprehensive theoretical model that can link diffusion measurements to the physical and geometrical tissue properties.

We also neglect the contribution of the background gradients (the gradients which are not meant to provide diffusion weighting) (Basser and Pierpaoli 1998). These background gradients also include a contribution due to the gradients that are generated within the sample itself. The deleterious effects of these background gradients on ADC quantification can be quite significant relative to imaging gradients since the gradients within the sample are active during the experiment. ADC values could therefore be over- or underestimated (Thomas *et al* 2000). Both, self-terms and cross-terms can be generated by the sample gradients, self-terms being eliminated by multiple acquisitions. Although this was a significant concern previously, the current design of diffusion EPI sequences with the bipolar gradient pairs placed around the 180° refocusing pulse reduces contributions from the cross terms to ~1% in signal attenuation effects (Basser and Pierpaoli 1998; Mattiello *et al* 1997).

We further assume that there is no diffusion attenuation in the b=0 (or T2-weighted image). Nonetheless crusher gradients of the sequence may in effect introduce some diffusion attenuation, but these have been reported to be negligibly small (~0.5%) compared to the b≠0 images. Another assumption made is that the parameters derived from the tensor, especially the FA maps are free of noise. Some reports have demonstrated that the noise-induce bias stemming from the low SNR of the method is carried over when quantifying FA, thereby inflating FA values of structures that are known to exhibit lower diffusion anisotropy (Kingsley and Monahan 2005; Pierpaoli and Basser 1996). Finally, the methods assume that the derived images are free of systematic artifacts such as ghosting artifacts from motion, magnetic susceptibility variations, distortions from eddy currents (Chapter 5), improperly calibrated gradients and field inhomogeneity effects. If unavoidable, these effects should be considered during the analysis of DWI/DTI data.

4.3.6 Limitations of the Diffusion Tensor Model

The estimate of the diffusion tensor within a voxel represents the bulk-averaged diffusion properties for that voxel. In the case of homogeneous tissue, the bulk average diffusion measure will reflect the underlying tissue microstructure. Considering a typical voxel in DTI (2.0 x 2.0 x 2.0 mm^3 volume) and the diameter of an axon (8-10 μm), it can easily be seen that a single voxel can contain multiple fiber populations and contributions from tissues with varying diffusivities. The problem of voxels containing tissues with different diffusivity values becomes more relevant at tissue/CSF interfaces rather than in normal brain parenchyma (where Trace/3 ADC values are relatively homogeneous in non-neonates). This gives rise to partial volume averaging (Jones 2005).

Partial volume averaging occurs when multiple tissue types are encompassed within a single voxel. Under these circumstances, the net voxel signal intensity is determined by the relative proportion and signal intensity of each constituent tissue. These effects can result in overestimating Trace/3 ADC and underestimating the diffusion anisotropy in brain regions proximal to ventricular and sulcal spaces (Falconer and Narayana 1997; Kwong *et al* 1991; Papadakis *et al* 2002). Partial voluming is directly related to noise, since image resolution must be increased (by implementing thinner slices), leading to decreasing the SNR (Mori and van Zijl 2002). Because post-processing enhancement of SNR will result in reduced resolution, thereby augmenting partial voluming, one approach to avoid this is to increase the number of measurements and analyze averaged data sets. More recently, the use of FLAIR (fluid attenuated inversion recovery) in DTI has been shown to reduce the effects of partial voluming by suppressing signals from CSF and enabling more accurate estimates of anisotropy (Ma *et al* 2004; Papadakis *et al* 2002), albeit at the cost of prolonged acquisition times.

Partial voluming also presents the problem that if there are multiple fibers inhabiting a given voxel, these fibers may be oriented at different angles to one another and because diffusion no longer occurs in preferentially one axis, the FA of the voxel average will be reduced. Multiple fiber orientations cannot be extracted from the tensor model due to its indication of only one eigenvector. This is a major limitation in fiber tracking where the goal is to reconstruct WM fiber pathways (Jones 2005). Several techniques have been proposed with the aim to resolve the problem of multiple fiber crossings for fiber tracking (Frank 2001; Tuch 2004; Wedeen *et al* 2005), but they all possess long acquisition times, prohibiting their use in clinical settings.

4.4 Methods of Analysis for DTI data

DTI serves as valuable tool for studying brain microstructure mainly because of the numerous WM tracts that can be visualized (from FA maps) and quantified for structural integrity. The most common methods used for analysis of DTI derived maps are the manual regions-of-interest analysis method and the automated voxel based morphometry (VBM) method. Since the bulk of the work in this thesis involves the use of the ROI analysis method, VBM will not be addressed in great detail.

The key point of the ROI analysis method is to trace an area of interest on a 2D image (in most cases) and extract various measurements (signal intensity, area, or quantitative diffusion measures) from that trace. A free hand ROI analytical scheme can be used to measures changes from the entire visible extent of a specific WM tract from multiple slices, and can yield an incisive measure of alterations in tissue microstructure. On the other hand, because free hand ROIs are user-dependent, some bias can be introduced in defining some regions. Furthermore, not all structures can be defined on 2D images. Also, the position of an ROI trace can influence the outcome of the final analysis. In cases, where one is interested in measuring global changes in the brain, VBM methods have been preferred over ROI analyses due to time constraints associated with carefully conducting ROI analysis on several structures per slice within the entire brain per subject. However, spatial normalization is a problem in VBM methods where it can be challenging to compare the same structure between individuals due to the natural variability of regions in the human brain.

Previous reports employing an ROI based analysis have used plain oval, box-shaped or circular traces for examining various WM tracts (Abe *et al* 2002; O'Sullivan *et al* 2001; Ozsunar *et al* 2004b; Shimony *et al* 1999). These methods although acceptable in the interest of time are not specifically targeted at a WM region, but tend to involve contributions from neighboring CSF or GM voxels as well, and are therefore compromised by effects of partial volume averaging. The end result is that the averaged anisotropy measure obtained from such an ROI trace is artificially decreased because of the net contributions from tissues (GM or CSF) other than pure WM fiber tracts. A better ROI method entails identifying individual tracts and regions using prominent atlases of neuroanatomy and then cross referencing them with FLAIR and standard T2-weighted images to ensure exclusion of neighboring GM and CSF-filled sulcal spaces. An advanced approach to ROI analysis entails defining specific regions using quantitative parameter thresholds (such as ADC) to limit the outer bounds of the measurements. This type of approach is especially useful when analyzing ischemic infarcts on Trace/3 ADC maps defined by a ≥30% reduction in Trace/3 ADC relative to the normal contralateral hemisphere. A more thorough discussion of this form of analysis is undertaken in the upcoming chapters (8 and 10).

4.5 Concluding Remarks

DTI is a powerful method for studying the microstructure of the brain. Various indices derived from DTI yield useful measures of mean diffusivity and relay information on structural integrity in terms of anisotropy. The assumptions made in the use of DTI and limitations of the tensor have been discussed in this chapter. Also, an in depth discussion of analytical methods was undertaken. Chapter 5 covers the echo planar imaging (EPI) method widely used for acquiring DTI data and further explores imaging artifacts encountered in diffusion studies of the brain.

5

ECHO PLANAR IMAGING

The Echo Planar Imaging (EPI) sequence is a rapid acquisition method that has become the clinical mainstay of diffusion, perfusion and functional MRI techniques. First proposed by Peter Mansfield in 1977 (Mansfield 1977), EPI allows the collection of data required for image reconstruction within a few hundred milliseconds. The relatively short acquisition time renders each section of an object as an instant snapshot resulting in high temporal resolution. This chapter rationalizes the need for faster imaging techniques such as EPI, and describes the workings of the EPI sequence comparing its traditional gradient-echo (GRE) variant to its spin-echo variant. Furthermore a discussion of the common EPI-related artifacts is initiated followed by an outline of the most common EPI sequences used in Diffusion MRI.

5.1 The Need to Speed up Acquisition

Conventional spin-echo and GRE imaging methods are characterized by a frequency encoding gradient being switched on during data acquisition causing the resonant frequency to become a function of location. The composite signal is then analyzed by means of a Fourier transform which assigns signal intensities of distinct frequency components to certain locations. In the second dimension perpendicular to the frequency-encoding gradient, the information about the position of the magnetization vector (phase) is used for encoding spatial information. The phase-encoding gradient is first switched on briefly to establish a difference in phase positions for the magnetization vectors within each voxel in the direction of the magnetic field gradient. This is followed by application of the frequency encoding gradient. In conventional spin-echo and GRE imaging, one line of data, also referred to as one phase-encoding step or one raw data line (a line in K-space) is collected in one repetition time (TR) period. The measurement time is equal to the number of phase encoding steps multiplied by the TR and multiplied by the number of acquisitions (or averages) (Cohen 1998; Nitz 2002).

Conversely in EPI, all Fourier lines are acquired after a single radiofrequency (RF) excitation pulse using multiple gradient echoes, each echo being uniquely phase encoded. Single-shot EPI acquisition times are in order of a few seconds (for multiple slices), thereby generating good quality images especially in patients who are unable to withstand

long acquisition scans (Davis *et al* 1996). Diffusion imaging with conventional acquisition strategies is susceptible to motion artifacts since the molecular motion is significantly smaller than the macroscopic motion due to breathing, involuntary head motion or pulsatile brain motion. EPI, with its ability to freeze bulk motion of the brain, can generate almost pure diffusion weighted images. The acute detection of ischemic brain tissue has been a stalwart application of diffusion imaging (Sotak 2002). In particular, the reduction of the apparent diffusion coefficient (ADC) of water within minutes after the onset of cerebral ischemia has highlighted the indispensable clinical importance of diffusion imaging for the sensitive and specific diagnosis of stroke (Hjort *et al* 2005; Moseley *et al* 1990b; Warach *et al* 1995). Diffusion and perfusion imaging with EPI provide earlier detection of affected areas relative to conventional sequences, where the diagnosis of infarcted tissue may be unreliable within the first 6-12 hours.

The limitations of using single-shot EPI are apparent in the quality of the derived images which are vulnerable to distortions and signal dropout (susceptibility artifacts) and to the misregistration of the fat signal (Chemical shift artifacts). To address these issues, various *ad hoc* acquisition schemes for diffusion imaging have been developed such as Interleaved EPI (Bammer *et al* 1999; Butts *et al* 1996), Rapid Acquisition with Relaxation Enhancement (RARE) (Alsop 1997), Line scan diffusion imaging (Gudbjartsson *et al* 1996; Gudbjartsson *et al* 1997), Spiral scanning (Butts *et al* 1997), radial acquisition of data with fast spin echo (Sarlls *et al* 2005; Trouard *et al* 1999), the radial scheme of Periodically Rotated Overlapping Parallel Lines with Enhanced Reconstruction (PROPELLER) (Forbes *et al* 2002; Pipe *et al* 2002) and the combination of single-shot EPI with Sensitivity Encoding (SENSE) (Bammer *et al* 2001; Bammer *et al* 2002; Jaermann *et al* 2004).

5.2 Background

In conventional imaging methods, the time between adjacent points along the phase encode direction is equal to TR since the signal whose T2 is in most cases longer than the 5 to 10 ms readout period, must be reformed in the interval between the accumulation of each readout line. Hence the phase encoding gradient is pulsed briefly, displacing the signal in the Ky or the phase direction in K space and the readout process is repeated. The cycle consisting of an excitation followed by phase encode followed by readout is repeated until the desired net displacement (or spatial resolution) along the phase encode axis is achieved. In the conventional K-space diagram, raw data lines are collected one at a time separated by a TR period ranging from 10 ms to 3000 ms. Before acquiring each data line, a gradient is applied along the phase encoding and readout axes, resulting in the displacement of the MR signal in K-space (Figure 5-1). Following this pre-encoding phase, the data are collected in the presence of the frequency encoding or readout gradient. After each data collection, the signal is then reformed in the TR period, usually by the application of one or more RF pulses. The encoding process is continually repeated with a different phase and frequency displacement in K-space, until a sufficient number of data lines are acquired (Cohen 1998).

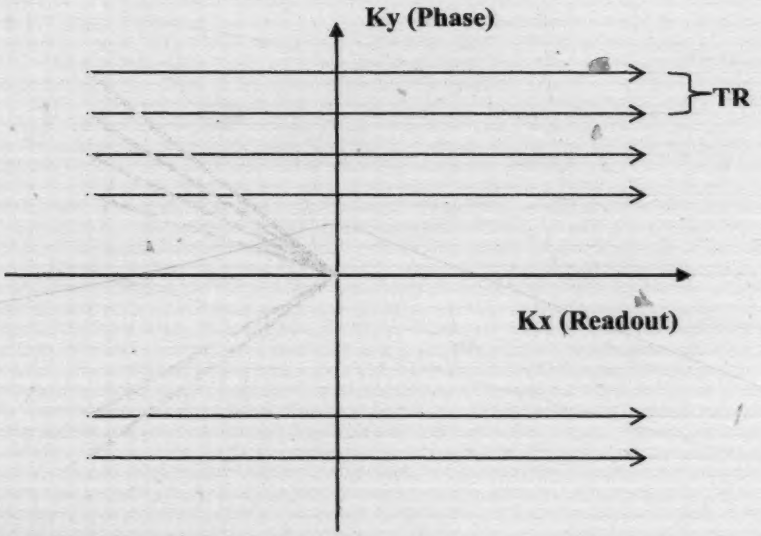

Figure 5-1: Conventional K-space encoding. In this approach, raw data lines are collected one at a time, distanced by a TR period.

In EPI, all data are acquired after a single excitation pulse, obviating the need for the signal to be repeatedly reformed. The main idea here is to employ higher gradient amplitudes and faster sampling so that the spatial encoding process is completed faster than the T2 decay, i.e., before the MR signal has decayed away. In the K-space profile for EPI, each line of data collection in the readout direction is separated by a brief pulse of the phase encoding gradient (Figure 5-2). Here it is crucial to acquire each readout line fast enough so that all data lines can be collected in the presence of the MR signal, which is a short duration. The EPI K-space trajectory forms a raster like path. The pattern of traversal of the alternate lines on the readout axis is reversed by switching the polarity of the readout gradients (Cohen 1998).

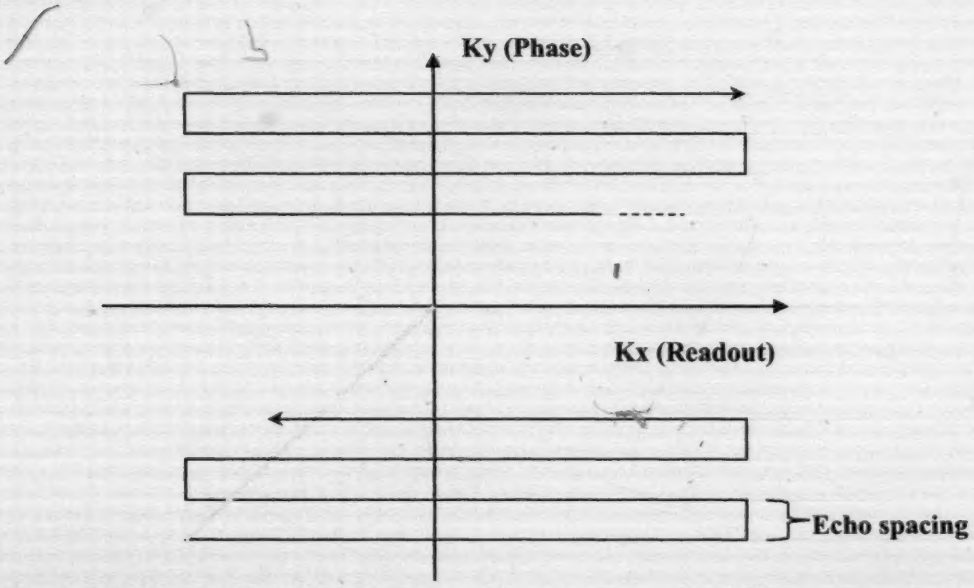

Figure 5-2: K-space trajectory for the most common form of EPI. Here, all data lines are acquired after a single excitation, each line being separated by a brief pulse of the phase encoding gradient.

5.3 EPI Pulse Sequence

In a typical EPI sequence using a single excitation pulse, the RF pulse is made slice selective by turning on a gradient along the slice selection axis as shown in Figure 5-3. A single slice is excited by transmitting the RF pulse in the presence of slice selection gradient, G_z. After this, brief negative pulses of the phase encoding (G_y) and readout (G_x) gradients displace the signal to the left corner of K-space. The schematic of the phase and readout gradients yields the K-space trajectory depicted in Figure 5-2. The positive and negative successions of the readout gradient generate the alternating positive and negative velocities on the readout axis in K-space. This allows the production of an echo train. The brief pulses or phase encode blips drive the data from line to line along the Ky axis.

During frequency encoding in EPI, each echo is generated as a GRE using the same bipolar structure of gradient dephasing-rephasing used in conventional GRE imaging (Wielopolski *et al* 1998). Despite the numerous echoes generated during frequency encoding, the effective echo time that outlines the image contrast depends on the time that the field echo is set to occur for the specific echo to which the center of K-space is assigned. The phase encoding gradient controls the echo at which the center of K-space is acquired (image contrast). For blipped-pulse sequences, the effective echo time (TE) occurs when the area accumulated under the blips cancels that of the dephasing gradient pulse. As will be discussed in more detail later, image artifacts due to chemical shift and

magnetic susceptibilities arise from various rate limiting factors along the phase encoding direction of the EPI sequence.

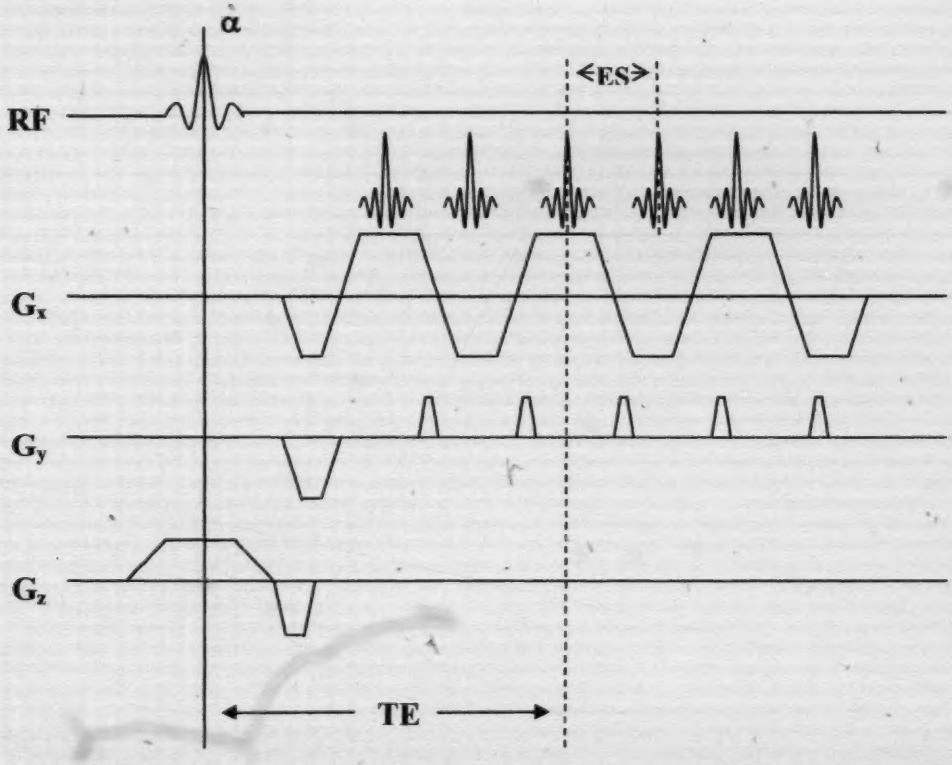

Figure 5-3: EPI Pulse sequence (Gradient echo type) used for outlining the K-space trajectory shown in Figure 5-2. G_x, G_y and G_z refer to the gradients on the frequency encoding (readout), phase encoding and slice selection axes respectively. The echo time (time to the center of K-space, Kx, Ky = 0) is given by TE; ES, echo spacing. Signal differences between tissues at TE determine the effective contrast in the image.

5.3.1 Burden on the Gradient System

The operation of an EPI sequence places considerable demands on the gradient system. If we desire 1.5 mm pixels with a 0.4 ms readout period per line (51.2 ms readout for 128 phase encode lines), then calculating the 1.5 mm resolution implies one cycle per 1.5 mm and that this must take place in 0.4 ms. In this case, the spin isochromats must differ by 2.5 KHz in 1.5 mm or 16.67 KHz/cm. This is a rather large gradient amplitude of (16.67 KHz/cm) / (4258 Hz/gauss) or 3.9 G/cm. For a 128 point readout resolution, 128 points must be sampled during the gradient pulse. However with readout periods of only 0.4 ms (2.5 KHz separation), the points must be sampled at 320 KHz (128 x 2.5 KHz) with 16

bit precision in most cases. This is all assuming the gradients have instant rise times and approaches modern day limits for analog to digital conversion (Cohen 1998).

5.3.2 Extent of Sampling

The number of points needed to be acquired depends on the final image resolution and desired field of view (FOV). The FOV is determined by the number of data points collected between K = 0 and K_{max}. For example 196 pixels of 1.5 mm width yield a 29.4 cm FOV. Additional lines in the Ky direction can be accomplished by extending the duration of the pulse sequence, albeit at the cost of image distortion since the T2* values of the sample (or tissue) may not be adequate enough to provide signal for the extended readout period. However, for matrix sizes of 128-196 lines (in Ky direction), readout periods of 50-80 ms are more or less common at present (Cohen 1998).

5.3.3 Image Contrast

Because of an infinite TR, differences in contrast for single-shot EPI, especially for 2D techniques, are common. Furthermore, to avoid chemical shift artifacts from fat, chemical shift fat saturation pulses are applied by using a Gaussian pulse centered on the fat frequency prior to excitation. In typical GRE-EPI sequences, phase encoding being sequential, there is a limit to how much TE can be reduced to minimize T2* weighting. One approach to maintain short TEs and reduce T2* weighting is that of centrically ordered phase encoding. On the other hand, a spin echo (SE) EPI scan is inherently centrically reordered with respect to the symmetry of the effects of field inhomogeneities and T2* about the center of K-space (Wielopolski *et al* 1998).

The image derived from a single shot EPI scan with an infinite TR demonstrates a proton density contrast with moderate T2 (for SE EPI) or T2* (for GRE EPI) weighting based on the TE value selected. The contrast in conventional scans depends on the magnitude of the longitudinal and transverse magnetizations during steady state conditions, i.e. in the case of fast low angle shot (FLASH) imaging. Hence a proper comparison between single-shot EPI and conventional scans requires a careful choice of parameters to facilitate a head to head comparison of the signal from both cases.

5.3.3.1 GRE EPI

In single shot GRE EPI, a selective RF pulse is used to collect the free induction decay image encoded using the EPI module (Figure 5-3). Longer TEs render T2* or susceptibility weighting to the images and this is well suited for T2*-weighted perfusion studies. Susceptibility weighted images are also used in acquiring the blood oxygen level dependent (BOLD) effect that has been used extensively for functional studies of the brain (Howseman and Bowtell 1999; Wielopolski *et al* 1998).

5.3.3.2 SE EPI

Conventional SE sequences use a 90°- 180° excitation to form the signal. For SE EPI, the EPI readout module is added after the 180° pulse to sample the echo signal (Figure 5-4). Here, the center of the EPI readout module coincides with the time of the SE, resulting in the SE EPI sequence being less susceptible to field inhomogeneities and characterized by a symmetric T2* profile (Wielopolski *et al* 1998).

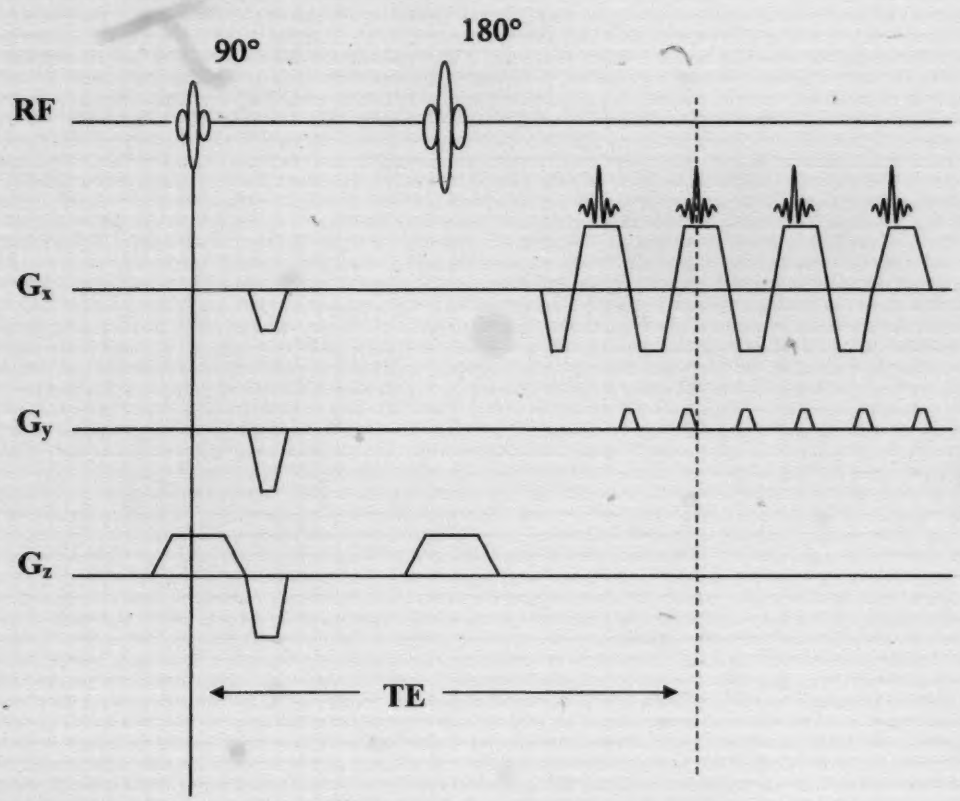

Figure 5-4: Pulse sequence diagram for a single shot SE EPI sequence.

5.3.4 Signal-to-Noise Ratio in EPI

The signal-to-noise ratio (SNR) in EPI is proportional to several imaging parameters ignoring the contrast generated by each imaging technique. The SNR is given by

$$SNR \propto \frac{\sqrt{NEX}\ \sqrt{N_x}\sqrt{N_y}\sqrt{N_z}\ \Delta x\ \Delta y\ \Delta z}{\sqrt{BW}} \qquad (5.1)$$

where NEX = number of excitations averaged
Δx, Δy and Δz represent voxel dimensions
Nx, Ny and Nz represent the number of points collected along the frequency, and both
phase encode axes respectively
BW is the acquisition bandwidth, the inverse of sampling rate Δt

Due to Bandwidth being proportional to the strength of the gradient applied during readout, large readout gradients translate into high readout bandwidths and consequently a reduction in SNR and a greater demand for the gradient amplifier (Wielopolski *et al* 1998). The SNR, although not high enough, compared to high flip angle conventional GRE scans with equal voxels, the SNR per unit time is considerably higher for single shot EPI. Additionally, all longitudinal magnetization may be available in the transverse plane following a single RF pulse. This suggests that some signal could be gained in comparison to conventional techniques when a finite TR may not allow complete recovery of the longitudinal magnetization between excitations (mainly for CSF due to its long T1) prior to each RF excitation (Wielopolski *et al* 1998).

SNR losses in EPI occur in regions with large susceptibility gradients. Thinner slices can be partly used to overcome this problem and may increase the signal from regions with poor field homogeneity compared to thicker slices. This is observed when one images regions such as the base of the brain near the sinuses where thinner slices are advantageous in recovering signal that may otherwise be lost from compete phase dispersion across the voxel (Wielopolski *et al* 1998). The SNR can also be improved by decreasing the acquisition bandwidth. However, this results in an increase in the echo spacing that increases geometrical distortions from a lower phase encoding gradient, signal loss and filtering from T2* decay and finally large chemical shift artifacts (Wielopolski *et al* 1998).

5.4 Artifacts in EPI

EPI can be extremely sensitive to image artifacts compared to conventional imaging techniques primarily due to the reversal of every second echo that takes place and the lengthy readout intervals (Fischer and Ladebeck 1998). Since every second echo is acquired under a negative gradient, the signal must be reflected with respect to time to utilize all echoes. Imperfections in the acquired signals either from eddy currents or from variations of the RF receive path, lead to an alternate line variation in the raw data, a phenomenon referred to as N/2 ghosting. Furthermore, the narrow bandwidth per pixel in the phase encoding direction can lengthen the overall acquisition time relative to conventional scans. The effects that result from this are 1) large fat-water shift, 2) geometric distortions arising from B_o inhomogeneity (through the magnet or patient), 3) dephasing induced signal loss, and 4) loss in resolution due to T2* filtering effects. The

first 3 cases can be considered as off-resonance effects (Fischer and Ladebeck 1998; Wielopolski *et al* 1998). This section details the causes of these artifactual effects in greater depth.

5.4.1 N/2 Ghosting

In EPI, every second line in K-space is read under a negative gradient. This negative gradient implies that this line goes backwards in K-space and it must be therefore reversed with respect to time. This is the main reason for EPI's susceptibility to modulations from line to line. These modulations result in a ghost image that is shifted by one half of the FOV.

5.4.1.1 Phase Errors

In the presence of an undesirable global field gradient, G' along the readout axis arising from 1D eddy currents or local inhomogeneities, the gradient causes a K-space shift given by the following relationship,

$$\Delta k_{shift,q} = (-1)^q \gamma G' T_{E,q} \qquad (5.2)$$

where q represents the qth gradient echo
$T_{E,q}$ is the echo time of the qth echo

The odd echoes have a K-space shift in a direction opposite (negative) to that of the even echoes (Figure 5-5). This is due to a negative read gradient and the odd data must be temporally reversed to reverse the direction of the shift also. This oscillating phase error (positive to negative phase) in K-space leads to N/2 ghosting in reconstructed images (Figure 5-6). This Δk shift is evident as a linear phase shift in an image reconstructed with the phase encode gradient turned off (a 1D reconstruction) (Haacke *et al* 1999).

This problem can be rectified by either phase subtraction or by the addition of a counteracting gradient G'' = -G'. Phase subtraction can be performed by mapping the phase modulation using a navigator scan, although this approach may not yield adequate results in the presence of a spatially varying gradient.

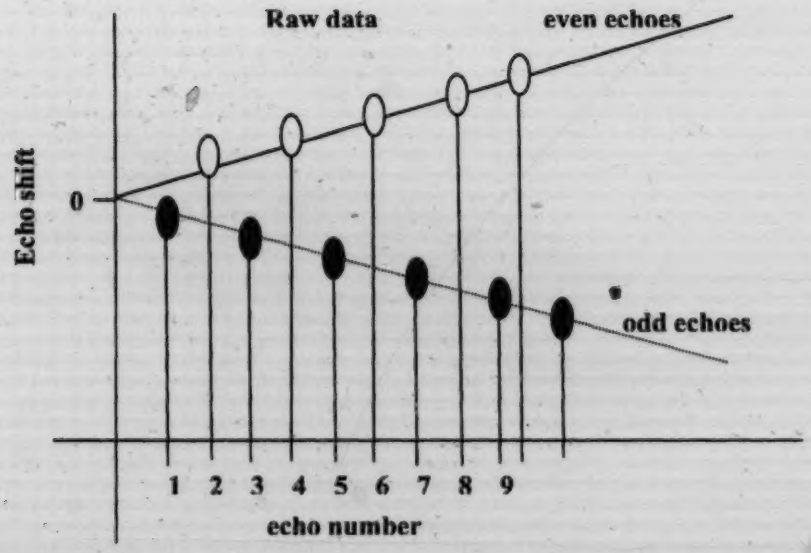

Figure 5-5: Phase profile in the presence of a static background gradient for even and odd echoes in an EPI sequence.

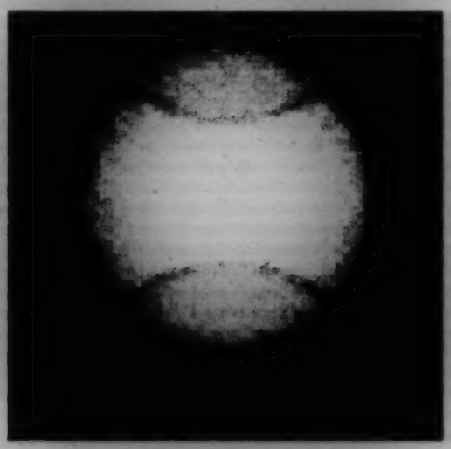

Figure 5-6: Example phantom image of N/2 ghosting. These ghosts are caused by the small line-by-line errors that are formed during spatial encoding.

5.4.1.2 Eddy Currents

Rapidly switching gradients induce so called eddy currents in proximal conductors including the RF coils and electromagnetic and thermal shielding. Mathematically, this can be written as,

$$emf = -\int_{\text{coil area}} dB/dt \cdot ds \qquad (5.3)$$

where emf = -dΦ / dt and Φ is the magnetic flux through a coil given by,

$$\Phi = -\int_{\text{coil area}} B \cdot ds \qquad (5.4)$$

Accordingly, by Lenz's law the induced current produced in the conductor always flows in such a direction that it opposes the change that is producing it

Eddy currents result in a time delay between the current in the coil and the gradient field, and the amplitude of the gradient field is reduced. The gradient field variation is shifted in time, and because of the time reversal of every second line, this manifests as a significant problem. The delayed gradient field causes the echoes to refocus late (Figure 5-7). Because of the time reversal of the second line, the echo in the second line in K-space refocuses earlier, i.e. it is shifted by the same time delay in the opposite direction. This K-space modulation causes N/2 ghosting.

This can be solved by adjusting the analog-to-digital converter (ADC) raster to match the gradient field. The time that the gradient field variation is shifted should be used to postpone the ADC triggering in order to be in phase with the gradient field (Fischer and Ladebeck 1998).

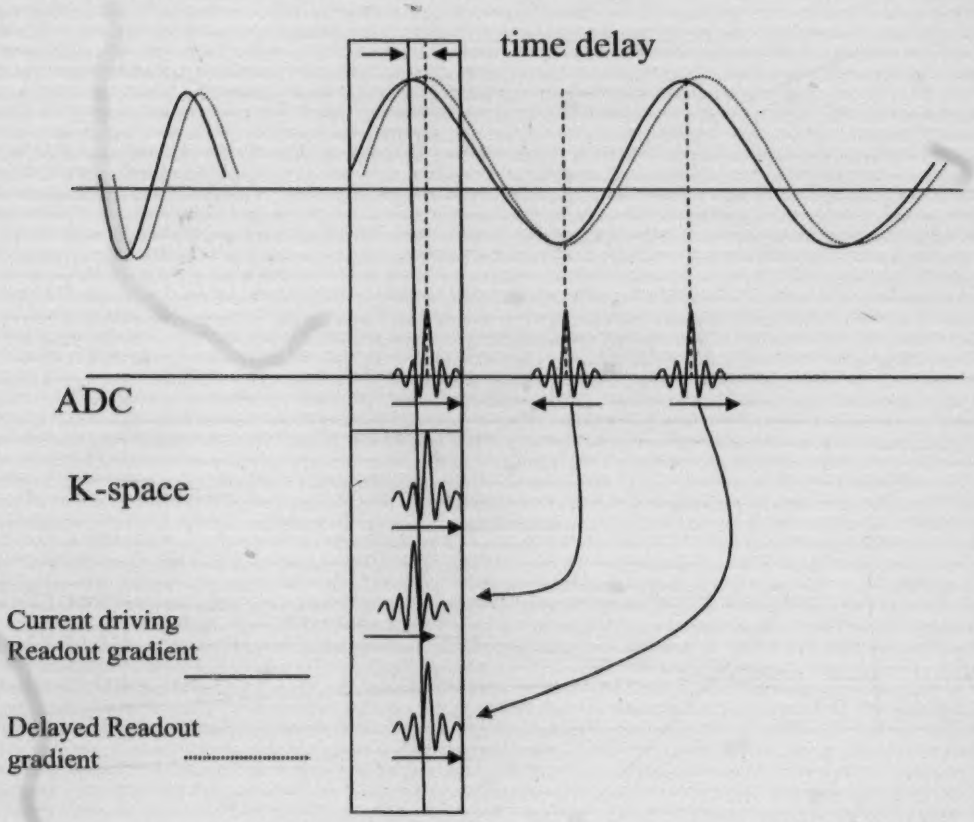

Figure 5-7: Delays between the gradient field and the analog-to-digital converter (ADC) timings result in N/2 ghosting. Because of the time reversal of every second echo, a shift is observed for alternate echoes leading to a zigzag pattern of echoes in K-space.

5.4.2 Artifacts Arising from Low Bandwidth

To understand the artifacts arising from low bandwidth, two generalities must be shown. They are the bandwidth (BW) of the readout and phase encoding gradients given by,

$$BW_{RO} = 1/T_{RO} \text{ and } BW_{PE} = 1/T_{acq}$$

where T_{RO} is the readout or acquisition time for a single line along the Kx axis
T_{acq} is the total acquisition time or time to acquire a single line along the Ky axis
and $BW_{RO} >> BW_{PE}$

Supposing T_{RO} has a value of 0.5 ms, and T_{acq} = 96 * 0.5 ms = 48 ms, their respective pixel bandwidths will be 2000 Hz and 20.8 Hz. The relative importance of these values

lies in the fact that low bandwidths, primarily along the phase encode direction, augments the susceptibility effect and is the likely cause of artifacts (Fischer and Ladebeck 1998).

5.4.2.1 Chemical Shift Effects from Fat-Water Shift

The resonance frequency in MR depends on the flux density at the position of the nucleus. The chemical shift is described as the effect the chemical environment can exert on the external flux density in terms of enhancing or weakening it (Fischer and Ladebeck 1998). This chemical shift is denoted by a relative number, i.e. the resonance frequency in one environment compared to that in another environment. The absolute frequency difference is proportional to the main flux density by,

$$\delta\omega = \gamma\sigma B_0 \qquad (5.5)$$

where σ is the flux density

A frequency shift, $\delta\omega$, in the presence of gradient G for frequency encoding results in an image shift d,

$$d = \delta\omega / (\gamma G) \qquad (5.6)$$

The chemical shift d_{csp} is related to BW in units of pixels by,

$$d_{csp} = \delta\omega / BW = \sigma \gamma B_0 / BW \qquad (5.7)$$

The displacement due to chemical shift is proportional to the main field B_o and inversely proportional to BW. The signal from protons of fat and water is usually visible when imaging biological samples. The fat protons possess a flux density of 3.3 ppm (parts per million). In EPI, G is typically not high enough in the low bandwidth direction (phase encode direction) to keep the fat-water shift below 1 or 2 pixels (see Figure 5-8). At 1.5T, the fat-water frequency difference $\delta\omega$ is 210 Hz and the fat water displacements due to the chemical shift in the frequency and phase encoding directions (using BWs calculated in section 5.4.2) are 0.11 pixels and 10.1 pixels, respectively. The shift in the phase encode direction is worse than the shift in the readout direction (approx. 11% of the FOV of 96).

Chemical shift effects are typically circumvented by applying the fat suppression pulse prior to excitation in EPI sequences. The most commonly employed technique is the pre-saturation or FATSAT where the fat is excited with a spectrally selective pulse and any residual transverse magnetization is spoiled or dephased with a gradient pulse. This can precede any imaging sequence. The longitudinal magnetization of fat does not have adequate time to reform following the pre-saturation pulse and therefore it does not contribute any signal when the subsequent slice-selection pulse (not spectrally selective) is applied. One disadvantage of this method is that the inhomogeneities of the static magnetic field will shift the resonance frequencies of both water and fat. This will result

in the pre-saturation pulse exciting some water instead or it may miss some of the fat (due to the saturation pulse frequency not equaling the fat resonance frequency), thereby leading to poor fat suppression (Keller *et al* 1987).

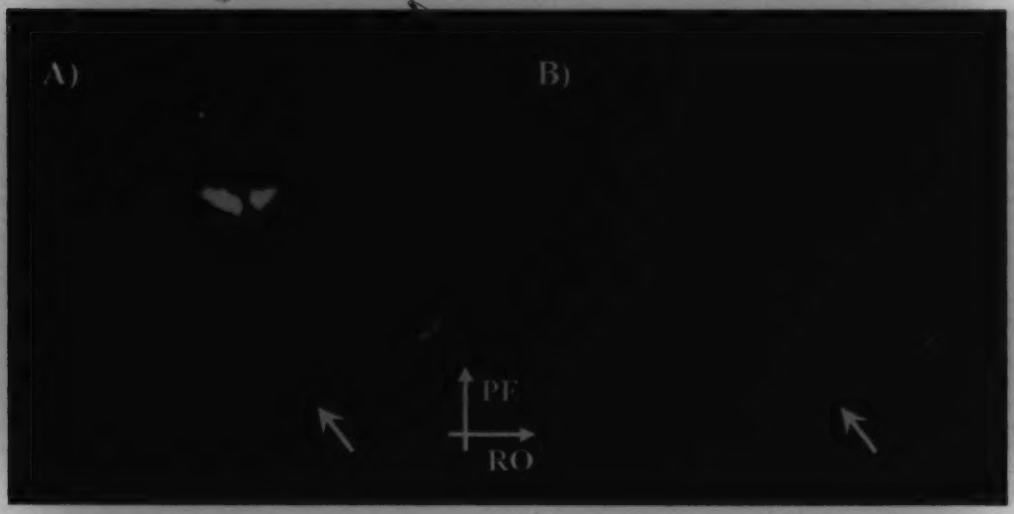

Figure 5-8: Examples of chemical shift artifacts in diffusion-weighted single shot echo planar axial images (A and B (arrows)). The artifacts are observed along the phase encode (PE) direction (RO, readout direction).

5.4.2.2 Geometric distortions and Susceptibility

Aside from dealing with inhomogeneities related to magnet imperfections, a second source of inhomogeneities arises when a sample is placed in a magnet. The magnetic flux density, B inside a sample of susceptibility is given by,

$$B = (1+\chi)\,\mu_o B_0 \qquad (5.8)$$

where μ_o is the magnetic field constant
B_0 is the magnetic field strength
χ is the susceptibility factor

Unlike the chemical shift effect, the off-resonant effect is not spatially constant and this gives rise to a geometric distortion. At the intersection of 2 substances with varying susceptibility levels χ_1 and χ_2, a local inhomogeneity exists such that,

$$\Delta B_o = (\chi_1 - \chi_2)\, B_0 \qquad (5.9)$$

The amount of local distortion, d is proportional to the field offset B_o and inversely proportional to the gradient amplitude. For EPI, this refers to the phase encode direction because it is characterized by low bandwidth. Local distortion is given by,

$$d = \Delta B_o / G \propto \Delta B_0 T_{acq} \qquad (5.10)$$

The geometric distortion is proportional to the data acquisition time and to the absolute value of field inhomogeneity, which scales with the strength of the external field. Magnet homogeneity is identified in units of ppm.

The flux density variation from the magnet undergoes a slow change across the imaging volume. The inhomogeneity from tissues with different susceptibilities is somewhat of a step function in the field which cannot be ameliorated through shimming (Fischer and Ladebeck 1998). This causes strong geometric distortions and becomes a huge limitation of *in vivo* applications of EPI. This artifact is aptly titled susceptibility artifact and occurs mainly at air-tissue and tissue-bone interfaces. The signal intensity can be bright where pixels are compressed. Distortions also induce stretching or compression of imaging voxels (Figure 5-9). Some means to address these artifacts, particularly for brain imaging are 1) use of thin slices to limit the extent of inhomogeneities across a pixel, 2) acquiring oblique slices (parallel to brain basis), and 3) post processing approaches with good knowledge of B_0 distribution.

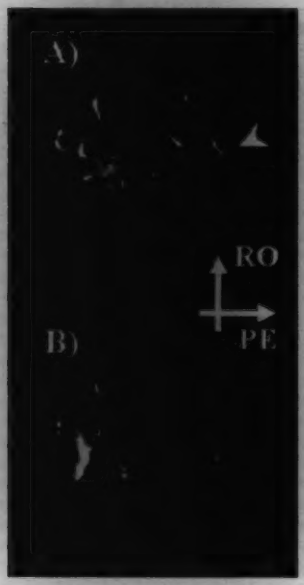

Figure 5-9: Examples of distortions and susceptibility artifacts along the PE direction (right-left) in terms of stretching of the left temporal lobe (A, arrowhead) and an artifactual bright signal at the junction of the right temporal lobe and cerebellum (B) in 2 diffusion-weighted single shot echo planar axial images at the level of the pons.

5.5 Shortening the EPI Readout Interval

In single shot EPI, blurring along the phase encode direction arises from the long readout times required to encode the entire raw data matrix relative to the T2* decay of most

tissues (Wielopolski *et al* 1998). This filtering effect is not significant along the frequency encoding direction as very little T2* decay occurs here during the collection of each line. One approach to mitigate these T2* filtering effects is that of partial Fourier imaging. Theoretically speaking, the method collects half of the K-space data to generate an image and take advantage of the conjugate symmetry of K-space to recreate the missing part of the raw data. The benefits are a shorter TE without loss in resolution along the phase encode direction, and with half the scan time per shot, reduced filtering effects from T2* decay. The following sub-sections discuss the conjugate symmetry of K-space, its advantages and how this property is exploited to perform partial Fourier imaging for single shot EPI.

5.5.1 The Conjugate Symmetry of K-space

The raw data can be decomposed into 2 components, one being symmetrical about the origin (a cosine wave) and the other being antisymmetric (a sine wave). Armed with this knowledge and that of the precise location of that point of symmetry, a full image can be created from only half the data since the symmetrical and antisymmetrical parts of the data are easily reconstructed (Cohen 1998).

The Fourier transform operates between functions of complex variables. Despite the input function only having real components its transform contains an imaginary component, represented as a separate dataset. So, for a real input signal (subject or phantom) 2 raw datasets (real and imaginary) are produced. Therefore, transformed MR data are over-specified, giving 2 transform points for every input point. This over-specification is evident in the MR raw data. Supposing the value of signal H(m,n) is C+iD, the value at H(-m,n) is C-iD, the complex conjugate. Knowing this, it is easy to calculate H(-m,n) if H(m,n) is known. The main advantage of conjugate symmetry is that it affords great time savings in EPI and conventional imaging because only half of the raw data points need to be acquired to form a whole image. Hence, only half the readout time is required (Figure 5-10). In practice, to determine the point of symmetry in the raw data, one needs to acquire slightly more than half the data (Cohen 1998).

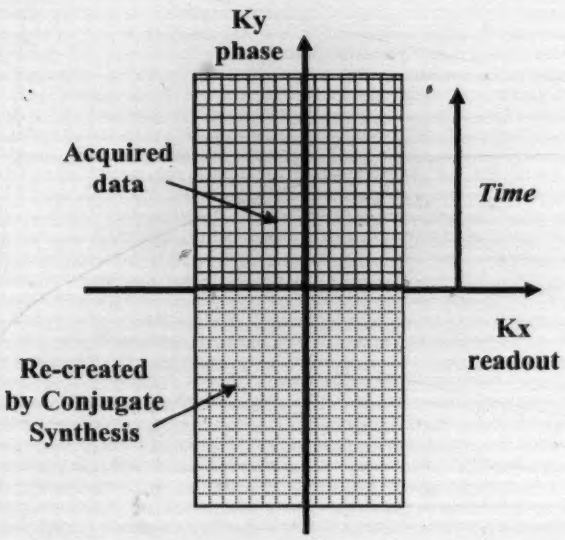

Figure 5-10: A depiction of conjugate synthesis. The top half is the acquired data and the bottom half is that portion calculated by using the conjugate K-space symmetry. This method may be used to reduce TE in EPI.

5.5.2 Partial Fourier Single Shot EPI

Partial Fourier imaging according to the method by Margosian *et al.* (1986) utilizes the conjugate symmetry of the Fourier transform and assumes a step function at the origin of K-space multiplying the raw data (Margosian *et al* 1986). However, because additional deleterious phase errors can be accrued, several additional lines after the K-space center are collected to compute a low resolution phase map (Figure 5-11). This map is applied to the original data before reconstruction to diminish the effects of slow varying phase errors such as intensity variations and extraneous signal cancellations in the final image reconstruction. The resulting image is computed from the real part of the 2D Inverse fast Fourier transform after applying a phase correction (Wielopolski *et al* 1998).

The immediate advantages of partial Fourier scanning for EPI are a reduction in TE and diminished T2* filtering effects. Furthermore, the drop in scan time per shot can be allocated for increasing the echo spacing to enable a lower bandwidth in the readout direction. This also affords a smaller FOV along the readout direction without losses in SNR or increase in imaging time. Nonetheless susceptibility and chemical shift artifacts will increase as the phase encoding gradient needs to be weakened from the longer interecho spacing. It should be mentioned that one drawback of partial Fourier imaging is that the acquisition of only part of the raw data translates to a reduction in SNR.

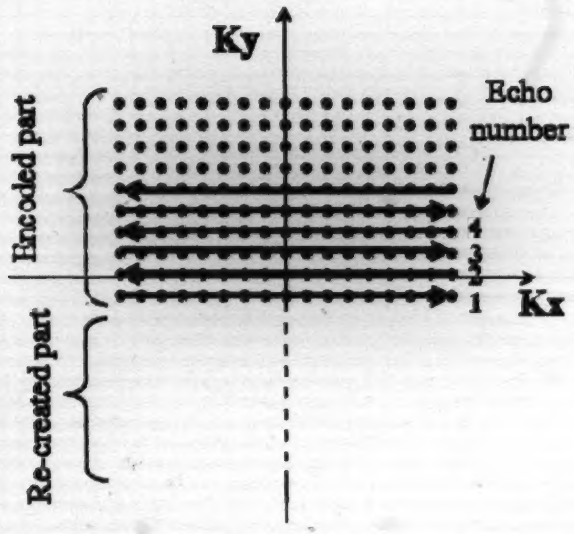

Figure 5-11: The K-space profile of an EPI sequence with the Partial Fourier technique.

5.6 EPI Sequences for Diffusion Studies

In the realm of conventional MRI methods, diffusion imaging is typically performed with standard SE sequences. However, due to the increased sensitivity of the diffusion weighting to any net translational motion of water molecules, even slight movements of the head during acquisition can render the images and resulting apparent diffusion coefficient measurements useless. Due to the lengthy acquisition phase (~10 min) of conventional MRI diffusion sequences, it is highly improbable to get acute stroke patients in a clinical setting to keep their heads immobile during scanning. This is where EPI subserves the role of a rapid method to perform multi-slice diffusion imaging with adequate spatial resolution in a reasonable time. This section highlights the role of two classes of sequences, namely, SE EPI and Twice-Refocused SE EPI used to perform diffusion imaging. Also, their relative strengths and weaknesses are explored as pertains to acquiring diffusion weighted data.

5.6.1 SE EPI

A diffusion weighted image can be obtained with the same SE EPI sequence structure that was discussed in section 5.3.3.2. A pair of strong diffusion sensitizing gradients are placed before and after the application of the 180° refocusing pulse (Figure 5-12). The strong gradients applied produce an increase in the intravoxel dephasing and loss of signal intensity in the presence of diffusion. These images are also prone to susceptibility and chemical shift related artifacts depending on the choice of parameters employed, mainly that of a lengthy TE. Another consequence of long TE is a decline in SNR from

T2 decay. SE EPI can also be restrictive in cases where tissues with short T2 values are of interest, since fast T2 decay would eliminate most of the signal left to generate an image acceptable for diffusion measurements (Wielopolski *et al* 1998).

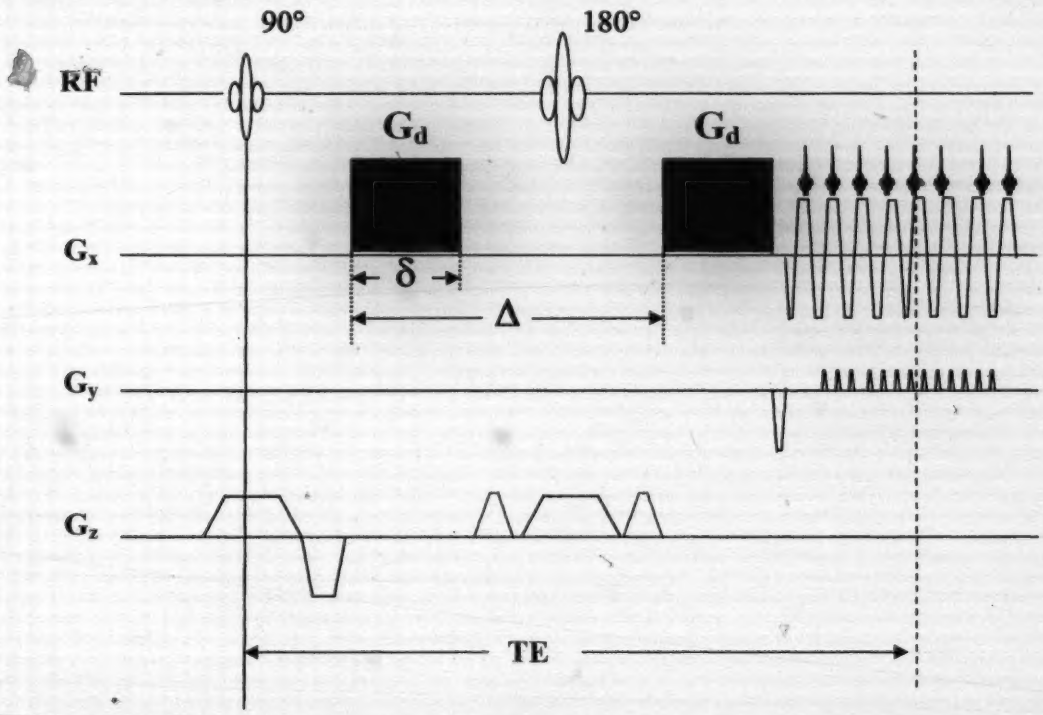

Figure 5-12: Diffusion-weighted SE EPI pulse sequence. A pair of diffusion gradients of equal amplitude G_d and duration δ are applied symmetrically around the 180° refocusing pulse. Here the diffusion gradients are applied along the readout direction, but they can be positioned on any axis. Δ, separation between the gradients

5.6.2 Twice-Refocused SE EPI

In diffusion imaging sequences including those used for DTI, gradient pulses are applied at high intensities with long durations, ultimately resulting in the development of persistent eddy currents. The detrimental effects of these eddy currents on the EPI echo train were reviewed in section 5.4.1.2. In typical SE EPI, these eddy currents wreak havoc on the echo planar readout and cause spatial distortions dependent on the direction of the applied diffusion gradients. This results in misregistration artifacts when multiple images with differing gradient directions are acquired. If the eddy currents decay rapidly between the on and off field gradient transitions, i.e. between the time of the applied field gradient transition and image readout, a spatially dependent alteration of the image phase

will not result in any discernible distortion. However, because the eddy currents decay slowly, a residual field lingers during the image readout behaving as a spatially encoding gradient, and inducing image distortions.

Several post-processing solutions have been provided to undo the effects of eddy currents on image data (Calamante *et al* 1999; Haselgrove and Moore 1996; Jezzard *et al* 1998). However, these methods entail added noise and processing time and require recalibration of sequence timings. Others have proposed changes in sequence design to minimize eddy currents (Alexander *et al* 1997; Boesch *et al* 1991), albeit with penalties that stem from long TE values and loss of scanning efficiency. However, a more recent sequence based approach minimizes eddy currents by inserting additional RF refocusing pulses into a traditional SE EPI diffusion sequence, and splitting the diffusion field gradient pulses into shorter pulses of alternating polarity (Reese *et al* 2003). Furthermore, these shorter gradient pulses have been modified to be unequal and asymmetric in duration to cancel any exponentially decaying residual fields. This method, which does not involve any extension in scanning duration or post processing of images, is referred to as the twice-refocused SE (TRSE) sequence.

The TRSE sequence has been shown in Figure 5-13. Essentially a spin echo diffusion sequence contains two RF refocusing pulses. Two bipolar field gradients of duration $\delta_1 + \delta_2$ and $\delta_3 + \delta_4$ are used with the RF refocusing pulses dividing each bipolar pair. The length of the first two gradients δ_1 and δ_2, is equal to the length of the next two gradients δ_3 and δ_4. In this idealized sequence,

$$\delta_2 + \delta_3 = TE/2 \qquad (5.11) \text{ and}$$

$$\delta_1 + \delta_4 = TE/2 - t_{pr} \qquad (5.12)$$

where t_{pr} is the sum of the preparation time after the excitation pulse and the readout time preceding the SE.

The sequence permits any diffusion gradient duration (or lengths) such that the time between the two refocusing pulses is TE/2 and the dephasing and rephasing due to the diffusion gradients is equal. The TRSE sequence design enables the cancellation of eddy current buildup (from the shorter time between on and off field gradient transitions) prior to the readout.

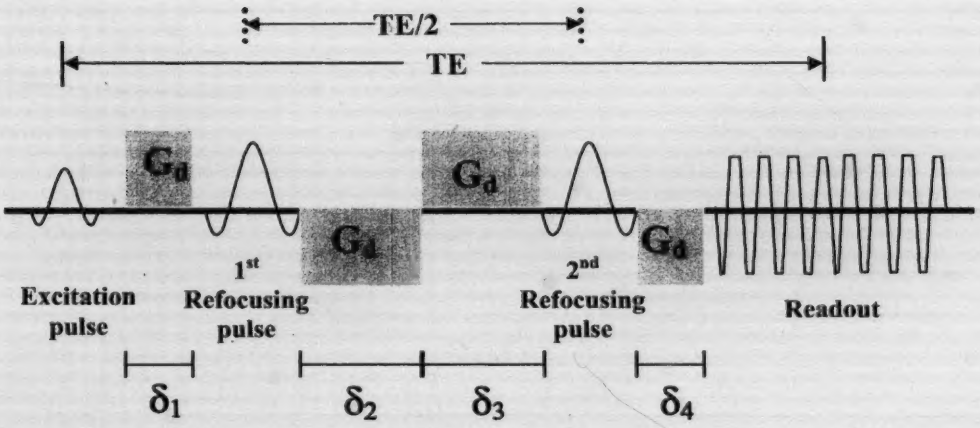

Figure 5-13: TRSE pulse sequence timing diagram. For simplicity, the slice selection and phase encoding gradients have been omitted. Diffusion gradients G_d of durations δ_1, δ_2, δ_3 and δ_4 are shown.

5.7 Concluding Remarks

This chapter has laid the background for the echo planar imaging method, and identified its strengths and limitations in general and also with respect to diffusion imaging. For the work documented in this thesis, EPI was used in diffusion imaging of acute stroke patients at 1.5T with the twice-refocused spin echo sequence and permitted acquisition of high quality images with adequate spatial resolution. Nonetheless, some of the acquired images did exhibit traces of geometric distortions from susceptibility effects, a problem that scales with external field strength.

6

FUNDAMENTALS OF PARALLEL IMAGING

The defining feature of parallel imaging is that it employs the spatial encoding inherent in the signals from an array of surface coils resulting in accelerated image acquisition. Initial studies performed ~18 years ago outlined the concept (in different approaches) that reception of signals from an object using multiple coils with distinctly overlapping regions of sensitivity can provide spatial information that can be considered as a temporally parallel spatial encoding method (Carlson and Minemura 1993; Hutchinson and Raff 1988; Kelton *et al* 1989; Ra and Rim 1993). However, this idea was not readily adopted by the MR imaging community perhaps due to Roemer's treatment of array coils (Roemer *et al* 1990) proposing the combination of signals from individual coils using a sum of squares at every image location, and overlooking the need to assess the spatial variation in coil sensitivities a la generating coil sensitivity maps, an integral component of parallel imaging.

The current era of parallel imaging was ushered in by Dan Sodickson's introduction of the K-space based method; Simultaneous Acquisition of Spatial Harmonics (SMASH) (Sodickson and Manning 1997), and was followed rapidly by Pruessmann's image domain based Sensitivity Encoding or SENSE method (Pruessmann *et al* 1999). SENSE is rooted in theory from the earlier papers and its concepts form the basis of the lingua franca used in the current implementations of image-domain based parallel imaging techniques.

This chapter begins with a discussion on the limitations of speed in conventional MRI techniques, and how they can be addressed by undersampling K-space and reconstructing images by means of either of the two classes of parallel imaging methods- K-space based and image domain based approaches. Key concepts and terms have been introduced and also the potential strengths and weaknesses of parallel imaging have been covered. The workings of two popular methods, Modified Sensitivity encoding (mSENSE), an offshoot of SENSE, and Generalized autocalibrating partially parallel acquisitions (GRAPPA), an advanced version of SMASH, have been described to provide the reader with a theoretical foundation to better comprehend the information presented in a later chapter, which deals with the application of mSENSE and GRAPPA in diffusion tensor imaging of the brain.

6.1 Limits of Speed in Conventional Imaging

Spatial information in MRI is typically encoded by the application of switched magnetic field gradients before and during echo acquisition. In this method, MR data are acquired in a sequential, i.e. one echo after another or line by line fashion. Then, after the repetition time TR, another excitation occurs and another line is acquired. Thus, scan time is equal to the number of phase encode lines (or echoes) multiplied by TR (Figure 6-1). Due to this reason, conventional MRI acquisition schemes are slow and this slowness can translate to lengthy acquisition times for techniques such as 3D imaging or in dynamic imaging of organs such as the heart. This lack of speed can also be a hindrance in dynamic imaging where long breath holds may be required, resulting in the accumulation of artifacts. An example of this case is abdominal imaging where to acquire a 256 x 256 matrix with a given TR of 10 ms, it takes 2.56 s for 1 slice and ~26 s for 10 slices. However, it may be challenging for a patient to perform a breath hold of that duration, especially if they suffer from emphysema or other respiratory ailments. Any motion occurring between TR's (e.g. diaphragmatic motion) may affect the integrity of the acquired data by making it inconsistent with the surrounding data. This can generate severe image artifacts even with minor inconsistencies that are observed as replications of the signal along the phase encode direction.

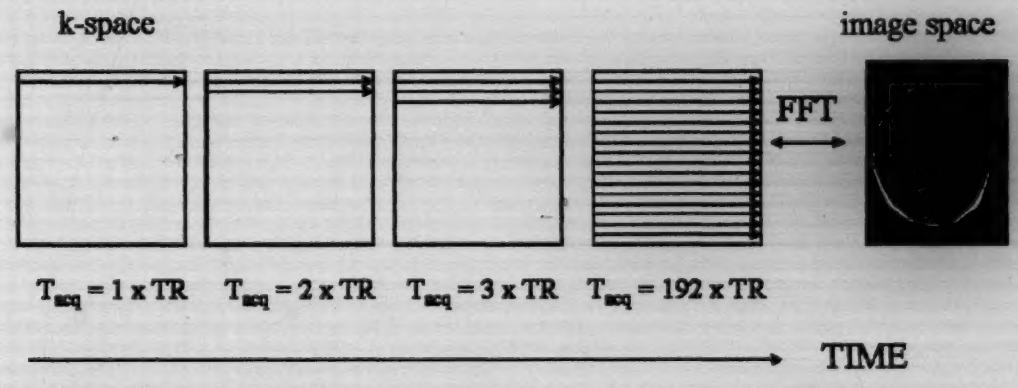

Figure 6-1: Sequential filling of K-space in conventional MRI. Although each data line is acquired in a few milliseconds (from left to right as shown here), successive lines or phase encodes are added slowly with each phase encode measurement being separated by one TR. Here, after 192 TRs enough data has been acquired to produce an image which is reconstructed from k-space by fast Fourier transformation (FFT); T_{acq}, acquisition time.

The speed of a given MRI method is assessed by how quickly the spatial encoding can be performed and how fast the echo data can be collected. The advent of faster and stronger gradient systems has substantially increased the acquisition speed by reducing the duration of image encoding. Current gradient systems have strengths of up to 50 mT/m

and switching rates on the order of 100 μs. Gradient boosted imaging methods permit improved spatial and temporal coverage and dramatically reduce the dead time periods during which no MR signal is acquired (Heidemann *et al* 2003).

On the downside, these gradient encoding based fast imaging methods exhibit certain hardware and methodological drawbacks. For one, they require a large number of fast, but nonetheless time-consuming gradient switching steps. Many of the fast imaging sequences in use such as EPI, fast low angle shot (FLASH), turbo spin echo (TSE), and spiral for example attain their high speeds by optimizing the strengths, switching rates and patterns of applied gradients and RF pulses. However several hardware and physiological factors place significant limits on how quickly these gradients can be switched, thereby limiting the minimal interecho spacing and minimum repetition times. By exceeding a certain threshold, rapidly switched field gradients can produce neuromuscular stimulation, while extremely dense RF pulse trains can result in very high levels of RF deposition and tissue heating. At present, most systems operate just below these levels so that in these conditions, no further improvements in imaging speed can be achieved by reducing the interecho spacing or the repetition time through gradient performance alone. Hence there are tradeoffs between imaging time and image quality with some concessions required to achieve reasonable results. Due to this, parallel imaging, which is not linked to advances in gradient performance, is a promising means of overcoming the constraints on imaging speed.

6.2 Undersampling K-space: A Time Savings Approach

One method of accelerating the acquisition in conventional imaging is to partially sample K-space or collect only a fraction of the data. The main feature of this approach is to understand exactly which lines to exclude. An image reconstructed from data only mapped to the center of K-space will contain mainly contrast and little detail or edge information, reflecting the omission of high frequency points and appear blurry (Figure 6-2b). Consequently an image reconstructed from data mapped only from the periphery of K-space will be devoid of contrast and contain edges and fine detail since the low spatial frequencies which encode contrast have been omitted (Figure 6-2c) (Hennig 1999). As can be observed from the results, both methods of undersampling are futile in terms of the images they yield.

Another means of speeding up acquisition through undersampling is by reducing the number of phase encoding steps by a reduction or acceleration factor, R by increasing the distance of equidistantly sampled K-space lines. For example, R=2 implies we have skipped every alternate line of K-space. This type of undersampling leads to a reduced field of view (FOV) in the phase encoding direction associated with fold-over or aliasing artifacts in image space as shown in Figure 6-3 (Blaimer *et al* 2004). This approach is at the heart of all parallel imaging methods where the goal is to provide the full K-space matrix or unaliased images by using the spatial information contained in an array of RF coils.

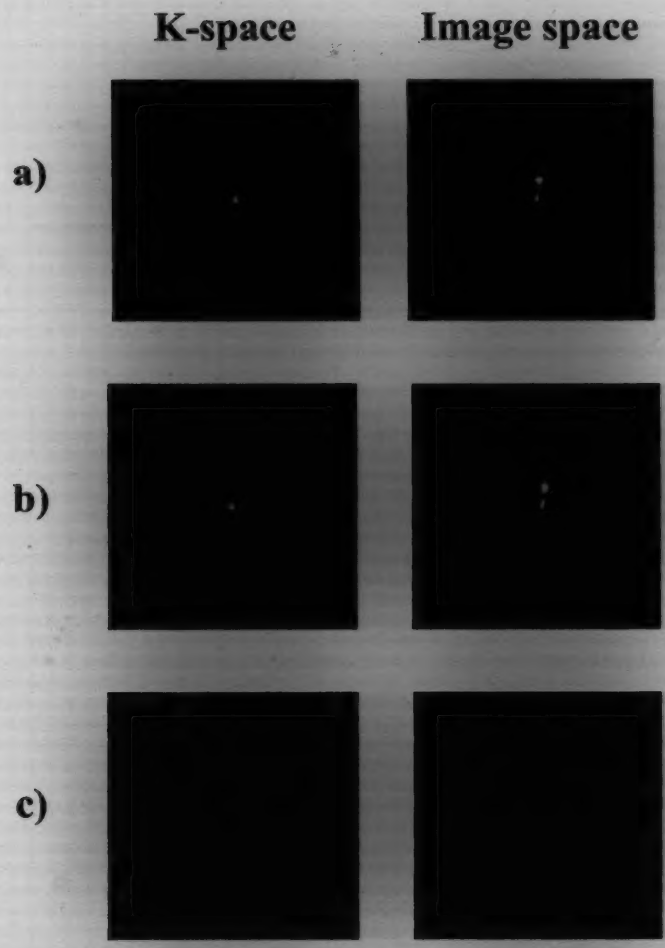

Figure 6-2: Effects of partial sampling of K-space data. **a**) Acquisition of the full data yields a high resolution gradient echo brain image. **b**) Acquiring only the central portion of K-space yields a low resolution image. **c**) An image reconstructed from the outer portions of K-space will only show edges and lack contrast information (Hennig 1999).

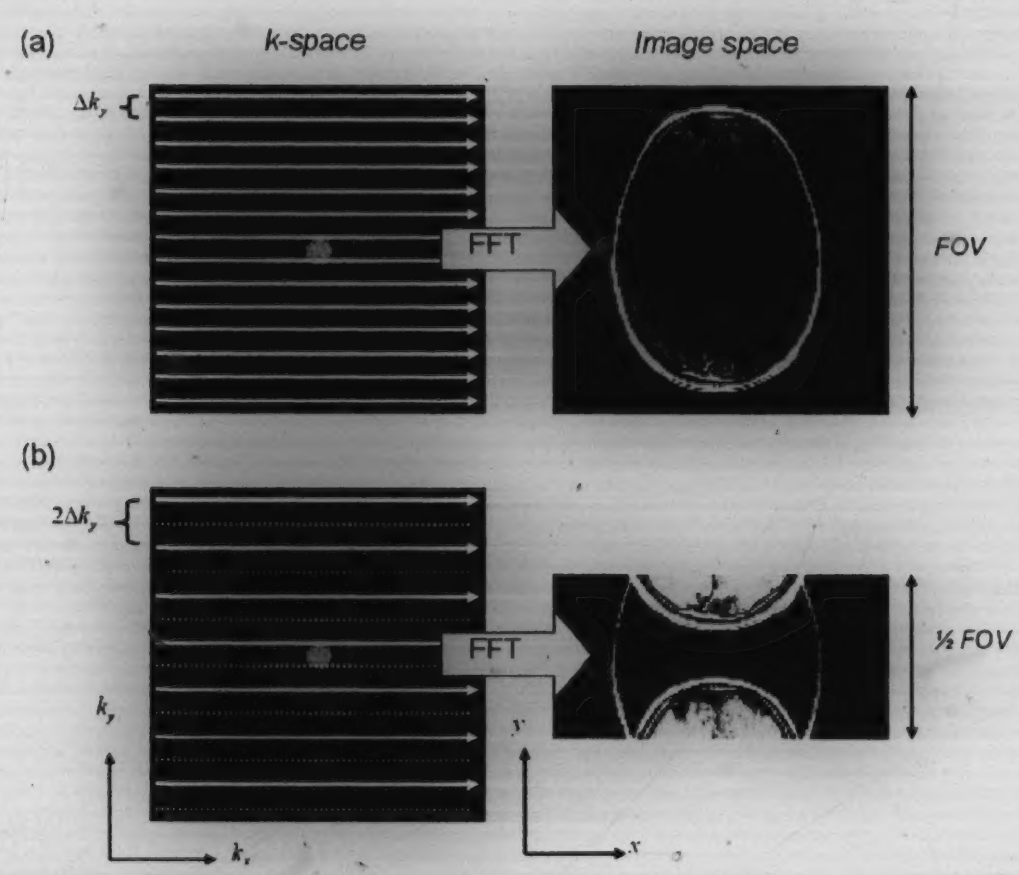

Figure 6-3: Undersampling K-space data. **a**) Conventional acquisition of fully sampled K-space generates a full FOV axial brain image following Fourier transformation (FFT). **b**) Undersampling K-space by an acceleration factor, R=2 results in a reduced FOV (FOV/2) with aliasing artifacts. The solid lines indicate acquired K-space lines and dashed lines reflect skipped K-space data (Blaimer *et al* 2004).

6.3 Features of Parallel Imaging

In parallel imaging, the number of phase encoding steps and therefore the acquisition times are reduced compared to conventional imaging. Due to the parallel imaging based reconstruction methods, the same FOV with the same spatial resolution as in conventional imaging can be obtained, but with reduced phase encoding steps. This is accomplished by using multiple independent receiver coils and the spatial information content of these array coils is exploited to encode and detect multiple MR echoes simultaneously (Figure 6-4). The underlying property of parallel imaging is the

application of multiple independent receiver coils with distinct sensitivities across the object. These coils are different from large volume RF coils where the inner volumes are fairly homogeneous and the sensitivity from one location does not vary significantly compared to that from a different location. Prior to the resurgence of parallel imaging in 1997, the purpose of phased array coils was to distribute the high signal to noise ratio (SNR) performance of their small component coils over a large area covered by the entire array with no increase in imaging time. Although phased array technology for conventional MRI has been used to improve image quality with acquisition times equal to those in large volume coil imaging, in parallel imaging this technology has been harnessed to reduce MR scan times (Heidemann *et al* 2003).

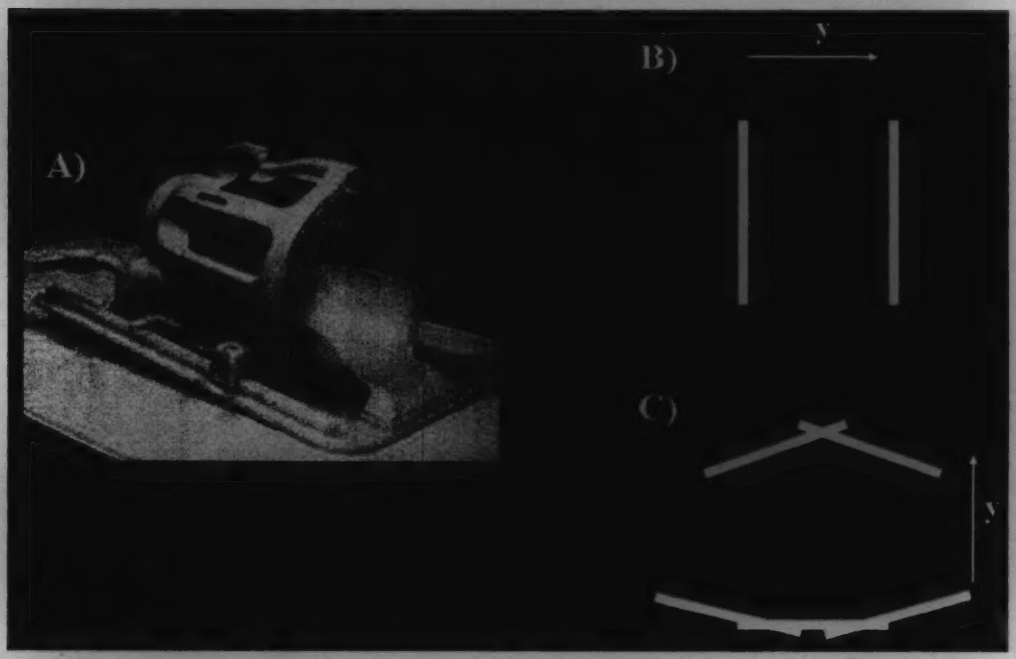

Figure 6-4: Examples of phased array coil formats. The phased array consists of multiple small coils arranged to efficiently cover a specific region and obtain high resolution, high SNR images of a large volume. A) An 8-element (or channel) phased array coil for neuroimaging (MRI Devices, Waukesha, WI) used on the Siemens 1.5T Sonata scanner. Each element has its own receiver. The diagrams on the right show how a two coil array can be used for brain imaging (B) and how a five coil array can be used for cardiac imaging (C). The arrows indicate the fold-over direction, y. Each element in the phased array coil formats shown here has a unique sensitivity profile of the sample (Pruessmann *et al* 1999).

6.3.1 Utility of Phased Array of Receiver Coils

The field of parallel imaging as it is known today is referred to as *partially* parallel imaging where data is acquired from more than one coil simultaneously. This is accomplished by using array coils consisting of multiple individual surface coils each feeding their own receiver channel. Each surface coil generates its own K-space and each such K-space can be reconstructed into an image. These images display the same geometrical plane through the object with the same FOV at the same resolution and with similar contrast properties. However, they vary due to the coil sensitivity profiles that affect the spatial distribution of signals within the images (Bammer and Schoenberg 2004; Larkman *et al* 2004).

It is evident that in the image domain, a surface coil spatially modulates the signal from the object. Regions of the object far from the coil produce little or no signal whereas portions of the object closest to the coil element yield high signal. An image produced by a surface coil can be perceived as being the multiplication of an object image with a smoothly varying coil sensitivity function (Figure 6-5). This intrinsically allows signals originating from areas that are either close to a coil or far from it to be distinguished from each other. When a surface coil is used for imaging, information regarding an area of K-space is measured rather than a discrete point, which is the case for uniform coils such as a body coil. The size of the area over which the data is spread is governed by the convolution kernel (Figure 6-5E) defined by the coil properties.

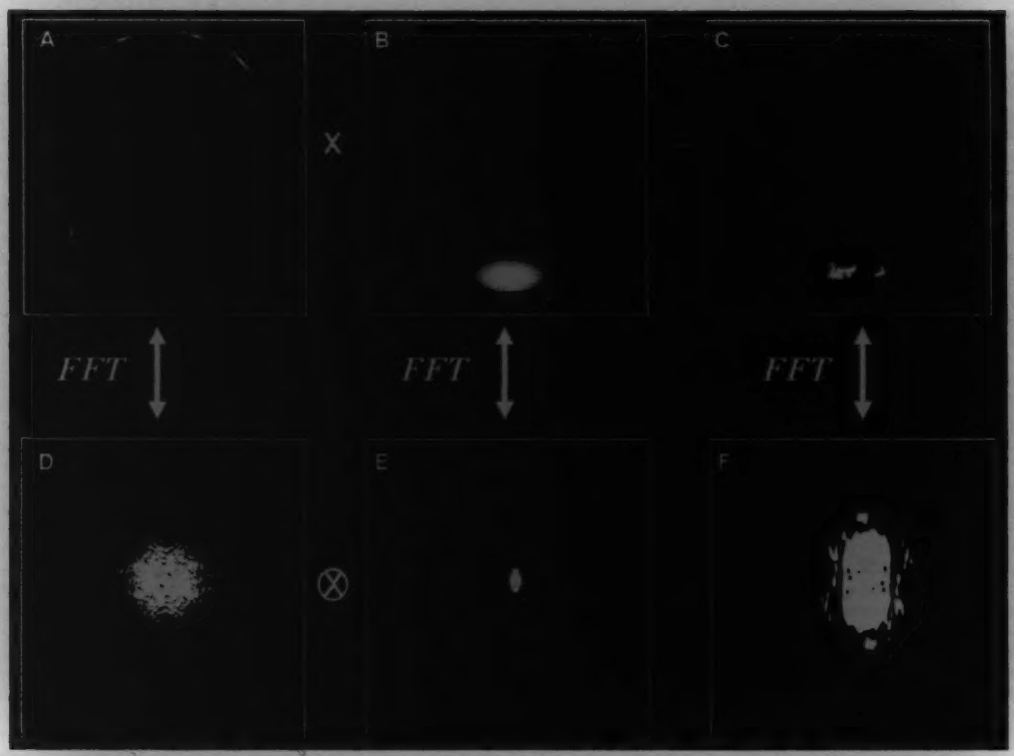

Figure 6-5: Surface coil images. The object A is imaged with a surface coil with sensitivity profile B in the image plane. The multiplication of A and B generates the final image, C. The K-space profiles of the object and the coil sensitivity are shown in D and E respectively. Judging from F, the K-space has been smeared by the convolution process (Larkman *et al* 2004).

6.3.2 Coil Sensitivity Profiles

In vivo calibration of coil sensitivity profiles is essential for accurate parallel imaging reconstructions. Therefore the most integral step is to measure the sensitivities of the various coil elements in an array. Since sensitivity varies with coil loading, the sensitivity profiles must be calibrated by an additional reference acquisition that is a part of the actual imaging exam. This can be achieved for instance by a low resolution fully Fourier encoded 3D acquisition received in each component coil, which permits arbitrary slice positioning (Figure 6-6) (Bammer and Schoenberg 2004). One method of obtaining sensitivity maps is by acquiring a component coil image and a body coil image and dividing the coil image by the body image. However, the presence of noise, mainly from the body coil image, can adversely affect this simple sensitivity map. Due to the underlying assumption that coil sensitivity profiles are relatively smooth, a local polynomial fit can be implemented to extract the noise contributions (Griswold *et al*

2006; Pruessmann *et al* 1999). Other methods of calculating sensitivity maps entail dividing each component coil image by one coil image to generate relative sensitivity maps. The reference scans used for making sensitivity maps can be low resolution gradient echo sequences with short TRs (Bammer and Schoenberg 2004).

Accurate coil sensitivity maps can provide optimal results. However any changes in sensitivity across an object between the prescan and actual image acquisition can lead to inaccuracies in reconstruction of the final images in the form of artifacts. This could include motion, flow, truncation artifacts, and distortions and chemical shift artifacts from EPI. These practical challenges can compromise coil sensitivity map calibration. This has given rise to autocalibrating techniques, where the sensitivity information can be acquired immediately before, during or immediately after the scan by acquiring a minimum number of extra data lines within the main imaging scan (Griswold *et al* 2006). This topic is addressed in more detail in later sections.

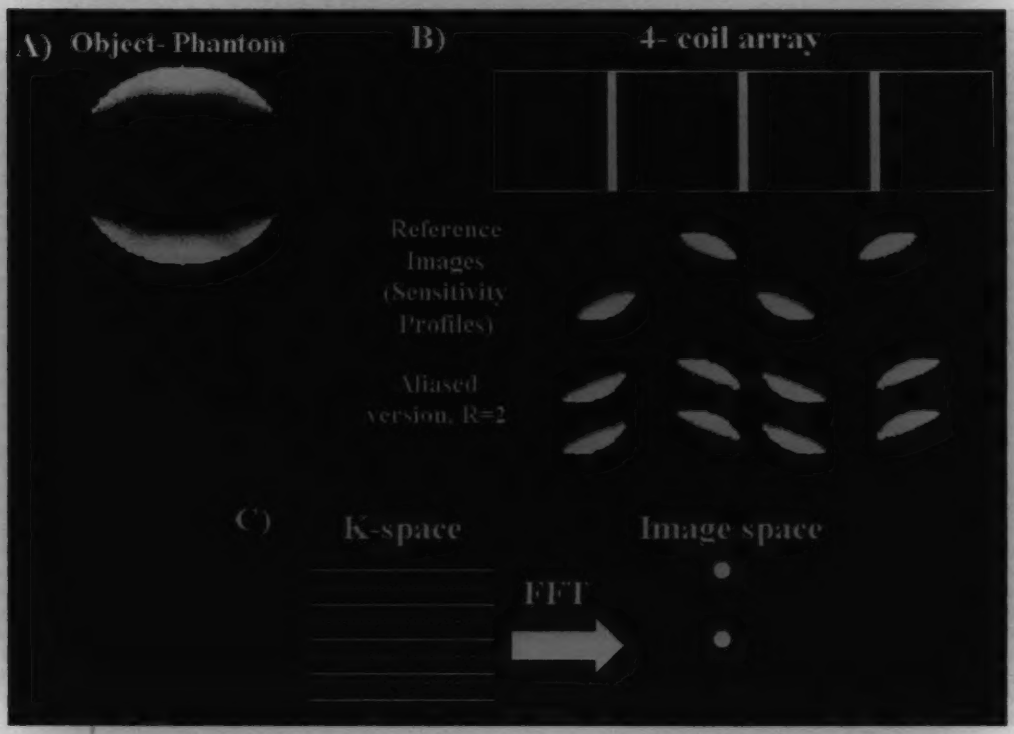

Figure 6-6: Example of sensitivity profiles (B) obtained from an object (A) using a 4 channel coil array. The aliased images shown in B, were generated by undersampling as shown by the K-space diagram in C by a factor, R=2 during sequence acquisition. The mismatch between the coil sensitivity and the apparent image data helps us identify the aliased information. In image space (C), a copy of the signal (in the center) from a specific location will get copied above as seen.

6.4 Parallel Imaging Methodology

Parallel imaging methods can be categorized into two groups. First, into the category of methods that explicitly estimates missing K-space lines prior to Fourier transforming the data. The forerunner of this category of K-space based methods is the SMASH method (Sodickson and Manning 1997). The second type of parallel imaging techniques first reconstructs the reduced FOV images for all coil elements of a phased array and then merges these different images by employing the coil sensitivity profiles into a single image with full FOV. The prime example of these image domain based methods is SENSE (Pruessmann *et al* 1999).

Both K-space and image domain based methods make use of the additional information that the combination of localized sensitivities and independent signals provide. This leads to partially parallel imaging in which conventional spatial encoding with gradients is partially replaced using spatial information in the form of the localized sensitivities of the coil elements in an array. These techniques enable images to be obtained with fewer phase encode steps, the rate limiting factor in conventional MRI.

6.4.1 K-space Based Methods

A K-space based approach such as SMASH exploits sensitivity changes in a surface coil array to substitute for modulations normally produced by phase encoding gradients. By relying on coil encoding (in place of gradient encoding), the entire K-space can be traversed using a reduced number of phase encoding gradient steps leading to a reduction in acquisition times. The function of the phase encoding gradients is to impose sinusoidal modulations of magnetization across the image plane. The MR signal integrated against these sinusoids represents spatial Fourier components of the image, or the known K-space lines (Figure 6-7). Sinusoidal modulations also called spatial harmonics of varying spatial frequency that result from spin evolution in phase encoding gradients can be represented against their associated K-space lines. In SMASH, some of these spatial harmonics are obtained by manipulations of component coil sensitivities rather than by gradient induced modulations of magnetization (Sodickson and Manning 1997; Sodickson 2000).

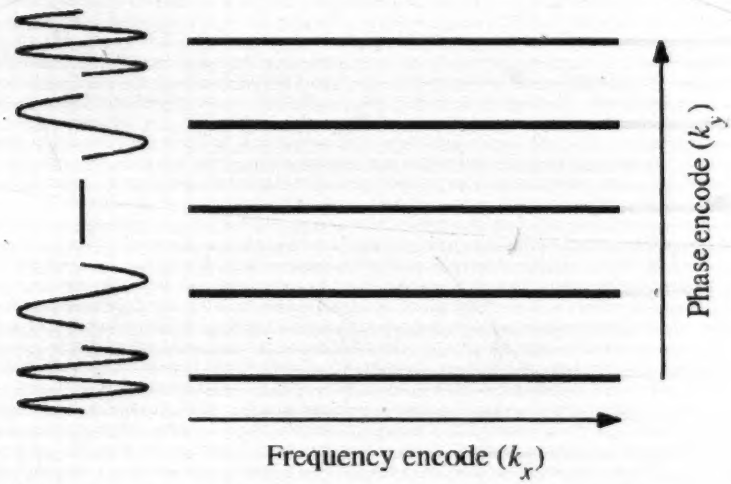

Figure 6-7: A K-space diagram depicting the spatial modulations from phase encoding gradients. The gradient steps on either side of the K-space center correspond to various spatial harmonics of spin modulation across the image plane (Sodickson 2000).

An array of RF coil elements contains spatial content in the form of its component coil sensitivities (Figures 6-5 and 6-6). For a linear surface coil array with adjacent components, each coil has a distinct but overlapping sensitivity $C_j(x,y)$. Arranging the appropriate linear combinations of component coil signals (Figure 6-8) allows the generation of composite sensitivity profiles C^{tot} which oscillate in the same manner as the gradient-induced modulations of Figure 6-7 and can be shown by the relationship,

$$C^{tot}(x,y) = \sum_j n_j C_j(x,y) \approx \exp(im\Delta k_y y) \qquad (6.1)$$

where n_j are complex weight factors

m is an integer

$k_y = 2\pi/FOV$ is the minimum K-space interval corresponding to the desired FOV

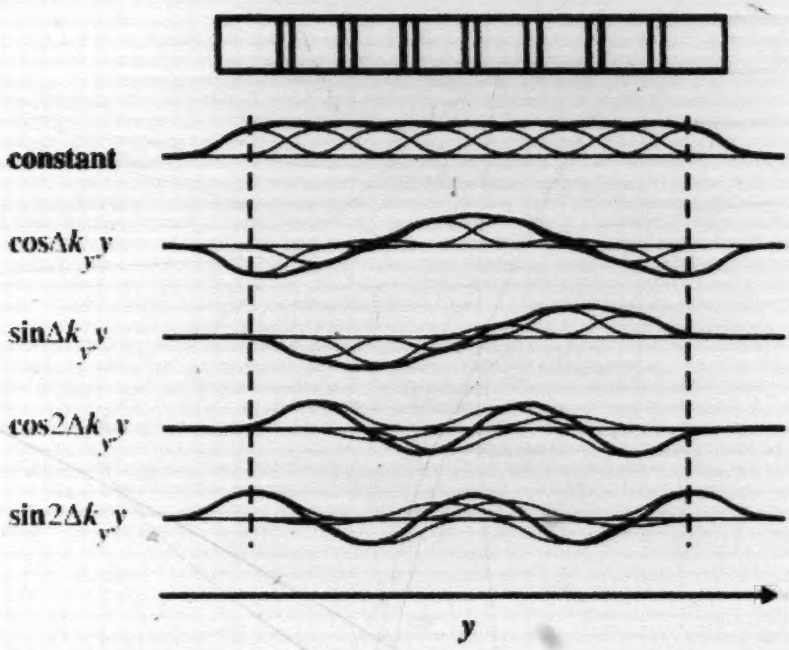

Figure 6-8: An overview of the several spatial harmonic profiles derived by linear combination of coil sensitivities in an 8-channel array (Sodickson 2000).

Providing a composite sensitivity profile obtained in this way forms an accurate spatial harmonic pattern, the same K-space step can be produced as would have resulted from a typical gradient step. To put it differently, each combined signal S^{tot}, produced from linear combinations of component coil signals S_j using weights n_j from equation 6.1 is shifted in K-space by an amount ($-m\Delta k_y$) such that,

$$S_j(k_x k_y) = \iint dx\ dy\ C_j(x,y)\ \rho(x,y)\ \exp\{-ik_x x - ik_y y\}$$

$$S^{tot}(k_x,k_y) = \sum_j n_j S_j(k_x,k_y)$$

$$= \iint dx\ dy\ \sum_j n_j C_j(x,y)\ \rho(x,y)\ \exp\{-ik_x x - ik_y y\}$$

$$= \iint dx\ dy\ C^{tot}(x,y)\ \rho(x,y)\ \exp\{-ik_x x - ik_y y\}$$

$$\approx \iint dx\ dy\ \rho(x,y)\ \exp\{-ik_x x - i(k_y - m\Delta k_y)y\}$$

$$\approx \tilde{\rho}(k_x, k_y - m\Delta k_y) \qquad (6.2)$$

where $\rho(x,y)$ characterizes the spatial distribution of spin density in the image plane

$\tilde{\rho}$ is the Fourier transform of $\rho(x,y)$

This K-space shift is exactly the same type of shift that would occur by evolution of spins with gyromagnetic ratio γ for time t_y in a y gradient of magnitude, G_y with the relationship,

$$\gamma G_y t_y = -m\Delta k_y \qquad (6.3)$$

This type of coil encoded K-space step can be combined with any gradient encoded K-space steps. When a multi-element coil array is used, several harmonics may be generated from a single data set (Figure 6-8). This results in less number of phase encoded lines that need to be acquired (Figure 6-9, black lines), thereby reducing acquisition time. The missing lines of K-space (Figure 6-9, gray lines) may be reconstructed using linear combinations of component coil signals. If a total of R spatial harmonics are produced, then R lines of K-space may be reconstructed, one for each phase encoding gradient step. The full signal matrix can be obtained in a fraction 1/R of the usual acquisition time (Sodickson and Manning 1997; Sodickson *et al* 1999; Sodickson 2000).

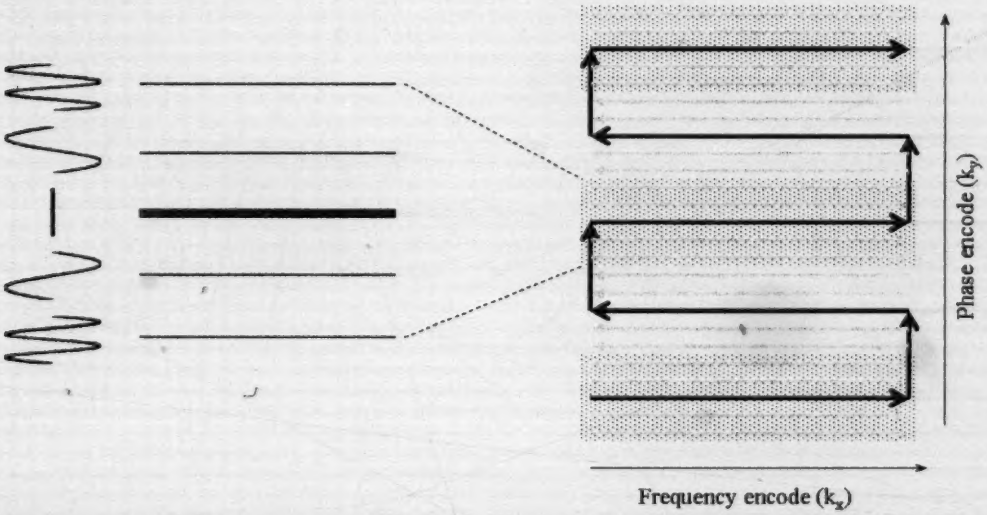

Figure 6-9: Diagram of the K-space trajectory for a partially parallel acquisition using five spatial harmonics. Black lines depict K-space lines corresponding to the applied phase encoding gradient steps. Gray lines typify additional K-space lines reconstructed from the linear combination shown in Figure 6-8. Additional reconstructed lines replace neglected phase encoding steps.

To implement a K-space based partially parallel imaging method, the first step consists of measuring the RF sensitivities of the various array elements. These sensitivities can be acquired from images of homogeneous phantoms, owing to the principle that any intensity variations in the images can be traced back to variations in coil sensitivity (Sodickson and Manning 1997; Sodickson *et al* 1999; Sodickson 2000). Sensitivity profiles may also be obtained in vivo by collecting component coil images. After sensitivity calibration, sensitivity profiles are fitted to the desired spatial harmonic functions using a numerical optimization algorithm with complex weight factors n_j as fitting parameters. For coil arrays with ideal geometries, the resulting fits can reasonably match the schematic fits shown in Figure 6-8.

6.4.1.1 Summary of K-space Based Approach

After obtaining the necessary complex weight factors or coil weights, MR data are acquired simultaneously in the coils of an array. A 1/R fraction of the usual number of phase encoding steps is applied with R times the usual spacing in K-space. The component coil signals acquired by this method are akin to images with a fraction 1/R of the desired FOV. However since only 1/R times fewer phase encoding steps were implemented, only a fraction 1/R of the time typically required for this FOV was consumed on data collection. Thereafter the proper R linear combinations of the component coil signals are generated to yield R shifted composite signal data sets. These composite signals are further interleaved to produce a full K-space data matrix. This K-space matrix is then Fourier transformed to give the final reconstructed image. Thus far, although the examples used in this chapter have revolved around the application of an acceleration factor, R=2, higher acceleration factors are possible with larger numbers of coil elements. Theoretically the maximum achievable R factor can equal the number of independent component coils in an array since a maximum of R distinct harmonics can be formed using a total of R independent coils. A K-space based approach such as SMASH can be combined with any sequence, since the formation of spatial harmonics is independent of the manner in which the gradient encoded K-space lines were generated.

6.4.1.2 Autocalibrating K-space Methods: An Introduction to GRAPPA

For accurate reconstruction, the SMASH method depends upon the precise knowledge of the RF coil sensitivity array maps in order to estimate the complex coil weights. The measurement of these array coil sensitivities can be non-trivial especially *in vivo* due to the effects of coil loading which are subject dependent and challenging to model. Furthermore, there may be inaccuracies in sensitivity determination that stem from tissue motion or regions of low SNR. Many of these issues can be addressed by acquiring the sensitivity information immediately before, during or soon after the scan. This helps mitigate problems of coil and patient movement in image reconstruction, since the coil sensitivity information can be continuously updated during acquisition. In the realm of K-space based parallel imaging methods, several autocalibrating methods such as AUTO-SMASH (Jakob *et al* 1998), variable density autocalibrated SMASH (VD-AUTO-

SMASH) (Heidemann *et al* 2001), and Generalized autocalibrating partially parallel acquisitions (GRAPPA) (Griswold *et al* 2002) have been developed.

The main feature of autocalibrating methods is to acquire a few extra lines temporally close to the image acquisition. The required reconstruction parameters are determined in K-space by fitting one or several lines to other lines in the calibration dataset. The data to data fitting approach obviates the need for a pure coil sensitivity map. There is also no requirement for any body coil images or intensity thresholds and normal appearing images are generated in the background. The principal difference between the various K-space based autocalibrating methods is the way in which the reference data is employed to solve the reconstruction parameters. While AUTO-SMASH and VD-AUTO-SMASH use relatively simple fitting models and sparse reference data, recent methods such as GRAPPA make use of expanded fitting with advanced methods for acquiring and using reference data (Griswold *et al* 2002; Griswold *et al* 2006).

In the GRAPPA method, uncombined images are obtained for each coil in an array by applying multiple blockwise reconstructions to synthesize the missing lines for each coil (Figure 6-10). Again, data acquired in each array coil (gray cylinders in Figure 6-10) are fit to the reference lines or autocalibrations signals (ACS, green cylinders). More importantly, data from multiple lines from all coils are used to fit an ACS line in a single coil (ACS line from coil 4 in Figure 6-10). This fit yields the weights which are then used to produce the missing lines (non-acquired lines) from that coil. Following a successful reconstruction of all lines for a particular coil, a Fourier transform can then be applied to generate the uncombined image for that coil. This process is then repeated for each coil of the array to yield a full set of uncombined images which are finally combined with the aid of a normal sum of squares reconstruction (Griswold *et al* 2002; Griswold *et al* 2006).

The GRAPPA reconstruction step for a missing K-space line can be mathematically expressed as a linear combination of other shifted lines given by,

$$S_j(k_x, k_y + m\Delta k_y) = \sum_l \sum_b n(j,l,m,b) S_l(k_x, k_y + bR) \qquad (6.4)$$

where $S_j(k_x,k_y)$ implies the k-space data at position (k_x,k_y) for coil j

R denotes the acceleration factor or the spacing between adjacent lines in the reduced dataset

b is an index used for counting through the multiple lines used in the reconstruction

n(j,l,m,b) are weights used in the linear combination to reconstruct a line at position $(k_x,k_y + m\Delta k_y)$ in coil j

GRAPPA is ideal for reconstructions with a minimal acquisition of extra information since the model equation above can be over determined with just a few extra lines. This is because one can perform the required fits for every point along the readout direction. Additionally, because the weights are determined using shifts in K-space, the absolute position of the lines is irrelevant. This makes it feasible to opt out of using lines in the

center of K-space in the event that intrinsic phase shifts in the object shift the center of K-space out of the region of extra acquired lines. Such an error could occur when working with a very minimal amount of extra lines (Griswold *et al* 2006).

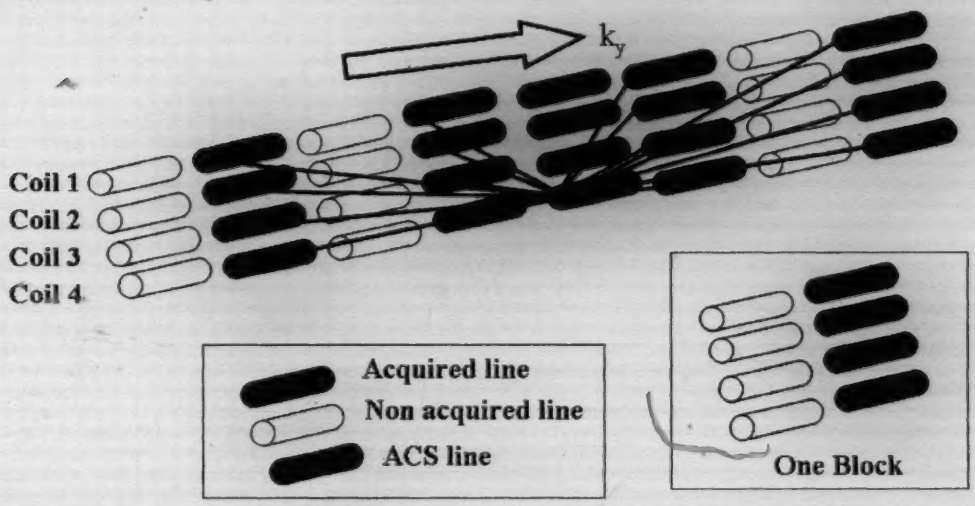

Figure 6-10: Schematic of the GRAPPA algorithm. Each cylinder represents a single readout line. The readout direction is into the page, whereas the phase encoding direction is horizontal or perpendicular to the page. In GRAPPA, more than one line acquired in each of the coils in the array is fit to a reference line or an autocalibration signal (ACS). In this example four acquired lines per coil are used to fit a single ACS line in coil 4. A block is defined as a single acquired line plus the missing lines adjacent to that line as shown above for R=2.

By using more blocks of data to fit each missing line, GRAPPA incorporates more information into every reconstructed line resulting in a substantially improved fit. Each possible reconstruction is performed for each non acquired line resulting in many different types of reconstructions for each line. These lines are then combined in a weighted average to generate the final reconstructed line, providing a firmer reconstruction of each missing line. The extended blockwise reconstructions as shown here can lead to reductions in imaging artifacts (Griswold *et al* 2002). A further merit of the autocalibrating approach of GRAPPA is that besides using the ACS lines to determine the coil weighting factors, these extra lines can be integrated into the final image reconstruction to improve image quality in terms of artifact levels and SNR.

6.4.2 Image Domain Based Methods

An image domain reconstruction starts at the same level as a K-space based reconstruction like SMASH with a set of component coil signals acquired with a reduced number of phase encoding steps. Fourier transformation of these signal-sets yields aliased component coil images, however after this step the final image reconstruction occurs entirely in the image domain (Blaimer *et al* 2004; Pruessmann *et al* 1999; Sodickson 2000). This section outlines the theory behind the SENSE image domain based algorithm.

The predominant feature of the SENSE method is that each pixel in an aliased image is in fact a superposition of multiple pixels from a correspondingly full unaliased image. In another sense, as a result of Nyquist aliasing, an R-times aliased image I^{fold} is related to the full image, I^{full} by,

$$I^{fold}(x,y) = I^{full}(x,y) + I^{full}(x,y+\Delta y) + I^{full}(x,y+2\Delta y) + ... = \sum_{m=0}^{R-1} I^{full}(x,y+m\Delta y) \tag{6.5}$$

Given a condition that if I^{fold} is acquired with a single coil, this superposition cannot be unfolded unless we possess a priori knowledge of the full image. The condition is different when we use an array of coils. The full image I_j^{full} in each coil j is composed of two parts: the spin density ρ and the coil sensitivity function C_j and is given by the relationship,

$$I_j^{full}(x,y) = C_j(x,y)\ \rho(x,y) \tag{6.6}$$

where in an array each component coil has a different sensitivity C_j

This affords multiple 'views' of the aliasing that can be used to infer by what amount each aliased pixel belongs at any position in the full image. Substituting equation 6.6 in 6.5 yields,

$$\begin{aligned} I_j^{fold}(x,y) &= \sum_{m=0}^{R-1} I_j^{full}(x,y+m\Delta y) \\ &= \sum_{m=0}^{R-1} C_j(x,y+m\Delta y)\ \rho(x,y+m\Delta y) \end{aligned} \tag{6.7}$$

For any aliased pixel (x,y), this can be summarized as,

$$I_j^{fold} = \sum_{m=0}^{R-1} I_{jm}^{full} = \sum_{m=0}^{R-1} C_{jm}\rho_m \tag{6.8}$$

where $I_{jm}^{full} \equiv I_{j}^{full}(x,\ y+m\Delta y)$,

$C_{jm} \equiv C_j\ (x,\ y+m\Delta y)$

$\rho_m \equiv \rho\ (x,\ y+m\Delta y)$

Considering the case in Figure 6-11, where a 4-coil array (N_c=4) is used with a factor of 4 aliasing (R=4), we may write,

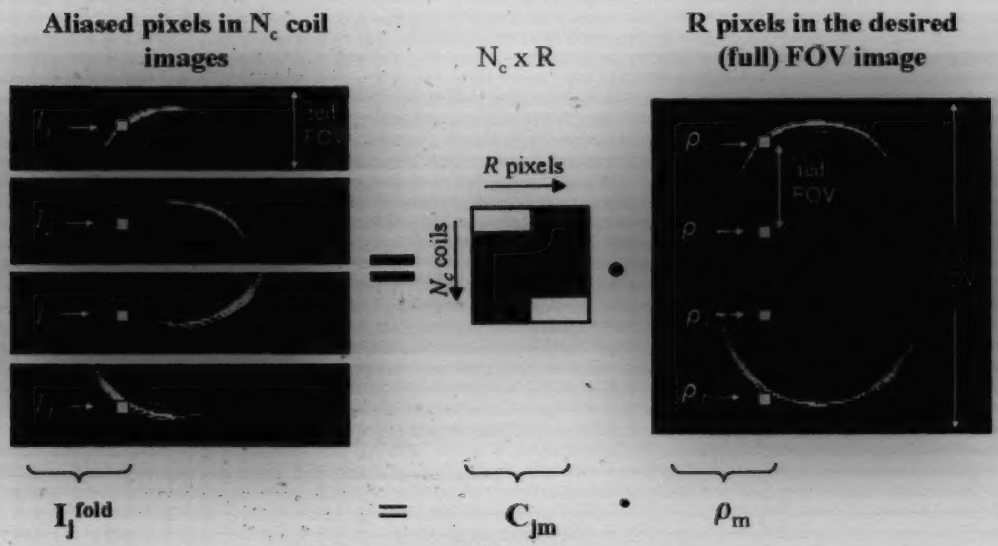

Figure 6-11: An example of the image domain based SENSE relation with an accelerated image acquisition with N_c = 4 channels or coils. I_j^{fold} contains the aliased pixels at a specific position in the reduced FOV images. C_{jm} gathers the corresponding sensitivity values of the component coils at locations of the implicated pixels (R=4) in the full FOV image ρ_m (Blaimer *et al* 2004). The inversion of this equation and hence the disentangling of pixel-by-pixel superpositions forms the essence of the SENSE technique (Pruessmann *et al* 1999).

$$
\begin{aligned}
I_1^{fold} &= C_{11}\rho_1 + C_{12}\rho_2 + C_{13}\rho_3 + C_{14}\rho_4 \\
I_2^{fold} &= C_{21}\rho_1 + C_{22}\rho_2 + C_{23}\rho_3 + C_{24}\rho_4 \\
I_3^{fold} &= C_{31}\rho_1 + C_{32}\rho_2 + C_{33}\rho_3 + C_{34}\rho_4 \\
I_4^{fold} &= C_{41}\rho_1 + C_{42}\rho_2 + C_{43}\rho_3 + C_{44}\rho_4
\end{aligned}
\qquad (6.9)
$$

Equation 6.9 can be rewritten in matrix form as,

$$\begin{bmatrix} I_1^{fold} \\ I_2^{fold} \\ I_3^{fold} \\ I_4^{fold} \end{bmatrix} = \begin{bmatrix} C_{11} & C_{12} & C_{13} & C_{14} \\ C_{21} & C_{22} & C_{23} & C_{24} \\ C_{31} & C_{32} & C_{33} & C_{34} \\ C_{41} & C_{42} & C_{43} & C_{44} \end{bmatrix} \bullet \begin{bmatrix} \rho_1 \\ \rho_2 \\ \rho_3 \\ \rho_4 \end{bmatrix} \qquad (6.10)$$

To put it differently,

$$I^{fold} = C\rho \qquad (6.11)$$

In so far as the number of coils N_c is greater than or equal to the acceleration factor R (as shown in Figure 6-11 for N_c=4, R=4), equation 6.11 can be inverted in the form,

$$\rho = C^{-1} I^{fold}$$

$$\text{or} \quad \rho = \left(C^H \cdot C\right)^{-1} \cdot C^H \cdot I^{fold} \qquad (6.12)$$

where the superscript H denotes the transpose and conjugate complex matrix operation

This process allows the unaliased spin density over the full FOV to be determined (Blaimer *et al* 2004; Sodickson 2000). The SENSE algorithm must be repeated for every pixel location in the reduced FOV to effectively reconstruct the full FOV image.

SENSE differs from SMASH in its approach to sensitivity calibration. Furthermore, both methods also vary in the distinctiveness and stability of their image reconstruction algorithms. Sensitivity estimates at each pixel location of the full FOV are generally needed to perform pixel by pixel matrix inversion of equation 6.12. In SENSE, the *in vivo* sensitivity calibration procedure entails dividing full FOV component coils images by additional full FOV body coil images and the resultant images undergo several stages of interpolation, filtering and thresholding (Pruessmann *et al* 1999). The primary algorithmic concern in image domain based reconstructions is the numerical stability of the inverse C^{-1}. This differs from the K-space based reconstructions such as SMASH where the quality of the reconstructions depends upon the goodness of spatial harmonic fits. In SENSE, using a pixel by pixel inversion gives the advantage of fine regional control over the reconstruction. However a drawback of the pixel by pixel approach is that in regions of low actual or apparent coil sensitivity, the C matrix may become poorly conditioned leading to error propagation through the inverse thereby resulting in increased effects of noise and sensitivity miscalibrations (Bammer and Schoenberg 2004; Sodickson 2000).

6.4.2.1 Autocalibrating Image Domain Methods: An Introduction to mSENSE

The concept of autocalibration is not limited to K-space related parallel imaging reconstruction methods because in principle the ACS lines required for a GRAPPA reconstruction can also be used to derive low resolution coil sensitivity maps for image domain based methods like SENSE within every subsequent parallel imaging experiment. This is used in the modified Sensitivity Encoding (mSENSE) method (Griswold *et al* 2004; Wang *et al* 2001). mSENSE uses an autocalibrating imaging sequence for coil sensitivity mapping similar to GRAPPA wherein extra lines are acquired during the acquisition. In addition, a set of noise scan data for purposes of calculating the noise correlation matrix are also acquired. From these reference lines, a set of low resolution images, $\hat{C}$ can be obtained. The weighting matrix $\hat{W}$ as shown below leads to a minimum noise and artifact power for a given signal intensity,

$$\hat{W} = (N \cdot e + \hat{C}^{H} \cdot \hat{C})^{-1} \cdot \hat{C}^{H} \qquad (6.13)$$

where N is the noise power level

The weighting matrix must be normalized by a diagonal matrix Λ to ensure that the resulting image has the usual sum of squares intensity distribution. This can be shown by,

$$\hat{C}_{ref} = \Lambda \cdot diag(\hat{W} \cdot \hat{C}) \qquad (6.14)$$

where $\hat{C}_{ref}$ is the low resolution image calculated according to the sum of squares method and the normalized weighting matrix is given by $W = \Lambda \cdot \hat{W}$

It can be demonstrated that by setting the noise power level N to zero, mSENSE gives results similar to the original SENSE method. However the advantage of mSENSE is that it optimizes both noise and artifact power levels together as opposed to just optimizing SNR at zero artifact levels (Wang *et al* 2001).

6.4.3 Practical Issues in Parallel Imaging

The most straightforward advantage of parallel imaging is the acceleration in imaging due to the reduction in the number of phase encode lines that need to be acquired to form an image at a given FOV and resolution. With R=2, only every other line in K-space is acquired and the imaging time is virtually halved. For autocalibrating methods such as GRAPPA or mSENSE, some of the efficiency of implementing parallel imaging is traded in for the autocalibration features of those methods, i.e., a few more K-space profiles are added to provide intrinsic calibration capabilities. These additional calibration lines

become more significant for smaller scan matrices since their calculation represents a larger fraction of the total scan time compared to the calibration lines calculated for larger scan matrices. The additional calibration profiles for mSENSE and GRAPPA need not be acquired together with the other K-space data but can be collected in a preceding scan, however this comes at the cost of greater motion sensitivity and mismatched calibration profiles (Bammer and Schoenberg 2004).

The accelerated imaging features can be used to reduce the overall exam times and improve patient throughput and exam efficiency. Parallel imaging methods are also advantageous for their potential to reduce imaging artifacts and improve spatial resolution due to the built-in rapidity of K-space traversal in these techniques. One can acquire more averages with parallel imaging within the same total scan time building upon the tenet that averaging can help diminish artifacts (Bammer and Schoenberg 2004). All of the above benefits can be achieved by following a list of essential elements needed for practical implementations of partially parallel imaging strategies including RF coil array requirements and accurate coil sensitivity calibration (as highlighted in 6.3.1 and 6.3.2). The underlying sections further highlight some other items that need to be considered for obtaining optimal images using mSENSE or GRAPPA.

6.4.3.1 Image Reconstruction through Ease of Implementation

Parallel imaging with GRAPPA and mSENSE has been observed to be beneficial in areas where accurate coil sensitivity maps may be difficult to obtain. This can be an important issue when imaging the lung or abdomen where determining precise spatial coil sensitivity information is difficult. In such cases, image quality of SENSE reconstructions can suffer from inaccuracies in sensitivity calibration. In contrast, in an autocalibrating method such as mSENSE, sensitivity map calibration is performed by acquiring extra lines within the accelerated acquisition itself that are not included in the final image reconstruction thereby providing good quality image reconstructions. In GRAPPA, central K-space lines are fit to calculate the reconstruction parameters. This fitting method involves global information and is not affected by localized inhomogeneities. The use of lines close to the center of K-space also guarantees that there is enough information to obtain good reconstruction quality (Blaimer *et al* 2004).

6.4.3.2 Reconstruction Related Artifacts

Not all parallel imaging methods are able to reconstruct aliased images without additional problems such as higher required acceleration factors or other modifications. This is mainly true for mSENSE where if the FOV is not larger than the object, aliased full FOV images that can cause discontinuities are obtained. Therefore erroneous coil sensitivity maps may be generated resulting in image artifacts following reconstruction (Blaimer *et al* 2004; Griswold *et al* 2004). In contrast, GRAPPA is able to reconstruct aliased images with the same appearance as a normal non-accelerated acquisition by using a smaller FOV. An aliased full FOV image corresponds to greater spacing in K-space than is

required by the Nyquist criterion. Since the spacing to the neighboring K-space lines and the hence the FOV size are not important for determining the signal for each individual line, the K-space lines are not corrupted by employing a smaller FOV. Because GRAPPA involves fitting of neighboring K-space lines, this type of reconstruction is not marred by the smaller FOV, permitting an optimal FOV acceleration for a given application (Blaimer *et al* 2004).

The differences between GRAPPA and mSENSE can also be appreciated in terms of the appearance of artifacts. In mSENSE, the reconstruction is performed in the image domain on a pixel by pixel basis. Nonideal conditioning in reconstruction can lead to local noise enhancement which appears localized in the unfolded image. However GRAPPA generates the missing lines in K-space and any inaccuracies in the calculation of missing K-space lines will generate aliasing artifacts in the reconstructed image clearly evident over the entire reconstructed FOV (Blaimer *et al* 2004).

6.4.3.3 SNR in Parallel Imaging

The SNR in images acquired with parallel imaging algorithms is reduced relative to acquisitions with conventional full K-space acquisition since SNR is proportional to the square root of the acquisition time. This has the same effect as in conventional imaging with a rectangular FOV. By acquiring fewer lines in K-space the SNR of an image is reduced by the square root of the acceleration factor, R (Bammer and Schoenberg 2004). Additionally, parallel imaging scans suffer an inherent SNR loss due to the special reconstruction schemes employed. In this context, it should be noted that with parallel imaging, the SNR over the FOV is no longer constant and can vary quite significantly. This is reflected by the geometry or g factor. Together with the FOV and acceleration factor, R selected, the g factor depends in a complex manner on size, number and orientations of the coils that are used for the given parallel imaging technique (Pruessmann *et al* 1999). The SNR of parallel imaging scans is given by the relationship,

$$SNR_{PI} = \frac{SNR_{full}}{\sqrt{R} \cdot g} \qquad (6.15)$$

where PI stands for parallel imaging and

SNR_{full} refers to the SNR of an image acquired without skipping any phase encode steps

For most clinical applications, a limitation of the acceleration factor is expected due to the SNR degradation by a factor of $\sqrt{R}$ from reduced scan times. Furthermore for higher R factors, the aliased points move closer together and due to the slowly varying coil sensitivities, the ability to separate superimposed pixels decreases. This leads to an additional spatially dependent noise amplification highlighted by an increased g factor. In 2D parallel imaging, data reduction is performed along one dimension, the phase

encoding direction with the acceleration factor not exceeding 4 or 5 for clinical applications (Augustin *et al* 2004; Bammer and Schoenberg 2004).

6.5 Combining Parallel Imaging with Echo Planar Imaging

Single shot echo planar imaging (EPI) methods acquire the entire image matrix after a single spin excitation, i.e. signal is acquired over more than one echo per TR. Depending on the echo train length (the number of echoes per TR), the time needed to form an image decreases significantly. Unfortunately the maximum available spatial resolution is limited by signal attenuation due to T2 or T2* relaxation over the course of the image acquisition (Chapter 5). Hence, signal that is acquired during every echo of the EPI readout is weakened by this signal decay and so is the corresponding K-space data. With the expanding length of the readout echo train, the K-space signal weakening heightens. This signal attenuation is responsible for significant image blurring in the PE direction and results in a loss of small object contrast. Besides relaxation imposes a limit on the total number of echoes that can be acquired since at some point, additional echoes will not have sufficient signal to contribute any useful information to the image. Considerable improvements in image quality and in some cases also SNR can be achieved by minimizing the total acquisition time through the use of a short interecho spacing (Augustin *et al* 2004; Bammer and Schoenberg 2004).

Unlike the majority of the applications for parallel imaging in use, the main outcome of combining parallel imaging with EPI is not time savings (for the needs of minimum TRs or multi-slice data), but improvements in image quality and reductions in the level of susceptibility artifacts.

6.5.1 Improved Spatial Resolution

The key features of implementing parallel imaging are 1) to speed up image acquisition and 2) to increase spatial resolution in a given experimental time or a combination of the two. The speed advantage of parallel imaging in EPI offers the possibility to shorten the readout train, the effective interecho spacing and the TE beyond previous limits. Parallel imaging combined with single shot EPI can reduce the effects of relaxation leading to resolution enhancement with decreased imaging time and sidestepping any increased gradient performances or RF power depositions. The improvement in spatial resolution emerges from improved definition of the point spread function (PSF) without actually altering the size of the acquisition matrix. Consequently the increased acquisition speed in parallel imaging offers some flexibility in ramping up the spatial resolution by changing the acquisition matrix size. However resolution in MRI is gained at the expense of reduced SNR with or without implementing parallel imaging (Augustin *et al* 2004; Bammer and Schoenberg 2004).

For an acceleration factor R=2, the length of the EPI acquisition time is theoretically halved. Hence for the same level of artifacts, parallel imaging affords double the

resolution in the readout direction. Similarly, using the same number of echoes per TR as in conventional gradient encoding, large fractions of K-space can be scanned per TR. For a given time, this also enables higher spatial resolution along the phase encode direction despite the fact that signal decay will mitigate this benefit. For example, with conventional encoding one acquires a matrix of 128 x 128 for Tacq = 2 min. In parallel imaging, since we only acquire half the phase encodes and reduce Tacq, one can opt to maintain the same Tacq but increase their matrix, so perform 256 x 256 with R=2 and still ensure a Tacq of 2 min because only 128 phase encodes are being acquired instead of 256.

It should be noted that when combined with parallel imaging, single shot methods such as EPI can even retrieve some SNR. This is not only due to the reduction in TE but also because in contrast to conventional sequences, late echoes with relatively low signal intensity are not contained in the shortened parallel imaging echo train.

6.5.2 Reduced Susceptibility Effects

In addition to the blurring and signal losses observed in single shot imaging methods, EPI has the added problem of image distortions and chemical shift artifacts. These artifacts arise from signal sources with off-resonant spin precession rates (relative to that of water) and the phase offsets accrued by the spins during the relatively long EPI readout period. For water and lipids, this dephasing is coherent for lipids relative to water and will manifest itself as a spatial shift of lipid protons relative to the water signal sources. A significant magnetic field inhomogeneity across a voxel can result in incoherent phase accrual and lead to intravoxel dephasing. Local susceptibility gradients, especially around auditory canals and frontal sinuses result in signal pile-up artifacts. In EPI, these artifacts occur along the phase encode direction. One means to reduce these artifacts is to traverse K-space as fast as possible. Higher K-space velocity translates into fewer artifacts (Augustin *et al* 2004; Bammer *et al* 2002).

In Diffusion imaging, speed is not the main reason to opt for EPI. Random bulk physiologic motion during the diffusion encoding phase results in phase accrual that may vary from shot to shot only being compounded with the intentional phase encoding. With single-shot EPI, one is guaranteed an equal motion induced phase error per phase encoding step that disappears following magnitude calculation.

The low bandwidth per pixel in the phase encoding direction can lead to geometric distortions. Parallel imaging can significantly reduce the number of phase encoding steps thereby increasing the bandwidth per pixel. This enables a reduction in the severity of artifacts with increasing acceleration factors. In single shot EPI diffusion imaging, this approach positively impacts image quality within one TR that would otherwise only be possible with multiple TRs with interleaved EPI. The loss in SNR of diffusion-weighted images can be overcome by averaging additional acquisitions. Furthermore, the theoretical SNR loss is mitigated by the shorter EPI readout. This permits a reduction in

echo times and less T2 signal decay (Augustin *et al* 2004; Bammer *et al* 2001; Bammer *et al* 2002).

6.6 Concluding Remarks

This chapter has outlined the theoretical aspects of parallel imaging methods for a K-space based approach with the SMASH method and an image domain based approach with the SENSE algorithm as fundamental examples of the two classes of parallel imaging. Furthermore, details on the workings of their respective autocalibrating off-shoots, GRAPPA and mSENSE were also discussed. The practical issues in implementing parallel imaging and benefits of combining parallel imaging with EPI were also uncovered. For the work documented in this thesis, the effects of the K-space based parallel imaging technique, GRAPPA and the image-domain based method, mSENSE were studied on diffusion tensor images and diffusion-weighted images of the human brain at 1.5T acquired using the twice-refocused spin-echo EPI sequence. The findings from those studies along with the relative merits and shortcomings of both methods in normal subjects and acute stroke patients have been outlined in chapters 9 and 11, respectively.

7

DIFFUSION ANISOTROPY IN SUBCORTICAL WHITE MATTER AND CORTICAL GRAY MATTER: CHANGES WITH AGING AND THE ROLE OF CSF-SUPPRESSION*

Diffusion tensor magnetic resonance imaging (DTI) (Basser *et al* 1994a; Basser *et al* 1994b) provides a quantitative means for evaluating the integrity of highly ordered tissue such as white matter of the brain in normal and diseased conditions (Horsfield and Jones 2002; Pierpaoli *et al* 1996). By estimating the diffusion tensor (**D**), several quantitative measures can be computed such as the three principal diffusivities (eigenvalues of **D**: $\lambda_1, \lambda_2, \lambda_3$), and the two rotationally invariant quantities, the trace of the diffusion tensor (Trace(**D**)), which corresponds to mean diffusivity, and fractional anisotropy (FA), a measure of the degree of diffusion directionality of water within the tissue microstructure (Basser 1995; Basser and Pierpaoli 1996).

Partial volume averaging of cerebrospinal fluid (CSF) with brain parenchyma results in a bias of measures such as apparent diffusion coefficients (Falconer and Narayana 1997; Kwong *et al* 1991) and relative anisotropy (Papadakis *et al* 2002) for major central white matter (WM) tracts adjacent to CSF-filled spaces. However, little quantitative data has been reported in the peripheral WM and gray matter (GM) areas of the brain, both of which may have diffusion anisotropy values impacted by partial volume contamination with isotropic, fast diffusing CSF in adjacent sulcal spaces.

---

*A version of this chapter has been published. Bhagat YA and Beaulieu C. (2004). Diffusion Anisotropy in Subcortical White Matter and Cortical Gray Matter: Changes with Aging and the Role of CSF-Suppression. *Journal of Magnetic Resonance Imaging*. 20(2):216-227. Copyright 2004 Wiley-Liss, Inc. Reprinted with permission of Wiley-Liss, Inc. a subsidiary of John Wiley & Sons, Inc.

Iterations of this study have previously been presented at:

1) 21st International Symposium on Cerebral Blood Flow, Metabolism and Function (Brain '03). 2003. Calgary, AB. 593 (poster presentation)

2) 11th annual scientific meeting of the International Society for Magnetic Resonance in Medicine. 2003. Toronto, ON. 2250 (poster presentation)

Studies of DTI in elderly subjects (>60 years) have shown microstructural degradation in some of the major deep WM structures such as the corpus callosum (Abe *et al* 2002; Pfefferbaum *et al* 2000), but have not focused on making quantitative anisotropy measurements in cortical and subcortical brain regions with aging. Furthermore, CSF-suppression using fluid-attenuated-inversion-recovery (FLAIR) prepared DTI, which could improve the accuracy of anisotropy measurements was not utilized in DTI studies of normal aging.

In this chapter, we present our results on how FLAIR-DTI affects the quantitative measures of anisotropy in subcortical WM (in the Gyri) and cortical GM in the young (21-25 years) and elderly (61-74 years) populations. Moreover, with FLAIR-DTI we also assessed the changes in water diffusion in the brain with normal aging.

7.1 Partial Volume Averaging in Diffusion MRI

Partial volume averaging of isotropic cerebrospinal fluid (CSF) with brain parenchyma results in a bias of measures such as apparent diffusion coefficients (ADC) (Kwong *et al* 1991), Trace(**D**) (Falconer and Narayana 1997; Zacharopoulos and Narayana 1998) and relative anisotropy (RA) (Papadakis *et al* 2002). The rapid diffusivity of CSF relative to surrounding brain tissue can lead to an overestimation of ADC (Kwong *et al* 1991) and Trace(**D**) (Falconer and Narayana 1997; Zacharopoulos and Narayana 1998) in those areas. This issue has been addressed by the use of fluid-attenuated inversion recovery (FLAIR) prepared diffusion imaging sequences, allowing the accurate quantification of ADC and Trace(**D**) values in the normal human brain (Falconer and Narayana 1997; Kwong *et al* 1991; Zacharopoulos and Narayana 1998) and in the clinical evaluation of stroke (Beaulieu *et al* 1999; Latour and Warach 2002). Previous studies which used CSF-suppressed DTI in the clinical realm have not investigated its advantage over standard DTI methods in characterizing anisotropy (Eriksson *et al* 2001; Nusbaum *et al* 2001).

Using a histogram analysis focused on the major central white matter (WM) tracts in a young adult population, Papadakis *et al.* demonstrated that CSF-suppressed, FLAIR-prepared DTI resulted in an extension of the quantitative area and an increase in the degree of anisotropy for major WM tracts close to CSF filled spaces (Papadakis *et al* 2002). However, the effect of CSF-suppression on the accuracy of DTI was not reported for the peripheral brain structures such as the subcortical WM in the gyri and cortical GM. Also, the use of histogram analysis, rather than mean values for tract specific regions-of interest, and RA, rather than the more ubiquitous fractional anisotropy (FA), makes the data more difficult to interpret for comparative purposes. The effect of CSF-suppression on the individual eigenvalues was also not reported in that study.

DTI studies of epilepsy (Eriksson *et al* 2001), Alzheimer's disease (Takahashi *et al* 2002), ischemic leukoaraiosis (Jones *et al* 1999a), and CADASIL patients (Chabriat *et al* 1999) have reported changes in mean diffusivity and anisotropy compared to normals in regions within subcortical WM and cortical GM. These peripheral regions of the brain lie adjacent to CSF-filled spaces such as sulci and so the potential for partial volume

averaging from CSF is greatly increased. A better characterization of diffusion anisotropy in these peripheral regions of the brain are required in order to have a solid basis for assessing changes in the wide range of diseases that may involve the subcortical WM and cortical GM.

7.1.1 Role of CSF-Suppression and Aging

Conventional MR imaging studies used for quantifying normative brain volumes have shown a 25-30% increase in cortical and ventricular CSF in late adulthood (50-80 years) from young and middle adult age groups (20-40 years) (Pfefferbaum *et al* 1994). This considerable increase in CSF fraction with age enhances the potential for partial volume averaging that could contribute to decreases of diffusion anisotropy in an elderly population relative to a younger one. The earlier study of CSF-suppression and anisotropy by Papadakis *et al.* focused on younger adults (25-42 years) (Papadakis *et al* 2002). The application of DTI to aging is of interest since elderly subjects (>60 years) have shown microstructural degradation in the form of increased diffusivity and decreased diffusion anisotropy in some of the major deep WM structures such as the genu and splenium of the corpus callosum, and centrum semiovale (Abe *et al* 2002; Moseley 2002; Nusbaum *et al* 2001; Pfefferbaum *et al* 2000). Other DWI and DTI studies in aging have included regions distal from the central WM structures, such as frontal, temporal, and/or occipital peri-callosal WM and GM areas (Abe *et al* 2002; Helenius *et al* 2002; O'Sullivan *et al* 2001) and shown results that parallel those of the deep major WM tracts. However, CSF-suppression was not used in these latter diffusion tensor studies on normal aging.

7.1.2 Goals of the Study

By measuring standard DTI and CSF-suppressed (i.e. FLAIR) DTI in normal young (21-25 years) and elderly (61-74 years) subjects, the purpose of this study was a) to determine the relevance of CSF-suppression in measuring FA in well-localized areas of the brain, particularly the subcortical WM within the gyri and cortical GM, in the young and elderly and b) to assess with FLAIR-DTI the changes in FA and the individual eigenvalues of water diffusivity in the brain with normal aging.

7.2 Methods

Images were obtained from a group of 18 healthy volunteers (14 males, 4 females, age range 21-74 years). They were divided into two groups based on their ages, young (N = 8, 21-25 years, mean age = 24±2 years) and old (N = 10, 61-74 years, mean age = 68±5 years). Written informed consent was obtained from all 18 volunteers. MRI protocols were approved by the Human Research Ethics Board of the University of Alberta. DTI was performed on a 1.5 T Magnetom Sonata scanner (Siemens Medical Systems, Erlangen, Germany) equipped with gradient coils producing a maximum amplitude of 40

mT/m and a maximum slew rate of 200 T/m/s. Volunteers were imaged in the standard Siemens circularly polarized head RF coil. Single-shot, diffusion-weighted, twice-refocused spin-echo echo planar imaging (Reese *et al* 2003) was used for standard and FLAIR prepared DTI with the following parameters: TR (standard) / TR (FLAIR) / TI (FLAIR) / TE / NEX = 3 s / 8.57 s / 2.2 s / 85 ms / 8, 96x128 matrix zero filled to 256x256, 22 cm FOV and twenty 3 mm-thick contiguous axial slices aligned with the AC-PC. The in-plane resolution was 0.85 x 0.85 mm after zero filling. The diffusion tensor was acquired for each slice with six sets involving diffusion gradients placed along non-collinear directions {b=1000 s/mm^2; (X, Y, Z) gradient directions = (1, 0, 1), (-1, 0, 1), (0, 1, 1), (0, 1, -1), (1, 1, 0), (-1, 1, 0)} and an individual set without diffusion weighting (b=0 s/mm^2). Cardiac gating was not felt necessary for this study because the diffusion-weighted images and resultant maps (Trace ADC, FA, eigenvalues) were of excellent quality with the parameters demonstrating low intra- and inter-subject variability. The acquisition time was 3 min and 8 min for standard DTI and FLAIR-DTI, respectively.

Images were post-processed offline using the method of Basser *et al.* (Basser *et al* 1994b; Basser and Pierpaoli 1996) to yield maps of the eigenvalues λ_1, λ_2, and λ_3, Trace/3 ADC, and FA (MRVision, Winchester, MA). Details of the image processing steps are outlined in Appendix 1.1. Recall that FA measures the magnitude of the anisotropic component of the diffusion tensor and ranges from 0, signifying complete isotropic diffusion, to 1, indicating highly anisotropic diffusion. A 2.0 L cylindrical Ni-doped water phantom (Siemens) with a diameter of 15 cm was used to ensure that standard and FLAIR-DTI yielded identical results. Measurements of the phantom using the standard and FLAIR DTI protocols were repeated on four separate days over a period of two weeks to assess the consistency of the DTI measurements. An identical scheme was implemented for evaluating the stability of diffusion metrics *in vivo* by repeating measurements on four separate days in one volunteer (age 25 years) over a period of two weeks.

7.2.1 Regions-of-Interest Analysis

Region of interest (ROI) analysis of 26 different regions per subject were stratified into categories such as major WM tracts, deep GM regions, subcortical WM within the gyri, and cortical GM. Deep GM regions comprising bilateral sections of the globus pallidus (GP), thalamus, and putamen were identified and traced on FLAIR b0 images and superimposed on FA maps. The ROIs for the individual structures encompassed the full outline of the globus pallidus or the putamen on a single slice whereas a small ROI (25 mm^2) was placed centrally in the middle of the thalamus. All WM tracts were indexed separately at a level yielding maximal coverage and traced on the FLAIR FA maps due to their increased conspicuity. The ROIs were then propagated onto the standard FA maps for comparison. Deep major WM tracts analyzed were the genu of the corpus callosum (GCC), splenium of the corpus callosum (SCC), and bilateral sections of the following regions: anterior limb of the internal capsule (AIC), posterior limb of the internal capsule (PIC), external capsule (EC), corona radiata (CR), and centrum semiovale (CS). It is important to note that in this study, subcortical white matter refers to peripheral white

matter within the gyri rather than the deep white matter tracts. Subcortical WM regions consisted of unilateral parts of the superior frontal gyrus (SFG), supra marginal gyrus (SMG), superior temporal gyrus (STG), middle occipital gyrus (MOG), and postcentral gyrus (PG). The posterior horn of the lateral ventricle was used for measurements of CSF from the standard DTI method.

The cortical GM regions were directly drawn on FLAIR FA maps and were divided into three groups for analysis: (1) cortical GM of a specific gyrus, (2) larger areas of GM from frontal, temporal and occipital regions, and (3) inferior to superior locations. In the first group, ROIs were traced around the subcortical WM tracts to outline portions of cortical GM of the gyri that lie adjacent to the WM areas. These regions were labeled as GM of SFG, SMG, STG, MOG and PG (see Figure 7-2). The second group of cortical GM ROIs included three areas: frontal GM (regions in front of the anterior margin of the GCC), temporal GM (bilateral regions bordered by the EC, cortical margins and the anterior and posterior WM association fibers) and occipital GM (regions behind the posterior margin of the SCC). The third group of cortical GM ROIs consisted of regions that were traced around visible subcortical and major WM tracts on three sets of 4 successive slices. They were indexed according to their anatomical locations as inferior cortical GM (at the level of the cerebral peduncles), middle cortical GM (at the level of the GCC and SCC), and superior cortical GM (at the level of CR). The individual values ($\lambda_1, \lambda_2, \lambda_3$, Trace/3 ADC, and FA) per slice were averaged for all subjects per ROI (inferior, middle or superior cortical GM). Furthermore, due to similarities in the diffusion metrics from various subcortical WM and cortical GM regions, individual values were averaged for all five subcortical WM gyri to yield combined subcortical WM values and for all eleven cortical GM ROIs to yield combined cortical GM values (Tables 7-2, 7-3, 7-4).

All subcortical WM and cortical GM ROI traces were cross-referenced with FLAIR and standard b0 images to avoid inclusion of obviously visible CSF. This allowed the visualization and exclusion of neighboring sulci, which otherwise would have artificially augmented CSF contamination of the eigenvalues, Trace/3 ADC, and FA measures. Means and standard deviations were calculated for each ROI. Paired *t*-tests were used to analyze differences between FA, Trace/3 ADC, and $\lambda_1, \lambda_2, \lambda_3$ values from the standard and FLAIR DTI maps ($p \leq 0.05$). Two-tailed unpaired *t*-tests were also conducted to assess differences of the above measures between the old (N=10) and young (N=8) age groups ($p \leq 0.05$).

7.3 Results

The Ni-doped water phantom did not display any significant differences in FA, Trace/3 ADC, and eigenvalues derived using either standard DTI or FLAIR DTI and was very reproducible over four trials for both methods (Table 7-1). The isotropic nature of the phantom is evident in the very low FA of 0.05 and the small differences between the eigenvalues, i.e. $\lambda 1 / \{(\lambda 2 + \lambda 3)/2\} = 1.07$). Nickel doping of water phantoms is typically performed to adjust the T1 and T2 relaxation times of the water solution so that it may be

imaged within a reasonable time with short TR values (T1/T2 = 289/265 ms for Ni-doped phantom). For DTI, where image contrast is not directly dependent on tissue relaxation times, the use of paramagnetic metal ions in water may not affect the measured diffusion parameters. We also measured FA and Trace/3 ADC in a tap water phantom (N=5 at 18.5°C) and observed similar values as seen in Table 7-1 for the Ni-doped water phantom (FA = 0.05 ± 0.01; Trace/3 ADC = 2.03 ± 0.01 x 10^{-3} mm^2/s). A guide to the reproducibility of quantitative diffusion was given by repeated measurements for one young volunteer over four time points in 2 weeks which showed a 2% variation in FA and 0.5% in Trace/3 ADC in the genu of the corpus callosum (data not shown).

Table 7-1: Standard DTI and FLAIR DTI derived diffusion measures for a Ni-doped water phantom (20°C)

Trial #	1	2	3	4	Mean ± SD
FA					
Standard DTI	0.05	0.05	0.04	0.05	0.05 ± 0.01
FLAIR DTI	0.05	0.05	0.04	0.05	0.05 ± 0.01
Trace/3 ADC (x10^{-3} mm^2/s)					
Standard DTI	2.15	2.17	2.15	2.17	2.16 ± 0.01
FLAIR DTI	2.15	2.17	2.16	2.17	2.16 ± 0.01
λ_1 (x10^{-3} mm^2/s)					
Standard DTI	2.26	2.26	2.25	2.27	2.26 ± 0.01
FLAIR DTI	2.26	2.27	2.25	2.27	2.26 ± 0.01
λ_2 (x10^{-3} mm^2/s)					
Standard DTI	2.15	2.16	2.15	2.17	2.16 ± 0.01
FLAIR DTI	2.14	2.17	2.16	2.17	2.16 ± 0.01
λ_3 (x10^{-3} mm^2/s)					
Standard DTI	2.06	2.07	2.06	2.07	2.07 ± 0.01
FLAIR DTI	2.05	2.07	2.07	2.07	2.07 ± 0.01

The signal-to-noise ratios (SNR) of brain parenchyma (signal measured in cortical GM) for the standard DTI and FLAIR DTI b0 images were 51±4 and 46±4, respectively, in the young group (N=8) and were 54±6 and 48±5, respectively, in the elderly group (N=10). The SNR differences of 10±4% ($p<0.001$) and 11±5% ($p<0.01$) between standard and FLAIR DTI in the young and elderly groups, respectively, is in accordance with theoretical considerations where an SNR difference of ~13% would be expected (assuming a T1 of 900 ms and taking into consideration that the shorter TR of 3s in the standard DTI reduces its relative SNR). The FLAIR inversion pulse reduced the b0 signal of the CSF in the ventricles to ~ 16% of the intensity of CSF in the non-FLAIR b0 images. The FLAIR method yielded good suppression of CSF in the ventricles and sulci

as observed on the FLAIR b0 image and Trace/3 ADC map (Figure 7-1). Qualitatively the standard and FLAIR FA maps of the young (Figure 7-2) and elderly (Figure 7-3) adult brains appear quite similar. Structures such as the genu and splenium of the corpus callosum and the subcortical WM appear to have extended outlines when CSF is suppressed in agreement with Papadakis *et al.*(Papadakis *et al* 2002). Furthermore, the contrast between the deep major white matter tracts and the peripheral brain regions on the FLAIR FA maps appears to be less relative to the standard FA maps. The darker "background" of the brain periphery in FA maps derived from standard DTI is due to contributions from isotropic CSF within the sulci.

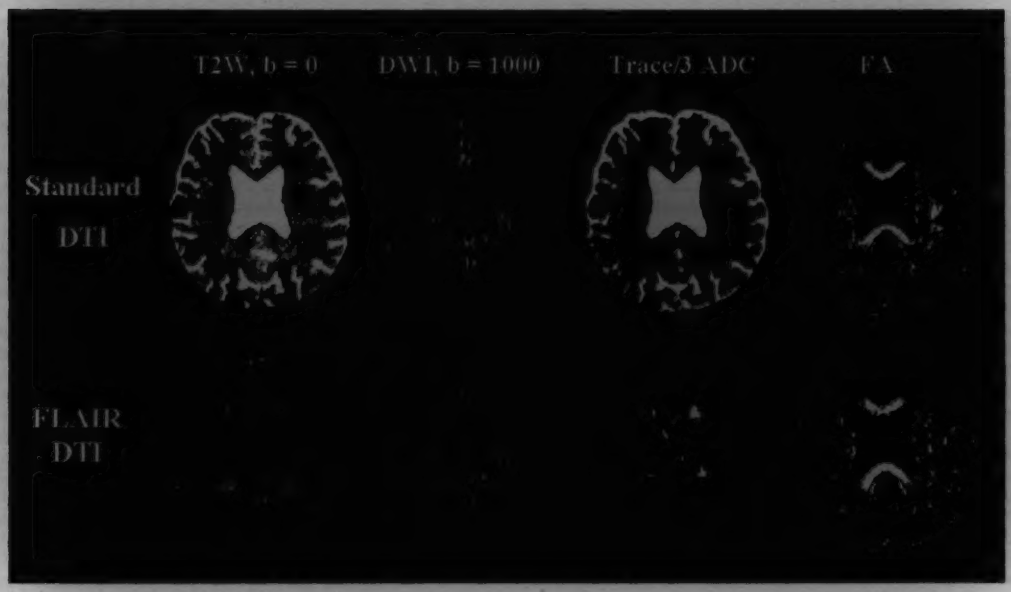

Figure 7-1: A set of standard (above) and FLAIR-DTI (below) derived T_2-weighted (T2W; b = 0 s/mm^2), diffusion-weighted images (DWI; b = 1000 s/mm^2), Trace/3 ADC maps, and FA maps from an elderly subject (age = 70 years). The SNRs of cortical gray matter for the standard DTI and FLAIR DTI b0 images were 48 and 43, respectively, in this subject.

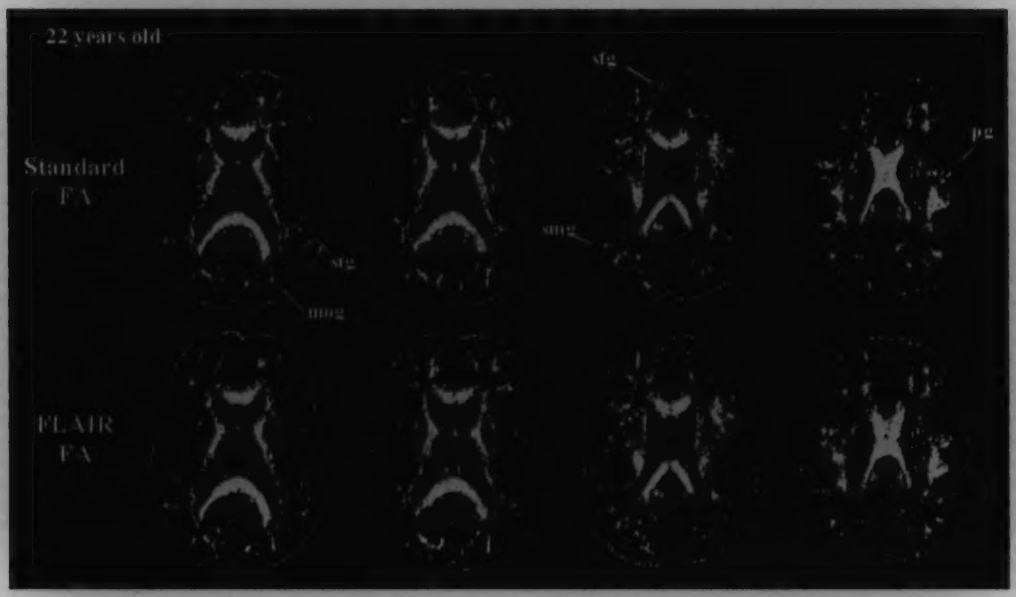

Figure 7-2: Representative sets of FA maps of four slices acquired on a young age group volunteer (22 years) using standard (above) and FLAIR (below) DTI sequences. The standard FA maps exhibit the subcortical WM ROIs used in the analysis: **stg**, superior temporal gyrus; **mog**, middle occipital gyrus; **smg**, supra marginal gyrus; **sfg**, superior frontal gyrus; **pg**, postcentral gyrus.

7.3.1 Effect of CSF-Suppression on Fractional Anisotropy

CSF-suppression yielded increases of FA in discrete regions of the brain including several of the major deep WM tracts, subcortical WM, and cortical GM (Table 7-2) in both the young and elderly groups. There was no significant difference of FA in the deep GM (globus pallidus, thalamus, or putamen) with CSF suppression (Table 7-2). Most of the deep major white matter tracts showed small increases of 3-6% in FA but the genu of the corpus callosum in the young group showed the largest change at 8%. FA values in subcortical WM within five individual gyri were elevated by 9-14% using FLAIR-DTI. The mean FA values averaged over all the subcortical WM regions increased from 0.45 ± 0.05 to 0.50 ± 0.04 in the young group and from 0.39 ± 0.04 to 0.43 ± 0.04 in the elderly group when CSF was suppressed. The FA values of the cortical GM (0.22-0.26) were much less than in WM but still significantly higher than that of CSF (0.14). The absolute increase of FA in cortical GM regions with CSF suppression was very small (0.01-0.03) but it was rather consistent between standard and FLAIR-DTI for all areas evaluated. The mean FA averaged over all the cortical GM regions increased from 0.22 ± 0.01 to 0.24 ± 0.02 in the young group and from 0.22 ± 0.02 to 0.24 ± 0.02 in the elderly group when CSF was suppressed. It must be stressed that obvious CSF areas on b0 maps were avoided when the cortical GM regions-of-interest were outlined; otherwise much larger changes would have been measured in FA with CSF-suppression. Furthermore, the

elderly population showed similar changes in FA with CSF suppression as the much younger group, presumably because of the avoidance of readily visible CSF in the first place.

Figure 7-3: Representative sets of FA maps of four slices acquired on an old age group volunteer (71 years) using standard (above) and FLAIR (below) DTI sequences.

Table 7-2: Standard and FLAIR FA values (mean ± SD) of major brain regions from the young (21-25 years) and old (61-74 years) age groups

Region	Young age group (n = 8)				Old age group (n = 10)			
	Standard FA	FLAIR FA	%DIFF[a]	p	Standard FA	FLAIR FA	%DIFF[a]	p
Combined Subcortical White Matter[b]	0.45 ± 0.05	0.50 ± 0.05	9%	<0.01	0.39 ± 0.04	0.43 ± 0.04	10%	<0.01
Combined Cortical Gray Matter[c]	0.22 ± 0.01	0.24 ± 0.02	7%	<0.01	0.22 ± 0.02	0.24 ± 0.02	8%	<0.01
Major White Matter								
Genu of Corpus Callosum	0.68 ± 0.03	0.74 ± 0.03	8%	<0.01	0.62 ± 0.04	0.65 ± 0.03	5%	<0.01
Splenium of Corpus Callosum	0.75 ± 0.03	0.77 ± 0.03	3%	<0.01	0.72 ± 0.04	0.75 ± 0.02	4%	<0.01
Anterior limb - Internal Capsule	0.63 ± 0.04	0.65 ± 0.04	---	0.19	0.60 ± 0.03	0.63 ± 0.04	4%	<0.01
Posterior limb - Internal Capsule	0.66 ± 0.02	0.68 ± 0.02	3%	<0.01	0.63 ± 0.04	0.64 ± 0.04	---	0.17
External Capsule	0.48 ± 0.03	0.50 ± 0.03	3%	0.02	0.42 ± 0.04	0.45 ± 0.04	6%	<0.01
Corona Radiata	0.56 ± 0.02	0.56 ± 0.02	---	0.36	0.55 ± 0.06	0.56 ± 0.07	3%	<0.01
Centrum Semiovale	0.45 ± 0.03	0.45 ± 0.04	---	0.77	0.41 ± 0.04	0.42 ± 0.04	2%	0.02
Deep Gray Matter								
Thalamus	0.39 ± 0.03	0.40 ± 0.05	---	0.46	0.36 ± 0.04	0.34 ± 0.04	---	0.14
Putamen	0.20 ± 0.02	0.20 ± 0.02	---	0.17	0.22 ± 0.03	0.23 ± 0.04	---	0.38
Globus Pallidus	0.32 ± 0.03	0.33 ± 0.03	---	0.50	0.28 ± 0.05	0.29 ± 0.05	---	0.09
CSF	0.14 ± 0.02	------	---	---	0.14 ± 0.03	-------	---	---

[a]%DIFF- % difference between standard and FLAIR FA values.
[b]The combined FA values reflect means (± SD) from all five subcortical white matter gyri.
[c]The combined FA values reflect means (± SD) from all eleven cortical gray matter ROIs.

CSF suppression yielded reductions in Trace/3 ADC values primarily in the cortical GM regions, namely decreases of 8-14% and 15-18% in the young and elderly groups, respectively (Figure 7-4a). Unlike FA, the impact of CSF suppression on Trace/3 ADC was greater for the elderly population. The FLAIR-DTI Trace/3 ADC values had a very

low variability between subjects and, interestingly, it is not perfectly uniform across the brain with a range of 0.69-0.80 $x10^{-3}$ mm^2/s in the young group (Table 7-3) and 0.71-0.83 $x10^{-3}$ mm^2/s in the elderly group (Table 7-4).

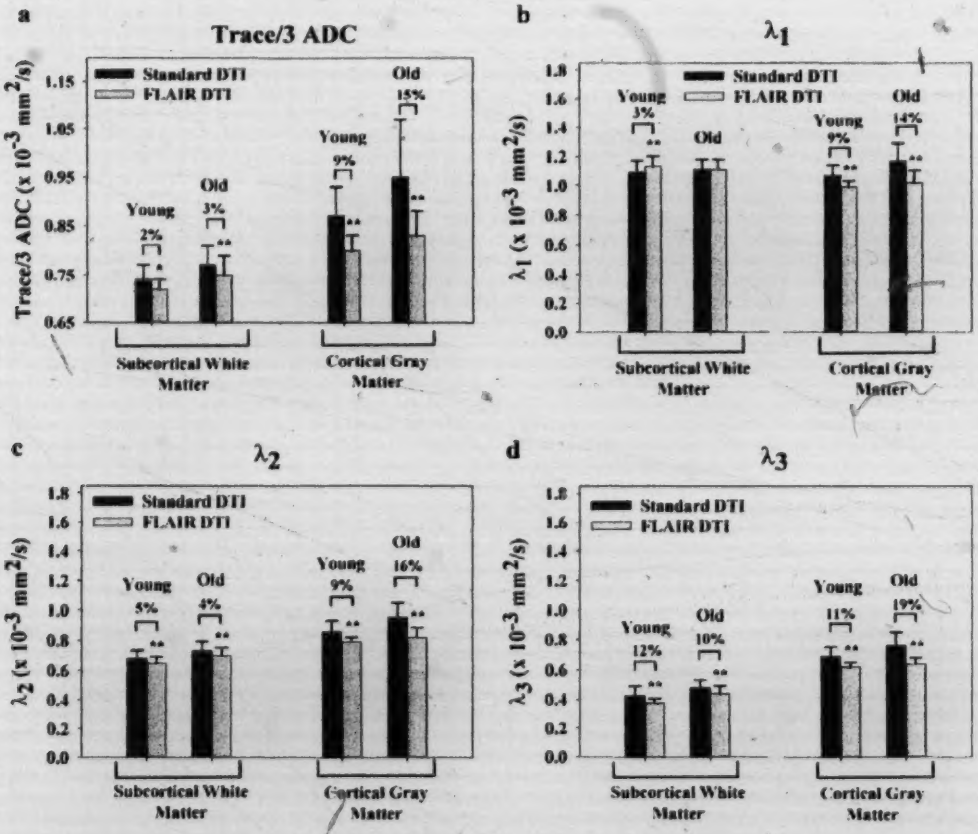

Figure 7-4: Comparisons of standard (black bars) and FLAIR (gray bars) DTI derived (a) Trace/3 ADC and (b, c, d) eigenvalues in the young (21-25 years) and old (61-74 years) age groups for the subcortical white matter in the gyri and cortical gray matter {*$p<0.05$, **$p<0.01$}. CSF-suppression yields a decrease in the Trace/3 ADC of subcortical white matter and cortical gray matter in both age groups. The parallel diffusivity, λ_1, either does not change or increases and the perpendicular diffusivities, λ_2 and λ_3, decrease in subcortical white matter when FLAIR is used for CSF-suppression. This leads to an increase in FA (as seen in Table 7-2). All three eigenvalues (λ_1, λ_2, and λ_3) decrease with FLAIR-DTI in the cortical gray matter relative to standard DTI.

Table 7-3: FLAIR DTI-derived diffusion measures (mean ± SD) of major brain regions from the young age group (21-25 years)[a]

Region	Trace/3 ADC	λ_1	λ_2	λ_3
Combined Subcortical White Matter in the Gyri[b]	0.72 ± 0.02	1.13 ± 0.07	0.65 ± 0.04	0.38 ± 0.03
Combined Cortical Gray Matter[c]	0.80 ± 0.03	0.99 ± 0.04	0.79 ± 0.03	0.62 ± 0.03
Major White Matter				
Genu of Corpus Callosum	0.76 ± 0.02	1.56 ± 0.06	0.48 ± 0.04	0.23 ± 0.03
Splenium of Corpus Callosum	0.74 ± 0.04	1.62 ± 0.08	0.40 ± 0.05	0.21 ± 0.06
Anterior limb-Internal Capsule	0.69 ± 0.01	1.28 ± 0.05	0.51 ± 0.04	0.28 ± 0.03
Posterior limb-Internal Capsule	0.69 ± 0.01	1.33 ± 0.05	0.49 ± 0.03	0.26 ± 0.02
External Capsule	0.71 ± 0.01	1.09 ± 0.05	0.66 ± 0.04	0.34 ± 0.03
Corona Radiata	0.68 ± 0.01	1.20 ± 0.15	0.57 ± 0.03	0.33 ± 0.04
Centrum Semiovale	0.69 ± 0.01	1.03 ± 0.06	0.65 ± 0.02	0.38 ± 0.05
Deep Gray Matter				
Thalamus	0.73 ± 0.02	1.05 ± 0.05	0.68 ± 0.03	0.47 ± 0.04
Putamen	0.69 ± 0.02	0.84 ± 0.04	0.69 ± 0.02	0.55 ± 0.02
Globus Pallidus	0.72 ± 0.02	0.96 ± 0.01	0.71 ± 0.03	0.49 ± 0.02

[a]Values are in units of: ($x10^{-3}$ mm^2/s); young group (n = 8).

[b]The combined Trace/3 ADC, λ_1, λ_2, and λ_3 values reflect means (± SD) from all five subcortical white matter gyri.

[c]The combined Trace/3 ADC, λ_1, λ_2, and λ_3 values reflect means (± SD) from all eleven cortical gray matter ROIs.

Table 7-4: FLAIR DTI-derived diffusion measures (mean ± SD) of major brain regions from the old age group (61-74 years)[a]

Region	Trace/3 ADC	λ_1	λ_2	λ_3
Combined Subcortical White Matter in the Gyri[b]	0.75 ± 0.04	1.11 ± 0.07	0.70 ± 0.06	0.44 ± 0.05
Combined Cortical Gray Matter[c]	0.83 ± 0.05	1.02 ± 0.08	0.82 ± 0.06	0.64 ± 0.04
Major White Matter				
Genu of Corpus Callosum	0.81 ± 0.04	1.58 ± 0.10	0.54 ± 0.04	0.32 ± 0.04
Splenium of Corpus Callosum	0.79 ± 0.04	1.70 ± 0.07	0.43 ± 0.05	0.24 ± 0.03
Anterior limb-Internal Capsule	0.72 ± 0.03	1.33 ± 0.07	0.53 ± 0.03	0.31 ± 0.03
Posterior limb-Internal Capsule	0.72 ± 0.03	1.33 ± 0.06	0.53 ± 0.05	0.30 ± 0.03
External Capsule	0.76 ± 0.05	1.13 ± 0.05	0.71 ± 0.06	0.43 ± 0.06
Corona Radiata	0.73 ± 0.04	1.22 ± 0.09	0.61 ± 0.07	0.37 ± 0.06
Centrum Semiovale	0.74 ± 0.04	1.09 ± 0.05	0.68 ± 0.08	0.45 ± 0.06
Deep Gray Matter				
Thalamus	0.77 ± 0.05	1.05 ± 0.09	0.76 ± 0.06	0.51 ± 0.05
Putamen	0.71 ± 0.06	0.89 ± 0.11	0.71 ± 0.06	0.54 ± 0.04
Globus Pallidus	0.77 ± 0.06	1.01 ± 0.10	0.75 ± 0.06	0.56 ± 0.04

[a]Values are in units of: ($x10^{-3}$ mm^2/s); old group (n = 10).

[b]The combined Trace/3 ADC, λ_1, λ_2, and λ_3 values reflect means (± SD) from all five subcortical white matter gyri.

[c]The combined Trace/3 ADC, λ_1, λ_2, and λ_3 values reflect means (± SD) from all eleven cortical gray matter ROIs.

Regional specific changes in the eigenvalues λ_1, λ_2, and λ_3 were observed with CSF suppression. Summary data from the five subcortical WM regions and the eleven cortical GM regions are presented since the eigenvalues from the individual ROIs were very similar. λ_1 was typically not altered with CSF suppression in the WM of either the young

or the elderly, although λ_1 of the subcortical WM showed a small increase (3%) in the young group. On the other hand, λ_1 of the cortical GM regions was significantly reduced by 9% and 14% with FLAIR-DTI in the young and elderly groups, respectively (Figure 7-4b). λ_2 values declined by 15% in the genu of the corpus callosum, 5% in subcortical WM, and 9% in cortical GM of the young group with FLAIR DTI (Figure 7-4c). CSF-suppression resulted in decreases of λ_3 in the young group in the genu of the corpus callosum (33%), subcortical WM (12%), and cortical GM areas (11%) (Figure 7-4d). Similar decreases in λ_2, and λ_3 with CSF suppression were noted in the elderly group (Figure 7-4c, d). Data from the genu of the corpus callosum is presented since it was the major white matter tract with the largest change of FA with CSF suppression. The other deep major white matter tracts with significant increases in FA also showed similar patterns with the eigenvalues, but to a smaller extent (data not shown). The eigenvalues for deep gray matter such as the globus pallidus and thalamus did not show any differences with CSF-suppression, which is in agreement with the lack of change in either FA or Trace/3 ADC, but the putamen demonstrated a 3%, 5%, and 8% decrease in λ_1, λ_2, and λ_3, respectively, in the elderly group for FLAIR-DTI relative to standard DTI. To summarize, although CSF suppression affected all three eigenvalues of cortical GM quite uniformly, WM was affected primarily in its diffusion coefficients perpendicular to the principal axis of diffusion. This reduction of the perpendicular diffusivities, particularly λ_3, coupled with the lack of change of the parallel diffusivity, λ_1, accounts for the increased FA in both deep and subcortical WM measured with CSF suppression.

7.3.2 Diffusion Changes Associated with Aging

Although qualitative differences in terms of decreased conspicuity of white matter tracts in the elderly group relative to the young group were observed in the FA maps, visual inspection is not adequate for revealing the changes in tissue microstructure. The diffusion parameters FA, Trace/3 ADC, λ_1, λ_2, and λ_3 obtained from the FLAIR-DTI were used for the aging comparison in order to ensure that differences in the healthy young (21-25 years old) and elderly (61-74 years old) groups were not due to greater contamination of the measurements by CSF in the elderly group. The FLAIR-DTI derived FA values for seven deep major white matter tracts, three deep gray matter regions, five combined subcortical white matter regions, and eleven combined cortical gray matter regions are listed in Table 7-2. The FA values of a subset of these brain regions are compared between young and old in Figure 7-5.

Of the deep major white matter tracts, only the genu of the corpus callosum (13%, $p<0.001$), splenium of the corpus callosum (3.4%, $p=0.05$), posterior limb of the internal capsule (5.5%, $p=0.04$), and the external capsule (13%, $p=0.004$) demonstrated a significant decline of FA with age (Figure 7-5). A significant decrease of anisotropy in the thalamus (15%, $p=0.02$) and a trend towards a decrease in the globus pallidus (13%, $p=0.06$) were observed with age but the putamen, on the other hand, showed a 14% *increase* in anisotropy ($p=0.04$) with age. All five subcortical white matter regions in the superior frontal gyrus (19%, $p<0.001$), supra marginal gyrus (17%, $p=0.002$), superior temporal gyrus (10%, $p=0.01$), middle occipital gyrus (17%, $p=0.004$), and postcentral

gyrus (15%, $p<0.001$) showed significant decreases of FA in the elderly group relative to the young. Of the eleven cortical GM regions, only the frontal GM showed a decrease in FA from 0.24 ± 0.01 in the young to 0.22 ± 0.02 in the elderly (9%, $p=0.02$).

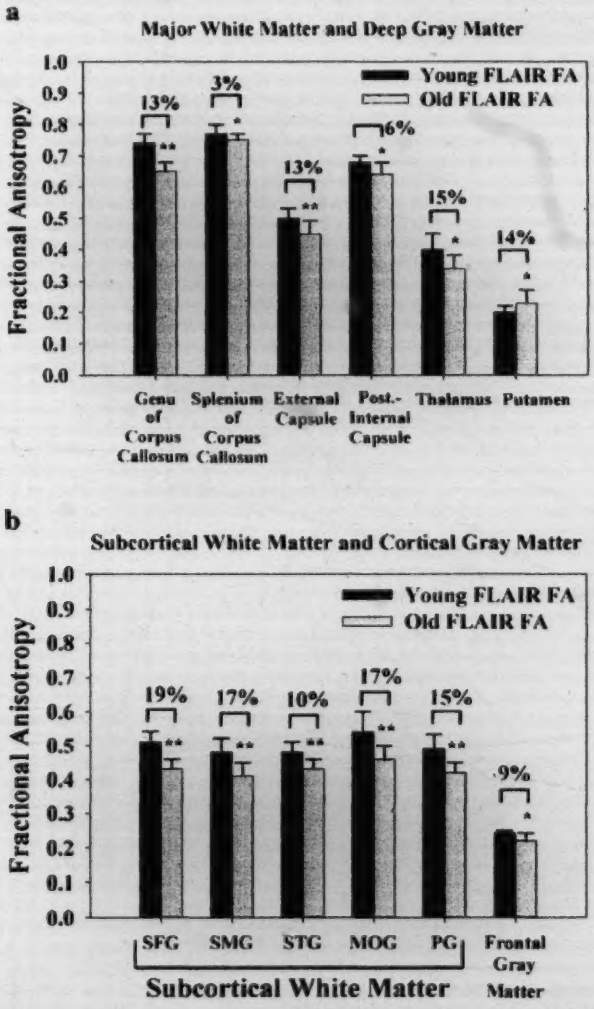

Figure 7-5: Comparisons of fractional anisotropy between the young (black bars, n = 8, 21-25 years old) and the older (gray, n = 10, 61-74 years old) age groups for (a) major white matter and deep gray matter regions, and (b) subcortical white matter in the gyri and cortical gray matter regions {*$p<0.05$, **$p<0.01$}. Please see Methods for detailed descriptions of subcortical white matter regions. FA is reduced with age in most brain structures such as the deep white matter, thalamus, and subcortical white matter. The frontal gray matter was the only cortical gray matter region out of the total eleven to show a significant change in FA. Curiously the putamen showed an increase in FA with age.

The FLAIR-DTI derived Trace/3 ADC values and eigenvalues are presented in Tables 7-3 and 7-4 for the young and elderly groups, respectively, and a direct age comparison of Trace/3 ADC, λ_1, λ_2, and λ_3 for select brain regions is given in Figure 7-6. The most consistent and significant increases in Trace/3 ADC with age were in all seven of the deep major white matter tracts: genu of corpus callosum (7%, p=0.004), splenium of corpus callosum (5.7%, p=0.04), anterior limb of internal capsule (4.5%, p=0.015), posterior limb of internal capsule (3.6%, p=0.021), external capsule (6.3%, p=0.015), corona radiata (7.1%, p=0.001), and centrum semiovale (7%, p=0.002) (Figure 7-6a). Increased Trace/3 ADC is reflective of greater bulk water mobility in the tissue. The globus pallidus (7.2%, p=0.015) was the only deep GM structure and the subcortical WM of the superior temporal gyrus (6%, p=0.03) was the only subcortical WM structure to show any increases in Trace/3 ADC with age. The multi-slice analysis of cortical gray matter at inferior, middle, and superior brain locations were the only cortical GM analyses that showed significant increases in Trace/3 ADC (3.1-4.6%, p<0.001). Note that the frontal GM region, which demonstrated a decrease in FA, showed no significant increase in Trace/3 ADC.

Further insights into the changes in anisotropy with age can be obtained by evaluating the eigenvalues λ_1, λ_2, and λ_3 which yield the principal ADC values along the length of the fiber tracts (λ_1) or across the fiber tracts (λ_2, λ_3) (Tables 7-3, 7-4). The splenium of the corpus callosum and the centrum semiovale demonstrated increases of ~5-6% in λ_1 but the majority of the remaining deep white matter structures, as well as the deep gray matter, subcortical white matter, and cortical gray matter, did not show significant increases in λ_1 with age (Figure 7-6b). The subcortical white matter of the superior frontal gyrus curiously showed a decrease in λ_1 unlike the other subcortical WM that showed no change. λ_2 showed increases with age in one major white matter tract (genu of corpus callosum, 12%, p=0.007), one deep gray matter structure (thalamus, 10%, p=0.005), and four of the five subcortical WM ROIs (5-10%, p<0.04) (Figure 7-6c). Significant increases of 12-27% in λ_3 values of the elderly subjects relative to the young were observed for four of the seven deep major white matter tracts (genu of corpus callosum, 27%, p<0.001; posterior limb of internal capsule, 14%, p=0.002; external capsule, 19%, p=0.002; centrum semiovale, 16%, p=0.02), all five subcortical WM regions (10-16%), and one deep GM area, the globus pallidus (13%, p<0.001) (Figure 7-6d). The increases in the perpendicular diffusivities coupled with the lack of change in parallel diffusivity results in the observed decreases in FA within the subcortical and deep white matter of the elderly group compared to the young.

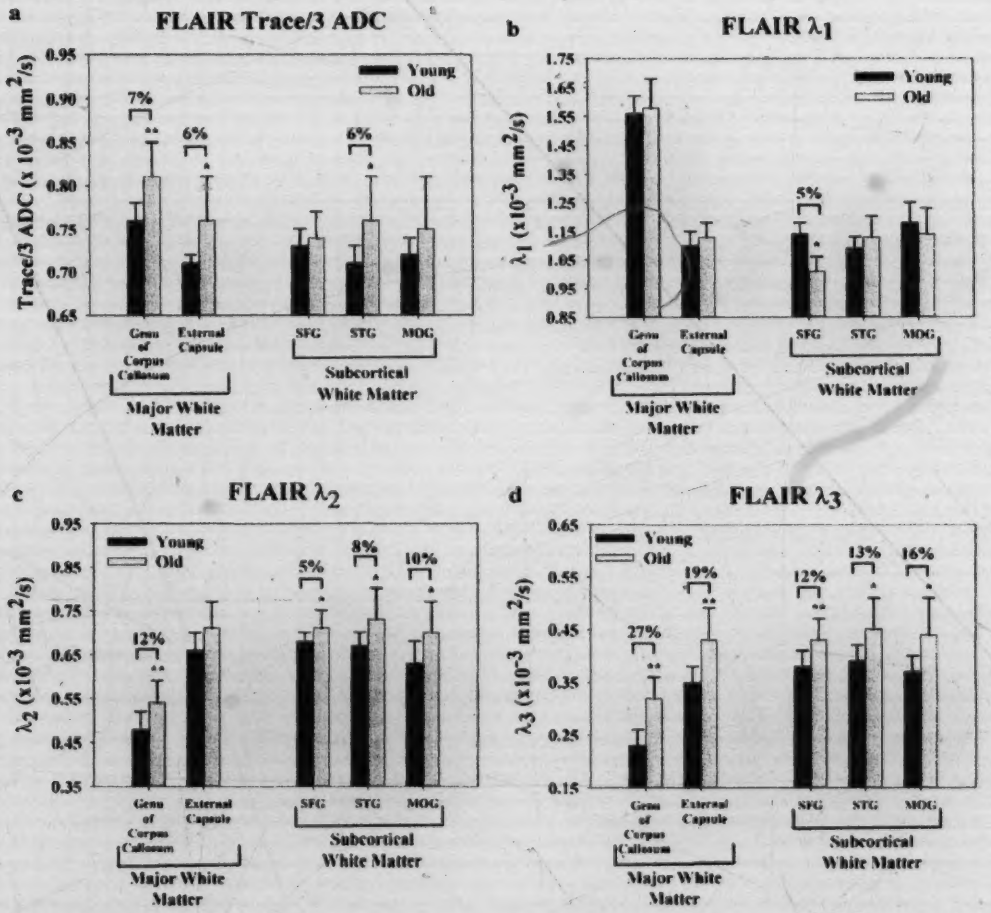

Figure 7-6: Comparisons of (a) Trace/3 ADC, (b) λ_1, (c) λ_2, and (d) λ_3 between the young (black bars; n = 8, 21-25 years old) and the older (gray; n = 10, 61-74 years old) age groups in the genu of the corpus callosum, external capsule, and subcortical white matter (superior frontal gyrus SFG, superior temporal gyrus STG and middle occipital gyrus MOG) {*$p<0.05$, **$p<0.01$}. The Trace/3 ADC increased significantly for all deep white matter structures, and one subcortical gyral white matter region with aging. The parallel diffusivity, λ_1, did not change significantly with aging for most brain areas with the exception of the subcortical white matter of the superior frontal gyrus (SFG). The perpendicular diffusivities, λ_2 and λ_3, increased with aging for the genu of the corpus callosum and the subcortical white matter regions shown in the figure. The external capsule did not show much change in λ_2 whereas there was a large increase in λ_3 with age.

7.4 Discussion

This report details our findings on (a) the effects of CSF-suppression on regional brain measurements of diffusion with a primary focus on fractional anisotropy in both young and elderly populations and (b) the alterations in regional water diffusion (Trace/3 ADC, fractional anisotropy, and principal eigenvalues) with normal aging (21-25 years old versus 61-74 years old). A major focus of our diffusion measurements was on the cortical gray matter and subcortical white matter (i.e. peripheral white matter in the gyri) that have not been reported previously in much detail. One potential confound in comparative studies of diffusion anisotropy is the potential bias due to varying contributions of noise (Pierpaoli *et al* 1996). The SNR of the FLAIR-DTI and standard DTI for either the young or elderly groups were all very similar (mean SNR ranged from 46-54 in the b0 images) and hence any differences in anisotropy reported in this study are not due to variations in SNR. Furthermore, the use of CSF-suppression in the aging study ensured that the expected greater contamination from partial volume averaging by CSF in the elderly subjects was not a factor in putative alterations in diffusion with age.

7.4.1 Effect of CSF-Suppression on Quantitative Measurements

There are several earlier studies on the evaluation of using CSF-suppression to provide more accurate measures of diffusion along either one direction or the trace diffusion (Falconer and Narayana 1997; Hirsch *et al* 1999; Kwong *et al* 1991; Latour and Warach 2002; Zacharopoulos and Narayana 1998), but there have only been two studies that have considered the role of CSF-suppression on the full diffusion tensor with a primary focus on anisotropy (Ma *et al* 2004; Papadakis *et al* 2002). Papadakis *et al.* studied young adult (25-42 years old) volunteers and reported a histogram analysis of relative anisotropy in five deep white matter regions-of-interest, namely the genu, splenium, and body of the corpus callosum, combined internal and external capsule, and the corona radiata (Papadakis *et al* 2002). We extended their study by (a) incorporating an elderly group in which partial volume averaging is expected to be more critical, (b) analyzing 26 individual regions-of-interest with a focus on the peripheral structures of the brain such as the subcortical white matter in the gyri and the cortical gray matter where CSF contamination is expected to be greater, (c) using mean values of the more ubiquitous fractional anisotropy within a structure as opposed to histogram analysis of relative anisotropy, and (d) reporting the influence of CSF-suppression on the individual eigenvalues in the various brain regions to better understand the basis of the changes in anisotropy. Reporting the mean FA value of a brain region is far more common in the literature than reporting an FA histogram because the former facilitates multi-site comparisons.

A more recent study by Ma *et al.* explores the role of CSF-suppression in DTI on measuring FA in frontal, parietal, and occipital gray matter, and the genu and splenium of the corpus callosum (Ma *et al* 2004). Although their results from the corpus callosum are in accordance with our data in Table 7-2, their nearly two-fold differences between standard and FLAIR-DTI for gray matter (FA from 0.10 to 0.20) are substantially greater

than ours (FA from 0.22 to 0.24). This discrepancy may partially lie in our choice of slice thickness (3 mm contiguous as opposed to 5 mm with a 2.5 mm gap in their article), but it is likely mainly due to differences in ROI analysis methods where we avoided the inclusion of neighboring CSF spaces such as the sulci. Their study used a "gray matter" mask defined as regions with an FA below 0.15 that would unfortunately also include voxels from isotropic CSF. We would have observed a greater difference in FA with CSF suppression if adjacent voxels from the CSF spaces were included in our ROIs.

The reduction of partial volume averaging of brain parenchyma with CSF is expected to improve the accuracy of diffusion anisotropy measurements. In addition to CSF-suppression using a FLAIR preparatory pulse, another method of reducing partial volume averaging is to acquire thinner slices (e.g. 2 mm compared to 5 mm); this has been shown to increase FA significantly in various tracts (Hunsche *et al* 2001). The study by Papadakis *et al.* in young adult volunteers, using 5 mm thick slices, demonstrated significant differences of relative anisotropy in the corpus callosum, a structure that happens to be close to the lateral ventricles, but not in the internal/external capsules, nor the corona radiata when FLAIR CSF suppression was utilized with DTI (Papadakis *et al* 2002). In our study using 3 mm thick slices, the genu of the corpus callosum showed the largest change of the deep white matter structures (up to 8%) but we did see small, but significant differences in the internal (up to 4%) and external capsules (up to 6%) (Table 7-2). Deep gray matter structures such as the thalamus, putamen, and globus pallidus did not show any differences in FA with FLAIR-DTI (Table 7-2).

As to be expected, the largest and most consistent increases of FA obtained with CSF suppression was at the periphery of the brain, namely in the subcortical white matter (~9-10%) and the cortical gray matter (~7-8%) (Table 7-2). The FA increase observed in cortical gray matter was significant even though the absolute change in FA of 0.02 (from 0.22 to 0.24) was quite small. It is interesting that the subcortical white matter showed the largest increases in fractional anisotropy yet demonstrated very little decrease in Trace/3 ADC (2-3%) with CSF-suppression, unlike the cortical gray matter whose Trace/3 ADC dropped by 9-15% (Figure 7-4a). The influence of CSF-suppression on the eigenvalues has not been reported previously. In effect, the increases of FA in white matter (e.g. genu of corpus callosum, subcortical white matter) with CSF-suppression are primarily due to a reduction in the perpendicular diffusivity, particularly λ_3, with a lack of change in the parallel diffusivity, λ_1 (Figure 7-4). On the other hand, cortical gray matter demonstrates marked reductions in all three eigenvalues with CSF-suppression.

The young adult group had 16/26 (62%) ROIs with significant increases in FA with CSF suppression whereas the elderly group, with larger CSF spaces, had 18/26 (69%) ROIs; all in all not much difference with age. The percentage difference between standard FA and FLAIR FA was not significantly different between the young and elderly groups for either combined subcortical white matter or combined cortical gray matter, which is not what we had expected (Table 7-2). On the other hand, the Trace/3 ADC values certainly demonstrated a larger change with CSF suppression in the cortical gray matter of the elderly group relative to the younger group (Figure 7-4a). Although our FLAIR-derived Trace/3 ADC values agree with the literature, the percentage change with CSF

suppression was not as great as the literature (Latour and Warach 2002) because our ROIs were drawn for specific anatomical substructures in the brain (as opposed to a large area reflecting a contralateral ROI for a lesion) and excluded obvious CSF spaces in sulci.

The effective in-plane resolution of the image acquisition prior to zero-filling was 2.3 x 1.7 mm and the slice thickness was 3 mm. The effect of larger slice thickness was not a focus of this study since many current DTI studies are using a slice thickness of 3 mm. Of course, the alterations in the diffusion parameters with CSF suppression would have been greater if we had used poorer in-plane spatial resolution or thicker slices. Furthermore, care in avoiding obvious areas of CSF when drawing the regions-of-interest in the gray or white matter was essential for not overestimating the effects of CSF-suppression. Qualitatively, the FLAIR FA maps look "grainier" in the peripheral regions of the brain than on the standard FA maps, primarily due to the absence of isotropic, low FA CSF within the sulci (Figure 7-2, 7-3). The use of CSF-suppressed DTI should be a consideration for quantitative studies of diffusion anisotropy, but, in particular, those studies interested in changes within the cortical gray matter or the subcortical white matter in the gyri regardless of age. The compromise for more accurate quantitative measurements of tissue microstructure is that the image acquisition for CSF-suppressed, FLAIR-DTI is much longer, in our case about 8 minutes compared to 3 min for standard DTI (for twenty slices, 6 gradient directions, 8 averages). This extended scan duration may be acceptable for chronic patients such as those with Alzheimer's disease or epilepsy, but may be impractical for more uncooperative patients such as those with acute stroke.

Normative values of diffusion anisotropy in the human brain have been reported in younger adult populations (Hunsche *et al* 2001; Pierpaoli *et al* 1996; Shimony *et al* 1999). However, a comprehensive, normative data set of fractional anisotropy, Trace/3 ADC, and the three principal eigenvalues obtained with CSF-suppression and thin slices (3 mm) in various brain regions of either healthy young adult or elderly subjects have not previously been reported. An age-matched normative diffusion data set (Tables 7-2 to 7-4) would be valuable for the evaluation of micro-structural changes associated with disease. The FA values in five different peripheral subcortical white matter regions within the gyri (e.g. frontal, temporal, occipital) were very consistent, as were FA values in cortical gray matter measured throughout the brain. As an aside, although cortical gray matter has a much smaller degree of fractional anisotropy (0.24) than the deep white matter (0.45-0.77), deep gray matter like the thalamus (0.40), or subcortical gyral white matter (0.50), it is considerably greater than CSF (0.14) or pure water phantom (0.05) FA values and, given the reproducibility of the eigenvalues (λ_1 is 1.6 times that of λ_3), it would be inappropriate to consider the cortical gray matter as an isotropic structure.

7.4.2 Age-Related Diffusion Changes

Many comprehensive studies on aging of the human brain have used structural T_1-weighted, 3D spoiled gradient echo (i.e. SPGR, MP-RAGE) sequences primarily to

measure volumetric changes with age, but some have also used the intensity of the 3D gradient-echo images as a "marker" of tissue concentration (Good *et al* 2001; Guttmann *et al* 1998). Although all studies seem to agree that there is a marked increase in CSF volume with aging, there is some discrepancy as to whether there is greater loss of gray matter volume (Good *et al* 2001) or of white matter volume (Guttmann *et al* 1998). Clearly, there are advantages for using DTI to investigate alterations of the tissue microstructure with age more directly (Moseley 2002). There is much interest in using diffusion to study "healthy" aging, as well as to create a normative basis from which to investigate diseases that are more prevalent in an elderly population, such as stroke or Alzheimer's disease. Water diffusion in tissue is known to change with age.

A few aging studies have focused purely on Trace/3 ADC with mixed results, one demonstrating ADC increases in the white matter (Engelter *et al* 2000) and the other showing no changes (although this latter study had very large ranges in ADC within age groups) (Helenius *et al* 2002). However, Trace/3 ADC is not ideally suited for assessing the tissue integrity (Beaulieu *et al* 1996; Pierpaoli *et al* 2001) and thus others have measured regional reductions in diffusion anisotropy as a function of age (Abe *et al* 2002; Nusbaum *et al* 2001; O'Sullivan *et al* 2001; Pfefferbaum *et al* 2000). Other than the genu and splenium of the corpus callosum, there is little consistency in the brain regions analyzed in these studies. Others have performed a histogram analysis of FA over the whole brain, but this sort of study is limited in its usefulness given the regional and tissue specific changes that are expected with aging (Rovaris *et al* 2003).

We focused on the micro-structural integrity, as indicated by changes of diffusion parameters, in numerous distinct brain regions rather than on tissue volumes. Our aging study went beyond the earlier studies by using thinner slices and CSF-suppression for image acquisition as well as by extending the data analysis by measuring more comprehensive ROIs, focusing on the gyral white matter (what we call subcortical white matter in this paper), cortical gray matter, and other regions that have never been reported, and measuring the eigenvalues. We also focused on a group comparison between younger (21-25 year) and older (61-74 years) adults unlike the earlier studies that performed correlative analyses over this full age range.

Although all of the FA values for young and old are listed in Table 7-2, a comparison of several select regions is shown in Figure 7-5. In agreement with earlier studies (Abe *et al* 2002; Pfefferbaum *et al* 2000), the genu of the corpus callosum showed a larger change (13%) in FA than the splenium of the corpus callosum (3%). There was no change of FA in the anterior limb of the internal capsule although we observed a 6% decrease of FA in the posterior limb of the internal capsule, as opposed to the unspecified increase (Nusbaum *et al* 2001) or no change (Abe *et al* 2002) reported by others. We also measured a 13% decrease of FA in the external capsule but no significant changes in the corona radiata or centrum semiovale (note: our observed FA change in the centrum semiovale from 0.45 in young to 0.41 in old agrees with Pfefferbaum *et al.* (2000) but did not reach significance ($p=0.09$)). The peripheral subcortical WM in the gyri showed the greatest and most consistent decreases in FA (10-19%) with the decrease in FA mainly due to a lack of change of λ_1 and an increase in diffusion perpendicular to the fiber tracts,

i.e. λ_2 and λ_3 (Figure 7-6).

To our knowledge, this is the first aging study to report the change in the principal eigenvalues. Although our data cannot determine the precise changes responsible for the increase in λ_3 and the decrease in FA, it is consistent with basic pathological studies that indicate decreases in myelin and neural fiber loss with aging (Kemper 1994; Meier-Ruge *et al* 1992; Tang *et al* 1997). The decrease in FA of the subcortical white matter in the gyri was in the absence of any changes in Trace/3 ADC for four of the five ROIs. In contrast, all seven deep white matter structures demonstrated significant increases of 4-7% in isotropic diffusivity, i.e. Trace/3 ADC. Aging studies that use white matter "concentration" obtained from T_1-weighted MP-RAGE structural scans seem to underestimate the degree of change in white matter with aging; as an example, the voxel-based morphometry study on 465 normal adults by Good *et al.* reported accelerated loss of white matter concentration only in the posterior limbs of the internal capsule (see Figure 7-5b in Good *et al.* (Good *et al* 2001)).

The study by Abe *et al.* is the only aging study that reports FA measurements in deep gray matter (Abe *et al* 2002). They did not find any differences of FA with aging in the thalamus or lentiform nucleus. Using thinner slices (3 mm rather than 5 mm) and CSF-suppression, we report a large 15% decrease of FA in the central part of the thalamus, no change in the globus pallidus (although there was a trend towards a 13% decrease $p=0.06$), and unexpectedly a 14% increase of FA in the putamen. The reduction in FA of the thalamus was mainly due to a reduction in λ_2 while λ_1 did not change with age. Given that the thalamus is the gateway for incoming information that is projected to the cortex, it is uncertain how the reduced integrity within the thalamus relates to the reduction of subcortical white matter integrity in the cortical gyri. Our results are in contrast to that of Good *et al.* who reported relative preservation of gray matter "concentration" in the thalamus, based on a T_1-weighted MP-RAGE structural scan (Good *et al* 2001). The putamen was the only structure in which we saw an increase of FA with age, but the pathophysiological reason for this finding is unknown. The Trace/3 ADC was elevated for the globus pallidus but did not differ for either the thalamus or putamen with aging. Presumably due to its lower values than white matter, FA measurements in cortical gray matter with aging have not been reported previously. Although previous structural MRI studies report a decrease in the volume of cortical gray matter in the elderly, our results indicate that there is no change in structural integrity of the residual cortical gray matter, as inferred by fractional anisotropy in most of the cortical regions. Of the eleven cortical GM regions that were measured, only the frontal GM demonstrated a significant (9%) decrease in FA with age.

The t-tests used in this study for comparing diffusion measures between the standard and FLAIR DTI methods for each age group and also for comparing the FLAIR-DTI derived diffusion measures between the young and elderly groups for various brain regions may have been better applied as post hoc analytical tests following a more comprehensive evaluation with a test such the multivariate analysis of variance (MANOVA).

7.5 Synopsis of Recent DTI Based CSF-Suppression/Aging Studies

FLAIR based DTI studies are challenging to implement in clinical settings owing to their lengthy acquisition times. This may explain the scarce number of publications in this area since we published our results in 2004. Since that time period, there are 2 notable studies of FLAIR based diffusion tractography that have evaluated WM tracts proximal to the periventricular spaces of the brain (Chou *et al* 2005; Concha *et al* 2005b). Concha *et al.* compared FLAIR based DTI to conventional non-FLAIR based DTI for diffusion tensor tractography of the limbic system in young adults and observed increases in volumes, reductions in mean diffusivity and increases in FA (4% to 13% increases) of WM tracts such as the cingulum and fornix with the FLAIR method relative to the conventional technique (Concha *et al* 2005b). Chou *et al.* compared FLAIR based diffusion tensor tractography to the conventional technique in periventricular regions such as the corpus callosum and corona radiata in young adults and noted a 17% increase in the volume of fibers with the FLAIR based approach relative to the conventional method (Chou *et al* 2005).

In the area of human adult brain aging there have been several DTI studies to date (since our report was published) that have replicated our findings of reduced diffusion anisotropy and increased mean diffusivity in primarily WM with aging that are suggestive of axonal declines, demyelination and increased water content. The most common findings between these studies are that 1) diffusion anisotropy is reduced in regions such as the corpus callosum, frontal WM, posterior limb of the internal capsule, thalamus and hippocampus and negatively correlates with age, 2) mean diffusivity is increased in similar regions and positively correlates with aging and 3) decreases in diffusion anisotropy tend to follow an anteroposterior gradient in the aging human brain (Abe *et al* 2006; Ardekani *et al* 2007; Camara *et al* 2007; Grieve *et al* 2007; Ota *et al* 2006; Persson *et al* 2006; Pfefferbaum *et al* 2005; Salat *et al* 2005; Sullivan *et al* 2006). Interestingly two of these studies have also observed an increase in diffusion anisotropy of the putamen with age (Abe *et al* 2006; Camara *et al* 2007) which is in line with our finding of a 14% increase in FA of the putamen in the elderly group (61-74 years) relative to the young group (21-25 years). However, a pathophysiological explanation for this observation has not been proposed by either of these studies.

The majority of histopathological studies focused on morphometric cell counting in the putamen have shown a negative correlation between age and cell counts with a substantial preservation of the small to large cell ratios (Bugiani *et al* 1978; Kemper 1994). Similarly, several structural MRI studies of aging using T1-weighted magnetization prepared rapid gradient echo (MP-RAGE), T1-weighted spoiled gradient echo (SPGR) or T2-weighted sequences have demonstrated 16% to 40% decreases in the volume of the putamen in normal elderly subjects (>60 years) compared to a younger population (20-30 years) (Gunning-Dixon *et al* 1998; McDonald *et al* 1991; Nunnemann *et al* 2007; Raz *et al* 2003). Volumetric decreases are more closely associated with reductions in anisotropy of a given structure due to the expected breakdown of the cytoarchitectural integrity, however depending on the course of the pathology where an increase in restrictive barriers to intracellular diffusion and a more tortuous extracellular

space may exist, an elevation in diffusion anisotropy could occur (Sotak 2002). In contrast to the findings of the histopathological and structural MRI studies above, other such reports have either observed a relative preservation of cell density in the putamen with aging (Pesce and Reale 1987) or noted age-related increases in the volume of the putamen on structural MR images (Brickman *et al* 2003; Walhovd *et al* 2005), which could also account for increases in diffusion anisotropy in the putamen with age.

7.6 Concluding Remarks

In conclusion, marked changes of diffusion anisotropy throughout the normal aging brain, particularly in the subcortical white matter of the gyri, are observed although the cognitive relevance is not known since cognitive performance was not measured in our healthy group of individuals. Suppression of contaminating signal from fast, isotropic diffusing CSF is shown to increase fractional anisotropy in numerous brain regions in both the young and the elderly. Hence, in order to avoid potential confounds such as partial volume averaging with CSF and if scanning time permits, CSF-suppressed DTI is recommended for incisive studies of tissue microstructure.

8

THE RELATIONSHIP BETWEEN DIFFUSION ANISOTROPY AND TIME OF ONSET AFTER STROKE*

Serial diffusion MRI studies have demonstrated that lesion evolution is dynamic over the first month of stroke (Beaulieu *et al* 1999; Schlaug *et al* 1997). Apparent diffusion coefficient (ADC) maps reveal low ADC values indicating cytotoxic edema in the acute to sub-acute stage and high ADC values in the chronic stage reflecting necrosis. Although there have been numerous attempts to characterize the changes in white matter (WM) diffusion anisotropy following ischemia in longitudinal and cross-sectional patient studies (Green *et al* 2002; Harris *et al* 2004; Munoz Maniega *et al* 2004; Sorensen *et al* 1999; Yang *et al* 1999), the results are variable and the trend in diffusion anisotropy following an ischemic stroke is not well established. The limitations of these previously published reports are 1) sampling mixed tissue areas (WM and gray matter (GM)) within the region-of-interest (ROI) in the ischemic core, and 2) grouping patient data ≤24 hours of stroke onset, thereby rendering the interpretation of any anisotropy-related trends (within that 24-hour period) as unclear.

This chapter details our results in characterizing the temporal changes of diffusion anisotropy by analyzing anatomically distinct ischemic WM regions at 3 time phases (2-5h, 7-14h and 18-34h) within the first 34 hours of stroke onset in 26 patients.

---

*A version of this chapter has been published. Bhagat YA, Emery DJ, Shuaib A, Sher F, Rizvi N, Akhtar N, Clare T, Leatherdale T and Beaulieu C. (2006). The Relationship Between Diffusion Anisotropy and Time of Onset After Stroke. *Journal of Cerebral Blood Flow and Metabolism*. 26(11):1442-1450.

Iterations of this study have previously been presented at:

1) 13th annual scientific meeting of the International Society for Magnetic Resonance in Medicine. Miami Beach, FL. 2005. 469 (oral presentation)

2) 5th World Stroke Congress. Vancouver, BC. 2004. (p 144; 969) (poster presentation)

8.1 Introduction

The reduction of the apparent diffusion coefficient (ADC) of water within minutes after the onset of cerebral ischemia has made diffusion-weighted imaging (DWI) an indispensable clinical tool for the highly sensitive and specific diagnosis of stroke (Hjort *et al* 2005; Moseley *et al* 1990b; Warach *et al* 1992). ADC remains low for the first few days following the onset of stroke symptoms, pseudonormalizes around 1 week (although this can occur earlier with successful reperfusion (Marks *et al* 1999)), and then is elevated at chronic time points (Fiebach *et al* 2002; Marks *et al* 1999; Schlaug *et al* 1997; Warach *et al* 1995). The increase in ADC values to a normal level at approximately 1 week post symptom onset is referred to as 'pseudonormalization' to indicate that the tissue is damaged, presumably non-viable and can be characterized by a normal ADC but elevated signal intensity on T2-weighted images (Copen *et al* 2001). DWI reversal or ADC normalization in the presence of thrombolytic vessel recanalization as observed on follow-up images of acute stroke patients may be a predictor of tissue salvage (Fiehler *et al* 2004; Kidwell *et al* 2000).

DWI of stroke typically uses data from three diffusion directions to minimize the effects of diffusion anisotropy in ordered tissue such as white matter (WM) and yields maps of mean diffusivity ("Trace ADC") that are quite uniform between gray and white matter. On the other hand, diffusion tensor imaging (DTI), which measures diffusion in a minimum of 6 directions (Basser *et al* 1994a; Basser *et al* 1994b), is better suited for a more comprehensive evaluation of diffusion changes in ischemic WM, and in particular by the degree of diffusion directionality of water within the tissue microstructure (i.e. anisotropy) (Pierpaoli *et al* 1996; Sotak 2002).

A rodent study showed that fractional anisotropy (FA) is elevated during the first hour of ischemia, but then begins to decline over the remaining time course (Carano *et al* 2000). Similar reports of experimental ischemia have showed that diffusion anisotropy is either elevated earlier (Does and Gore 2000) or preserved for 24 hours post onset, after which it decreases progressively (Song *et al* 2003). Diffusion anisotropy, unlike "Trace ADC" which remains consistently low during the first few days following stroke onset, may provide a means of distinguishing, even coarsely, time of onset after stroke.

8.1.1 DTI Based Studies of Stroke

Many attempts have been made at using Diffusion Tensor Imaging (DTI), in particular indices of diffusion anisotropy, to characterize the progression of ischemic lesions within 24 hours and to predict the severity of the ischemic insult and outcome after stroke in humans (Green *et al* 2002; Harris *et al* 2004; Munoz Maniega *et al* 2004; Ozsunar *et al* 2004a; Schaefer *et al* 2003; Sorensen *et al* 1999; Sotak 2002; Yang *et al* 1999). However, studies reporting changes in FA have been variable with either reductions (Munoz Maniega *et al* 2004; Sorensen *et al* 1999), elevations (Schaefer *et al* 2003), a mixture of changes (Green *et al* 2002; Ozsunar *et al* 2004a; Ozsunar *et al* 2004b; Yang *et al* 1999), or no change (Harris *et al* 2004). Elevations of 8-45% in FA have been noted to occur

from <4 hours up to 24 hours post symptom onset (Green *et al* 2002; Ozsunar *et al* 2004a; Schaefer *et al* 2003; Yang *et al* 1999). Interestingly, similar studies have also reported FA reductions of 2-44% in individual patient data from 4 hours up to 27 hours post symptom onset (Green *et al* 2002; Yang *et al* 1999). Although biological variability is certainly plausible, the wide discrepancy in FA results following stroke onset may be analytical in nature arising from the practice of sampling larger regions-of-interest that encompass different types of WM tracts or both WM and gray matter areas within the ROI in the ischemic core (Green *et al* 2002; Harris *et al* 2004; Ozsunar *et al* 2004a; Schaefer *et al* 2003) and/or that patient data from ≤24 hours was grouped for analysis thereby obscuring any time-dependent trends (Munoz Maniega *et al* 2004; Sorensen *et al* 1999).

8.1.2 Goal of the study

The purpose of this study was to characterize changes of diffusion anisotropy in the early phases of human stroke by focusing on discrete WM tracts within the infarcts (due to differences in normal FA values of various WM regions (Pierpaoli *et al* 1996)), and separating patient data into three distinct time phases post stroke, namely hyperacute (2-5h), acute (7-14h) and subacute (18-34h).

8.2 Methods

Twenty-six patients (15M, 11F; mean age = 66±17 years) presenting with a non-hemorrhagic acute ischemic stroke within 34 hours of onset were enrolled in the MRI study after CT scanning and standard treatment (Table 8-1). Only patients with known times of onset were included in this study. Ten patients were administered with drug treatment within 3 hours of symptom onset (38%), including 8 patients with intravenous tissue plasminogen activator (rt-PA), 1 patient with rt-PA and the neuroprotectant, ONO-2506 (Merck & Co.), and 1 patient who was entered into the SAINT-II trial involving a 72-hour intravenous infusion of Cerovive (AstraZeneca Pharmaceuticals). MRI protocols were approved by the Human Research Ethics Board and written informed consent was obtained from all patients or their next of kin.

Table 8-1: Characteristics of Patient Population

Patient No.	Sex/Age (yr)	Treatment	Arterial Distribution	Lesion Location		Time of MRI (hr)	NIHSSS	Lesion Volumes (cm^3)		
				Major WM Tracts	Subcortical WM Tract Involvement			Total	Major WM Tracts	Subcortical WM Tracts in Gyri
1	M/51	None	L MCA	GCC, CS, CR, AIC, EC, OT	Yes	2	24	84.0	8.2	49.1
2	F/71	None	R PCA/ MCA	CF, PIC, CR	Yes	3	30	101.3	44.8	12.6
3	F/49	None	Cerebellum	CF	No	4	5	3.8	3.8	------
4	F/28	None	R MCA	AIC, PIC, EC, CS	Yes	5	10	40.0	9.0	14.7
5	M/44	rt-PA	L MCA	EC, CR	No	5	14	1.0	0.2	------
6	M/71	None	L MCA	None	Yes	5	7	0.5	----	0.5
7	F/83	None	RMCA	EC, PIC, CR	Yes	5	15	35.5	4.5	20.2
8	F/82	rt-PA	R PCA	EC	Yes	7	20	14.5	1.0	5.0
9	M/64	rt-PA	R MCA	AIC, EC, CR, CS	Yes	7	18	177.5	8.4	60.2
10	M/72	None	LMCA	CS	Yes	9	7	7.0	1.3	2.7
11	M/55	None	Pontine Perforation	ML	No	9	7	0.1	0.1	------
12	M/82	None	R ACA	CS	Yes	9	4	5.5	1.8	1.3
13	F/41	rt-PA and ONO	L MCA	CC, CR, CS	Yes	9	16	29.1	1.2	20.3
14	M/68	None	L MCA	EC, AIC, PIC, CR, CS	Yes	10	20	16.5	8.3	1.6
15	M/46	None	Deep WM Perforating Vessel	CS	No	11	5	1.0	0.4	------
16	M/79	None	Deep WM Perforating Vessel	CS, CR	No	13	6	0.3	0.3	------
17	F/79	rt-PA	Midbrain	CP	No	14	19	1.0	0.2	------
18	M/87	rt-PA	R MCA	CS, CR, EC, Claustrum	Yes	14	13	36.1	5.2	12.7
19	F/80	rt-PA	R MCA	None	Yes	18	9	6.0	----	3.3
20	M/72	rt-PA	R MCA	None	Yes	19	19	8.4	----	8.2
21	M/91	None	R MCA	None	Yes	20	5	12.7	----	12.4
22	M/51	rt-PA	R MCA	AIC, EC, CR, CS	Yes	21	18	10.0	1.6	0.6
23	M/87	None	R MCA/ L MCA (multiple emboli)	None	Yes	24	6	3.1	----	2.7
24	F/69	None	LMCA	PIC, EC, CR	No	27	14	2.7	2.7	------
25	F/58	SAINT	R MCA	CS, CR, EC, PIC	Yes	29	13	11.0	6.2	1.0
26	F/64	None	R MCA	CS, CR, EC	Yes	34	8	13.7	2.5	6.0

rt-PA, tissue plasminogen activator; ONO, ONO-2506 treatment; SAINT, SAINT-II trial Cerovive treatment; PCA, posterior cerebral artery; MCA, middle cerebral artery; ACA, anterior cerebral artery; WM, white matter; NIHSSS, National Institutes of Health Stroke Scale Score. GCC, genu of corpus callosum, CS, centrum semiovale; CR, corona radiata; AIC and PIC, anterior and posterior limb of internal capsule; EC, external capsule; OT, optic tract; CF, cerebellar fibers; ML, medial lemniscus; CC, corpus callosum; CP, cerebral peduncle.

8.2.1 MRI Acquisition and Post-processing

DTI was part of a 20-min stroke protocol performed on a 1.5T Sonata scanner (Siemens Medical Systems, Erlangen, Germany). Single-shot diffusion weighted, twice-refocused spin-echo echo planar imaging (EPI) (Reese *et al* 2003) was used for DTI with: TR/TE/NEX = 3.2s/88ms/8, 96x128 matrix zero-filled to 256x256, 22cm FOV, 6/8 phase partial Fourier, and twenty 5mm-thick contiguous axial slices aligned with the anterior and posterior commissures, b = 0 s/mm^2 and six sets with b = 1000 s/mm^2. Additionally an EPI based T2*-weighted sequence (EPI-GMWM) was also performed to highlight distinct gray and white matter regions (to assist with ROI placement) with: TR/TE/TI/NEX = 5.5s/57ms/200ms/4, and with an identical matrix, FOV, and slice coverage as DTI. The acquisition time was 3:04min for DTI and 57secs for EPI-GMWM. Raw data was post-processed off-line to yield maps of the eigenvalues λ_1, λ_2, and λ_3, Trace/3 ADC, and FA using MRVision (Winchester, MA). Details of the image processing steps are outlined in Appendix 1.1. The eigenvalues yield directional ADC values along the length of the fiber tracts (λ_1) or perpendicular to them (λ_2, λ_3) and FA is a parameter highlighting deviations from isotropic diffusion and ranges from 0 for perfect isotropic diffusion to 1 for highly anisotropic diffusion.

8.2.2 Regions of Interest Analysis

Discrete WM regions within the acute ischemic lesion (defined by ≥30% drop in Trace/3 ADC relative to the contralateral side) were traced using a free hand ROI with the aid of the EPI GMWM images and FA maps. A semi-automated procedure was used to threshold the ADC maps and all ROI traces were cross-referenced with b=0 s/mm^2 images to avoid inclusion of obviously visible cerebrospinal fluid. The ROIs for all patients were rigorously drawn by the same non-blinded individual (Y.A.B.). Measurements of FA, λ_1, λ_2, λ_3, and T2-weighted (wt) signal intensity (measured on b=0 s/mm^2 images) of the corresponding WM in the normal contralateral hemisphere were used as a reference. Individual tracts had to be measured separately given the wide range of absolute FA values in normal WM. For example, major central WM tracts such as the corpus callosum, internal capsule, etc. demonstrate an FA range of 0.41-0.72, whereas peripheral subcortical gyral WM areas have FA values of 0.37-0.42 in elderly healthy controls (Table 7-2, Chapter 7).

Relative (r, ipsilateral/contralateral) values were computed per ROI in order to combine data from different tracts within and between individuals. Absolute FA values even of specific tracts from different patients could not be combined because of the known variability of FA with age (28-91 years in our cohort) (Moseley 2002). All slices demonstrating the lesion were analyzed since this provides a more representative measure of the diffusion parameters than on a single slice alone. Data was separated into categories of major WM tracts and peripheral subcortical WM (in the gyri). Relative values for each ROI measurement per patient were averaged over all patients within a distinct time phase, with respect to the two tissue categories, to facilitate group comparisons between the hyperacute (2-5h), acute (7-14h) and subacute (18-34h) phases

of stroke. Selection of the range of times post onset for the 3 phases was arbitrary, with 6h being the cut-off for the hyperacute group. The percentage of total ROIs showing changes in rFA were calculated per patient (also averaged over all patients per time phase), where significant increases or decreases were considered to be ±10% of contralateral values. Intermediate values within this range were regarded as demonstrating no relative change in FA.

8.2.3 Statistical Analysis

Paired t-tests were used to analyze differences between the ipsilateral and contralateral Trace/3 ADC, FA, λ_1, λ_2, λ_3, and T2-wt signal intensity ($p<0.05$). Linear regression analyses were performed with Pearson's correlation coefficient and significance level of the F test to assess correlations between rT2-wt signal intensity versus rFA across the entire time course. Results were considered statistically significant at levels of $p<0.05$.

8.3 Results

Fourteen patients had involvement of both major and subcortical (in the gyri) WM tracts and out of the remaining 12, 7 had only major WM tracts and 5 had only subcortical gyral WM areas within the Trace/3 ADC-defined infarct (Table 8-1). Figure 8-1 displays example image sets containing EPI T2-weighted (mean signal-to-noise ratio (SNR) of 92 ± 11 in normal subcortical WM on b=0 s/mm^2 images), DWI, Trace/3 ADC and FA images from the hyperacute (2 hours) and acute (14 hours) phases of stroke onset, respectively. Although regions of elevated FA are apparent, albeit subtle in the hyperacute group (see Figure 8-2), quantitative ROI analysis is required to investigate the FA differences within the lesion relative to the homologous contralateral WM structure.

The absolute mean Trace/3 ADC values of the infarcts and the corresponding normal contralateral regions for major WM tracts were 0.45 ± 0.08 x 10^{-3} mm^2/s and 0.76 ± 0.07 x 10^{-3} mm^2/s in the hyperacute phase, 0.46 ± 0.09 x 10^{-3} mm^2/s and 0.81 ± 0.08 x 10^{-3} mm^2/s in the acute phase, and 0.48 ± 0.10 x 10^{-3} mm^2/s and 0.78 ± 0.08 x 10^{-3} mm^2/s in the subacute phase, respectively. Similar ipsilateral and contralateral Trace/3 ADC values were observed for subcortical WM (in the gyri) as well. The absolute FA values in the normal contralateral hemisphere were 0.38 ± 0.05 for the external capsule, 0.50 ± 0.08 for the anterior limb of the internal capsule, 0.57 ± 0.06 for the posterior limb of the internal capsule, 0.50 ± 0.09 for the corona radiata, 0.42 ± 0.08 for the centrum semiovale, and 0.36 ± 0.07 for subcortical gyral WM tracts. Subsequent ipsilateral FA values from lesions are presented as relative values to these due to the different WM tracts within the ischemic lesion.

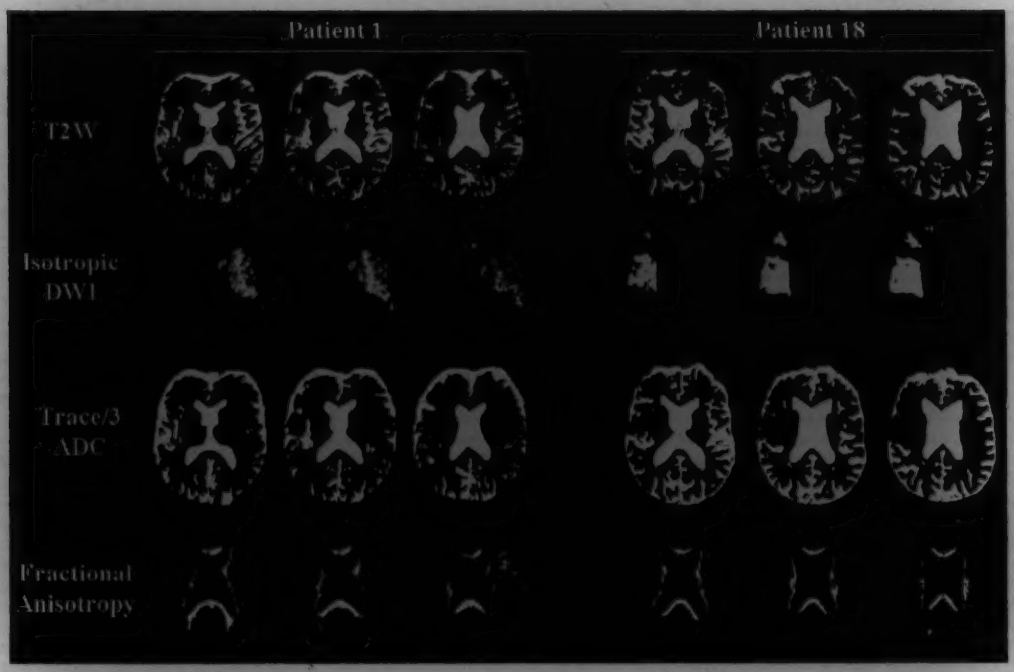

Figure 8-1: Representative set of T_2-weighted images (T2W; b = 0 s/mm^2), isotropic diffusion-weighted images (DWI; b = 1000 s/mm^2), Trace/3 ADC maps, and FA maps from 2 patients depicting hyperacute (Patient 1; 2 hours post symptom onset) and acute (Patient 18; 14 hours post symptom onset) infarcts in the MCA distribution involving major WM tracts and subcortical WM regions (refer to Table 8-1). Over 19 slices in patient 1 (51 year-old male), 75% of the major WM ROIs evaluated showed an increase in rFA whereas 25% showed reductions in rFA. For subcortical WM in patient 1, 88% of the ROIs demonstrated an increase in rFA, 3% showed reductions, and 9% remained constant. In contrast, over 11 slices in patient 18 (87-year old male), 0% of the ROIs evaluated for major WM tracts revealed an increase in rFA, whereas 57% showed reductions, and 43% remained constant, respectively. For subcortical WM in patient 18, 7% of the ROIs showed increases in rFA, 64% demonstrated decreases in rFA and 29% remained constant.

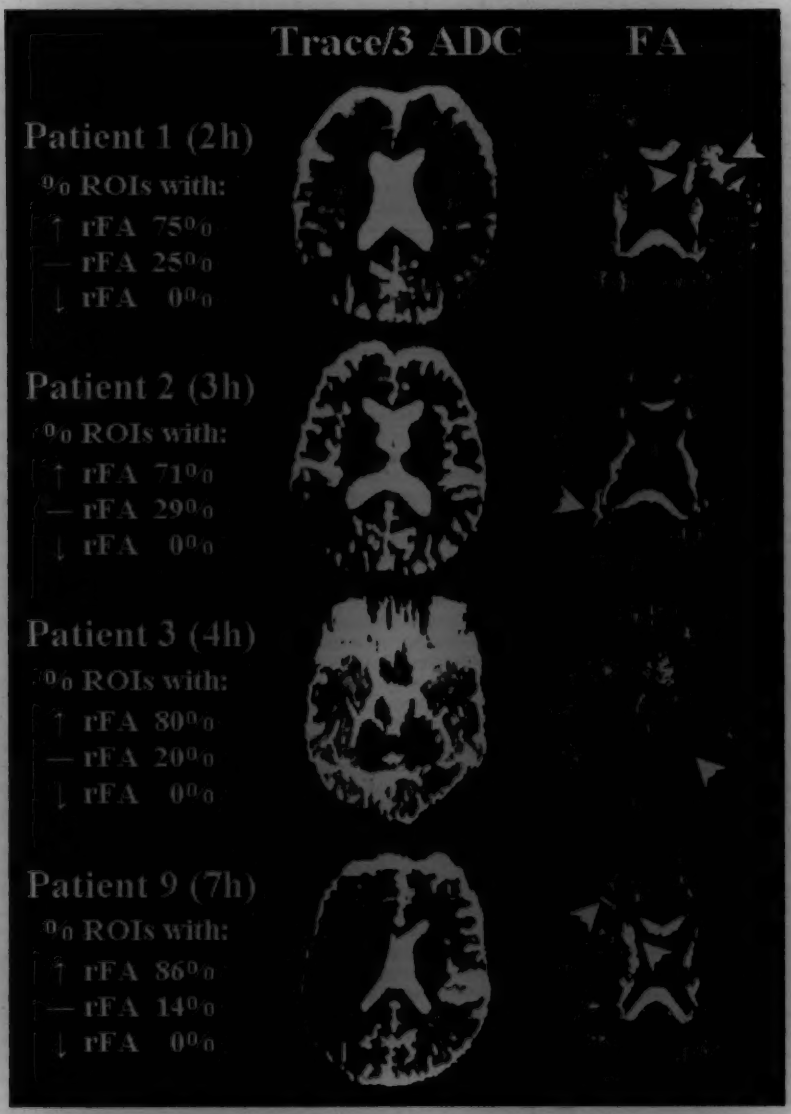

Figure 8-2: Representative sets of Trace/3 ADC and FA maps from 4 patients with elevated relative (r) FA values in major white matter tracts ≤7 hours post symptom onset. Refer to Table 8-1 for patient details. The arrowheads on the FA maps point to regions within the ischemic core where FA values were greater than those on the normal contralateral side. The percentage of ROIs with increased (↑), decreased (↓) or constant (—) rFA values are listed for major WM tract lesions only. The mean rFA values were 1.19 ± 0.18 (Patient 1), 1.14 ± 0.10 (Patient 2), 1.25 ± 0.27 (Patient 3), and 1.24 ± 0.09 (Patient 9). Note that the contrast of the FA maps has been made extreme in order to visualize the elevated FA.

8.3.1 Diffusion Anisotropy in Major WM Tracts

The time course of relative FA (i.e. rFA, ipsilateral FA/contralateral FA) and rTrace/3 ADC changes in 21 patients with lesions involving major WM tracts is displayed in Figures 8-3A and 8-3B. Although Trace/3 ADC was consistently low (~40% decrease), an increase in rFA was observed in the first 3 patients between 2 and 4 hours post onset. Of the three patients at 5 hours post onset, two showed constant FA values and one demonstrated reduced rFA. Of the two patients at 7 hours post onset, one demonstrated elevated FA and the other reduced FA values; however no elevations in mean rFA were noted in the major WM tracts of any patient after 8 hours post symptom onset (Figure 8-3A). Lesions demonstrated an average rFA of 1.11 ± 0.18 ($p<0.01$) during the hyperacute (2-5h) phase (Figure 8-5A), whereas in the acute (7-14h) and subacute (18-34h) phases, rFA declined to 0.90 ± 0.20 ($p<0.01$) and 0.88 ± 0.12 ($p<0.01$), respectively. It is interesting to note that 60% of the evaluated WM ROIs in the hyperacute phase showed an increase in rFA as opposed to only 17% or 0% of the ROIs evaluated at the acute and subacute phases, respectively (Figure 8-6A). Furthermore, 55% and 59% of the ROIs demonstrated reductions in rFA at the acute (7-14h) and subacute (18-34h) phases respectively, as opposed to only 7% at the hyperacute (2-5h) time-point.

Interrogation of the eigenvalues is useful to understand the basis of changes in FA since the latter is calculated from the eigenvalues. On average, in the 4 patients that showed significantly elevated FA in major WM tract lesions from 2-7 hours post onset (Figure 8-3A), the relative principal (λ_1), secondary (λ_2) and tertiary (λ_3) eigenvalues declined by 37%, 40% and 49%, respectively (Table 8-2). The steeper decline of $r\lambda_3$ relative to $r\lambda_1$ and $r\lambda_2$ ($p<0.01$) accounts for the increased FA. In 13 patients demonstrating reduced FA in major WM tracts from 9-34 hours post onset (Figure 8-3A), $r\lambda_1$, $r\lambda_2$, and $r\lambda_3$ declined by 47%, 37%, and 34% respectively. Here, a ~11% greater reduction in $r\lambda_1$ relative to $r\lambda_2$, and $r\lambda_3$ explains the decrease in FA. Relative rT2-weighted signal intensity was also elevated by 11%, 18%, and 21% from the hyperacute to the subacute phase ($p<0.01$) (Figure 8-5A), with an inverse correlation between mean rFA and rT2-weighted signal intensity ($R=-0.37$, $p<0.01$) (Figure 8-7A).

Table 8-2: Mean (±SD) ipsilateral and contralateral eigenvalues (λ_1, λ_2 and λ_3) in select patients from 2-7 hours after stroke demonstrating elevated relative FA values in major WM tracts (4/8 patients) and subcortical WM (in the Gyri, 4/7 patients)

	Major WM (2-7h; N=4)				Subcortical WM (2-7h; N=4)			
	Contralateral	Ipsilateral	%DIFF[a]	p	Contralateral	Ipsilateral	%DIFF[a]	p
λ_1	1.14 ± 0.11	0.71 ± 0.11	37%	<0.01	1.15 ± 0.17	0.65 ± 0.13	43%	<0.01
λ_2	0.76 ± 0.13	0.46 ± 0.14	40%	<0.01	0.82 ± 0.15	0.46 ± 0.12	42%	<0.01
λ_3	0.49 ± 0.08	0.25 ± 0.05	49%	<0.01	0.53 ± 0.11	0.26 ± 0.08	51%	<0.01

Values are $x10^{-3}$ mm^2/s; [a]%DIFF, % difference between ipsilateral and contralateral eigenvalues

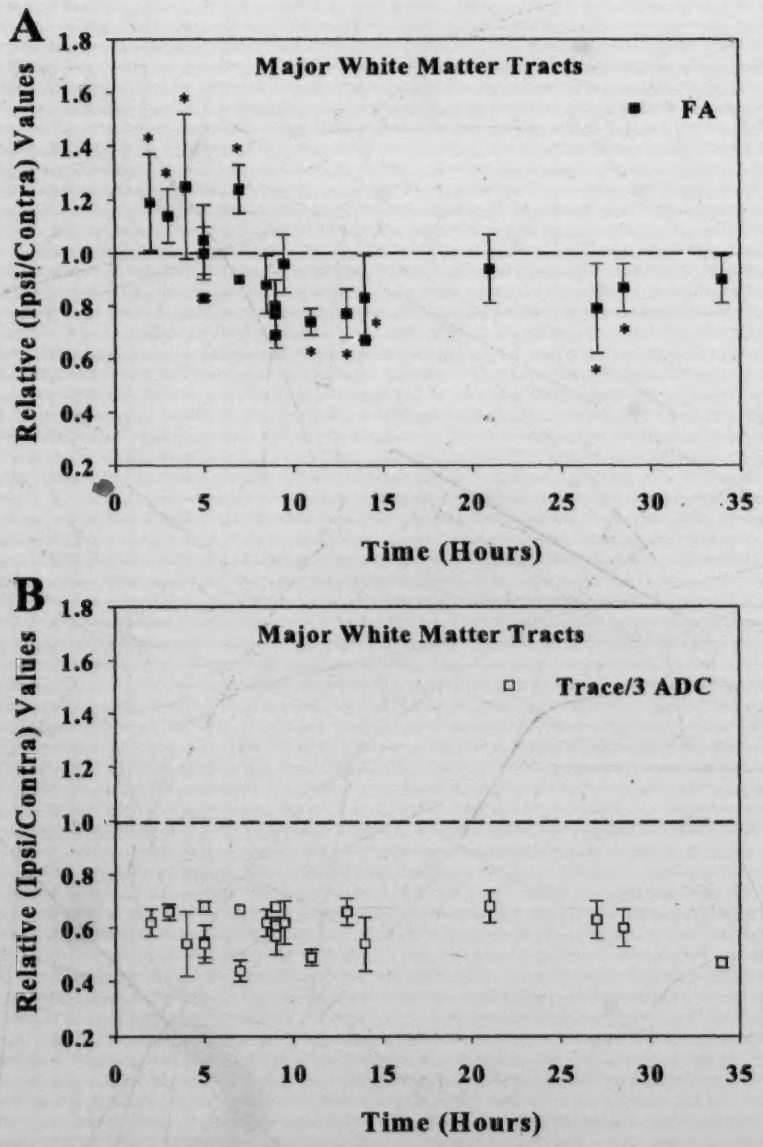

Figure 8-3: Time course of relative (r) FA (A) and Trace/3 ADC (B) changes in major WM tracts in 21 patients following ischemic stroke onset. The error bars reflect the standard deviation over the ROIs measured for each patient. * denotes significant differences between ipsilateral and contralateral FA values for each patient. (A) Significant increases of rFA in major WM tracts were observed at 2-4 hours and 7 hours post symptom onset, whereas rFA was typically reduced at later time points. (B) Relative Trace/3 ADC was predominantly lower (~40% reduction) in all patients, across all time points observed ($p<0.05$).

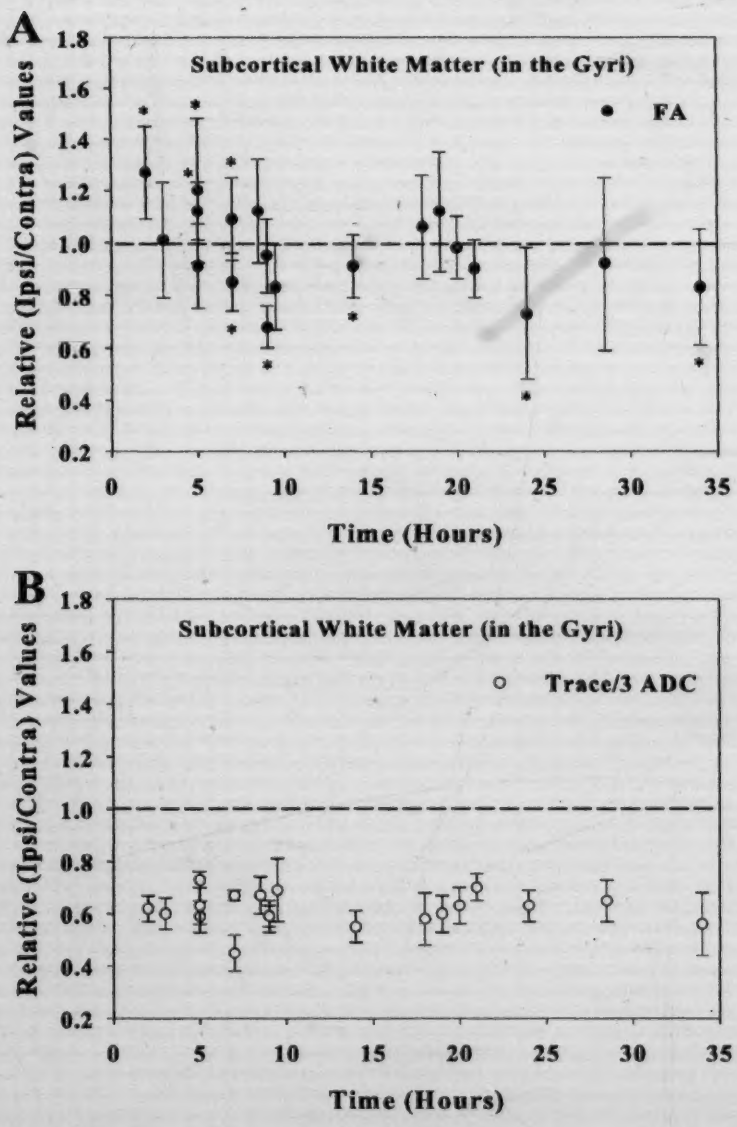

Figure 8-4: Time course of relative (r) FA (A) and Trace/3 ADC (B) changes in subcortical WM (in the Gyri) in 19 patients after ischemic stroke. The error bars reflect the standard deviation over the ROIs measured for each patient. * denotes significant differences between ipsilateral and contralateral FA values for each patient. (A) The results in subcortical WM in the gyri were more variable compared to major WM tracts but 3/5 patients at ≤5 hours and 1/2 patients at 7 hours showed increases in rFA. (B) Relative Trace/3 ADC was predominantly lower (~40% reduction) in all patients, across all time points observed ($p<0.05$).

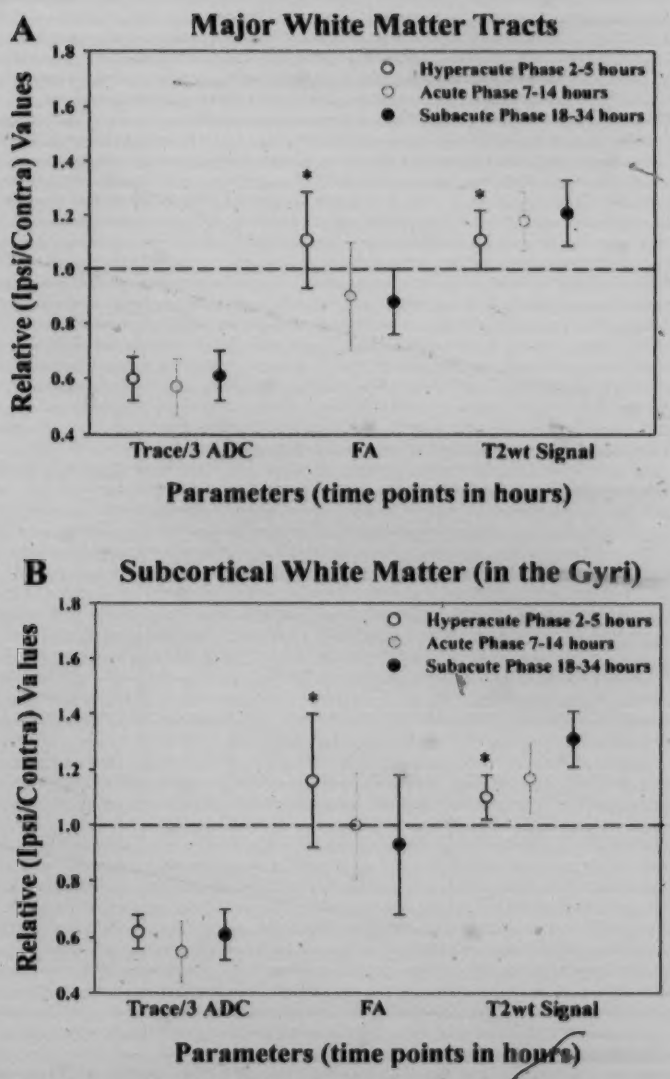

Figure 8-5: Comparisons of the mean ± SD values (all ROIs measured in 26 patients) for relative (r) Trace/3 ADC, FA and T2-weighted signal intensity in (A) ischemic major WM tracts and (B) subcortical WM (in the gyri) for the hyperacute (2-5 hours, N=7), acute (7-14 hours, N=11) and subacute (18-34 hours, N=8) phases following stroke onset. Ipsilateral versus contralateral values for all three parameters were statistically significant ($p<0.05$) for both WM tract groups at all time phases. In both, major and subcortical WM tracts, rTrace/3 ADC was reduced by ~40% in the hyperacute phase and remained consistently low during the acute and subacute phases. However, rFA values increased hyperacutely, but were subsequently reduced in the acute and subacute periods. Conversely, a steady increase in T2-weighted signal was noted from the hyperacute to the subacute phase in both tissues. * denotes significant ($p<0.05$) differences between the hyperacute and acute/subacute groups.

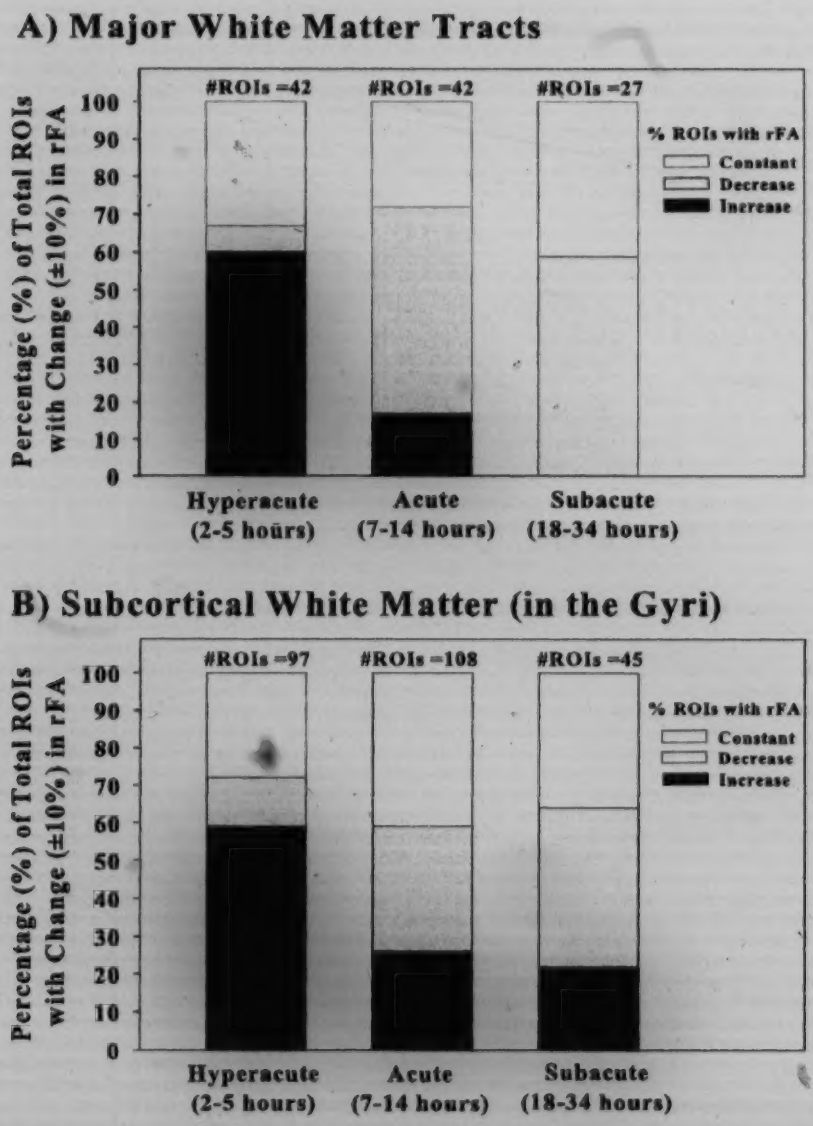

Figure 8-6: Percentage of (A) major and (B) subcortical WM (in the gyri) tracts with either increase, decrease, or no change of rFA in 26 patients. In both major and subcortical WM tracts, ~60% of the ROIs showed an increase in rFA in the hyperacute phase. Although a greater proportion of the ROIs (~37% to 57%) in the acute and subacute phases were characterized by reduced rFA, a small proportion of ROIs (~17% to 24%) showed elevated rFA in mainly subcortical WM for both time phases.

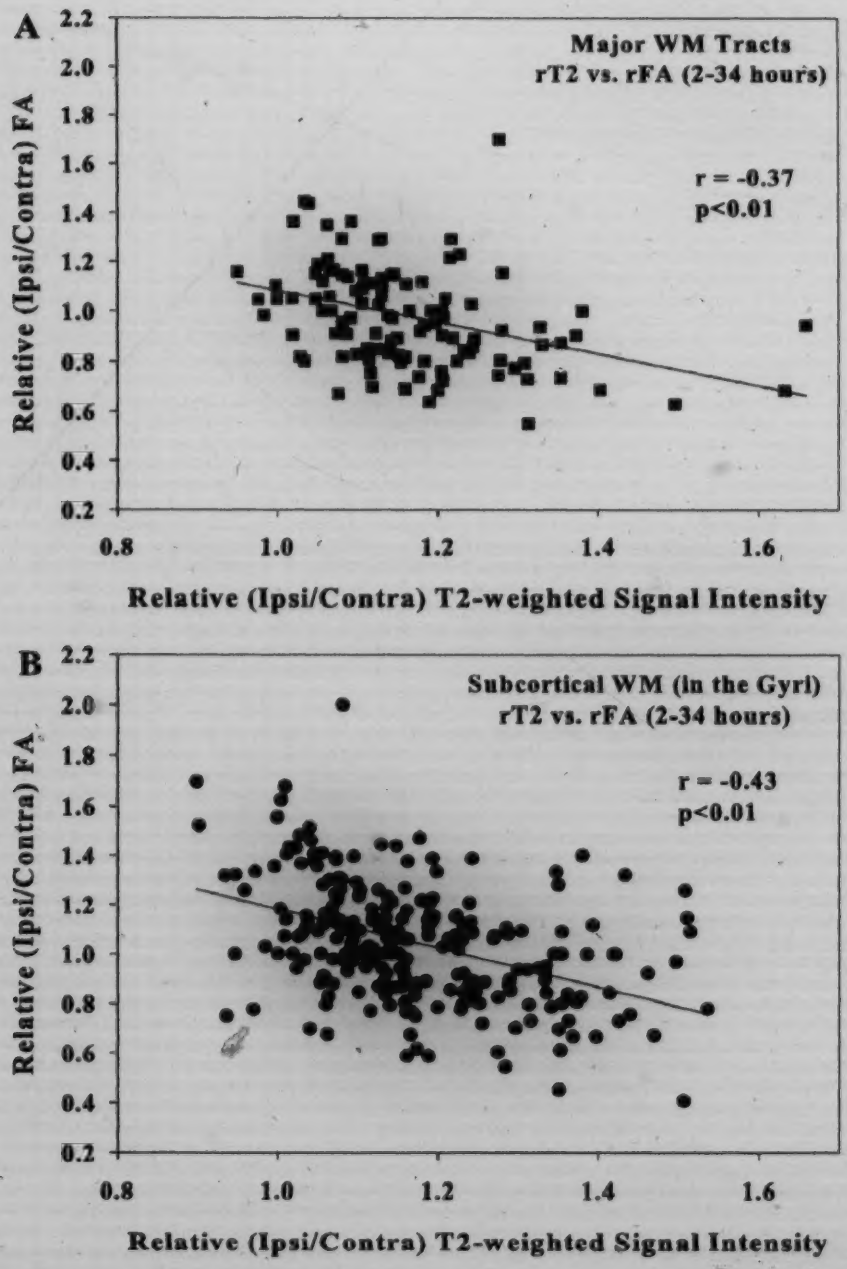

Figure 8-7: Trends of rT2-weighted signal intensity versus rFA in major WM tracts (A) and subcortical WM (in the Gyri) (B) from 2-34 hours following stroke in 26 patients.

8.3.2 Diffusion Anisotropy in Subcortical WM (in the Gyri)

Trends of rFA and rTrace/3 ADC values for lesions involving subcortical WM in 19 patients are displayed in Figures 8-4 (A, B). Although Trace/3 ADC remained consistently low, FA was elevated in 3/4 patients within 5 hours post symptom onset. A significant increase in rFA was also noted at 7 hours post onset (patient 9), however, after that time point, no significant elevations were observed throughout the time course. Also within the first 7 hours post symptom onset, one patient at 3 hours showed constant FA values and two patients at 5 hours and 7 hours demonstrated reduced FA values. Grouping the individual patient data in discrete time points, subcortical WM regions (with some variability) demonstrated changes in rFA similar to major WM tracts with increases in mean rFA hyperacutely (1.16 ± 0.24, $p<0.01$), and reductions subacutely (18-34h; 0.93 ± 0.25, $p=0.01$) (Figure 8-5B). Interestingly, 59% of the WM ROIs in the hyperacute phase showed increased rFA values, as opposed to 26% or 22% at the acute and subacute phases, respectively (Figure 8-6B). Correspondingly, 33% and 42% of the ROIs demonstrated reductions acutely and subacutely, as opposed to only 13% at the hyperacute (2-5 h) time point.

The alterations in eigenvalues (Table 8-2) and correlation between rFA and rT2-weighted signal intensity ($R=-0.43$, $p<0.01$) (Figures 8-5B and 8-7B) for subcortical WM were similar to those observed for major WM tracts.

8.4 Discussion

This report details our findings on the alterations of water diffusion (Trace/3 ADC, FA and eigenvalues) from 2-34 hours following ischemic stroke onset in 26 patients. For major white matter tracts, diffusion anisotropy was elevated in 4/8 patients ≤7h after stroke onset (mean rFA = 1.20 ± 0.16 ($p<0.01$) in these 4 patients) and 0/13 patients >7h. Subcortical white matter in the gyri demonstrated similar elevated rFA findings with 4/7 patients ≤7h (mean rFA = 1.17 ± 0.21 ($p<0.01$) in these 4 patients) and 0/12 patients >7h. Our findings are in agreement with five human DTI studies that have reported elevations of FA less than 6 hours (13-21% rise) (Green *et al* 2002; Ozsunar *et al* 2004a; Ozsunar *et al* 2004b; Schaefer *et al* 2003; Yang *et al* 1999). However, one study had 3 patients less than 6 hours with one showing elevated FA (Green *et al* 2002), and another acquired only 3-direction diffusion-weighted images in the majority of their patients (Yang *et al* 1999).

Three of the aforementioned studies used an ROI analysis method that was not specific for measuring FA changes in different fractions of WM and GM within the lesion (Green *et al* 2002; Ozsunar *et al* 2004a; Schaefer *et al* 2003), despite the large FA differences between these two tissue classes and the difficulty in matching the gray/white proportion in a contra-lateral ROI. Although Ozsunar *et al.* demonstrate that 9/15 patients within 6h show elevated FA, their "mixed" tissue is evident in their low mean absolute FA value of 0.33. The other two reports employed a tissue classification scheme based on segmenting lesions as WM, GM or mixed regions (GM and WM) (Ozsunar *et al* 2004b; Yang *et al* 1999). However, the problem with this segmentation is that there are large variations of

FA even within healthy white matter. In our report, we overcame these limitations by measuring unique white matter tracts separately within the lesion and in the homologous contralateral white matter.

8.4.1 Comparison with Previous DTI based Stroke Studies

Serial human stroke studies by Zelaya *et al.* and Munoz Maniega *et al.* have identified a decreasing trend of FA (~8-54% decreases) from <24 hours to 90 days post onset (Munoz Maniega *et al* 2004; Zelaya *et al* 1999). Sorensen *et al.* focused on characterizing FA between WM and GM within 24 hours following stroke, and noted a decline (14% drop) of FA in WM relative to GM (Sorensen *et al* 1999) for similar decreases of ADC in both tissues. Our data agree with these previous human reports in that we note consistent FA reductions of 6-14% throughout the 9-34 hour time period (Figures 8-3, 8-4 and 8-5). In contrast two studies have reported elevated FA at much later times, namely up to 27 hours (Green *et al* 2002) and 96 hours (Yang *et al* 1999). Although averaging all the ROIs for a particular patient demonstrated none with elevated rFA after 7h in our study, 3% and 18% of individual ROIs from major and subcortical WM tracts demonstrated increased FA values over their homologous contralateral ROI from 9-34h. In the context of human stroke, reductions in FA are more severe at much later time points of 2 days to 1 year post onset within the infarct (~40-70% decreases) and in regions downstream from the infarct such as the internal capsule, pons and cerebral peduncles (~8-39% decreases) (Buffon *et al* 2005; Pierpaoli *et al* 2001; Thomalla *et al* 2004; Thomalla *et al* 2005; Werring *et al* 2000; Zelaya *et al* 1999).

DTI studies in animal models of ischemia appear to support our elevated FA results in the hyperacute phase and the reductions observed in the acute and subacute phases. Carano *et al.* reported an acute elevation of FA in subcortical and cortical regions (~20% rise) as early as 1 hour following middle cerebral artery occlusion in rats, with a progressive decline of ~25-40% noted by 3 hours up to 5 days post stroke (Carano *et al* 2000). In another study, Does and Gore suggested that diffusion anisotropy is slightly elevated 10 minutes post-mortem in the trigeminal nerve of a 'global ischemia' rat model (Does and Gore 2000). In their study, greater reductions in ADC values measured perpendicular to the nerve (26-31% drops) relative to ADC values measured parallel to the nerve (14-19% drops) accounted for the increased anisotropy. These findings are analogous to those we report for steeper reductions in $r\hat{\lambda}_3$ relative to $r\lambda_1$ in the 4 patients demonstrating elevated FA ≤7h post onset (Table 8-2). A further restriction of water movement perpendicular to the fiber direction, and the subsequent elevations in anisotropy, could be interpreted that cellular swelling (either axons or the cells between the axons) causes both (i) more water to be restricted in the axoplasm environment and (ii) an increased extracellular tortuosity because of less spacing between the myelin fiber bundles (Sotak 2002). A recent analytical modeling study of diffusion in WM predicted an ~29% increase in anisotropy during cytotoxic edema, which was attributed to changes in the microstructural geometrical properties of the WM; it was suggested that the degree of anisotropy is largely determined by the extraaxonal dimensions (Sen and Basser 2005).

Although the Trace/3 ADC, indicative of cellular swelling, remains consistently low throughout our entire time span of 2 to 34 h (Figures 8-3B, 8-4B and 8-5), the anisotropy is not elevated but rather appears to be slightly reduced for subjects after 8 h post stroke onset. Progressive loss of diffusion anisotropy has been observed in animal models of cerebral ischemia (Carano *et al* 2000) or retinal ischemia (Song *et al* 2003). In this latter study, the early decrease of anisotropy was because of a reduction in parallel diffusion ($\lambda_{//}$ or λ_1) with preservation of perpendicular diffusion ($\lambda_\perp = (\lambda_2 + \lambda_3)/2$), whereas later, more substantial decreases of anisotropy were mainly because of increases in perpendicular diffusion. It was proposed that the parallel and perpendicular eigenvalues themselves may hold promise as specific markers of axonal and myelin injury, respectively. Along these lines, we noted greater declines in $r\lambda_1$ compared with $r\lambda_2$ and $r\lambda_3$ in the ischemic major WM of 13 patients who showed reduced FA from 9 to 34 h after onset. These observations are similar to an earlier study where FA values were reduced < 24 h after stroke onset because of a greater decrease in λ_1 compared with λ_2 and λ_3 in ischemic WM (Sorensen *et al* 1999). Therefore, it is possible that these small reductions in λ_1 and FA are reflecting early axonal injury after stroke. However, as we do not have follow-up scans on our patients, we cannot comment at this time on whether these parameters have a predictive role for ischemic tissue outcome.

8.4.2 Limitations of the Study

The main limitations of the present study are the low number of patients early after stroke onset and the cross-sectional design, whereas serial scans would have been preferable. Although the number of patients is small, 6/9 patients within 7 hours post symptom onset showed elevated FA in ischemic lesions (defined by at least 30% reduction in Trace/3 ADC) in either major WM or subcortical WM of the gyri. In addition to our good quality FA maps, further refinements in the image analysis relative to previously published reports yields confidence to the observation of early elevated FA in human stroke. Although free-hand ROI analysis is user-dependent, the same methods were used for all patients and the boundaries of the analysis were automated by a ≥30% drop in mean diffusivity. A free-hand ROI method is best suited for acquiring FA values from specific WM structures within an infarct. A semi-automated FA threshold method would not work given the range of FA values in various healthy white matter tracts.

Unlike Schaefer et al (2003), we did not measure FA in regions outside the ADC-defined lesions, namely in areas of perfusion–diffusion mismatch. Notably, in the 9 patients ≤7 h in our study (where we note elevations in rFA), 4 showed a perfusion > diffusion mismatch (patients 1, 2, 4, and 5), 3 showed a perfusion-diffusion match (patients 6, 7, and 9), 1 showed a perfusion < diffusion mismatch, and 1 showed no perfusion abnormality (on time-to-peak) at all. Another practical limitation of our study in the era of aggressive stroke therapy is that 10 of the patients were treated with either rtPA (N= 8), a neuroprotectant (N= 1), or both (N= 1) (Table 8-1). We do not believe that these have had marked effects on our study as (a) the 2 neuroprotective and 5 of the rtPA patients were scanned after 7 h where no elevations in rFA are observed and the reduced rFA findings are rather consistent, and (b) of the 3 patients ≤7h who had rtPA and major

WM tract involvement, 2 showed constant rFA values (patient 5, perfusion > -diffusion mismatch; patient 8, no perfusion lesion) and 1 showed increased rFA (patient 9, perfusion– diffusion match). If the treatment had altered the natural progression of the lesion, it may not have changed our results much as we limited our analysis to the region with markedly reduced Trace/3 ADC.

8.4.3 Re-evaluation of Statistics for Multiple Group Comparisons

In this cross-sectional stroke study, we compared relative FA and T2-weighted signal intensity values for major and subcortical WM regions between the hyperacute, acute and subacute phases post stroke using unpaired t-tests. The use of multiple t-tests may be a simplistic statistical method for this purpose and increases the likelihood of encountering a Type I error where a false significant effect can be obtained when there is none (Zou *et al* 2003). Ideally a one-way analysis of variance (ANOVA) should be used to compare the means of more than two distributions. In this manner, the means of two or more independent groups can be evaluated to determine the relative variability between the groups compared with the variability within the groups. To rectify our previous analysis, we performed a one-way ANOVA with repeated measures on the relative FA and T2-weighted signal intensity values to determine statistical significance between the hyperacute, acute and subacute time periods following stroke onset. If a significant ($p<0.05$) difference between any of the time periods was noted, post hoc analyses were performed using the Bonferroni t-test for pair-wise comparisons (Tello and Crewson 2003).

In terms of rFA values, for major WM tracts we observed a 21% difference ($p<0.01$) between the hyperacute and acute phases (Figure 8-5A) and a 23% difference ($p<0.01$) between the hyperacute and subacute periods post stroke. Similar findings were also noted in subcortical WM when comparing rFA values between the three phases. In terms of rT2-weighted signal intensity, for major WM tracts we saw a 7% increase ($p<0.01$) in mean rT2-weighted signal intensity from the hyperacute to the acute phase and a 10% increase ($p<0.01$) from the hyperacute to the subacute period. Similar findings for rT2-weighted signal intensity were seen in subcortical WM between the 3 time phases post stroke.

8.5 Concluding Remarks

Multiple MR parameters, including ADC, FA, T2, and perfusion maps in the study of cerebral ischemia, may hold the potential to better identify ischemic tissue and its fate. The role of anisotropy in the evaluation of acute (<24 h) ischemic lesions is not firmly established, but FA may serve as a potential marker for classifying symptom onset in the clinical realm, especially in instances where the time of onset comes into question. The limitations of using FA for timing the onset of stroke or possibly predicting irreversible damage are that, unlike Trace/3 ADC, FA maps are non-uniform, making the visualization of acute lesions challenging, and also that changes are not apparent on FA

maps unless quantitative measurements are undertaken. Although there are challenges to overcome, quantitative DTI may yet play a role in the diagnosis and prognosis of the acute stroke patient. Due to their homogeneous character, DTI generated maps of Trace/3 ADC can aid in the visualization of ischemic lesions and help quantify reductions in ADC relative to the contralateral hemisphere. Maps of FA can yield tissue-specific measures of diffusion anisotropy relative to the non-affected hemisphere which can be used to infer the severity of the lesion and possibly predict the time of onset following symptoms.

9

COMPARISON OF GRAPPA AND mSENSE FOR DIFFUSION TENSOR IMAGING*

While EPI is one of the fastest types of imaging sequences in the clinical realm, its long echo train length renders deleterious image artifacts such as signal dropout, gross image distortions, and blurring. By utilizing the spatial dependency of arrays of radiofrequency (RF) coils to speed up data acquisition by factors of two to four, parallel imaging is a new method that could yield better quality images for more sensitive and specific diagnosis of disease. Parallel imaging uses spatial information from arrays of RF coils to perform some portion of the spatial encoding normally accomplished using gradients and RF pulses. Multiple MR signal data points are acquired simultaneously rather than one after the other (Sodickson and McKenzie 2001). The two primary methods are Simultaneous Acquisition of Spatial Harmonics (SMASH) and Sensitivity Encoding (SENSE).

In SMASH, image correction is performed prior to the data being Fourier transformed, whereas in SENSE, reconstruction is performed after Fourier transformation. The role of parallel imaging for DTI of acute stroke patients has not been thoroughly evaluated. Although SENSE imaging has proven beneficial in diffusion-weighted EPI of subacute stroke patients (Bammer *et al* 2001; Willinek *et al* 2003) and DTI of normal individuals (Bammer *et al* 2002; Jaermann *et al* 2004), SMASH imaging or its variant GRAPPA have not yet been evaluated with diffusion single-shot EPI.

This chapter presents the details of our implementations (methods and results) of two parallel imaging methods based on the original SENSE and SMASH techniques for use with DTI.

---

*A version of this chapter has been published. Bhagat YA, Emery DJ, Naik S, Yeo T and Beaulieu C. (2007). Comparison of GRAPPA and mSENSE for Diffusion Tensor Imaging. *American Journal of Neuroradiology.* 28(2):293-298.

Iterations of this study have previously been presented at:

1) 2nd International Society for Magnetic Resonance in Medicine (ISMRM) Workshop on Methods for Quantitative Diffusion MRI of Human Brain. 2005. Lake Louise, AB. 10 (poster presentation)

2) 12th annual scientific meeting of the ISMRM. 2004. Kyoto, Japan. 336 (poster presentation)

9.1 Background

Parallel acquisition techniques (PAT) when combined with single-shot echo planar imaging (EPI) methods can ameliorate artifacts such as signal dropout, gross geometric distortions, and blurring due to lengthy echo trains and T2* decay associated with the EPI readout interval. In the case of conventional diffusion-weighted EPI, such artifacts lead to image degradation mainly at the base of the skull, in infratentorial aspects of the brain, and around the auditory canals or frontal sinuses, potentially impeding the accurate detection of ischemic lesions in diseases such as stroke (Augustin *et al* 2004; Bammer *et al* 2001; Kuhl *et al* 2005; Willinek *et al* 2003). Parallel imaging utilizes the spatial information from arrays of radiofrequency (RF) coils to perform some portion of the spatial encoding normally accomplished using gradients (Bammer and Schoenberg 2004). The benefits are accelerated image acquisition (i.e. shorter echo train length for EPI) due to a reduction in the number of phase-encoding steps that need to be acquired, diminution of imaging artifacts, and resolution enhancement. A more common approach for accelerating image acquisition is the partial Fourier method referred to as the phase partial Fourier (PPF) method by Siemens (McGibney *et al* 1993), which samples *k*-space asymmetrically and thereby decreases the amount of phase encoding steps required, albeit with artifacts incurred due to phase errors and penalties in signal-to-noise ratio (SNR). However for both, PAT and PPF, some SNR can be regained due to shorter spin-echo times (Jaermann *et al* 2004; Jaermann *et al* 2006).

9.1.2 Parallel Imaging Based DTI Studies

The image domain based technique Sensitivity Encoding (SENSE) (Pruessmann *et al* 1999) when used with single-shot EPI based Diffusion Tensor Imaging (DTI) of the brain yielded images with improved spatial resolution and reduced geometric distortions at 1.5T (with R=2) (Bammer *et al* 2002) and 3T (with R=2.4 and 3) (Jaermann *et al* 2004; Jaermann *et al* 2006). These aforementioned studies also utilized PPF of 60-80% with all DTI scans. However, the impact of these SENSE-related benefits on the quantitative measures derived from DTI (Trace/3 apparent diffusion coefficient (ADC) and fractional anisotropy (FA)) was not determined relative to the conventional DTI technique. Furthermore, to our knowledge, there are no published systematic evaluations of the newer self calibrating parallel imaging methods, Modified SENSE (mSENSE) (Wang *et al* 2001) or *k*-space based Generalized Autocalibrating Partially Parallel Acquisitions (GRAPPA) (Griswold *et al* 2002) with DTI.

9.1.3 Parallel Acquisition Techniques- Methodology

Like SENSE, mSENSE accelerates imaging by undersampling *k*-space and generating reduced field of view (FOV) or aliased images. By using the spatial information inherent in each receiver coil in the form of coil sensitivity maps, the image reconstruction process then effectively unfolds the aliased image (Pruessmann *et al* 1999; Wang *et al* 2001). However, for SENSE, coil sensitivity maps are calibrated from a separate scan, whereas

for mSENSE, sensitivity map calibration is performed by acquiring extra lines within the accelerated acquisition itself that are not included in the final image reconstruction, a property defined as autocalibration. GRAPPA also employs autocalibration, but here the missing lines of *k*-space for final image reconstruction are calculated from the small amount of acquired lines in the *k*-space domain, prior to Fourier transforming the data (Griswold *et al* 2002). Besides in GRAPPA, the extra lines acquired for coil sensitivity calibration can be integrated into the final reconstruction to reduce the effects of any residual aliasing artifacts that may be present (Blaimer *et al* 2004; Griswold *et al* 2004).

9.1.4 Non-DTI Based mSENSE and GRAPPA Studies

Previous studies comparing mSENSE and GRAPPA for various applications other than DTI have concluded that GRAPPA was superior to mSENSE in terms of image quality, SNR and restricting aliasing artifacts for True FISP (Free induction with steady state precession) sequences in cardiac cine imaging (Hunold *et al* 2004), and T2-weighted Turbo spin echo sequences in lumbar spine imaging (Ruel *et al* 2004). However one study noted significant merits of mSENSE over GRAPPA with respect to image quality and lesion conspicuity in the case of 3-D VIBE (volume interpolated breath-hold exams) for liver imaging (Vogt *et al* 2005).

9.1.5 Goals of the Study

The purpose of our study was to compare the qualitative aspects of the images and quantitative diffusion parameters obtained with mSENSE and GRAPPA-based DTI with higher acceleration factors (up to R=4, no PPF) versus conventional DTI with and without phase partial Fourier. A rectangular FOV with right-left (R/L) phase encoding was used to further reduce the echo train length and capitalize on shorter echo times for gains in SNR. We hypothesized that both GRAPPA and mSENSE would improve the conspicuity of detailed image features and generate more reliable quantitative Trace/3 ADC and FA values especially in regions compromised by the common EPI-related artifacts.

9.2 Methods

Images were obtained from a group of 5 normal subjects (mean age = 28 ± 3 years). DTI was performed on a 1.5 T Magnetom Sonata scanner (Siemens Medical Systems, Erlangen, Germany) equipped with gradient coils producing a maximum amplitude of 40 mT/m and slew rate of 200 T/m/s. An 8-channel phased array RF coil (MRI Devices, Waukesha, WI) was used with conventional DTI (R=1) with and without PPF, and mSENSE DTI and GRAPPA DTI without PPF (commercial parallel imaging software, Siemens 2004A). Conventional single-shot spin-echo diffusion EPI (R1-no PPF) used: TR / TE / NEX = 3.3 s / 107 ms / 8, matrix 96 x 128, rectangular FOV 195 x 260 mm,

twenty 3 mm thick contiguous axial slices, bandwidth of 1446 Hz/pixel, echo spacing of 0.8 ms, R/L phase encode direction, scan time 3:10 min.

The diffusion tensor was acquired with diffusion gradients along six non-collinear directions {b=1000 s/mm^2; (X, Y. Z) gradient directions = (1, 0, 1), (-1, 0, 1), (0, 1, 1), (0, 1, -1), (1, 1, 0), (-1, 1, 0)} and one without diffusion weighting (b=0 s/mm^2, b0). DTI data was reacquired for R1 with PPF (6/8) and R of 2, 3, and 4 for both mSENSE and GRAPPA without PPF (24 reference lines). To better compare results from the two image acceleration methods (i.e., PPF and parallel imaging), PPF was not incorporated with parallel imaging based DTI sequences. The geometric acquisition parameters, number of averages (8) and TR (2.8 s) were kept constant for these sequences, and TE was minimized for each value of R as shown in Table 9-1. The TR was kept constant to avoid any T1-discriminating effects that may arise from implementing an effectively lower TR for the parallel imaging methods (R=2 to 4). TR could have been reduced by 0.3 to 0.8 s relative to R1-PPF. The constant number of averages permitted a clinically reasonable acquisition time for each sequence. A 2-L Ni-doped water bottle was used as an isotropic phantom (N=5). DTI measurements were repeated on one volunteer (N=4) over a one week period to evaluate the stability of diffusion metrics in vivo for conventional DTI and mSENSE and GRAPPA based DTI. Trace/3 ADC and FA maps were generated using MRVision image analysis software (Winchester, MA). Details of the image processing steps are outlined in Appendix 1.1.

Table 9-1: Acquisition times (min) and echo times (TE, ms) for conventional DTI with and without phase partial Fourier (PPF) and mSENSE or GRAPPA based DTI sequences with varying acceleration factors (R). [a]Note that the repetition time was kept constant at 2.8 s.

	Conventional DTI (R=1)		Parallel Imaging with no PPF		
Acceleration Factor	**with PPF (6/8)**	**without PPF**	**R=2**	**R=3**	**R=4**
Acquisition Time (min)	2:44	3:10	2:55	3:01	3:04
TE (ms)	82	107	81	76	71

[a]TR was kept constant at 2.8 s for DTI with PPF and parallel imaging, whereas it was 3.3 s for DTI without PPF.

The b0 and b1000 images and Trace/3 ADC and FA maps of all five subjects were reviewed by a group of three experienced neuroradiologists (D.J.E, S.N., T.Y.) blinded to the method used (GRAPPA, mSENSE, R1-PPF or R1-no PPF) and its acquisition parameters. A group consensus was reached with regard to the quality of the images with each set of images ranked from 1 to 4 with 1 being the best and 4 the worst. Image sharpness and presence or absence of artifacts within the brain, were the two

characteristics most useful in differentiating between images acquired with the different methods.

9.2.1 SNR Calculations

The SNR was calculated on b0 images according to a modification of the dual acquisition subtraction method (Firbank *et al* 1999; Price *et al* 1990) proposed by Reeder *et al.* for magnitude images acquired with parallel imaging (Reeder *et al* 2005). Two sequential acquisitions of identical images S_1 and S_2 were acquired in this method. An estimate of the mean signal was obtained from a region of interest from the sum of S_1 and S_2. The standard deviation (SD) of the difference within the same ROI was obtained from the subtraction of one image from the other. The SNR was calculated according to

$$SNR = \frac{mean(S_1 + S_2)}{\sqrt{2}\ SD(S_1 - S_2)} \qquad (9.1)$$

Due to the varying noise profile of accelerated images, the SNR, neglecting the effect of autocalibrating lines is given by (Pruessmann *et al* 1999; Reeder *et al* 2005)

$$SNR_{PAT} = \frac{SNR_{full}}{g\ \sqrt{R}} \qquad (9.2)$$

where SNR_{full} is the SNR of the conventional image, and g is the geometry or g-factor which describes the noise enhancement across the image for a given coil configuration. The g-factor depends on the spatial location within the image, the R factor and geometrical properties of a specific coil array. Based on these features, the measurement of noise in a region different from that of the signal measurement can lead to incorrect interpretations of regional SNR.

9.2.2 Regions-of-Interest Analysis

Region of interest analysis of 6 different regions per subject were stratified according to their respective range of FA values into categories such as the major white matter (WM) tracts (genu and splenium of corpus callosum, FA = 0.67-0.76), subcortical WM (superior temporal gyrus and middle temporal gyrus, FA = 0.44-0.47), and cortical gray matter (GM regions adjacent to the 2 gyri mentioned above, FA = 0.16-0.19). The ROI traces encompassed the full visible outline of the structure on one 2D slice and were cross-referenced with b0 images to avoid inclusion of obviously visible cerebrospinal fluid-filled spaces. To account for effects of spatial warping primarily at the edges of peripheral structures and at the basal levels of the brain, and to avoid ensuing partial volume averaging with neighboring tissues, the ROIs were consistently either re-positioned or re-drawn for images of the conventional and parallel imaging methods.

Paired t-tests were used for statistical analysis of SNR, Trace/3 ADC and FA obtained from conventional DTI (R=1) versus mSENSE DTI and GRAPPA DTI. The reproducibility of quantitative diffusion for R=1-PPF, and mSENSE R=2 and GRAPPA R=2 were assessed by repeated measurements for one subject over 4 scans and showed up to a 4% variation in FA and 5% in Trace/3 ADC in the genu of the corpus callosum (data not shown).

9.3 Results and Discussion

In the qualitative image analysis, the b0, b1000 and Trace/3 ADC images were evaluated as a group whereas the FA maps were evaluated separately. For the b0, b1000 and Trace/3 ADC group, images acquired using mSENSE R=2 were consistently found to be the best in all 5 subjects, followed by those obtained using GRAPPA R=2 (both without PPF) (Figures 9-1 and 9-2). Images derived using R1-PPF and R1-no PPF were found to be poorer in quality for all cases. GRAPPA and mSENSE R=2 derived images appeared sharper and were less vulnerable to typical EPI artifacts and blurring observed in images acquired with the more commonplace R1-PPF method (i.e. "standard" DTI). Results from evaluation of the FA maps were less consistent and contrary to that of the b0 and diffusion images, and Trace/3 ADC maps. FA maps of the R1-PPF technique were found to be superior in four of the five subjects. This technique generally provided the best overall FA map of both subcortical and deep white matter in terms of sharpness and contrast relative to the background gray matter. However, closer inspections of the FA maps obtained with parallel imaging demonstrated fewer distortions especially for basal structures and yielded better-defined WM regions as seen on magnified sections of the FA maps. Our qualitative findings are in good agreement with previous studies (Bammer *et al* 2002; Jaermann *et al* 2004; Nagae-Poetscher *et al* 2004; Yamada *et al* 2003).

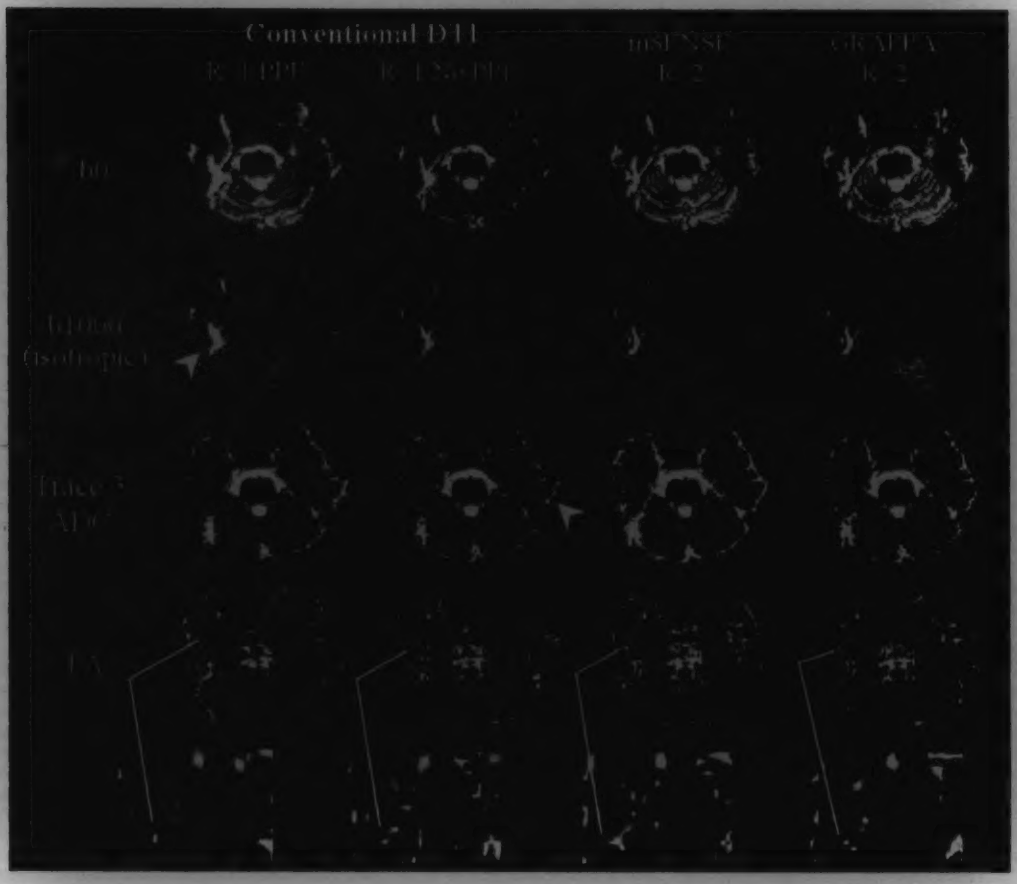

Figure 9-1: Representative sets of b0 (T2-weighted), b1000 (isotropic diffusion weighted) images and Trace/3 ADC and FA maps of one inferior slice (level of pons) from one subject with conventional (R=1), and mSENSE and GRAPPA R=2 based DTI. Compared to R1-PPF and R1-no PPF, a reduction in distortions and off-resonance effects (arrowheads) are apparent with images obtained with mSENSE and GRAPPA R=2 DTI. Although FA maps obtained with R1-PPF were deemed to be the best in 4/5 subjects based on their higher SNR and smoother profiles (qualitative analysis by neuroradiologists), closer inspection showed that peripheral white matter structures such as the middle temporal gyrus (magnified, below FA maps) affected by the distortions with conventional DTI were better resolved with the mSENSE and GRAPPA R=2 based DTI methods.

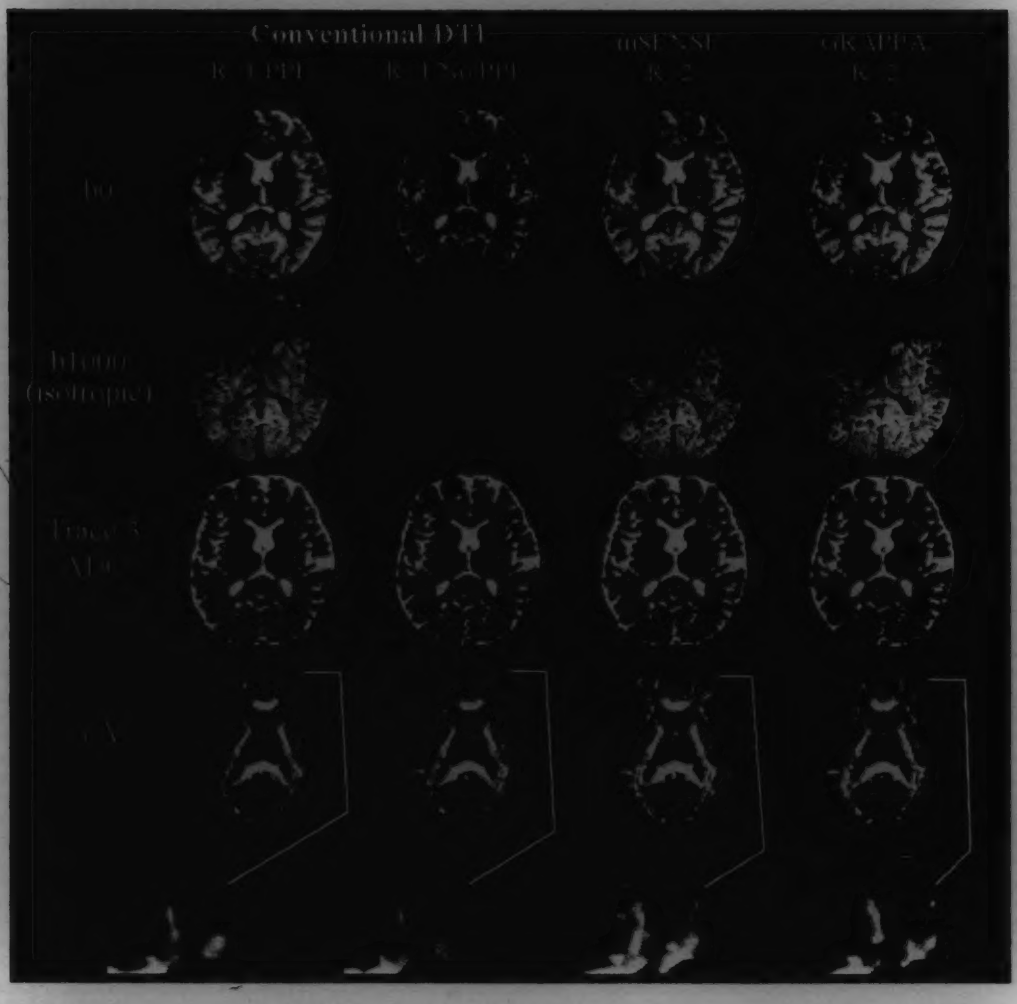

Figure 9-2: Image sets (b0, b1000) and Trace/3 ADC and FA maps of a middle slice (level of corpus callosum) from one subject with conventional (R=1), and mSENSE and GRAPPA R=2 based DTI. Qualitative analysis of the b0 and b1000 images, and Trace/3 ADC maps indicated that mSENSE and GRAPPA R=2 DTI generated the sharpest images and were more adept at handling spatial warping effects seen in images of the R1-PPF and R1-no PPF methods. Although FA maps derived from R1-PPF were considered to be smoother due their intrinsically higher SNR in 4/5 cases, an in-depth comparison of these maps to those obtained using mSENSE and GRAPPA R=2 DTI showed that incorporating parallel imaging allowed better visualization of thinner white matter tracts such as the middle frontal gyrus (magnified, below FA maps).

9.3.1 Higher 'R' factors

Images acquired with higher acceleration factors (R=3 and 4) suffered from pernicious reconstruction artifacts such as aliasing and structural noise enhancement as apparent in the post-processed Trace/3 ADC and FA maps (Figure 9-3), thereby precluding their use for the previous qualitative analysis or the subsequent quantitative analysis. Potential reasons for the hindered performance of these techniques at higher R factors relate to nonideal conditioning in reconstruction leading to localized noise enhancement in the unfolded images for mSENSE, or inaccuracies in calculations of missing *k*-space lines which generate aliasing in the case of GRAPPA (Blaimer *et al* 2004). Furthermore, in GRAPPA, incorporating a single-shot EPI calibration scan (for derivation of coil weights) in the actual DTI sequence as opposed to performing a separate scan may cause artifacts due to an incompatibility with the applied diffusion encoding gradients (Bammer and Schoenberg 2004). Our results are specific to our current implementation of parallel imaging, which is an evolving field on its own, and vary from previous reports which have demonstrated high quality diffusion tensor images of the brain with SENSE R=3 (Jaermann *et al* 2004; Nagae-Poetscher *et al* 2004), which unlike mSENSE, obtains sensitivity maps from separate calibration scans.

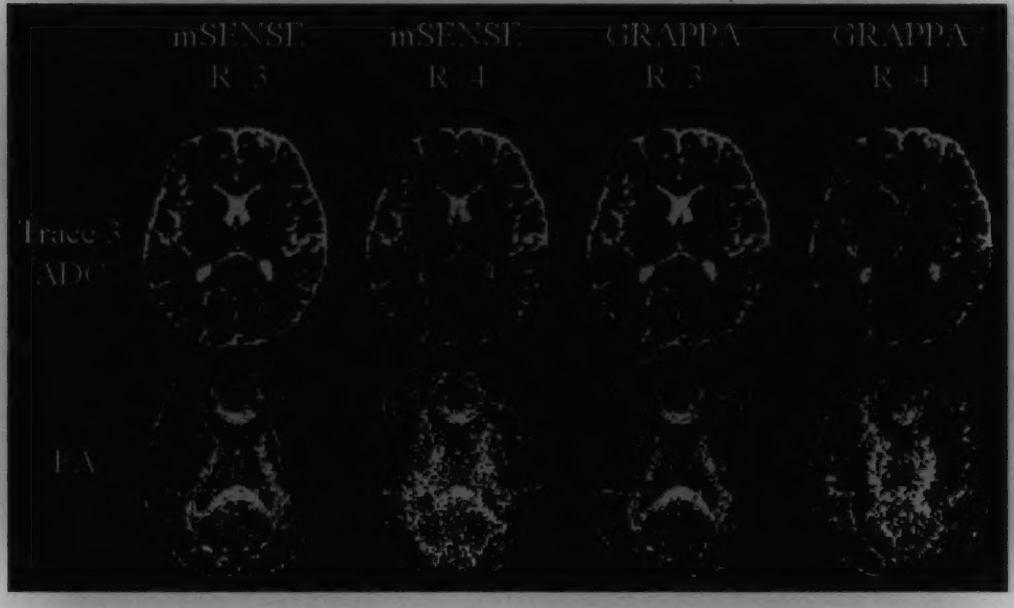

Figure 9-3: Poor quality Trace/3 ADC and FA maps of one middle slice (level of corpus callosum) from one subject using mSENSE and GRAPPA R=3 and 4 based DTI. Maps obtained from mSENSE R=4, and GRAPPA R=3, 4 suffered from reconstruction artifacts such as aliasing and were not considered for quantitative analysis. Trace/3 ADC maps from mSENSE R=3 revealed regions with enhanced noise centrally and were also excluded from further analysis.

9.3.2 Quantitative Findings

Quantitatively, we observed elevations of mean FA with R1-no PPF (0.05 ± 0.01), mSENSE R=2 (0.08 ± 0.01) and GRAPPA R=2 (0.07 ± 0.01) relative to R1-PPF (0.04 ± 0.01) in an isotropic water phantom (Figure 9-4a). However, Trace/3 ADC values in the phantom fluctuated to a lesser extent (3%) when comparing R1-PPF to R1-no PPF and GRAPPA R=2, and comparing R1-no PPF to mSENSE and GRAPPA R=2 (Figure 9-4b). The elevations in FA encountered with parallel imaging relative to conventional DTI are not unexpected given the known noise-induced bias in FA quantification particularly at low FA values (Kingsley and Monahan 2005). Figure 9-5 displays a plot of mean relative SNR values (R2 / R1-PPF) for the phantom and 3 brain regions in 5 subjects. Although we expect only a $\sqrt{2}$ loss in SNR with parallel imaging under ideal conditions for g = 1.0 (Pruessmann *et al* 1999), the steeper declines in relative SNR with mSENSE and GRAPPA R=2 are due to the higher standard deviations (mSENSE ≅ 17, GRAPPA ≅ 15) relative to R1-PPF (~6) measured in ROIs from the difference images of those methods. This is a result of noise enhancement which may be a consequence of the variations in the g-factor owing to coil configuration or slice location with respect to elements of the coil array (Pruessmann *et al* 1999). Others have noted that enhancing the distance between the phantom or subjects and the coil elements can moderate the steep variance in coil sensitivity profiles proximal to the coil and limit errors in image reconstruction, thereby optimizing image quality and refining SNR (Bammer *et al* 2001). In our study, although this feature was easy to implement for the smaller cylindrical phantom, it was not feasible for an adult human head relative to the sensitive volume of the coil (24 cm).

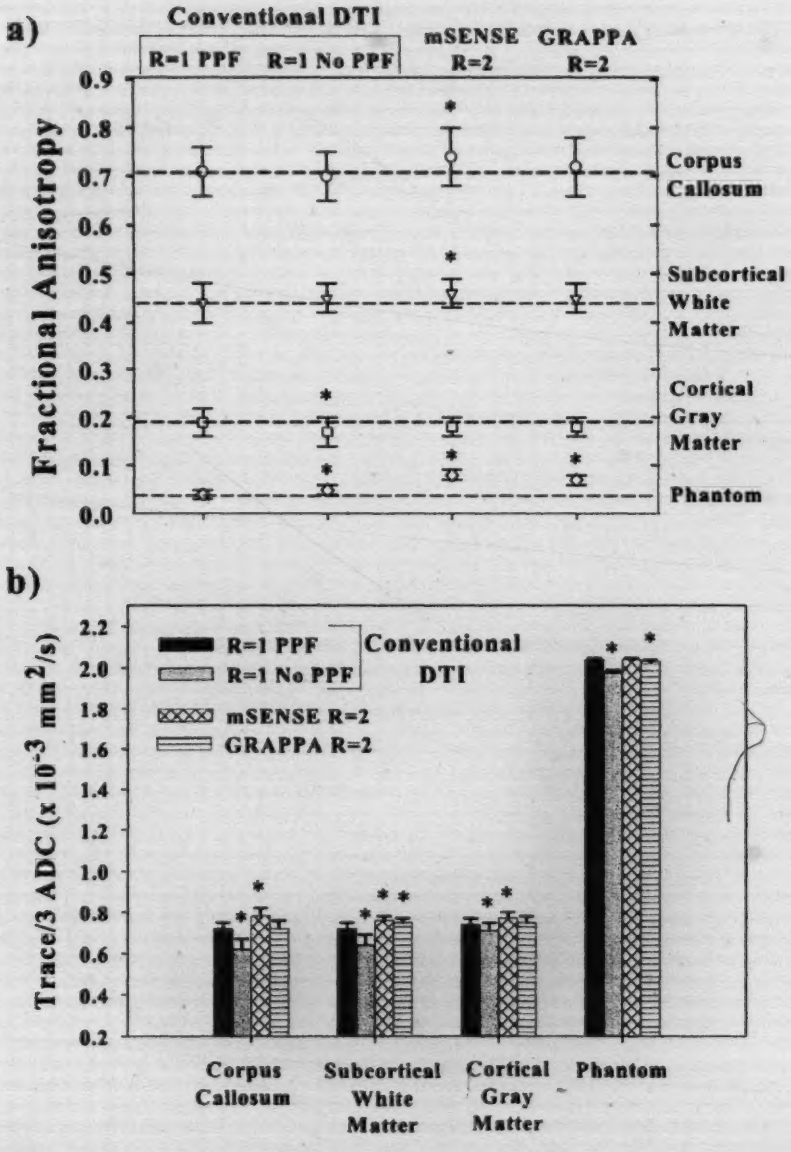

Figure 9-4: Fractional anisotropy (**a**) and Trace/3 ADC (**b**) values (mean ± SD) for three brain regions in 5 normal subjects using conventional DTI R1-PPF, R1-no PPF and mSENSE and GRAPPA R=2 DTI methods. The dashed lines in (a) indicate FA values obtained with conventional R1-PPF for different structures and help demonstrate the extent of variations with measurements made using other techniques. Although subtle differences are evident, the values appear to be fairly consistent between parallel imaging and conventional DTI. Values for mSENSE and GRAPPA R=3, 4 methods are not shown due to the poor quality of the maps. * indicates significant ($p<0.05$) paired differences of R1-PPF versus R1-no PPF, mSENSE R=2 and GRAPPA R=2 methods.

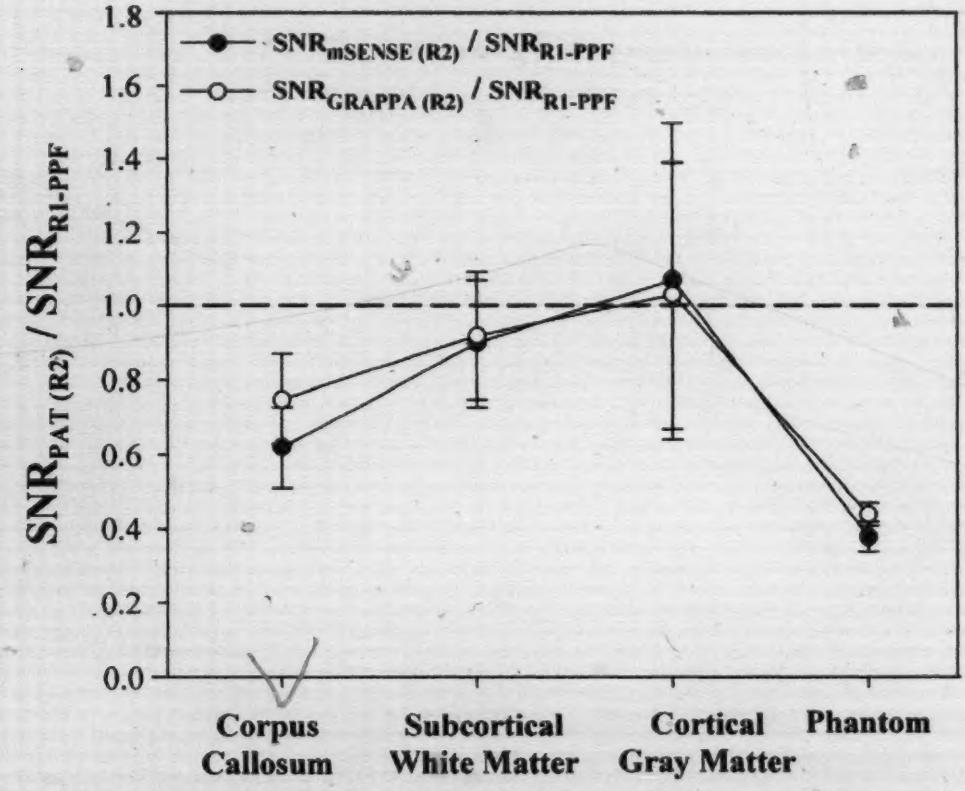

Figure 9-5: Relative (Parallel Acquisition Technique (PAT (R=2) / R1-PPF) signal-to-noise ratio (SNR) measurements (mean ± SD) of mSENSE or GRAPPA R=2 for three brain regions in 5 normal subjects. SNR values were fairly close between mSENSE and GRAPPA R=2 methods for the 3 structures evaluated. Relative SNR values were reduced by 25-38% and 8-10% in the corpus callosum and subcortical white matter in the gyri, respectively. Cortical gray matter demonstrated relative SNR values closer to unity with a higher percentage of error (35-40%) in the measurements. Relative SNR values in the phantom decreased by 56% and 62% for the GRAPPA and mSENSE R=2 methods respectively, in accordance with theoretical considerations reflecting higher (>1.0) coil g-factors (Pruessmann *et al* 1999).

FA values *in vivo* remained fairly consistent for all acquisition methods revealing small increases for the mSENSE R=2 technique of up to 5% for the corpus callosum and subcortical WM (Figure 9-4a). Using R1-PPF as the basis of comparison, the Trace/3 ADC values were observed to fluctuate with decreases for R1-no PPF (4-17%) and increases of 4-7% for the mSENSE R=2 and GRAPPA R=2 methods for the corpus callosum, subcortical WM, and cortical GM areas (Figure 9-4b). Although our normative FA values for R1-PPF based DTI (the pseudo-gold standard) are in firm agreement with those published previously (Alexander *et al* 2000), recent PAT-based DTI studies of the brain do not mention *in vivo* FA values (Bammer *et al* 2002; Jaermann *et al* 2004; Nagae-

Poetscher *et al* 2004; Yamada *et al* 2003), limiting our ability to draw comparisons between their data and our mSENSE and GRAPPA R=2 derived measures. Mean SNR values measured using the R1-PPF method ranged from 35-45 in the corpus callosum, subcortical WM and cortical GM. Overall, relative SNR ($SNR_{PAT(R2)}$ / $SNR_{R1\text{-}PPF}$) was reduced to a greater extent in central structures such as the corpus callosum compared to peripheral structures such as subcortical WM (Figure 9-5), and is likely responsible for the small systematic changes in the diffusion parameters obtained with parallel imaging. However, in a separate study where we performed mSENSE and GRAPPA R=2 DTI with 16 averages, and compared the data to R1-PPF and R1-no PPF with 8 averages in 4 subjects, the results were no different, suggesting that alterations in Trace/3 ADC and FA are not entirely SNR-dependent (data not shown).

Our choice of the right-left phase encoding direction with a rectangular FOV of 75% enabled a faster *k*-space traversal and reduction in echo train length which yielded gains in SNR and marked reductions in geometric distortions in the frontal regions of the brain that are synonymous with anterior-posterior (A/P) phase encoding with a square FOV (Bammer *et al* 2001). Our results would translate well to single-shot EPI based DTI at higher fields (3.0T and above) since the common EPI related susceptibility artifacts and T2* blurring seen here are more pronounced at high field and can be minimized by use of parallel imaging (Jaermann *et al* 2004; Jaermann *et al* 2006). Furthermore, in addition to gaining SNR from significant reductions in TE as a result of the shorter echo train length, parallel imaging can confer enhancements in resolution (Figures 9-1, 9-2) and yield improved anatomical detail for more precise Trace/3 ADC and FA measures.

Unlike earlier studies (Bammer *et al* 2002; Jaermann *et al* 2004; Jaermann *et al* 2006), our study did not incorporate PPF into parallel imaging based DTI for further comparisons. However, to test the effects of PPF on PAT, we performed mSENSE and GRAPPA DTI with 6/8 PPF (R/L phase encoding) for acceleration factors up to 4 in one subject. The use of PPF resulted in a shorter TE of 72 ms, 68 ms and 67 ms for R=2, 3 and 4, respectively. Nonetheless image and diffusion map quality, although acceptable with R=2-PPF, suffered from blurring and lack of sharpness (data not shown) compared to the R=2 (no-PPF) images in the present study. It is important to note that the differences between conventional DTI and parallel imaging based DTI can be more dramatic when the image acquisition uses purely axial slices rather than obliques, A/P phase encoding without rectangular FOV, larger matrix, and fields higher than 1.5T.

9.3.3 Re-evaluation of Statistics for Multiple Group Comparisons

In this DTI-based parallel imaging study, we compared FA and Trace/3 ADC values in 3 distinct brain regions and a phantom between the conventional DTI (R1-PPF) method versus R1-noPPF and the mSENSE and GRAPPA R=2 methods using paired t-tests. The use of multiple t-tests may be a simplistic statistical method for this purpose and increases the likelihood of encountering a Type I error where a false significant effect can be obtained when there is none (Zou *et al* 2003). Ideally a one-way analysis of variance (ANOVA) should be used to compare the means of more than two distributions. In this

manner, the means of two or more independent groups can be evaluated to determine the relative variability between the groups compared with the variability within the groups. To rectify our previous analysis, we performed a one-way ANOVA with repeated measures for statistical analysis on the FA and Trace/3 ADC values obtained with these 4 methods. If a significant ($p<0.05$) difference between any of the methods was noted, post hoc analyses were performed using the Bonferroni t-test for pair-wise comparisons (Tello and Crewson 2003).

In the isotropic water phantom, we observed significant ($p<0.01$) elevations of mean FA with R1-noPPF and mSENSE and GRAPPA R=2 compared to the gold standard R1-PPF method. However, the Trace/3 ADC values in the phantom fluctuated to a lesser extent, with significant ($p<0.01$) reductions for the R1-noPPF and GRAPPA R=2 methods compared to R1-PPF. FA values in the human brain remained fairly consistent for all methods demonstrating small increases for the mSENSE R=2 technique (up to 5%) relative to R1-PPF for the corpus callosum and subcortical WM. With respect to Trace/3 ADC values, minor increases of 4-7% ($p<0.01$) were seen with mSENSE and GRAPPA R=2 in the corpus callosum and subcortical WM. Compared to R1-PPF, no significant differences were detected for any of the methods in cortical GM for FA and Trace/3 ADC values.

9.4 Concluding Remarks

We have shown images and Trace/3 ADC and FA maps of good quality with mSENSE and GRAPPA R=2 based DTI at 1.5T. Improvements in FA contrast at borders between gray and white matter regions were primarily observed in peripheral brain areas. Despite decreases in SNR, the parallel imaging methods addressed issues of susceptibility and off-resonance artifacts noted with conventional DTI (R1-PPF and R1-no PPF) and yielded higher quality images. Quantitative Trace/3 ADC and FA measurements were accurate and reproducible with both parallel imaging methods with an acceleration factor of 2.

10

SERIAL DIFFUSION TENSOR IMAGING OF STROKE

Following ischemic stroke onset, the average water mobility in terms of the trace apparent diffusion coefficient (Trace/3 ADC) remains consistently low for the first few days (Hjort *et al* 2005; Moseley *et al* 1990b; Warach *et al* 1992) (unless reperfusion is established (Marks *et al* 1999)), pseudonormalizes at 1 week and is elevated at chronic time points (Beaulieu *et al* 1999; Schlaug *et al* 1997). However diffusion anisotropy (given by fractional anisotropy (FA)) of ischemic brain regions is variable during the first few days. Cross-sectional DTI-based human studies have shown that FA of ischemic regions (mixed gray matter (GM) and white matter (WM) tissue) is significantly elevated (up to 45%) from 4 hours to 24 hours post stroke onset (Green *et al* 2002; Ozsunar *et al* 2004a; Schaefer *et al* 2003), with one of those studies also demonstrating reductions in FA (~34%) within that same time frame (Green *et al* 2002). In a more recent cross-sectional DTI study of ischemic WM regions, we showed that FA was only significantly elevated (up to 25%) ≤7 hours of symptom onset, but consistently reduced (~15% declines) from 8-34 hours after stroke (Chapter 8, Figure 8-3). Therefore, FA is yielding discriminating data on the microstructural status of tissue beyond that given by the uniformly low Trace/3 ADC values over the initial time frame after stroke.

10.1 Serial Studies of Diffusion Anisotropy

A serial characterization of diffusion parameters following ischemic stroke offers more utility than a cross sectional study for tracking changes in individual patients and evaluating the fate of ischemic tissues during a given time course post symptom onset. Although there are several published reports of DTI studies on longitudinal stroke patients, the majority of these reports detail FA reductions in the chronic phase (2 days to 1 year) of stroke as "final" outcome of the affected tracts within the lesion or regions remote (upstream or downstream) from the primary lesion such as the corpus callosum, corona radiata, centrum semiovale, thalamus, internal capsule, pons and cerebral peduncles (Buffon *et al* 2005; Gupta *et al* 2006; Herve *et al* 2005; Pierpaoli *et al* 2001; Thomalla *et al* 2004; Thomalla *et al* 2005; Werring *et al* 2000). Within that chronic time frame of up to 1 year post onset, the majority of these serial reports show severe decreases in FA within the lesion (~29% to 70% reductions) and in regions remote from the primary lesion (~8% to 40% declines) (Buffon *et al* 2005; Gupta *et al* 2006; Pierpaoli

et al 2001; Thomalla *et al* 2004; Thomalla *et al* 2005; Werring *et al* 2000). Interestingly, in a study by Hervé *et al.* focused on characterizing diffusion changes within the ipsilateral thalamus from 1-week to 6 months following middle cerebral artery infarction, although they observed significant increases in mean diffusivity (Trace/3 ADC) during that time period (1-week, and 1, 3 and 6 months after onset), they did not see any changes in FA (Herve *et al* 2005).

Serial longitudinal studies of animal models of ischemia have shown that FA is elevated (up to 20%) within the first 5 hours of onset in rats (Carano *et al* 2000) and monkeys (Liu *et al* 2007), but then declines over the ensuing time course. To the best of our knowledge, serial DTI reports of human stroke that characterize changes in diffusion anisotropy within 24 hours of stroke onset are sparse. Of the 3 known serial studies of human ischemic stroke within 24 hours of onset, one study by Yang *et al.* focused on characterizing diffusion anisotropy in distinct ischemic WM and GM regions demonstrated mixed findings with elevations (10%-45%) and reductions (5% to 25%) in FA from 4 to 96 hours post onset (Yang *et al* 1999). Other longitudinal studies of human stroke (within 24 hours following stroke) have noted a more gradual decline (~8% to 54% decreases) in FA from 24 hours to 90 days after onset (Munoz Maniega *et al* 2004; Zelaya *et al* 1999).

The wide discrepancies in the trends of diffusion anisotropy within the early phases (≤24h) of stroke may be attributed to biological variability, data acquisition schemes or analytical factors. Yang *et al.* acquired 3-direction diffusion-weighted images in the majority of their patients and combined gyral WM and GM areas together for analysis (Yang *et al* 1999). Zelaya *et al.* also used a similar analytical approach where they did not segment the WM and GM tissue components for separate analysis within the infarcts of their patients (Zelaya *et al* 1999). Given the known variability in FA values between WM and GM regions, grouping those tissues within the lesions for analysis may result in ambiguous FA values. Another cause of the variability in the trends of FA over time in stroke may be that patient data from ≤24h of onset was grouped for analysis such as by Munoz-Maniega *et al.*, whereas individual patient data would have allowed the visualization of any time-dependent trends in FA (Munoz Maniega *et al* 2004).

10.1.2 Purpose

The purpose of this study was to characterize serial diffusion anisotropy changes during the initial (≤7h) and follow-up (21.5-29h) phases of human stroke in a group of 13 patients by focusing on discrete WM and GM regions within the infarcts (due to the variability in normal FA values within these regions).

10.2 Methods

Thirteen patients (6M, 7F, mean age = 65 ± 12 years) presenting with a non-hemorrhagic ischemic stroke and known times of onset were enrolled in the magnetic resonance

imaging (MRI) study after computed tomography and standard treatment (Note that these patients belong to a different cohort than the ones in Chapter 8). They were initially scanned within 2.5-7 hours of symptom onset (median of 5 hours), and then subsequently scanned within 21.5-29 hours for a follow-up session (median of 26 hours; Table 1). Baseline National Institutes of Health stroke scale scores (NIHSSS) ranged from 4-24 for the initial phase (median NIHSSS = 7) and 3-24 for the follow-up phase (median NIHSSS = 7) after stroke. Out of the total 13, 10 patients were administered with drug treatment within 3 hours of symptom onset (77%), including 5 patients with intravenous tissue plasminogen activator (rt-PA), 3 patients with rt-PA and enrollment into the ALIAS (Albumin (therapy) in acute stroke) trial, 1 patient with rt-PA and enrollment into PRoFESS (Prevention regimen trial for effectively avoiding second strokes), and 1 patient enrolled into ALIAS only. Few patients within our cohort were not ideal given that they had old strokes (patients 1 and 9) and periventricular WM hyperintensities (patients 9 and 13) (Table 10-1).

The local human research ethics board approved the MRI protocols and written informed consent was obtained from all patients or their next of kin.

10.2.1 MRI Acquisition and Post-processing

DTI was part of a 16-min parallel imaging-based protocol including a turbo spin echo T2 (TR/TE = 5800/99 ms; Tacq = 1:05), FLAIR (TR/TE/TI = 7450/94/2400 ms; Tacq = 1:31), gradient echo (TR/TE = 663/23 ms; Tacq = 0:44), Time of Flight MRA (TR/TE= 35/6.45 ms; Tacq = 3:41), perfusion-weighted with single shot gradient echo EPI (PWI) (TR/TE = 1320/50 ms; 60 measurements; Tacq = 1:29), T1-weighted (TR/TE = 680/17 ms; Tacq = 0:46) post-gadolinium and three 3-scan trace DWI sequences performed on a 1.5T Sonata Magnetom scanner (Siemens Medical Systems, Erlangen, Germany). The spin echo T2-weighted, FLAIR, gradient echo and T1-weighted sequences were acquired with 19, 5 mm thick slices with a 1.5 mm gap. With the exception of two 3-scan trace DWI sequences, all sequences including DTI were coupled with the modified sensitivity encoding (mSENSE) method using an R=2 acceleration factor. This approach helped minimize the susceptibility and off-resonance effects typically associated with conventional echo planar imaging (EPI) based DTI acquisition methods (Chapter 9, Figures 9-1 and 9-2). The parameters for the 3-scan trace DWI sequences were: Standard DWI (R=1; TR/TE = 3000/86 ms; Tacq = 0:56), mSENSE-R=2 DWI (TR/TE = 2600/86 ms; Tacq = 0:59) and Generalized autocalibrating partially parallel acquisitions (GRAPPA)-R=2 DWI (TR/TE = 2600/86 ms; Tacq = 0:59). In the 3-Scan trace DWI sequence, diffusion measurements are made in 3 orthogonal directions. Three scans are required per slice location and b value (for $b \neq 0$). Because of the intensity variations in the directionally acquired diffusion-images, the individual images are not saved, and what we obtain are trace-weighted images. Further details regarding the 3-scan trace DWI sequences are given in Chapter 11 (Section 11.2.1). PWI followed the bolus of intravenously injected contrast agent (0.2 mmol/Kg Gd-DTPA (5 ml/s); Magnevist, Bayer Schering Pharma, Wayne, NJ) using a Medrad power injector (Medrad Inc., Warrendale, PA) 15 seconds after the initial acquisition of 10 EPI scans. PWI was

acquired with 13, 5 mm thick slices with a 1.5 mm gap that overlapped the central 13 slices of the Standard 3-scan trace DWI sequence.

Single shot diffusion-weighted twice-refocused spin-echo EPI with mSENSE was used for DTI with: TR / TE / NEX = 2.5s / 81ms / 8, 96 x 128 matrix, 195 x 260 mm rectangular field-of-view (FOV) with right-left phase-encode direction, and 20, 3-mm thick contiguous axial slices aligned with the anterior and posterior commissures, b = 0 s/mm^2 and six sets with diffusion gradients placed along non-collinear directions {b=1000 s/mm^2; (X, Y, Z) gradient directions = (1, 0, 1), (-1, 0, 1), (0, 1, 1), (0, 1, -1), (1, 1, 0), (-1, 1, 0)}. The 20, 3 mm thick contiguous slices for DTI were centered on the lesion and did not afford full brain coverage (unlike the 20, 5 mm thick slices used in our previous cross sectional work (Chapter 8, Section 8.2.1)). However the main goals of this study were to obtain good resolution and adequate brain coverage, with emphasis on maintaining a short scan time of 2 min 37 s for stroke patients. Raw data were post-processed off-line to yield maps of the eigenvalues λ_1, λ_2, and λ_3, Trace/3 ADC, and FA using MRVision (Winchester, MA, USA). Details of the image processing steps are outlined in Appendix 1.1. The eigenvalues reflect the directional ADC values along the length of the fiber tracts (λ_1) or perpendicular to them (λ_2, λ_3) and FA is a metric signifying deviations from isotropic diffusion ranging from 0 for perfect isotropic diffusion, to 1 for highly anisotropic diffusion.

For PWI, the series of gradient echo images was processed pixel-by-pixel with polynomial fitting (MRVision) to yield maps of time-to-peak (TTP), which was found to give the most distinctive boundary between normal and abnormally perfused brain tissue. Relative TTP corresponds to the time of peak contrast agent concentration or maximum contrast agent concentration (i.e. when the MR signal is at its minimum). In MRVision, the perfusion polynomial fit procedure fits a fifth order polynomial function to the $\Delta R2^*$ curves for each pixel. Fitting such a continuous function to the data allows for a more accurate estimate of the peak and TTP signal change. More importantly, integrating the fitting function permits a more accurate estimation of the relative cerebral blood volume and the relative mean transit time. However, no sophisticated post-processing of the PWI data was employed since perfusion was not the main focus of our study.

Table 10-1: Characteristics of Serial Patient Population

Patient No.	Sex/Age (yr)	Treatment	Arterial Distribution	Time of Initial/Serial MRI scans (hr)	Initial/ Follow-up NIHSSS	Regions Involved within Infarct Major and Subcortical WM Deep and Cortical GM
1	M / 56	None	L MCA	2.5 / 25.0	13 / 7	MWM, SWM, CGM
2	M / 45	rt-PA and ALIAS	L MCA	3.0 / 24.5	7 / 7	MWM, SWM, CGM
3	M / 75	rt-PA and ALIAS	R Lenticulo-striates	3.5 / 26.0	11 / 8	MWM, DGM
4	M / 48	rt-PA	R PCA	4.0 / 21.5	4 / 3	MWM, SWM
5	F / 74	rt-PA	L MCA	4.0 / 22.0	6 / 5	SWM, CGM
6	F / 67	rt-PA	L MCA	4.5 / 25.0	13 / 12	MWM, SWM, CGM
7	F / 79	rt-PA	L MCA	5.0 / 23.0	7 / 4	MWM, SWM, DGM, CGM
8	M / 54	rt-PA and ALIAS	L MCA	5.0 / 26.0	7 / 5	SWM, CGM
9	F / 78	rt-PA and PRoFESS	L MCA	5.0 / 26.0	8 / 10	SWM, CGM
10	M / 68	rt-PA	L MCA	5.0 / 28.0	24 / 24	MWM, SWM, DGM, CGM
11	F / 68	None	L Lenticulo-striates	6.5 / 28.5	4 / 6	MWM
12	F / 58	ALIAS	L PCA	7.0 / 28.0	7 / 11	MWM, SWM, DGM
13	F / 80	None	L ACA	7.0 / 29.0	16 / 14	MWM, SWM

rt-PA, tissue plasminogen activator; ALIAS, Albumin (therapy) in acute stroke; PRoFESS, Prevention regimen (with Antiplatelet therapy and Angiotensin receptive blockers) for effectively avoiding second strokes; PCA, posterior cerebral artery; MCA, middle cerebral artery; ACA, anterior cerebral artery; NIHSSS, National Institutes of Health Stroke Scale Score; MWM, Major white matter (tracts); SWM, Subcortical white matter; DGM, Deep gray matter; CGM, Cortical gray matter.

10.2.2 Regions-of-Interest Analysis

Discrete WM and GM regions within the acute ischemic lesion (defined by ≥30% drop in Trace/3 ADC relative (r) to the contralateral side (Shen *et al* 2003)) were traced using a free-hand Region-of-interest (ROI) method with the aid of the FA and Trace/3 ADC maps, and b = 1000 s/mm^2 images separately for scans from the initial and follow-up periods. A semi-automated method was employed to threshold the ADC maps and all ROI traces were cross-checked with b = 1000 s/mm^2 images to avoid inclusion of any visible sulcal spaces. This was particularly important in cases where regions adjacent to cerebrospinal fluid (CSF) filled sulcal spaces such as subcortical WM (in the gyri) and cortical GM were part of the ischemic core. Due to the complexity associated with

demarcating the boundaries of cortical GM regions adjacent to CSF-filled sulcal spaces, an additional step was undertaken to address partial volume averaging of cortical GM with CSF. Based on the mean FA of sulcal CSF in the normal contralateral hemisphere of all 13 patients (Table 10-1) in our cohort (0.12 ± 0.02), a semi-automated method was used to threshold the FA maps to highlight the CSF-filled areas and avoid their inclusion when outlining the ROIs for cortical GM. Areas of periventricular WM disease and hemorrhagic transformation of the infarct observed on follow-up scans (patients 6, 9, 10 and 13) (Table 10-1) were confirmed using structural MR images, and excluded from analysis.

The ROIs for all patients were drawn by the same individual (Y.A.B) adhering to strict guidelines of including the entire visible extent of a WM or GM structure within the ischemic core. Measurements of FA, λ_1, λ_2, λ_3, and T2-weighted signal intensity (measured on $b = 0$ s/mm^2 images) of the corresponding WM and GM regions in the non-impacted contralateral hemisphere were used as a reference. The remaining steps of the ROI analysis were performed as described in our previous report (Chapter 8, section 8.2.2). Data were separated into categories of major WM tracts, peripheral subcortical WM (in the gyri), deep GM and cortical GM. The lesion volumes for the different tissues involved per patient are given in Table 10-2. Relative (ipsilateral/contralateral) values for each ROI measurement per patient were averaged over all patients within a distinct scanning period, with respect to the 4 tissue categories, to facilitate group comparisons between the initial scans (2.5 to 7 h) and follow-up scans (21.5 to 29 h) post stroke onset. It should be noted that the ROIs at the two time points are not identical to account for lesion growth or brain shifts as the ROIs are only based on regions where the Trace/3 ADC falls by 30% or more relative to regions on the contralateral side.

10.2.3 Statistical Analysis

Paired t-tests were used to examine differences between the ipsilateral and contralateral Trace/3 ADC, FA, λ_1, λ_2, λ_3 and T2-weighted signal intensity ($p<0.05$). Linear regression analyses were performed with Pearson's correlation coefficient and significance level of the F-test to assess correlations between rT2-weighted signal intensity versus rFA across each distinct time frame (initial and follow-up periods). Results were attributed significance at levels of $p<0.05$.

10.3 Results

Of the 13 patients with serial or longitudinal scans, 2 patients demonstrated involvement of all 4 tissue categories (major WM tracts, subcortical WM, deep GM and cortical GM), 4 had a combination of 3 different tissues, 6 had a combination of 2 different tissues and 1 patient had only major WM tracts involved within the Trace/3 ADC-defined infarct (Table 10-1). Figure10-1 shows example T2-weighted and isotropic diffusion-weighted images, and Trace/3 ADC and FA maps from the initial and follow-up scanning periods of 2 patients (10 and 1, Table 10-1) post stroke onset. Areas of elevated FA within the

Trace/3 ADC-defined infarct during the initial scanning phase were mainly apparent in patients when an extreme level of contrast was used to view the FA maps (Figure 10-1 A, B). However, the differences in FA within the lesions relative to regions within the normal contralateral hemisphere can only be fully realized by performing quantitative ROI analyses. Example Trace/3 ADC and FA maps from the initial and follow-up scans of all 13 patients are shown in Figures 10-2, 10-3 and 10-4.

The absolute mean Trace/3 ADC values of the infarcts and the corresponding normal contralateral regions for major WM tracts were 0.46 ± 0.07 and 0.76 ± 0.11 ($x10^{-3}$ mm^2/s), respectively during the initial phase and 0.46 ± 0.08 and 0.81 ± 0.09 ($x10^{-3}$ mm^2/s), respectively in the follow-up phase. For subcortical WM (in the gyri) the ipsilateral and contralateral Trace/3 ADC values were 0.46 ± 0.06 and 0.79 ± 0.08 ($x10^{-3}$ mm^2/s), respectively, during the initial phase, and 0.43 ± 0.07, and 0.81 ± 0.08 ($x10^{-3}$ mm^2/s), respectively, in the follow-up phase. For deep GM the ipsilateral and contralateral Trace/3 ADC values were 0.48 ± 0.06 and 0.77 ± 0.10 ($x10^{-3}$ mm^2/s), respectively, in the initial phase and 0.49 ± 0.04 and 0.79 ± 0.04 ($x10^{-3}$ mm^2/s), respectively in the follow-up phase. For cortical GM the ipsilateral and contralateral Trace/3 ADC values were 0.50 ± 0.04 and 0.83 ± 0.07 ($x10^{-3}$ mm^2/s) during the initial period and 0.48 ± 0.05 and 0.85 ± 0.08 ($x10^{-3}$ mm^2/s) in the follow-up period. The absolute FA values in the normal contralateral hemisphere were 0.76 ± 0.08 for the corpus callosum, 0.54 ± 0.04 for the anterior limb of the internal capsule, 0.60 ± 0.06 for the posterior limb of the internal capsule, 0.40 ± 0.06 for the external capsule, 0.40 ± 0.07 for subcortical gyral WM, 0.36 ± 0.02 for the thalamus, 0.30 ± 0.04 for the head of the caudate nucleus, and 0.23 ± 0.05 for cortical GM regions. The ipsilateral FA values are presented as relative to these contralateral values due to the variability in the absolute measures of WM tracts and GM areas within the ischemic lesions (Sorensen *et al* 1999; Zelaya *et al* 1999).

Table 10-2: Lesion Volumes of Serial Patient Population

Patient No.	Total Lesion Volumes (cm^3, Initial/Serial)	Volumes (cm^3, Initial/Serial) of all ROIs analyzed			
		Major WM Tracts	Subcortical WM in Gyri	Deep GM	Cortical GM
1	16.3 / 27.1	2.1 / 1.7	6.5 / 17.0	---/---	4.8 / 1.1
2	29.4 / 57.9	2.0 / 0.6	10.0 / 20.5	---/---	1.1 / 9.3
3	1.2 / 1.2	1.0 / 1.1	---/---	0.1 / 0.1	---/---
4	1.6 / 9.2	0.8 / 1.9	0.5 / 2.9	---/---	---/---
5	3.4 / 0.4	---/---	2.3 / 0.2	---/---	0.1 / 0.1
6	24.9 / 19.7	0.3 / 6.6	18.4 / 7.8	---/---	3.9 / 2.2
7	0.2 / 7.2	0.1 / 2.5	---/ 2.1	0.1 / 0.4	0.1 / 0.4
8	9.5 / 14.8	---/---	5.3 / 8.7	---/---	0.5 / 1.1
9	2.8 / 0.9	---/---	1.0 / 0.5	---/---	1.5 / 0.1
10	55.7 / 202.5	9.1 / 16.7	21.2 / 57.2	1.6 / 2.8	1.9 / 9.4
11	0.2 / 0.6	0.2 / 0.6	---/---	---/---	---/---
12	19.8 / 31.2	0.5 / 0.5	10.8 / 14.2	2.4 / 4.5	---/---
13	3.1 / 2.9	0.3 / 0.3	2.5 / 2.3	---/---	---/---

Refer to Table 10-1 for patient characteristics. WM, white matter; GM, gray matter. Note that the lesion volumes for white and / or gray matter regions analyzed per patient do not sum up to the entire lesion volume as many areas within the lesion (e.g. CSF-filled sulcal spaces) were excluded from analysis.

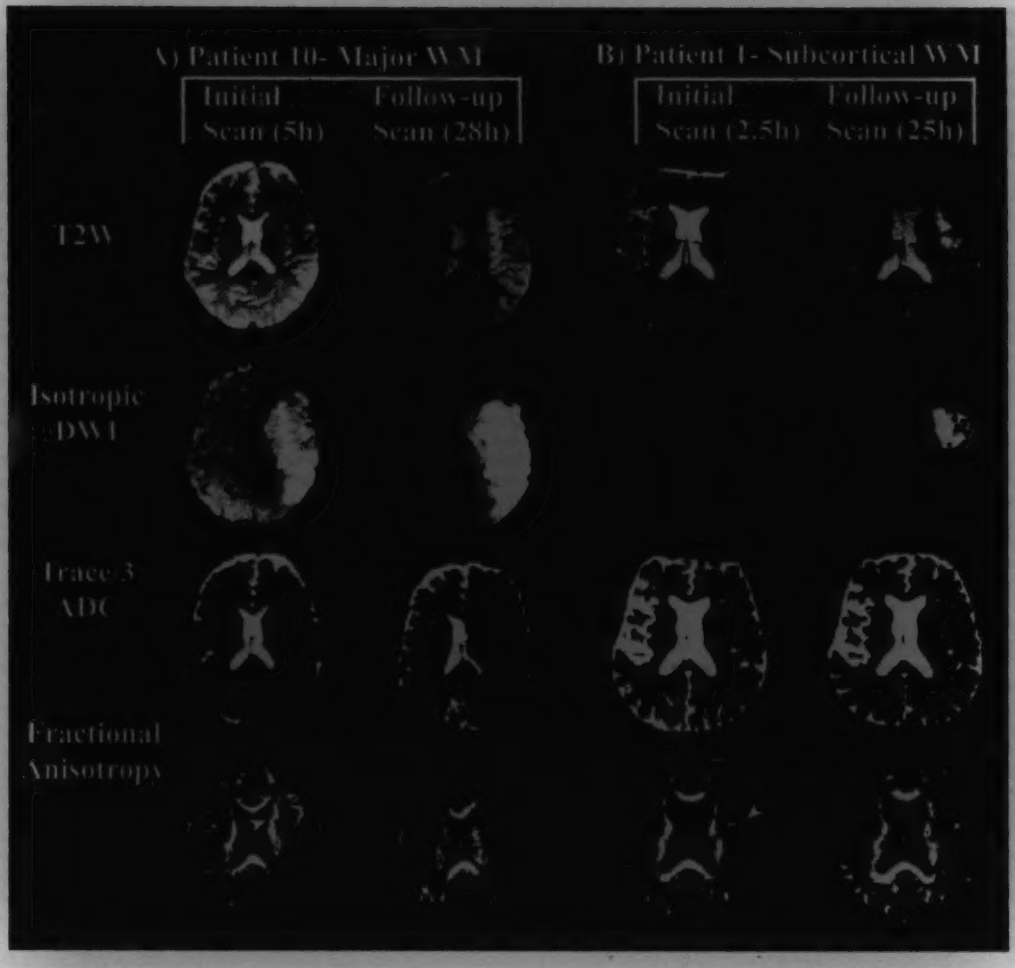

Figure 10-1: T2-weighted images (T2W; b = 0 s/mm^2), isotropic diffusion-weighted images (DWI; b = 1000 s/mm^2), Trace/3 ADC and FA maps of one slice from 2 patients (patient 10 (A) and patient 1 (B); Table 10-1) during the initial and follow-up scanning phases post stroke onset. Note that the contrast of the FA maps for both time periods in both patients was made extreme. This allowed the visualization of A) major WM tracts such as the anterior limb of the internal capsule (arrowheads) within the ischemic core of patient 10, where FA was elevated (up to 28%) relative to the contralateral side during the initial phase (5h) and declined (11% decrease) in the follow-up phase (28h) post symptom onset. B) Similarly subcortical WM regions such as the precentral gyrus in patient 1 (arrowhead) showed elevated rFA (27% increase) during the initial period (2.5h), and constant rFA (but reduced from the initial phase) at 25 hours post stroke onset.

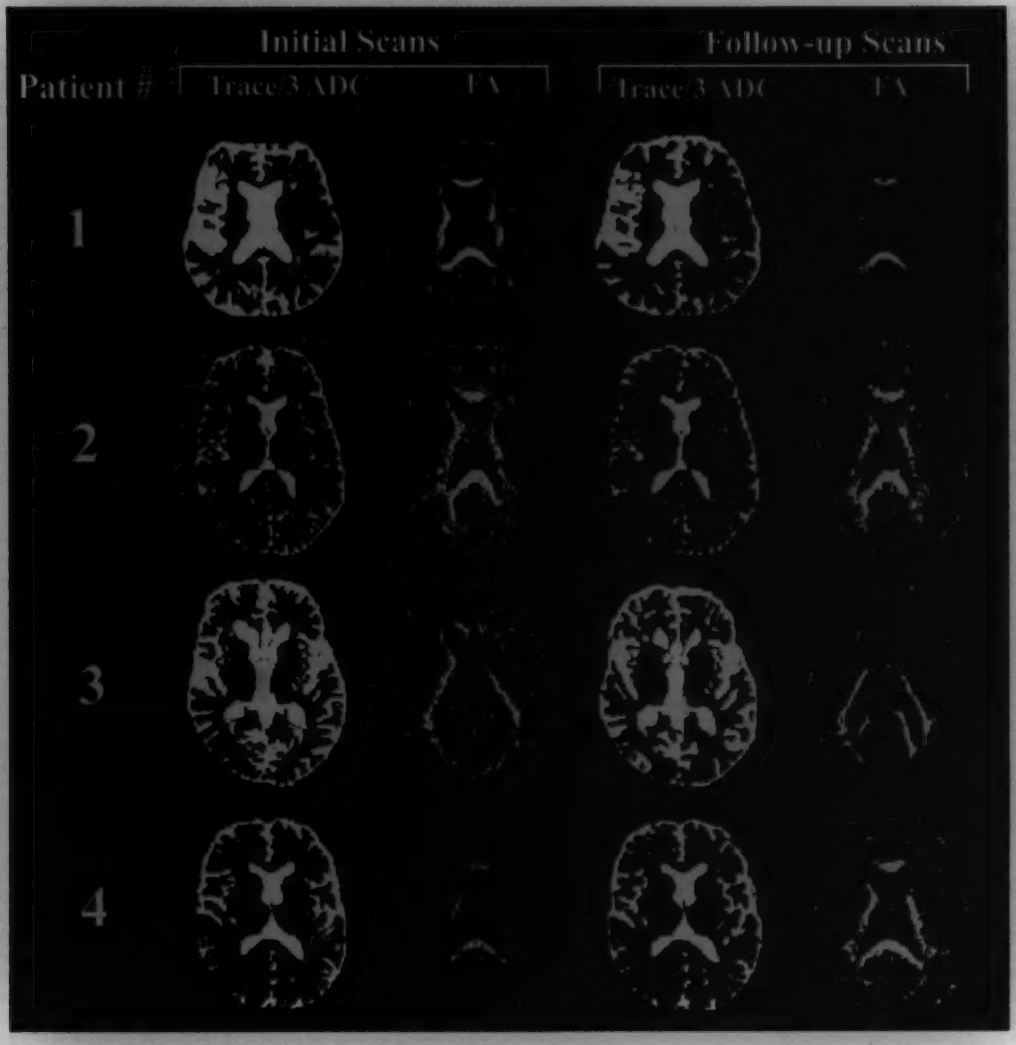

Figure 10-2: Trace/3 ADC and FA maps of one slice from the initial and follow-up scanning phases of patients 1 to 4 (Refer to Table 10-1 for patient details) post stroke onset.

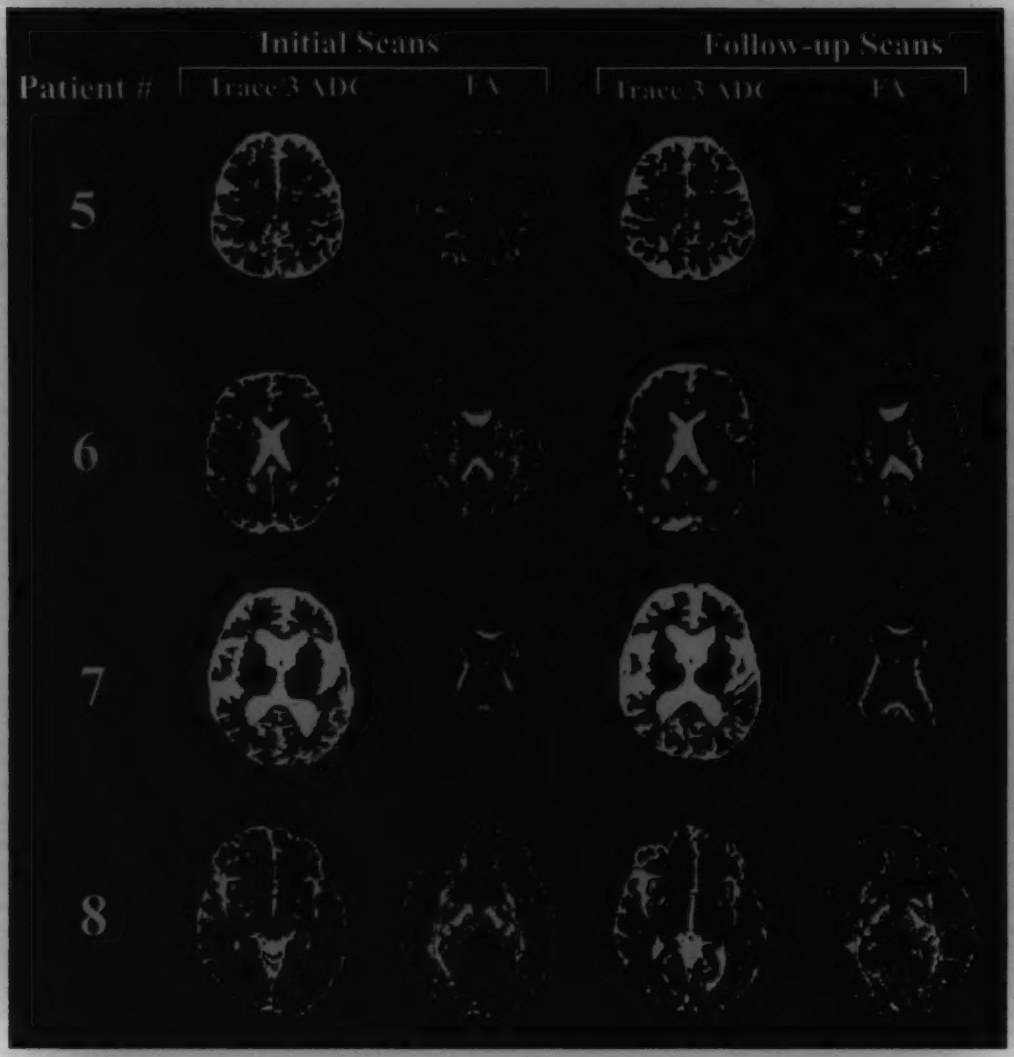

Figure 10-3: Trace/3 ADC and FA maps of one slice from the initial and follow-up scanning phases of patients 5 to 8 (Refer to Table 10-1 for patient details) after stroke.

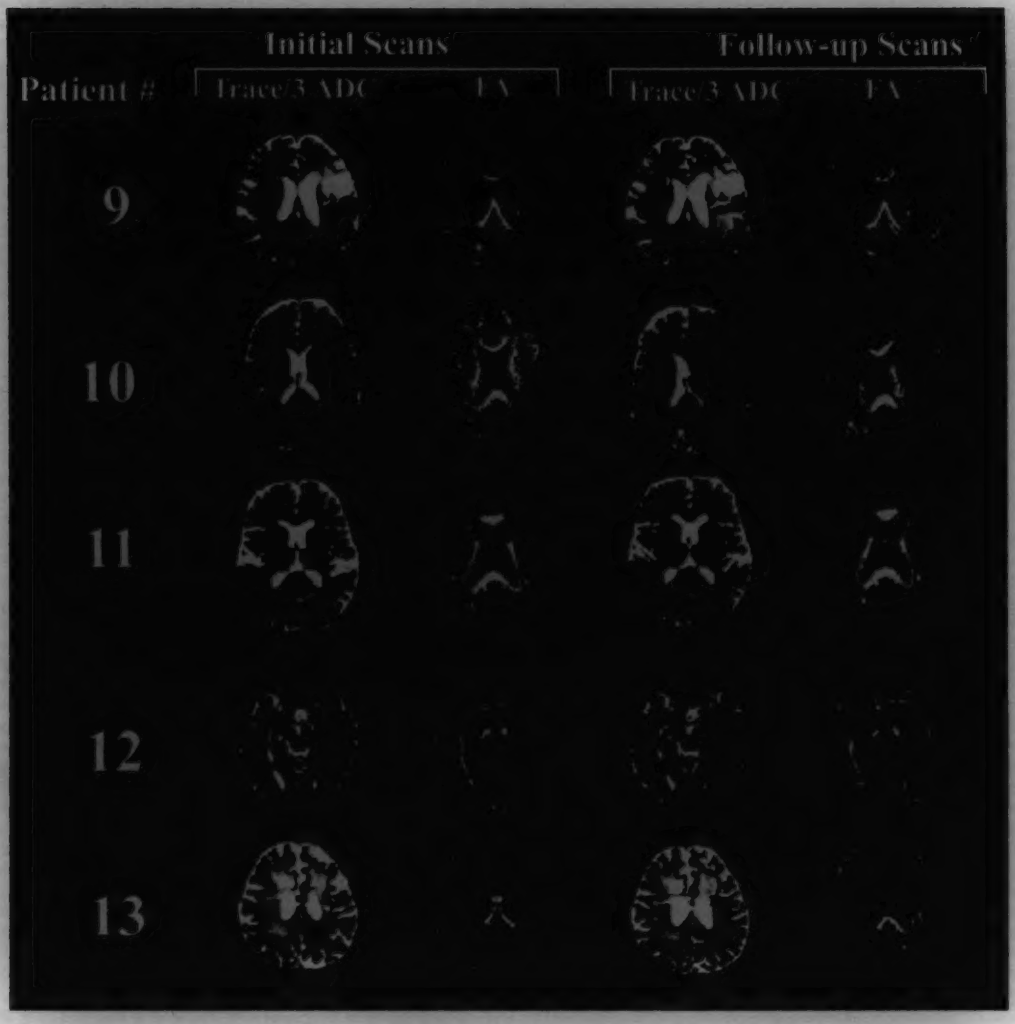

Figure 10-4: Trace/3 ADC and FA maps of one slice from the initial and follow-up scanning phases of patients 9 to 13 (Refer to Table 10-1 for patient details) following stroke onset.

10.3.1 Longitudinal Changes of Diffusion Anisotropy in White Matter

The initial (≤7h) and follow-up (21.5-29h) time course of relative FA (rFA, ipsilateral/contralateral FA), rTrace/3 ADC and rT2-weighted signal intensity changes in the 10 patients with lesions involving major WM tracts and subcortical WM regions is shown in Figures 10-5, 10-6 and 10-7. Although 10 patients demonstrated subcortical WM lesions during the initial and follow-up phases post stroke onset (Figure 10-5B), one patient (patient 7) had subcortical WM involvement only within the follow-up period after stroke. Consistently low (~40% decline) Trace/3 ADC values were observed in major and subcortical WM for all patients during both phases of onset (Figure 10-6 A, B); however, rFA was elevated in the initial phase (above unity) in several patients and predominantly reduced in the follow-up phase for most patients (Figure 10-7 A, B). Steady increases in rT2-weighted signal intensity were seen in major WM tracts and subcortical WM from the initial to the follow-up phase post symptom onset (Figure 10-6 A, B).

The mean relative Trace/3 ADC, FA and T2-weighted signal intensity values for 10 patients showing major WM tract lesions in the initial and follow-up phases post stroke are given in Table 10-3. By grouping data in the major WM tract category (for all ROIs of patients with major WM tract lesions), we observed a significant increase in mean rFA (6% elevation, $p<0.01$) within the initial phase and a subsequent decline (8% reduction, $p<0.01$) during the follow-up phase of stroke onset (Table 10-3). Of the 10 patients that had major WM tract lesions, 4 showed increased FA values (7% to 21% rise), 1 patient demonstrated reduced rFA (22% decline) and 5 others displayed constant FA values within the initial phase of stroke onset (2.5-7h, Figure 10-5A). Of the 4 patients showing increased FA values within the initial phase, only one (Patient 1) demonstrated persistent elevated FA during their follow-up scan at 25 hours post symptom onset, although reduced by 9% from the initial phase (Figure 10-7A). The mean rFA values in these 4 patients were 1.10 ± 0.11 ($p<0.01$) and 0.96 ± 0.12 ($p=0.03$) during the initial and follow-up (21.5-29h) time periods, respectively. The root of these FA changes can be accounted by the changes in the eigenvalues since FA is computed from the eigenvalues. On average, in the 4 patients showing elevated rFA in major WM tracts in the initial phase (2.5-7h), the relative principal (λ_1), secondary (λ_2) and tertiary (λ_3) eigenvalues declined by 39%, 43% and 47%, respectively (data not shown). The greater reduction of $r\lambda_3$ relative to $r\lambda_1$ and $r\lambda_2$ provides a rationalization for the increased FA. In this same group of patients, during the follow-up phase (21.5-29h), $r\lambda_1$, $r\lambda_2$ and $r\lambda_3$ decreased by 50%, 44% and 49%, respectively. The slightly greater reduction of $r\lambda_1$ (~3.5% decrease) relative to $r\lambda_2$ and $r\lambda_3$ accounts for the small decrease observed in rFA values (4% drops) during the follow-up phase. The absolute ipsilateral and contralateral eigenvalues of major WM tracts from the 4 patients are not shown due to known variations in eigenvalues of the different major central WM tracts (Chapter 7, Table 7-4).

On average in all patients showing major WM tract lesions, relative T2-weighted signal intensity increased up to 19% ($p<0.01$) (Table 10-3) from the initial to the follow-up phase with an inverse correlation between mean rFA and rT2-weighted signal intensity ($R= -0.29$, $p=0.03$) observed during the initial phase only (Figure 10-8 A, B).

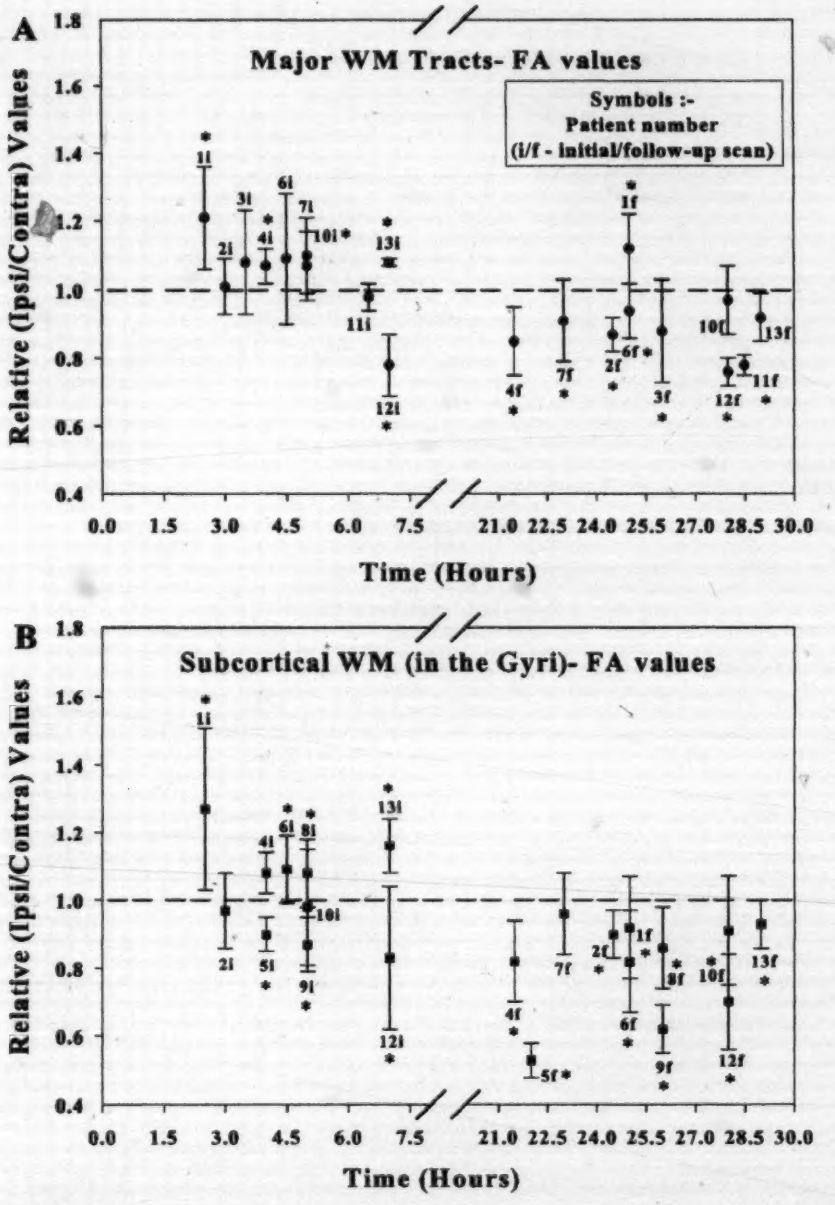

Figure 10-5: Initial (≤7 hours) and follow-up (21.5–29 hours) time course of relative (r) fractional anisotropy (FA) changes in A) major WM tracts (N=10) and B) subcortical WM (in the Gyri, N=11) after ischemic stroke onset (refer to Table 10-1 for patient details). The error bars reflect the standard deviation over the ROIs measured per patient. * denotes significant differences between the ipsilateral and contralateral FA values for each patient.

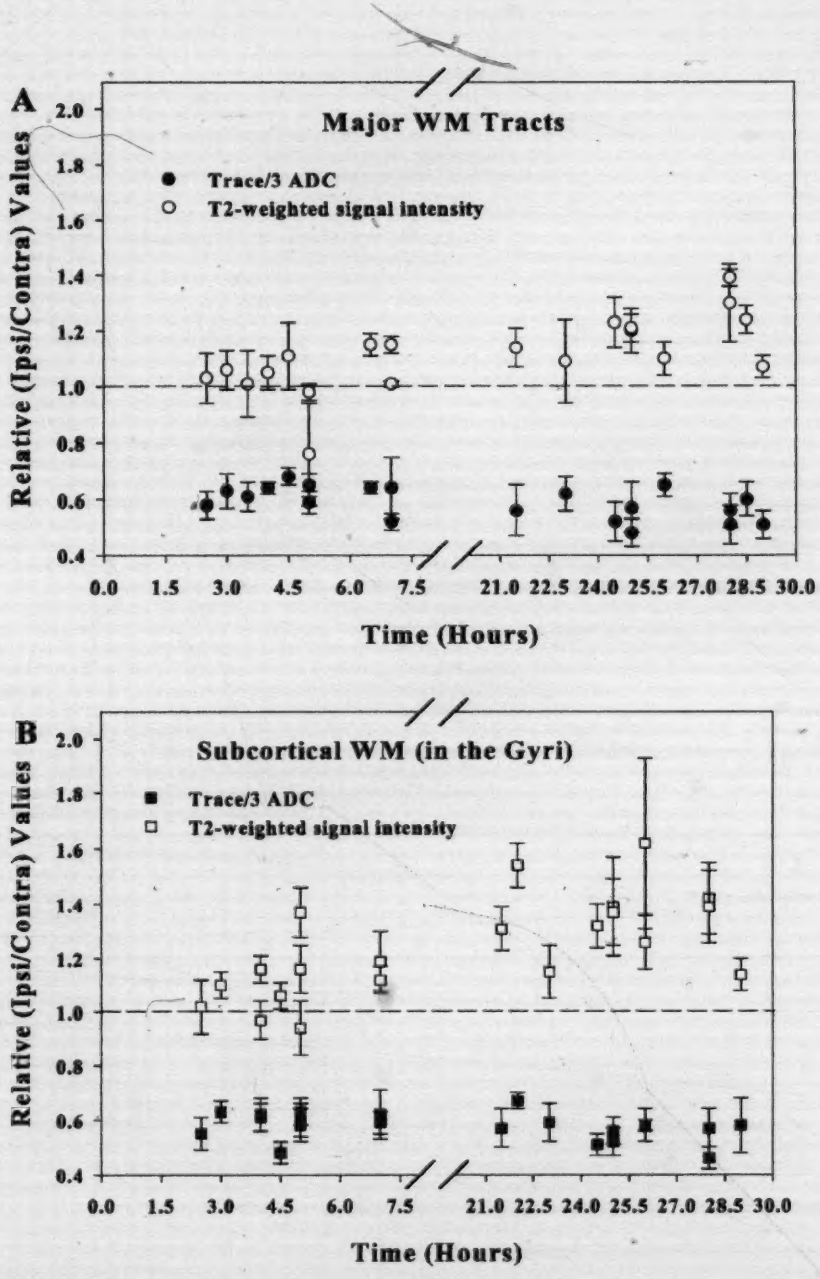

Figure 10-6: Initial (≤7 hours) and follow-up (21.5–29 hours) time course of relative (r) Trace/3 ADC and T2-weighted signal intensity changes in A) major WM tracts (N=10) and B) subcortical WM (in the Gyri, N=11) after ischemic stroke onset. The error bars reflect the standard deviation over the ROIs measured per patient.

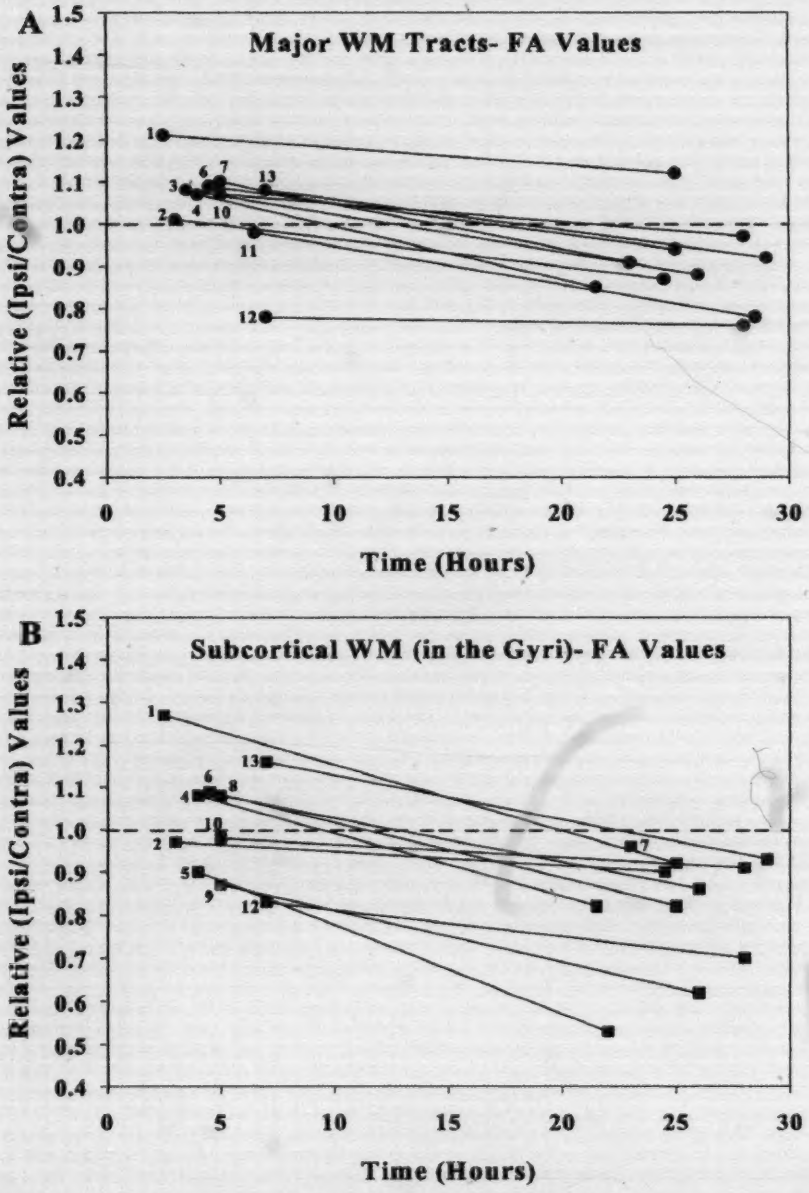

Figure 10-7: Time course of Relative FA in (A) major WM tracts (N=10) and (B) subcortical WM (N=11) following stroke onset. The solid lines connect the mean rFA serial data points of each patient between the initial (≤7h) and follow-up (21.5-29h) scanning phases post symptom onset. Relative FA values were consistently reduced from the early time point in both tissue categories during the follow-up phase after stroke, even if the initial value from the early time point was elevated at or below unity.

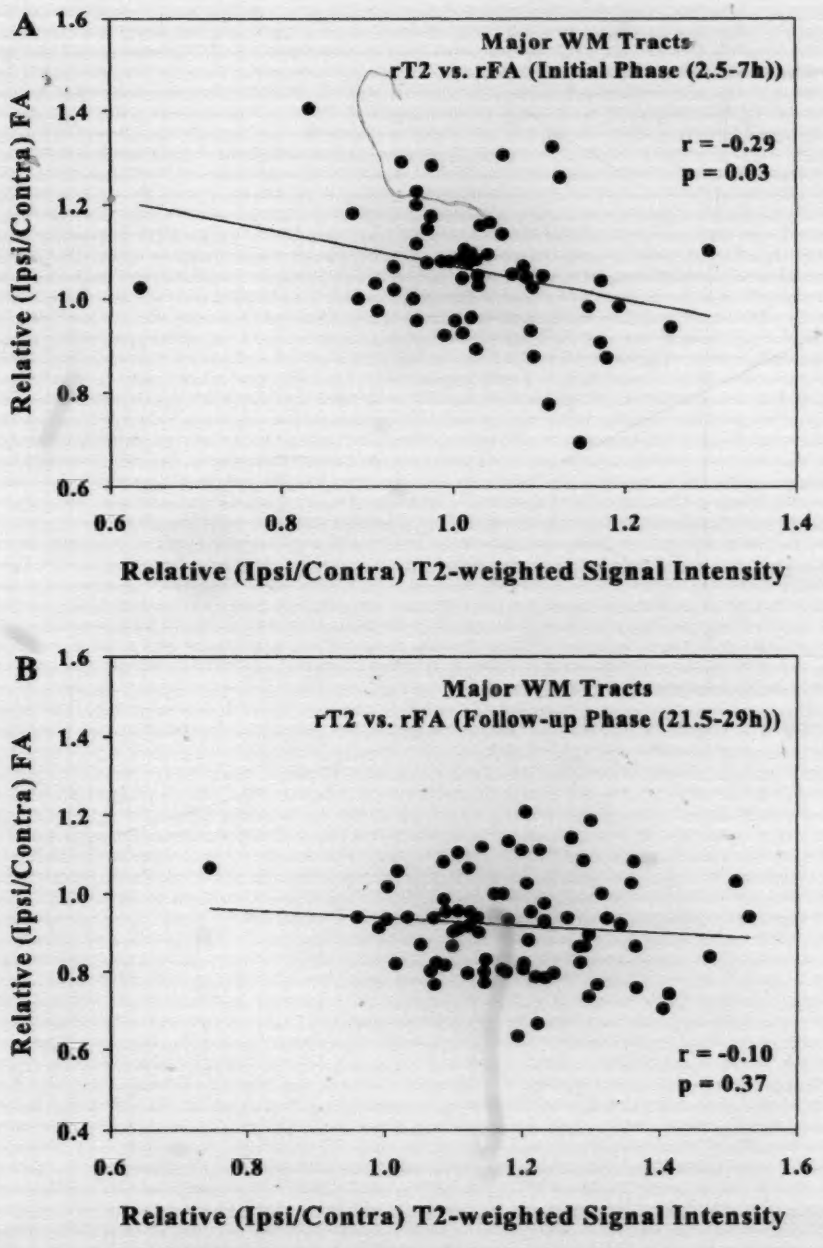

Figure 10-8: Trends of rT2-weighted signal intensity (on b = 0 s/mm^2 EPI images) versus rFA during the (A) initial (56 ROIs) and (B) follow-up (77 ROIs) phases post stroke in 10 patients with major WM tract lesions. The follow-up phase T2 increases are greater (up to 50%) than the initial phase (up to 30%), however no significant correlations were observed between rT2 and rFA in the follow-up period.

Table 10-3: Mean (±SD) relative (r) Trace/3 ADC, FA and T2-weighted signal intensity values in 13 patients with major and subcortical WM tract lesions within the initial (2.5-7h) and follow-up (21.5-29h) phases post stroke onset

	Major WM Tracts (N=10)		Subcortical WM (in the Gyri) (N=11)	
	Initial Phase (p)	Follow-up Phase (p)	Initial Phase (p)	Follow-up Phase (p)
rTrace/3 ADC	0.61 ± 0.06 (<0.01)	0.56 ± 0.09 (<0.01)	0.59 ± 0.07 (<0.01)	0.53 ± 0.07 (<0.01)
rFA	1.06 ± 0.13 (0.01)	0.92 ± 0.12 (<0.01)	1.10 ± 0.18 (0.77)	0.86 ± 0.16 (<0.01)
rT2-weighted signal intensity	1.03 ± 0.11 (0.07)	1.19 ± 0.13 (<0.01)	1.09 ± 0.13 (<0.01)	1.35 ± 0.15 (<0.01)

Relative Trace/3 ADC, FA and T2-weighted signal intensity values were significantly different ($p<0.01$) between the initial and follow-up phases in both, major and subcortical WM tract categories.

The mean relative Trace/3 ADC, FA and T2-weighted signal intensity values for 11 patients showing subcortical WM lesions in the initial and follow-up phases post stroke are given in Table 10-3. Although we did not observe a significant increase in rFA in grouped data of patients with subcortical WM lesions, of the 10 patients that had subcortical WM (in the Gyri) involvement within their Trace/3 ADC-defined ischemic lesions in the initial phase (2.5-7h), 4 showed elevated FA values (8% to 27% increases), 3 showed reduced FA values (10% to 17% decreases) and 3 demonstrated constant FA values (Figures 10-5B and 10-7B). Interestingly the same 4 patients with increased FA values in the initial phase showed significantly reduced FA values (7% to 18% declines) in the follow-up phase within their subcortical WM lesions. The mean rFA values in these 4 patients were 1.13 ± 0.14 ($p<0.01$) and 0.89 ± 0.14 ($p<0.01$) during the initial and follow-up (25-29h) time periods, respectively. On average, in the 4 patients showing elevated rFA values in subcortical WM tracts in the initial phase (2.5-7h), the relative principal (λ_1), secondary (λ_2) and tertiary (λ_3) eigenvalues declined by 41%, 42% and 47%, respectively, similar to the trend observed in patients showing elevated FA of major WM tract lesions. The greater reduction of $r\lambda_3$ relative to $r\lambda_1$ and $r\lambda_2$ ($p<0.01$) accounts for the increased FA. In this same group of 4 patients, during the follow-up phase (25-29h), $r\lambda_1$, $r\lambda_2$ and $r\lambda_3$ decreased by 47%, 42% and 39%, respectively. Here, a ~7% greater decrease in $r\lambda_1$ compared to $r\lambda_2$ and $r\lambda_3$ leads to the reduction of rFA values during the follow-up phase. The absolute mean (±SD) ipsilateral and contralateral eigenvalues of the subcortical WM tracts from the 4 patients are given in Table 10-4. This data has been presented due to the uniformity of gyral WM diffusion parameters throughout the brain (Chapter 7, Table 7-4).

On average, in all patients showing subcortical WM lesions, relative rT2-weighted signal intensity was elevated by 9% and 35% in the initial and follow-up periods ($p<0.01$, Table 10-3), respectively, with inverse correlations between mean rFA and rT2-weighted signal intensity during the initial ($R= -0.33$, $p<0.01$) and follow-up ($R= -0.40$, $p<0.01$) phases (Figure 10-9 A, B).

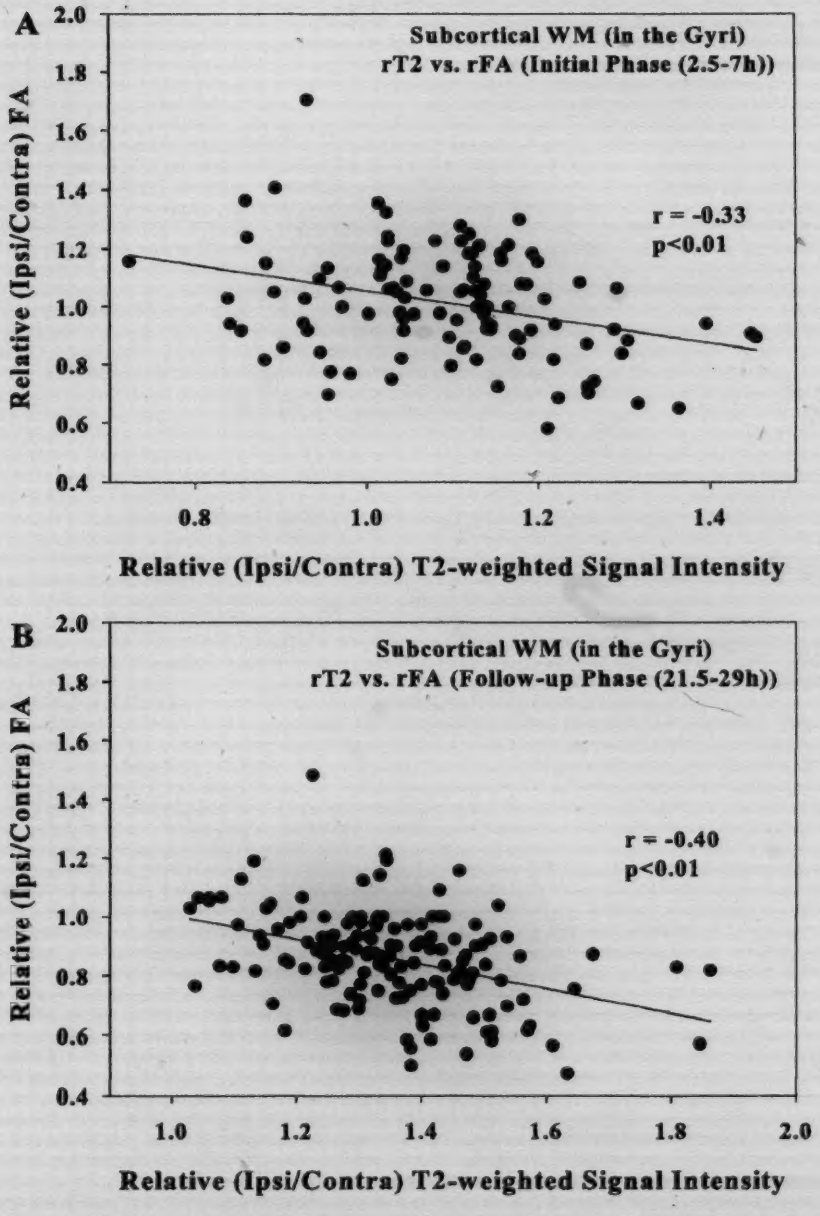

Figure 10-9: Trends of rT2-weighted signal intensity (on b = 0 s/mm^2 EPI images) versus rFA during the (A) initial (108 ROIs) and (B) follow-up (149 ROIs) phases post stroke in 11 patients with subcortical WM lesions. Note that the follow-up phase T2 increases are much larger (up to 85%) than the initial phase increases (up to 45%) and that a substantial number of ROIs are darker on T2 in the lesion than on the contralateral side (i.e. rT2<1) only in the 2.5-7h time frame post stroke.

Table 10-4: Mean (±SD) ipsilateral and contralateral eigenvalues (λ_1, λ_2 and λ_3 ($x10^{-3}$ mm^2/s)) in 4 patients (patient 1, 6, 8 and 13; Table 10-1) with subcortical WM lesions showing elevated rFA in the initial phase and reduced rFA in the follow-up phase post symptom onset.

	Initial Phase (2.5-7h)				Follow-up Phase (25-29h)			
	Contralateral	Ipsilateral	%DIFF[a]	p	Contralateral	Ipsilateral	%DIFF[a]	p
λ_1	1.13 ± 0.09	0.66 ± 0.10	41%	<0.01	1.21 ± 0.10	0.63 ± 0.06	47%	<0.01
λ_2	0.79 ± 0.06	0.46 ± 0.07	42%	<0.01	0.78 ± 0.07	0.45 ± 0.05	42%	<0.01
λ_3	0.55 ± 0.08	0.29 ± 0.06	47%	<0.01	0.50 ± 0.07	0.30 ± 0.05	39%	<0.01

Values are $x10^{-3}$ mm^2/s; [a]%DIFF, % difference between ipsilateral and contralateral eigenvalues

10.3.2 Longitudinal Changes of Diffusion Anisotropy in Gray Matter

Trends of rFA, rADC and rT2-weighted signal intensity values for the initial (≤7h) and follow-up (21.5-29h) time periods in the 10 patients showing deep and cortical GM involvement within their ischemic lesions are shown in Figures 10-10, 10-11 and 10-12. Trace/3 ADC values were consistently low (~40% decline) for deep and cortical GM lesions (Figure 10-11 A, B) over time, however rFA values differed in time for both tissue categories and were comparable to WM in that FA was increased (above unity) in the initial phase (2.5-7h) and subsequently reduced in the follow-up phase (22-28h) in most patients post stroke onset (Figure 10-12 A, B). In line with the major WM tract lesions, increases in rT2-weighted signal intensity were also seen in deep GM and cortical GM from the initial to the follow-up phase post symptom onset (Figure 10-11 A, B).

The mean relative Trace/3 ADC, FA and T2-weighted signal intensity values for patients showing deep (N=4) and cortical (N=8) GM lesions in the initial and follow-up phases post stroke are given in Table 10-5. Unlike cortical GM, deep GM did not demonstrate a significant increase in mean rFA within the initial phase. However, both tissue categories showed reduced mean rFA (7%-19% drops) in the follow-up periods (Table 10-5). Of the 4 patients demonstrating deep GM lesions, one (patient 10) showed elevated rFA values during the initial phase (1.07 ± 0.06, p=0.02) and subsequent decreases in the follow-up phase (0.76 ± 0.09, p=0.01) after symptom onset (Figure 10-10A). Of the remaining 3 patients, 1 showed reduced rFA and the 2 others did not demonstrate any significant changes in mean rFA during the initial scanning phase of stroke onset. The mean pattern of rT2-weighted signal intensity changes in deep GM were equivalent to subcortical WM with increases of 9% and 51% in the initial and follow-up phases ($p<0.05$) (Table 10-5), respectively, and inverse correlations between mean rFA and rT2-weighted signal intensity during the initial (R= -0.57, p=0.01) and follow-up (R= -0.53, p=0.02) phases (Figure 10-13).

In the group of 8 patients with cortical GM lesions, 5 demonstrated significantly elevated FA values, whereas the other 3 patients showed constant FA values within the initial phase (2.5-5h) of stroke onset (Figure 10-10B). By grouping the individual 5 patients with elevated FA values in the initial phase, we noted cortical GM changes in rFA that were equivalent to the subcortical WM group of 4 patients, with a rise in mean rFA in the initial phase (1.22 ± 0.13, $p<0.01$) and decreases in the follow-up phase (0.84 ± 0.11, $p<0.01$). Variations in the eigenvalues and increases in T2-weighted signal intensity from the initial to the follow-up phase for cortical GM were similar to those noted for subcortical WM. However, no correlations were seen between rFA and rT2-weighted signal intensity during the initial or follow-up phases post stroke for cortical GM (Figure 10-14).

Table 10-5: Mean (±SD) relative (r) Trace/3 ADC, FA and T2-weighted signal intensity values in 10 patients with deep and cortical GM lesions within the initial (2.5-7h) and follow-up (22-28h) phases post stroke onset

	Deep GM (N=4)		Cortical GM (N=8)	
	Initial Phase (p)	Follow-up Phase (p)	Initial Phase (p)	Follow-up Phase (p)
rTrace/3 ADC	0.62 ± 0.05 (<0.01)	0.62 ± 0.05 (<0.01)	0.60 ± 0.05 (<0.01)	0.56 ± 0.06 (<0.01)
rFA	1.07 ± 0.18 (0.11)	0.81 ± 0.11 (<0.01)	1.16 ± 0.15 (<0.01)	0.93 ± 0.14 (<0.01)
rT2-weighted signal intensity	1.09 ± 0.15 (0.02)	1.51 ± 0.19 (<0.01)	1.17 ± 0.18 (<0.01)	1.56 ± 0.18 (<0.01)

Relative FA and T2-weighted signal intensity values were significantly different ($p<0.01$) between the initial and follow-up phases in both, deep and cortical GM categories. Relative Trace/3 ADC values were significantly different ($p<0.01$) between the initial and follow-up phases for cortical GM only.

Overall in our serial stroke study, 9/13 patients within 7h post symptom onset showed elevated FA in at least one of the four tissue categories, and within the same cohort 11/13 patients showed reduced FA in ischemic WM and GM regions from 21.5-29h after stroke.

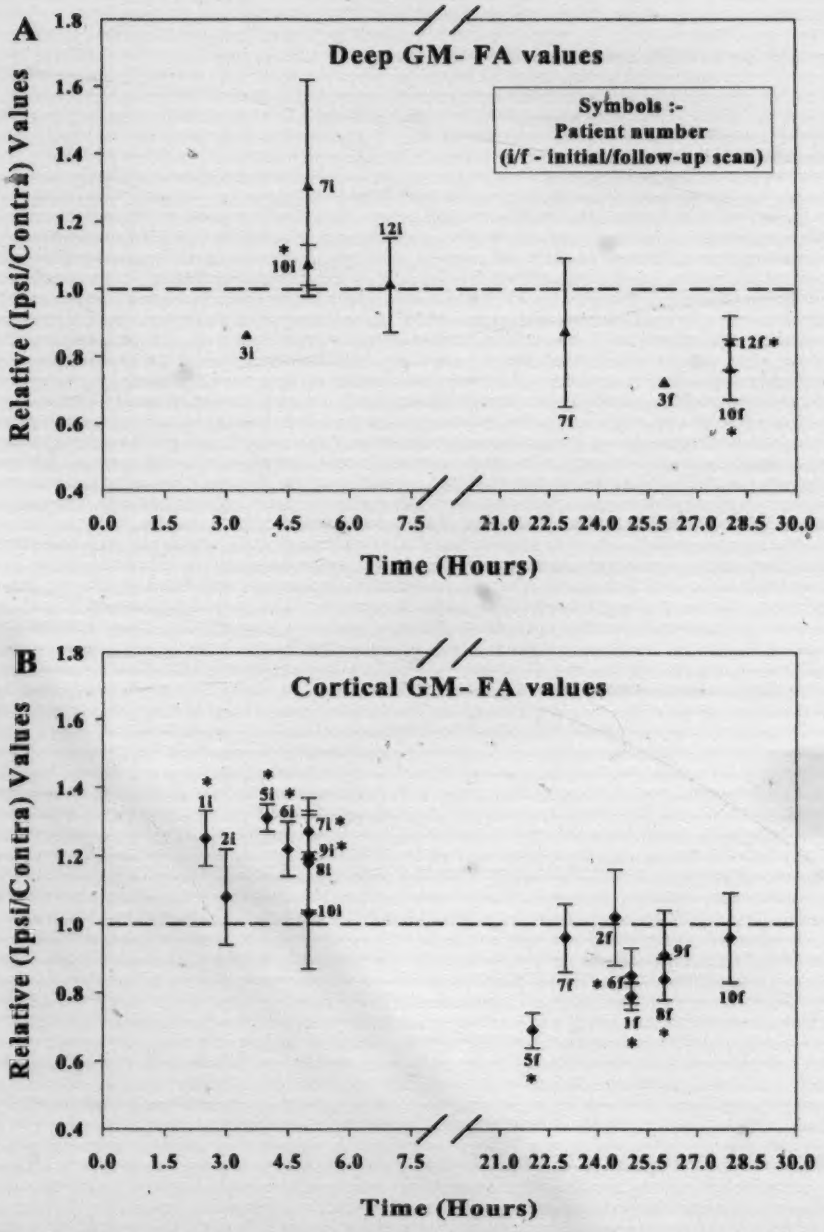

Figure 10-10: Initial (≤7 hours) and follow-up (22–29 hours) time course of relative (r) fractional anisotropy (FA) changes in A) deep GM (N=4) and B) cortical GM (N=8) after ischemic stroke onset (refer to Table 10-1 for patient details). The error bars reflect the standard deviation over the ROIs measured per patient. * denotes significant differences between the ipsilateral and contralateral FA values for each patient.

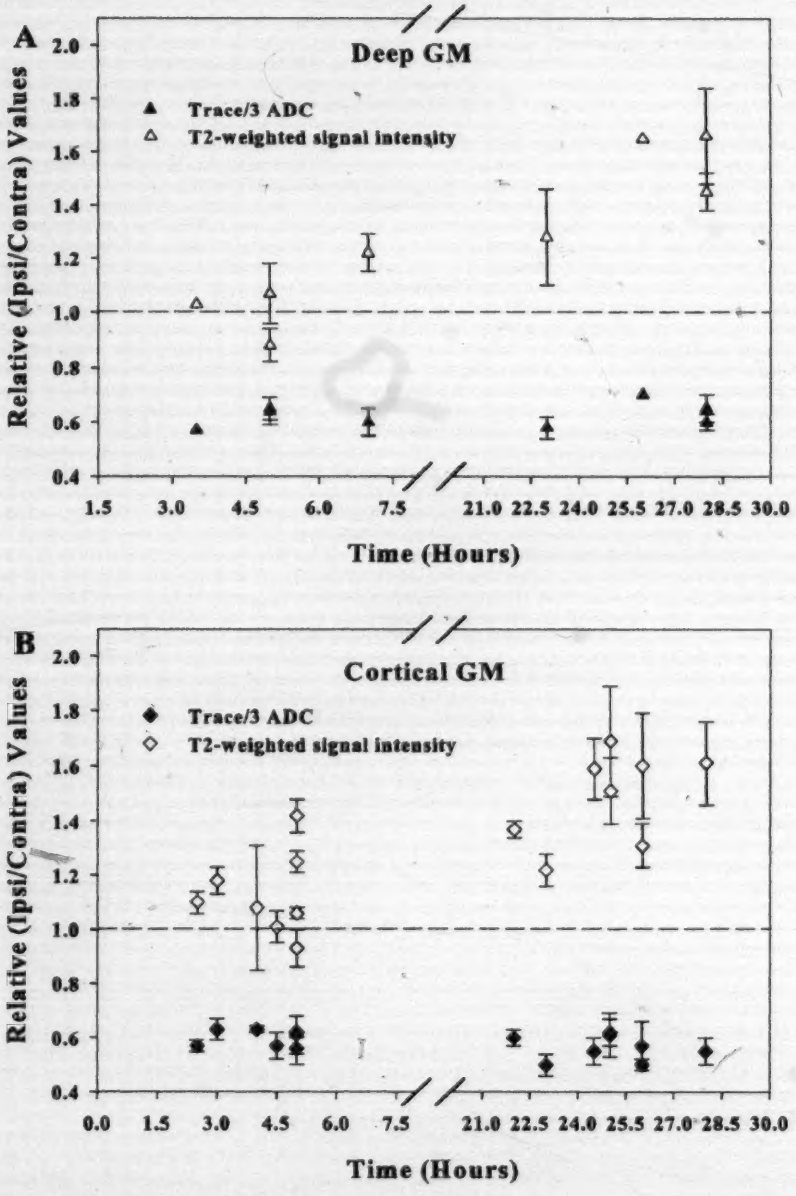

Figure 10-11: Initial (≤7 hours) and follow-up (22–29 hours) time course of relative (r) Trace/3 ADC and T2-weighted signal intensity changes in A) deep GM (N=4) and B) cortical GM (N=8) after ischemic stroke onset. The error bars reflect the standard deviation over the ROIs measured per patient.

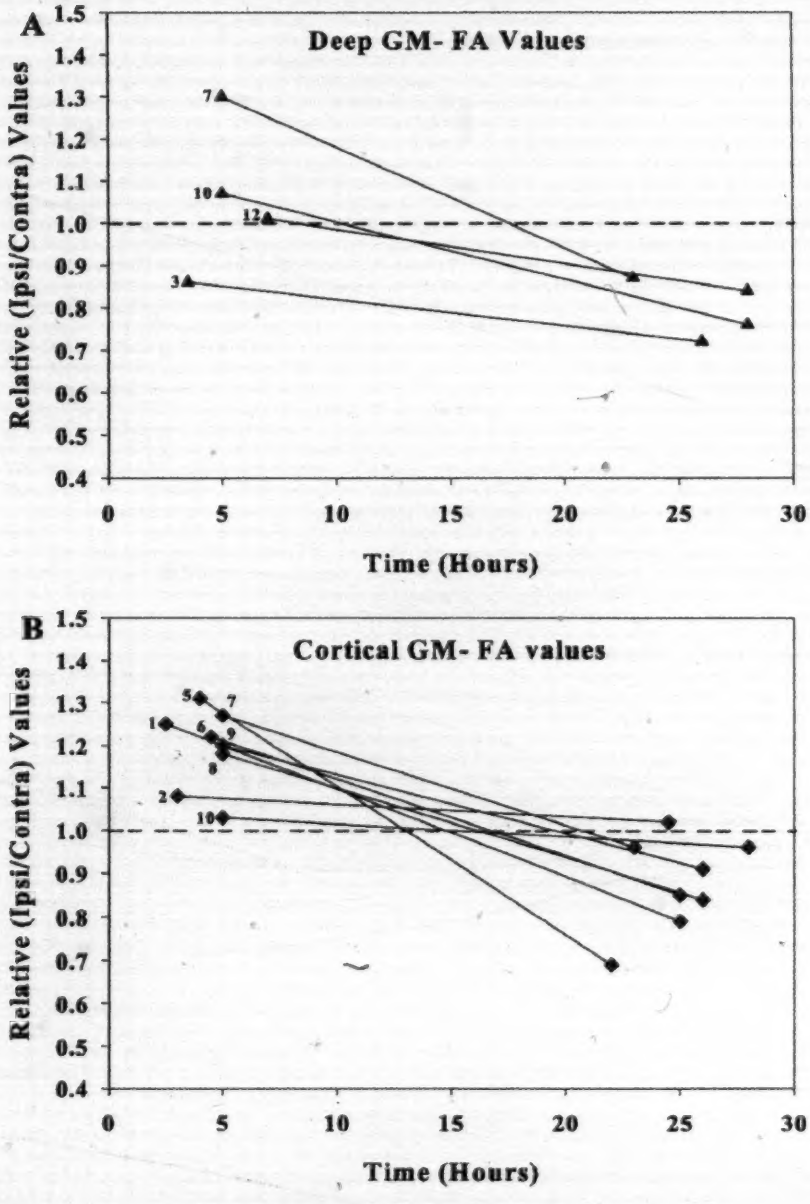

Figure 10-12: Time course of Relative FA in deep GM (N=4), cortical GM (N=8) following stroke onset. The solid lines connect the mean rFA serial data points of each patient between the initial (≤7h) and follow-up (22-29h) scanning phases post symptom onset.

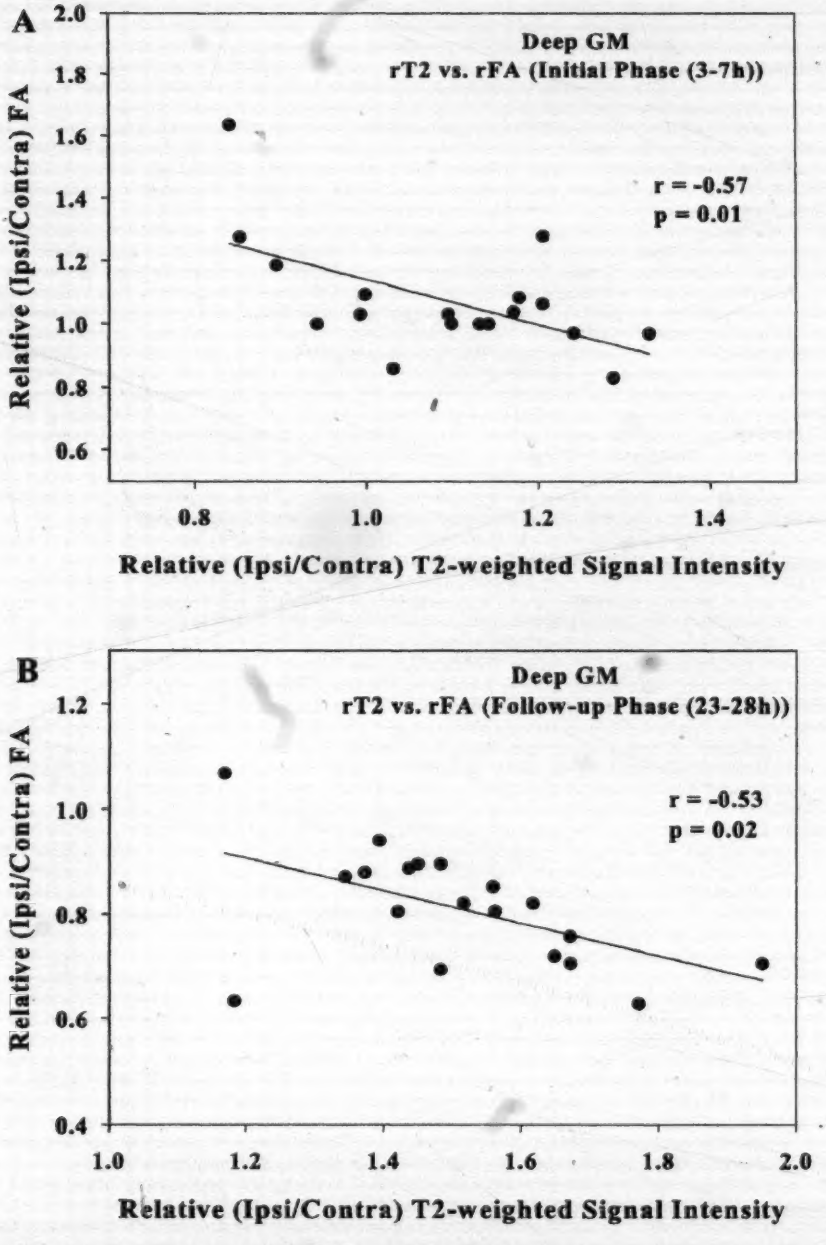

Figure 10-13: Trends of rT2-weighted signal intensity (on b = 0 s/mm^2 EPI images) versus rFA during the (A) initial (18 ROIs) and (B) follow-up (19 ROIs) phases post stroke in 4 patients with deep GM lesions. Note that the follow-up phase T2 increases are much larger (up to 95%) than the initial phase increases (up to 33%).

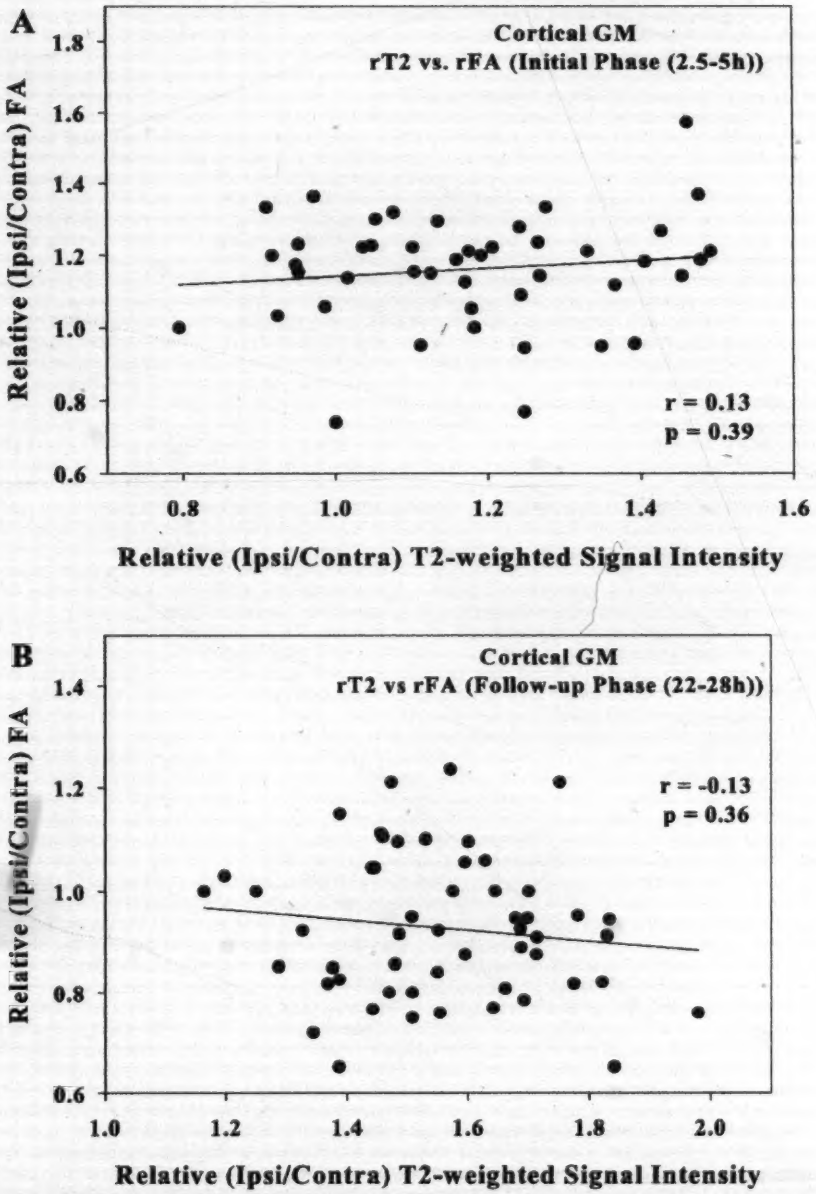

Figure 10-14: Trends of rT2-weighted signal intensity (on b = 0 s/mm^2 EPI images) versus rFA during the (A) initial (45 ROIs) and (B) follow-up (53 ROIs) phases post stroke in 8 patients with cortical GM lesions. Note that the follow-up phase T2 increases are twice as large (up to 98%) as the initial phase increases (up to 48%). No significant correlations between rT2 and rFA were observed during the initial and follow-up periods in this tissue category.

10.4 Discussion

The major focus of our study was on diffusion metrics in discrete ischemic WM and GM regions located centrally (major WM tracts and deep GM areas) and peripherally (subcortical WM and cortical GM), defined by >30% drops in Trace/3 ADC. These regions were analyzed individually to identify any varying responses between the four subsets of tissues. The most novel finding of our study in a group of 13 patients scanned during 2 phases, the initial (2.5-7h) and follow-up (21.5-29h) phase post ischemic stroke onset was that rFA was significantly elevated in major WM tracts (4/10 patients, mean rFA increase = 10%), subcortical WM (4/10 patients, mean rFA increase = 13%), deep GM (1/4 patients, 7% increase in rFA) and cortical GM (5/8 patients, mean rFA increase = 22%) in the initial phase and reduced (mean decrease ≅ 10%) in the same patients during the follow-up phase. Elevations in diffusion anisotropy occurred mainly in the initial phase (≤7h) after stroke (with the exception of patient 1 who demonstrated elevated rFA in major WM during the follow-up phase (Figure 10-5A)). Furthermore, the pattern of reductions in the eigenvalues provided support for the changes observed in rFA. A greater reduction in the perpendicular diffusivity ($r\lambda_3$) relative to the parallel diffusivity ($r\lambda_1$) was observed during the initial phase, accounting for the elevations in mean rFA, whereas a reverse pattern of decreases in the eigenvalues with a greater reduction in $r\lambda_1$ compared to $r\lambda_2$ and $r\lambda_3$, was noted during the follow-up phase resulting in reductions of mean rFA for major and subcortical WM tracts, and deep and cortical GM areas. We observed significant negative correlations of rT2-weighted signal intensity versus rFA during the initial and follow-up periods in subcortical WM and deep GM, and only for the follow-up phase in major WM tracts.

10.4.1 Trace/3 ADC Changes in White and Gray Matter

Trace/3 ADC values (~40% reductions) during both, the initial and follow-up time periods post stroke onset were consistently low in all 4 tissue categories. Overall, during the initial phase (2.5-7h), no significant differences in Trace/3 ADC values were observed between the centrally located ischemic major WM and deep GM, and between the peripheral ischemic subcortical WM and cortical GM regions, as previously reported (Sorensen *et al* 1999). However, in the follow-up phase (21.5-29h), a steeper decline in rTrace/3 ADC of major WM tracts ($0.56\pm0.09 \times 10^{-3}$ mm^2/s) relative to deep GM areas ($0.62 \pm 0.05 \times 10^{-3}$ mm^2/s), and subcortical WM ($0.53 \pm 0.07 \times 10^{-3}$ mm^2/s) compared to cortical GM ($0.56 \pm 0.06 \times 10^{-3}$ mm^2/s) was observed ($p<0.01$) (Tables 10-3 and 10-5; Figures 10-6 and 10-11). Our follow-up findings are similar to those reported by others who have noted a 5% to 20% greater decrease in Trace/3 ADC of ischemic WM tracts relative to GM in grouped data ≤24h of stroke onset, thereby suggesting that WM due to its significantly higher anisotropic microstructural characteristics is compromised to a greater extent than GM in subacute (~24h) stroke (Mukherjee *et al* 2000; Munoz Maniega *et al* 2004; Yang *et al* 1999).

10.4.2 Comparison with Previous Serial DTI Reports of Ischemic Stroke

Of the 3 serial DTI studies of human stroke reporting FA changes from ≤24 hours following stroke onset (Munoz Maniega *et al* 2004; Yang *et al* 1999; Zelaya *et al* 1999), only 1 study by Yang *et al.*(Yang *et al* 1999) reported elevations in FA in individual patients for WM, cortical GM and mixed tissue areas ≤7h post stroke (5% to 40% increases). Although our initial phase (2.5-7h) findings are in agreement with their FA reports of ≤7h, they also showed elevations in FA (20% to 45% increases) up to 96 hours post onset in some of their serially scanned patients. The latter trends in FA contrast with our data where we show that reductions (3% to 47% decreases) in rFA occur within all 4 tissue categories during the follow-up period (21.5-29h; Figures 10-7 and 10-12), with only 2 exceptions (patient 1 showed increased rFA in major WM at 25h, and patient 2 showed constant rFA in cortical GM at 24.5h post onset). Furthermore, Yang *et al.* (1999) acquired only 3-direction diffusion-weighted images in most of their patients, and combined gyral WM and GM regions together for analysis, despite the known variations in FA between those tissues. We employed the full diffusion tensor in our patient cohort and overcame any segmentation-related limitations by measuring unique WM and GM regions distinctly within the lesion and in the corresponding contralateral hemisphere. Although we did not measure FA changes in the time period between the 2 phases (initial and follow-up) of stroke onset in this study, we have previously reported consistent FA reductions (9% to 26% drops; $p<0.05$) from 9-21h in a cross-sectional patient population (Chapter 8, Figures 8-3 and 8-4) Other serial studies of human stroke have observed a decreasing trend of FA (~8-54% reductions) from <24h to 90 days following stroke onset (Munoz Maniega *et al* 2004; Zelaya *et al* 1999).

Results from serial studies in animal models of ischemia are consistent with our findings of elevated FA in the initial phase and reduced FA within the follow-up phase after stroke. Liu *et al.*(Liu *et al* 2007) reported elevations of FA in mixed tissue lesions (~13% increases) as early as 30 mins following transient (3-hour) or permanent middle cerebral artery (MCA) occlusions in macaque monkeys, with progressive declines of ~5% to 40% observed from 5h to 30 days after stroke. Carano *et al.* (Carano *et al* 2000) have noted a similar time course of FA changes within subcortical and cortical regions in a rodent MCA occlusion model with ~20% increases in FA 1h after occlusion and ~25-40% decreases by 3h up to 5 days following stroke. Another report of a 'global ischemia' rat model uncovered a small increase in diffusion anisotropy 10mins post-mortem in the trigeminal nerve (Does and Gore 2000). The authors observed greater reductions in ADC values measured perpendicular to the nerve (26-31% decrease) compared to ADC measured parallel to the nerve (14-19% decrease) that supported the increase in anisotropy. Similarly, we noted steeper declines in $r\lambda_3$ relative to $r\lambda_1$ in subcortical WM (4 patients), major WM (4 patients) and cortical GM (5 patients) that accounted for the elevated FA during the initial phase (2.5-7h) in these tissues.

The biological implications for elevated anisotropy within hyperacute (≤7h) ischemic stroke are still evolving. In WM, the restricted water diffusion perpendicular to the fiber direction, and the attendant increases in anisotropy are suggestive of cellular swelling

from cytotoxic edema that results in a) additional water restriction in the axoplasm and b) a more tortuous extracellular environment due to a decrease in space between the myelin fiber bundles (Sotak 2002). In a modeling study of diffusion in WM, Sen and Basser (2005) predicted increases in anisotropy (up to 29%) during cytotoxic edema, which were associated with changes in the microstructural geometrical properties of the tissue. They suggested that the degree of anisotropy was highly dependent on the extraaxonal dimensions (Sen and Basser 2005).

Unlike the initial phase (2.5-7h), the follow-up phase (21.5-29h) of our study was mainly characterized by reduced anisotropy in ischemic tissue of most patients who demonstrated elevated FA initially (Figures 10-5, 10-7, 10-10 and 10-12). Serial reductions in diffusion anisotropy have been reported in animal models of cerebral ischemia (Carano *et al* 2000; Liu *et al* 2007) and retinal ischemia (Song *et al* 2003; Sun *et al* 2006). The latter studies of retinal ischemia attributed an early (3d) reduction in anisotropy to decreases in parallel diffusivity (λ_1) with unchanged perpendicular diffusion ($(\lambda_2+\lambda_3)/2$), consistent with histological findings of axonal degeneration; however the more precipitous declines in anisotropy later (5-14d) were mainly tied to increases in perpendicular diffusion reflecting demyelination. Human studies of ischemic stroke (Sorensen *et al* 1999) (<24h) and corpus callosotomy (Concha *et al* 2006) (1-week post surgery) have also observed reduced anisotropy, which was attributed to greater decreases in λ_1, compared to λ_2 and λ_3 in WM tracts. In uniformity with these reports, we noted greater decreases in $r\lambda_1$, compared to $r\lambda_2$ and $r\lambda_3$ in ischemic major (7/10 patients) and subcortical (10/11 patients) WM tracts that showed reduced FA during the follow-up phase (21.5-29h), suggestive of early axonal injury after stroke.

During the initial and follow-up periods post stroke onset, inverse correlations between rT2-weighted signal intensity and rFA were noted in subcortical WM and deep GM. An inverse correlation between rT2-weighted signal intensity and rFA was observed only during the initial phase in major WM tracts. In an effort to establish a biophysical link between FA and T2-wt signal intensity, Ozsunar *et al.* showed an inverse correlation between these two parameters in their hyperacute (<12 h) stroke study of 26 patients (Ozsunar *et al* 2004a). They hypothesized that during the progression of the ischemic insult, an increase in extracellular water, and thereby an expansion in the extracellular space would lead to a decrease in FA and an increase in T2-weighted signal intensity (Ozsunar *et al* 2004a). We observed this type of pattern, where FA was markedly reduced and T2 was elevated in the follow-up phase within subcortical WM and deep GM regions (Figures 10-9B and 10-13B).

During the initial phase (2.5-7h) of our study, a small proportion of ROIs in each of the tissue categories showed increases in rFA (>1.0) and reductions in rT2-weighted signal intensity (<1.0) in major WM (15/56 ROIs; Figure 10-8A), subcortical WM (12/108 ROIs; Figure 10-9A), deep GM (4/18 ROIs; Figure 10-13A) and cortical GM (8/45 ROIs; Figure 10-14A). These signal reductions on the b = 0 s/mm^2 EPI scans were not observed in the follow-up phase (21.5-29h). Decreases in T2*-weighted signal intensity have been observed on serial gradient-echo EPI images in ischemic GM (6% to 8% drops) and WM (4% drop) during the first 2 minutes following transient middle cerebral artery occlusion

in the cat brain (De Crespigny *et al* 1992). The authors suggested that this was related to the deoxygenation of available hemoglobin which affects image contrast similar to a magnetic susceptibility T2* shortening contrast agent by reducing the signal intensity on T2*-weighted images (De Crespigny *et al* 1992). In the clinical context, Tamura *et al.* observed reductions in mean T2*-weighted signal intensity (4% decreases measured on gradient echo EPI images) on the ipsilateral side in 6 patients from 1.5h to 3.3h hours following stroke onset that suggested greater deoxyhemoglobin concentrations in the ipsilateral (ischemic) regions (Tamura *et al* 2002).

10.4.3 Limitations of the Study

A limitation of this serial study of acute stroke is that we did not exclude patients who had previous strokes. Two patients (patient 1 and patient 9) presented with old infarcts within the contralateral hemisphere (patient 1) and ipsilateral hemisphere (patient 9). In patient 1, the old infarct was observed in the right middle cerebral arterial (MCA) distribution encompassing the inferior frontal gyrus, and in patient 9, the old infarct was seen in the left MCA territory in the area of the inferior and middle frontal gyri (Figure 10-4). Although the presence of these infarcts did not impair our selection of the ample contralateral (homologous precentral gyri for patient 1) or ipsilateral (postcentral and precentral gyri of the new lesion for patient 9) regions in the ROI analysis of these patients, we cannot rule out the secondary degenerative effects the previous primary lesions may have had on adjacent WM tracts (within the same hemisphere) (Pierpaoli *et al* 2001; Thomalla *et al* 2004; Werring *et al* 2000). In patient 1, we observed increases in mean rFA (27% rises) of ischemic subcortical WM within the initial phase (2.5h) and decreases (8% drops) during the follow-up period (25h). In patient 9, the ischemic pre- and postcentral gyral tracts showed a reduction in mean rFA (13% drops) during the initial period (5h) with further declines (38% drops) noted in the follow-up phase (26h). However, this trend of significantly reduced FA from the initial to the follow-up phase was also seen in new lesions of 2 other patients (patients 5 and 12 (~13% decreases during the initial phase and ~38% decreases in the follow-up period in these 2 patients, Figure 10-5B)), who did not present with old infarcts. Nonetheless, future studies of serial DTI in acute stroke should consider such cases and either evaluate them in isolation or exclude them from the cohort of new strokes.

The free-hand ROI analysis methods to segment discrete tissues (governed by ≥30% reduction in Trace/3 ADC) were strictly kept the same between patients and time-points, thereby adding more reliability to our FA findings in this longitudinal study of human stroke. However, since our ROI methods were confined to the Trace/3 ADC-defined infarcts, we did not measure FA in the outer perfusion-diffusion mismatch areas (Schaefer *et al* 2003). We acquired perfusion data on 6 patients within the initial phase, out of which 2 showed a perfusion>diffusion mismatch (patients 2 and 4), 2 showed a perfusion<diffusion mismatch (patients 8 and 9) and 2 showed a perfusion-diffusion match (patients 1 and 5) (on TTP maps defined by >20% difference in lesion volumes between DWI and TTP) (Figure 10-15). Furthermore, given the current expeditious treatment regimens for acute stroke, 10 of the patients in this study were treated with

rtPA (N=5), a neuroprotectant (N=1) or both (N=4) (Table 10-1). However, it does not appear that there were any confounding effects from these treatments as 2/3 non-treated patients (patient 1 (perfusion-diffusion match) and patient 13) demonstrated elevated FA values in ischemic WM and GM areas within the initial period, akin to the patients given therapy (patients 4 to 10; Figures 10-5 and 10-10). Nonetheless the total lesions volumes of the patients in this report (Table 10-2) are smaller compared to a previous report where out of 9 patients scanned ≤7h, 3 were given rtPA treatment (Chapter 8, Table 8-1). Lesion volume growth (obtained from final outcome scans) was not addressed in this study as we did not acquire outcome 30-day scans on these patients.

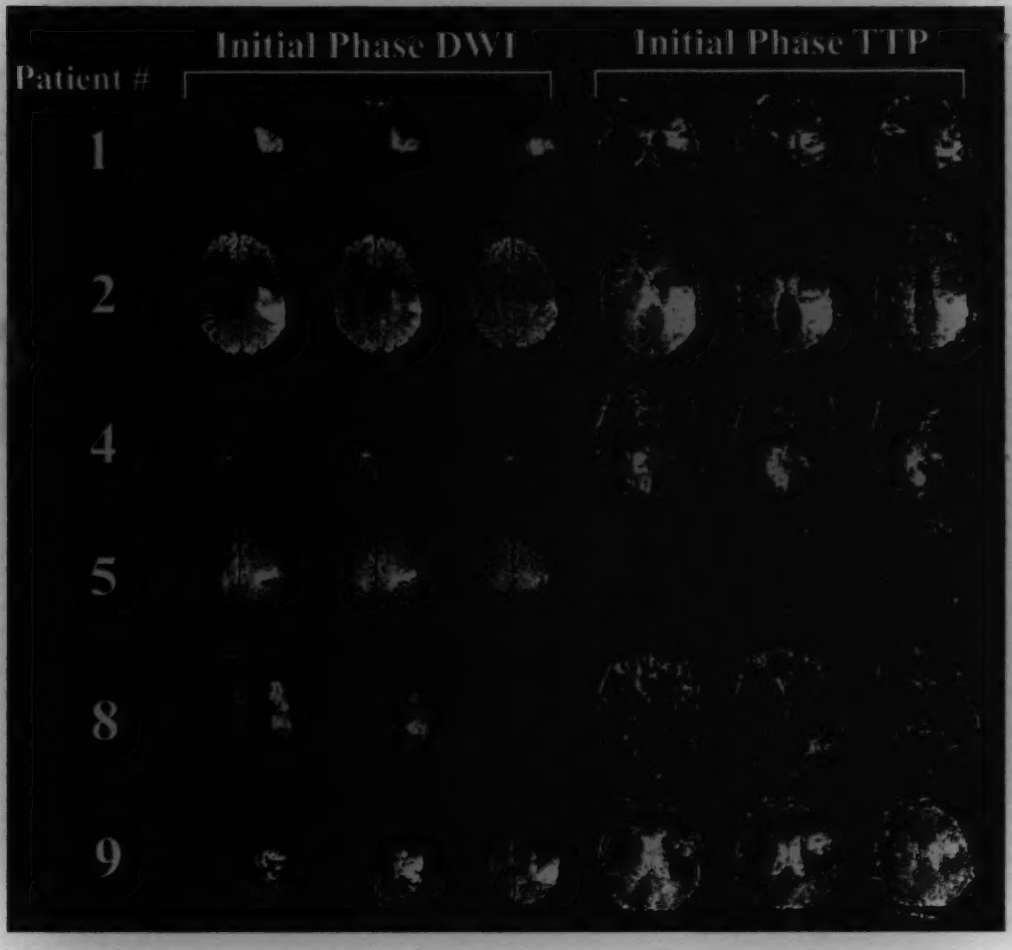

Figure 10-15: Example diffusion-weighted images (DWI; b = 1000 s/mm^2) and time-to-peak (TTP) maps of 3 matching consecutive slices from 6 patients during the initial phase (2.5-5h) of stroke onset. Of the 6 patients on whom perfusion data were acquired, patients 2 and 4 demonstrated a perfusion>diffusion mismatch, patients 8 and 9 showed a perfusion<diffusion mismatch and patients 1 and 5 demonstrated a perfusion-diffusion match.

10.5 Concluding Remarks on Serial Study of Diffusion Anisotropy

Previously, changes of diffusion anisotropy in stroke lesions ≤24h were reported to be elevated, reduced or a mixture of the two. Our results from this serial DTI study of human cerebral ischemia show that the phenomenon of elevated diffusion anisotropy is mainly associated with the hyperacute phase (≤7h) of stroke, with reduced anisotropy primarily noted in the subacute (~24h) follow-up phase. Although we do not believe that the therapeutic interventions in our patient cohort contributed to any confounding effects of the FA data, future longitudinal studies of DTI in human stroke should consider this factor and evaluate the treated patients separately. The clinical significance of these findings of early (≤7h) elevations and subsequent (>21.5h) declines of diffusion anisotropy suggest that FA may serve as a marker of symptom onset in the clinic, albeit far from perfect, particularly in patients presenting with unknown times of stroke onset. Quantitative DTI provides an insightful means of evaluating tissue status and understanding changes in the microstructure of the brain tissue after stroke over time.

10.6 Supplementary Data from a Cross-Sectional Study of Diffusion Anisotropy Changes in Gray Matter

In our previous cross-sectional DTI study of stroke, we demonstrated that FA of ischemic WM tracts was significantly elevated (up to 25%) within 7 hours of symptom onset, but was reduced (~15% decreases) for the rest of the time course from 8 to 34 hours after stroke onset (Chapter 8, Figure 8-3). However in that study we did not characterize the trend in diffusion anisotropy of ischemic GM areas within the infarcts during that time course.

Although there are several serial and cross-sectional published reports on characterizing diffusion anisotropy in ischemic lesions within 24 hours of stroke onset (Green *et al* 2002; Harris *et al* 2004; Ozsunar *et al* 2004a; Schaefer *et al* 2003), there are very few reports focused primarily on assessing diffusion anisotropy changes in distinct ischemic GM regions of the brain (separate from WM tracts) (Munoz Maniega *et al* 2004; Sorensen *et al* 1999; Yang *et al* 1999). Yang *et al.* acquired 3-direction diffusion weighted images in most of their patient cohort and reported changes in diffusion anisotropy after stroke with elevations in cortical GM (~10-40% increases) beyond 24 hours (up to 96 hours) post onset and consistent reductions in deep GM areas (down by 22%) as early as 5 hours until 24 hours following symptom onset (Yang *et al* 1999). Others have reported that FA remains constant in ischemic GM areas within 24 hours after stroke (Munoz Maniega *et al* 2004; Sorensen *et al* 1999). Therefore, based on these previous reports the changes in FA of ischemic GM areas within 24 hours are variable and no consistent trend has emerged.

This section of Chapter 10 presents our supplementary findings on GM diffusion anisotropy changes in a cross sectional patient population. The purpose of adding this section was to use this data to provide ancillary evidence for the serial changes of

diffusion anisotropy in GM regions. Unlike in our serial study of stroke, where we scanned patients at two distinct time phases, the initial (2.5-7h) phase and the follow-up (21.5-29h) phase, the patients in this cross-sectional study were scanned (only once) from 2h to 26.5h post onset and separated into 3 distinct time phases, namely, hyperacute (2h), acute (13-14h) and subacute (16.5-26.5h).

10.6.1 Methods

Eleven patients (7M, 4F, mean age = 73 ± 17 years) presenting with a non-hemorrhagic ischemic stroke and known times of onset were enrolled in the MRI study (after computed tomography and standard treatment) within 26.5 hours post symptom onset (Table 10-6) for a single scan session. They were separated into 3 distinct time phases post onset, namely, the hyperacute phase (2 hours), acute phase (7-14 hours) and subacute phase (14-26.5 hours). In this cross-sectional group, 3 patients were given rt-PA, including one patient who was also enrolled into the ALIAS trial.

Written informed consent was obtained from all patients or their next of kin. The data acquisition, post-processing, and ROI analysis methods were the same as for the serial group of patients (Section 10.2) except only deep GM and cortical GM regions within the ischemic core were measured for changes in diffusion anisotropy. Here, the relative values for each ROI measurement per patient were averaged over all patients within a distinct time phase, with respect to the 2 tissue categories, to facilitate group comparisons between the hyperacute (2h), acute (13-14h), and subacute (16.5-26.5h) phases of stroke. The choice of the range of times after onset for the 3 phases was arbitrary, but was based on the range of time frames delineated in our previous cross sectional study of ischemic WM changes following stroke (Chapter 8).

Paired t-tests were used to examine differences between the ipsilateral and contralateral Trace/3 ADC, FA, λ_1, λ_2, λ_3 and T2-weighted signal intensity ($p<0.05$). Linear regression analyses were performed with Pearson's correlation coefficient and significance level of the F-test to assess correlations between rT2-weighted signal intensity versus rFA across the entire time course in the case of patients with cross sectional scans. Results were attributed significance at levels of $p<0.05$.

Table 10-6: Characteristics of a Cross Section of Patients Demonstrating Gray Matter Lesions

Patient No.	Sex/Age (yr)	Treatment	Arterial Distribution	Lesion Location		Time of MRI (hr)	NIHSSS	Lesion Volumes (cm^3)		
				Deep GM	Cortical GM Involvement			Total	Deep GM	Cortical GM
1	M / 80	None	Thalamic Perforation	Thalamus	No	2.0	12	0.6	0.4	------
2	F / 55	rt-PA	R MCA	None	Yes	13.0	16	164.3	------	24.4
3	F / 56	None	L MCA	Putamen, Caudate nucleus	Yes	14.0	25	89.8	2.3	3.2
4	M / 71	None	R MCA	Putamen	No	16.5	12	2.2	0.3	------
5	M / 91	None	L MCA	None	Yes	17.5	6	0.7	------	0.3
6	M / 83	None	L MCA	None	Yes	18.0	6	9.6	------	4.4
7	F / 86	None	R Recurrent artery of Heubner	Putamen, Caudate nucleus	No	19.0	5	5.2	1.4	------
8	M / 38	rt-PA and ALIAS	L MCA	None	Yes	20.5	14	60.4	------	9.6
9	M / 84	rt-PA	R Lenticulo-striates	Putamen, Caudate nucleus	No	22.5	6	7.4	2.5	------
10	M / 78	None	L MCA	None	Yes	25.0	4	3.3	------	0.3
11	F / 85	None	L ACA/MCA	Putamen	Yes	26.5	22	195.5	0.6	27.0

rt-PA, tissue plasminogen activator; ALIAS, Albumin therapy in ischemic stroke; <CA, middle cerebral artery; ACA, anterior cerebral artery; GM gray matter; NIHSSS, National Institutes of Health Stroke Scale Score. The 'Total' lesion volume per patient not only reflects ischemic deep and cortical GM areas, but also white matter regions and CSF-filled spaces that were not analyzed.

10.6.2 Results

Of the 11 patients in this group, 2 patients demonstrated both deep and cortical GM lesions. Out of the remaining 9 patients, 4 showed only deep GM lesions and 5 showed only cortical GM lesions within the Trace/3 ADC defined infarct. Figure 10-16 displays example image sets containing EPI T2-weighted, DWI, Trace/3 ADC and FA images from the hyperacute (2h) and subacute (26.5h) phases of stroke onset, respectively. Although regions of diminished FA are slightly apparent in the subacute patient (Figure 10-16, right column), a quantitative ROI analysis is essential in probing differences within the lesions relative to the non-affected contralateral deep and cortical GM areas.

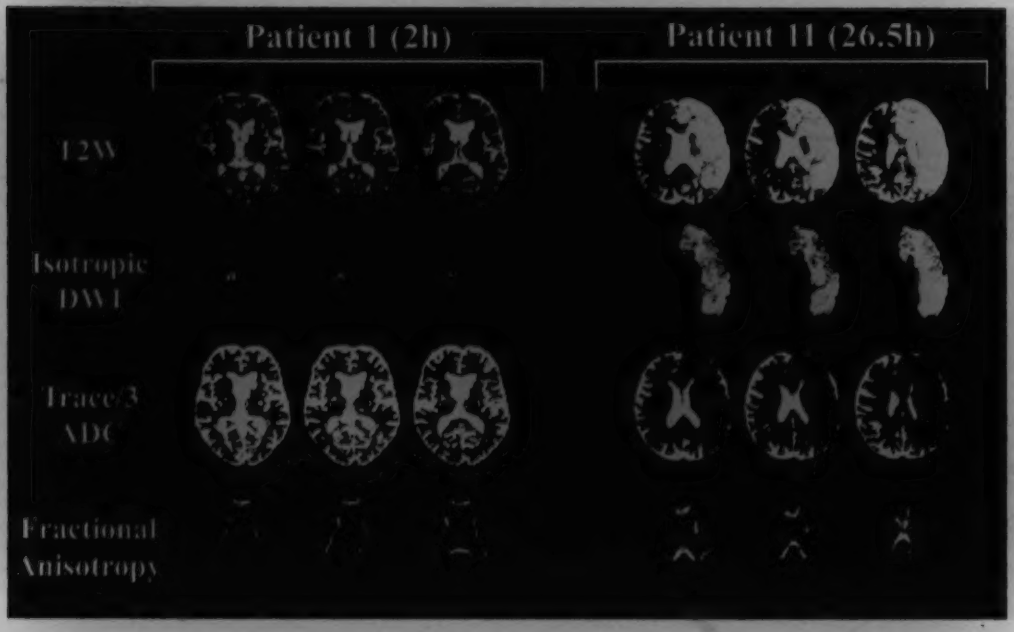

Figure 10-16: (Refer to Table 10-6 for patient characteristics) T2-weighted images (T2W, b=0 s/mm^2), isotropic diffusion-weighted images (DWI, b=1000 s/mm^2), Trace/3 ADC and FA maps from 2 patients who presented with hyperacute (patient 1; 2h post symptom onset) and subacute (patient 11; 26.5h post stroke onset) infarcts in the thalamus and the anterior and middle cerebral arterial territories, respectively.

The time dependence of rFA, rTrace/3 ADC and rT2-weighted signal intensity changes in 6 patients with lesions involving deep GM regions is displayed in Figure 10-17 (A, B). Trace/3 ADC was consistently low (reduced by 40%) in all patients whereas rFA was more variable. An increase in rFA (1.05 ± 0.05, p=0.01) was observed in one patient (patient 1, Table 10-6) at 2 hours post onset. From 14h to 26.5h following stroke, no elevations in rFA were observed in the 5 patients within that time frame. In the subacute phase (16.5-26.5h), lesions showed an average rFA of 0.86 ± 0.11 ($p<0.01$). This mean reduction in rFA reflected the greater decrease of the relative principal eigenvalue, $r\lambda_1$ (41% decline) compared to declines in the secondary and tertiary (λ_2, λ_3) eigenvalues (reduced by ~37%). The mean relative T2-weighted signal intensity increased by up to 50% during the time course from 2h to 26.5 h post onset (Figure 10-17B) with an inverse correlation between mean rFA and rT2-weighted signal intensity ($R= -0.50$, $p<0.01$).

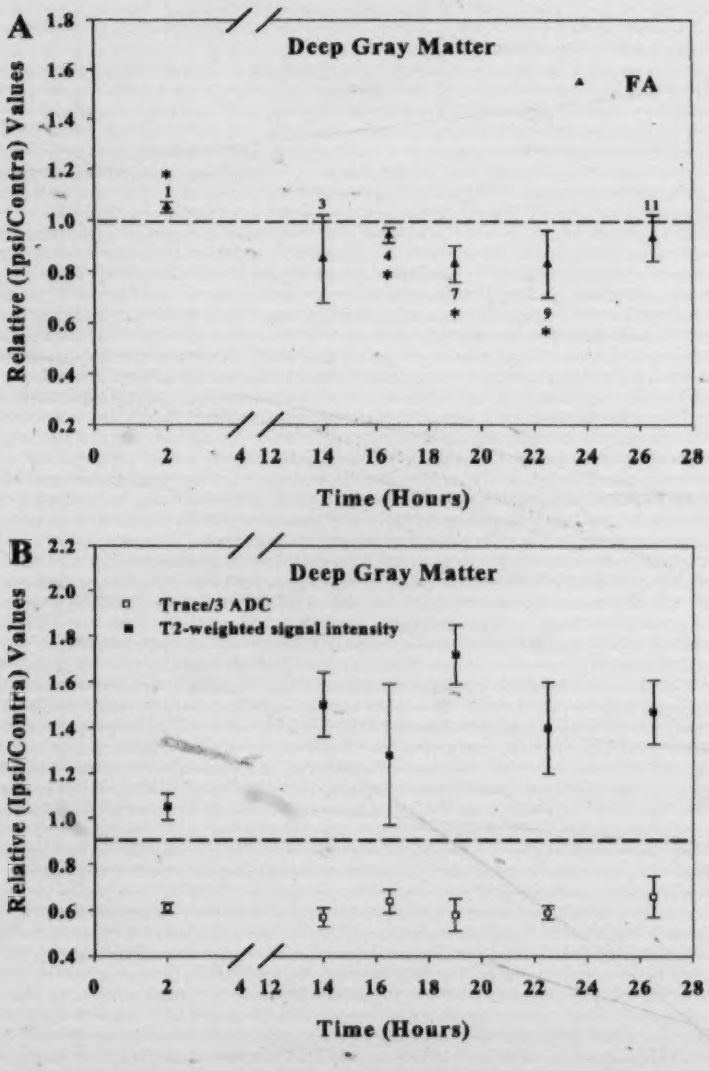

Figure 10-17: Time course of relative (r) (A) fractional anisotropy (FA), and (B) Trace/3 apparent diffusion coefficient (ADC) and T2-weighted signal intensity (on b=0 s/mm^2 images) changes in deep GM in 6 patients after ischemic stroke onset (refer to Table 10-6). The error bars denote the standard deviation over the ROIs measured for each patient. * refers to significant differences between the ipsilateral and contralateral FA values per patient.

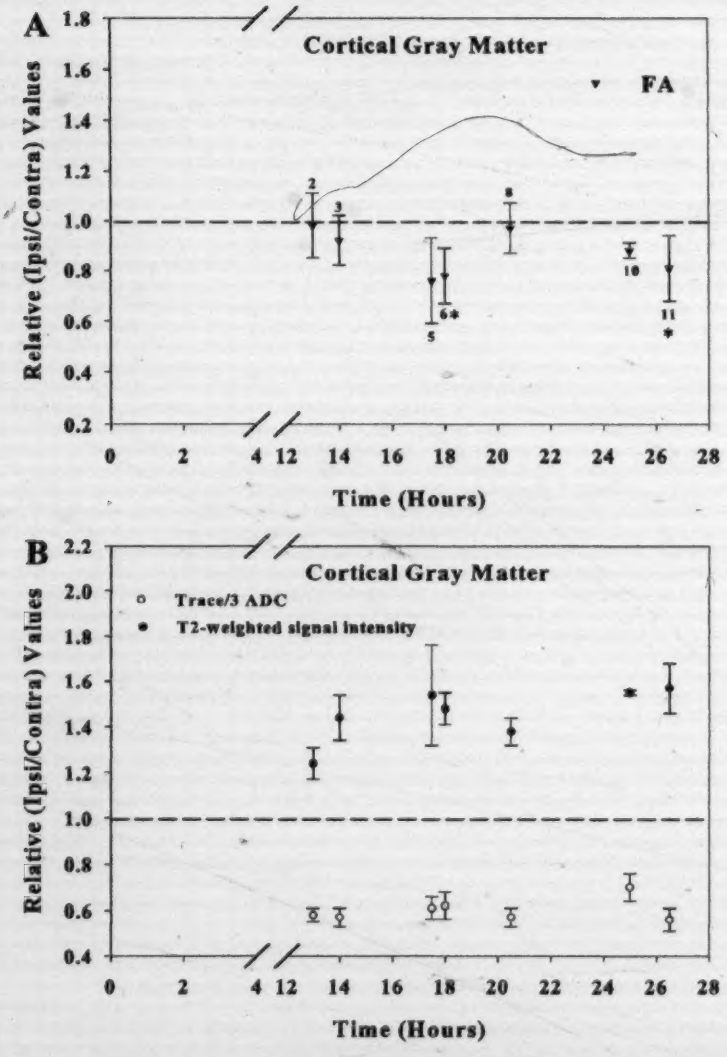

Figure 10-18: Time course of relative (r) (A) fractional anisotropy (FA), and (B) Trace/3 apparent diffusion coefficient (ADC) and T2-weighted signal intensity changes in cortical GM in 7 patients after ischemic stroke onset (refer to Table 10-6). The error bars denote the standard deviation over the ROIs measured for each patient. * refers to significant differences between the ipsilateral and contralateral FA values per patient.

Trend of rFA, rTrace/3 ADC and rT2-weighted signal intensity values for lesions involving cortical GM in 7 patients are displayed in Figures 10-18 (A, B). Trace/3 ADC remained consistently low, and no patients demonstrated elevations in rFA throughout the time course. In the acute phase (13-14h), although the mean rFA of ischemic cortical GM was slightly reduced in 2 patients (0.96 ± 0.13, $p=0.08$), it did not attain significance. In

the subacute phase (16.5-26.5h), mean rFA declined to 0.84 ± 0.14 ($p<0.01$) in 5 patients. Elevations in mean relative T2-weighted signal intensity were seen from the acute (30% increases) to the subacute (50% increases) phase (Figure 10-18B). Changes in the eigenvalues and the correlation between rFA and rT2-weighted signal intensity ($R= -0.55$, $p<0.01$) for cortical GM were similar to those observed for deep GM regions.

The limitations of this study are its cross sectional design with a patient selection bias and the low number of patients early after stroke onset (especially the lack of patients within 7 hours of onset). Furthermore, the same user dependent ROI analysis methods used previously in the WM cross sectional study (Chapter 8) and the serial DTI study in the earlier part of this chapter were used to segment the distinct deep and cortical GM areas for this GM cross sectional study also. Nonetheless, all patient data was analyzed in the same manner with the infarcts outlined by a ≥30% drop in mean diffusivity relative to the normal contralateral side. Another practical limitation of this study was that we acquired perfusion data on only one patient (patient 1, Table 10-6), who showed a perfusion<diffusion mismatch (on TTP maps). Of the 3 patients who received rtPA including 1 patient who received rtPA and albumin therapy (patients 2, 8 and 9), 2 showed no change in rFA within their cortical GM lesions (patients 2 and 8) and 1 demonstrated a significant decrease in mean rFA of ischemic deep GM at 22.5 hours (patient 9) post stroke onset. However, these patients were scanned ≥13 hours after stroke, where reductions in FA are in line with our previous findings from the cross sectional WM study (Chapter 8, Figure 8-3).

10.6.3 Concluding Remarks on Cross-Section of Stroke Patients with Gray Matter Lesions

Overall, for both deep and cortical GM lesions, significant increases in FA were only noted earlier on (patient 1, Table 10-6) within 2 hours of stroke onset, whereas significant decreases in FA were observed later from 16.5-26.5 hours post onset. The data from this group of patients provides support for results from our serial study, where significant elevations in FA of infarcted GM mainly occurred during the initial phase (≤7h), and marked FA reductions were seen in the later follow-up phase (21.5-29h) of stroke onset (Figure 10-10 A, B). Furthermore, data from this cross-sectional patient evaluation also suggests that reductions in FA within GM areas may have started to occur in the time interval between the initial and follow-up phases of ischemic stroke in the serial group of patients.

It is interesting to note that the trends in rFA and rT2-weighted signal intensity observed in the cross-sectional group of patients showing deep and cortical GM lesions parallels results from our earlier cross-sectional WM study in acute ischemic stroke (Chapter 8).

11

EVALUATION OF PARALLEL ACQUISITION TECHNIQUES mSENSE AND GRAPPA IN DIFFUSION-WEIGHTED IMAGING OF ACUTE STROKE

Previously we had used two parallel acquisition techniques, Modified sensitivity encoding (mSENSE) and Generalized autocalibrating partially parallel acquisitions (GRAPPA) with echo planar imaging (EPI) to address the issues of susceptibility-related artifacts and distortions that tend to plague the diffusion tensor images (DTI) acquired with EPI in normal subjects (chapter 9). Our results demonstrated that the application of mSENSE and GRAPPA methods with acceleration factors (R) of 2 yield high quality Trace/3 apparent diffusion coefficient (ADC) and fractional anisotropy (FA) maps and improve the visualization of peripheral white matter (WM) fiber tracts. Furthermore, with both methods, the quantitative parameters of Trace/3 ADC and FA are accurate and reproducible. A more recent study by Ardekani *et al.* focused on comparing GRAPPA and mSENSE for DTI at 3.0T on normal volunteers and found that GRAPPA based DTI with R=2 performed better than mSENSE in terms of systematic and random noise and reproducibility of Trace/3 ADC and FA (Ardekani *et al* 2006).

Studies of the original SENSE method for diffusion-weighted imaging (DWI) with EPI have shown how the detrimental effects of susceptibility-related artifacts can wreak havoc on diffusion images of stroke patients and impair diagnostic accuracy primarily in areas around the auditory canals and frontal sinuses (Bammer *et al* 2001; Kuhl *et al* 2005; Willinek *et al* 2003). In a very recent study, Skare *et al.* compared SENSE reconstruction to GRAPPA reconstruction for multi-shot DWI at 3.0T in normal subjects and found GRAPPA to perform better than SENSE. They also showed how GRAPPA-derived DW images were able to improve lesion conspicuity in acute stroke patients compared to conventional single-shot EPI methods (Skare *et al* 2007).

This chapter presents our work on comparing mSENSE and GRAPPA with R=2 for use with DWI of acute stroke patients.

11.1 Introduction

Although DWI with single-shot EPI is the most common method used in clinical acute stroke, it suffers from artifacts such as gross geometric distortions and blurring due to lengthy echo-trains and T2* decays associated with the EPI readout interval. The resultant blurring and poor spatial resolution can further impair the diagnostic accuracy of an acute stroke exam, especially when the artifacts occur in areas at the base of the skull, infratentorial brain regions, and around the frontal sinuses.

Parallel acquisition techniques when used in association with single-shot EPI are a well-known means of reducing the typical susceptibility-related artifacts associated with that method (Augustin *et al* 2004; Bammer *et al* 2001). In parallel imaging, multiple sets of receiver coils (array coils) are used to acquire data from a sub-sampled *k*-space. The result is accelerated image acquisition, which translates to a shorter echo train length for EPI by virtue of a reduced number of phase encoding steps, reduction in imaging artifacts and resolution enhancement.

The image domain based SENSE technique when used with single-shot EPI based DWI studies of acute (5-42 hours post symptom onset) (Willinek *et al* 2003) and subacute (Bammer *et al* 2001) stroke patients at 1.5T (R=2) demonstrated improved image quality and lesion conspicuity compared to conventional (R=1) DWI methods. A SENSE based DWI study by Kuhl *et al.* of subacute to chronic stroke patients at 3.0T with R=2 further demonstrated refinements in image quality and enhanced lesion conspicuity for lesions in the posterior fossa and temporal lobes relative to conventional DWI (Kuhl *et al* 2005). The common EPI-related artifacts and T2* blurring are more pronounced at high fields (3.0T and above) and can impair image quality to a greater degree (Jaermann *et al* 2004; Jaermann *et al* 2006). Recently a DWI study using multi-shot EPI compared the SENSE reconstruction algorithm to GRAPPA and found that the GRAPPA method was better at resolving minute ischemic lesions in the temporal lobes of acute stroke patients (Skare *et al* 2007).

In applications remote from stroke, Vogt *et al.* have noted significant advantages of mSENSE over GRAPPA in terms of image quality and lesion conspicuity in the case of 3D volume-interpolated breath hold exams for detecting hepatic metastases (Vogt *et al* 2005). However, in another study where mSENSE was used with T2-weighted Turbo spin echo (TSE) in local staging of rectal carcinoma, Oberholzer *et al.* found no diagnostic benefits in using mSENSE over conventional T2-weighted TSE (Oberholzer *et al* 2005). To our knowledge, there are no published systematic studies comparing the self-calibrating methods, image domain based mSENSE (Griswold *et al* 2004; Wang *et al* 2001) to *k*-space based GRAPPA (Griswold *et al* 2002) with single-shot EPI based DWI in acute stroke patients. For a detailed description of these methods, the reader is referred to chapter 6.

The purpose of our study was to compare the qualitative aspects of the images acquired with mSENSE- and GRAPPA-based DWI with R=2 compared to conventional DWI for acute stroke patients presenting with ischemic lesions. We hypothesized that both

GRAPPA and mSENSE would improve the quality of DW images and Trace/3 ADC maps, and enhance lesion conspicuity mainly in regions affected by the EPI-related artifacts.

11.2 Methods

In all, 36 patients (19M, 17F; mean age= 68 ± 14 years) presenting with a non-hemorrhagic acute ischemic stroke within 38 hours of onset were enrolled in the magnetic resonance imaging (MRI) study after computed tomography scanning and standard treatment. Thirty patients had known onset times (mean time to MRI in these patients, 12 ± 9 hours post symptom onset). Out of the remaining 6 patients, 5 patients awoke with their symptoms and 1 had an uncertain time of onset. A National Institutes of Health Stroke Scale Score (NIHSSS) cutoff of 4 was used to enroll patients in this study (mean NIH scores of all 36 patients = 11±3). For the purpose of qualitative analysis, the patients were divided into groups of arterial distributions based on the observation of their DWI lesions: anterior cerebral artery (ACA, 2 patients), middle cerebral artery (MCA, 17 patients), posterior cerebral artery (PCA, 3 patients), Lenticulostriate occlusions (7 patients), multi-territory infarcts (3 patients), posterior inferior cerebellar artery (PICA, 1 patient), pontine perforation (1 patient), recurrent artery of Heubner (1 patient), and thalamic perforation (1 patient).

Magnetic resonance imaging protocols were approved by the Human Research Ethics Board and written informed consent was obtained from all patients or their next of kin.

11.2.1 MRI Acquisition and Post-processing

DWI was performed on a 1.5T Magnetom Sonata scanner (Siemens Medical Systems, Erlangen, Germany) equipped with gradient coils producing maximal amplitude of 40 mT/m and slew rate of 200 T/m/s. An 8-channel phased array RF coil (In Vivo, Orlando, FL) was used. The DWI scans were part of a 16-min parallel imaging based protocol where all conventional MRI (non-DWI) sequences were coupled with mSENSE (R=2). Conventional single-shot spin-echo diffusion EPI (R=1) was performed with a 3-scan Trace method and used: TR/TE/NEX = 3.5 seconds/ 86 ms/ 4; PPF = 6/8; matrix, 128x128 zero-filled to 256x256; FOV, 220x220; 19 5-mm thick oblique sections with 1.5 mm gap; bandwidth of 1396 Hz/Px; echo spacing of 0.8 ms; anterior-posterior phase-encode direction; scan time, 56 seconds. DWI data were reacquired for R=2 for both mSENSE and GRAPPA without PPF (24 reference lines) and TR/TE = 2.6 seconds/ 86 ms. The remaining parameters for the parallel acquisition methods were the same as those for the conventional DWI method, and the acquisition time was 59 seconds for each method. The constant number of averages permitted a clinically acceptable acquisition time for each sequence. Trace/3 ADC maps were generated using MRVision image analysis software (Winchester, MA). Details of the image processing steps are outlined in Appendix 1.2..

Figure 11-1: An axial DWI (b=1000 s/mm^2) section of a 79-year old female hyperacute stroke patient within 5 hours of symptom onset for the conventional (R=1) and mSENSE and GRAPPA (R=2) DWI methods. The extent of the lesion in the left MCA arterial distribution is better appreciated on the mSENSE and GRAPPA (R=2) images compared to the blurry conventional (R=1) image.

11.3 Results and Discussion

From the qualitative image analysis thus far, DWI (b=1000 s/mm^2) images and Trace/3 ADC maps of mSENSE and GRAPPA R=2 were found to be of higher quality compared to images derived using the conventional (R=1) DWI method (Figures 11-1, 11-2, and 11-3). R=2 images were sharper and less vulnerable to the commonly seen EPI artifacts and blurring observed with images of the R=1 methods (Figure 11-1). The susceptibility artifacts and off-resonance effects encountered with the conventional R=1 method impaired lesion conspicuity and full visibility of the lesion area compared to mSENSE and GRAPPA R=2 images (Figure 11-2). Furthermore, because of the attenuation of the artifactually bright regions on DW images derived with mSENSE and GRAPPA R=2, the contrast of the lesions on those images was better appreciated relative to images of the R=1 technique (Figure 11-3). The R=1 Trace/3 ADC maps appear blurrier due to residual T2* effects. Our qualitative findings are in good agreement with those of other studies performed at 1.5T (Bammer *et al* 2001; Willinek *et al* 2003).

We did not evaluate mSENSE and GRAPPA techniques with higher acceleration factors (R= 3, 4) since we have observed deleterious reconstruction artifacts such as aliasing and structural noise enhancement as apparent in the Trace/3 ADC and FA maps (Figure 9-3) obtained in our previous study (Chapter 9). A limitation of this current study is that we cannot make any inferences as to the signal-to-noise ratio (SNR) within our mSENSE and GRAPPA R=2 images as compared to the R=1 derived images. Reductions in SNR as characterized by a $\sqrt{R}$ decrease inherent to mSENSE and GRAPPA are well known (Pruessmann *et al* 1999). However, because the noise profile is highly variable within accelerated images, it has been proposed that the SNR of these images be calculated

according to the dual acquisition subtraction method (Chapter 9, Section 9.2.1) (Reeder *et al* 2005).

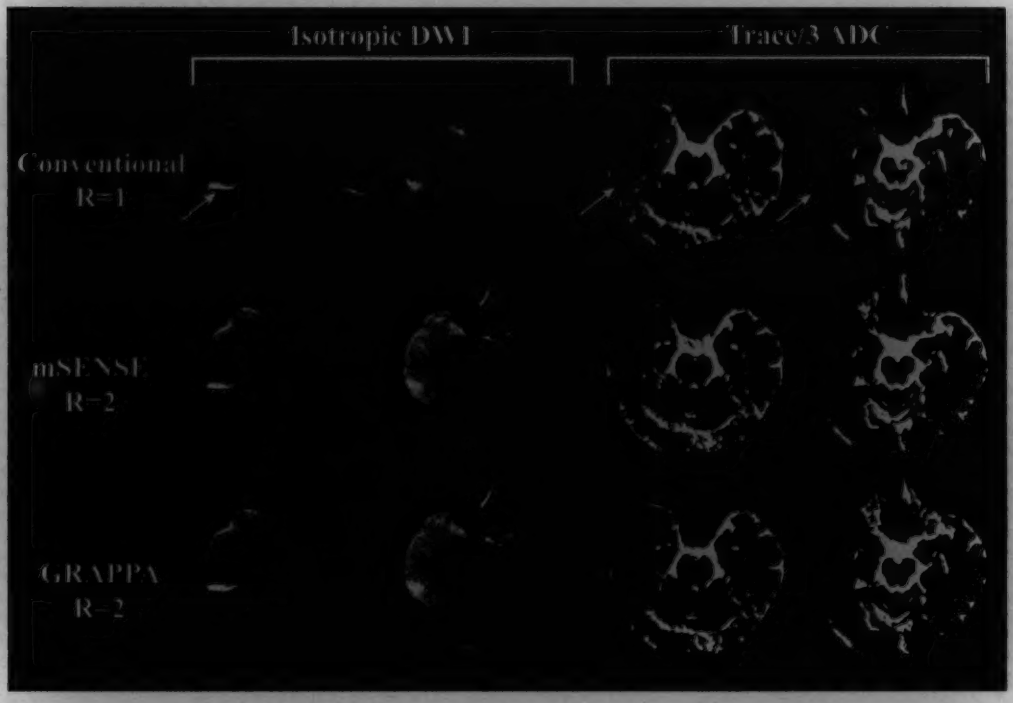

Figure 11-2: Two axial DWI (b=1000 s/mm^2) sections and corresponding Trace/3 ADC maps of a 55-year old acute stroke patient within 13 hours of symptom onset for the conventional (R=1) and mSENSE and GRAPPA (R=2) DWI methods. Compared with R=1 DWI, a reduction in distortions and off-resonance effects (arrows) within the lesion in the right MCA distribution are evident with images obtained with mSENSE and GRAPPA R=2 DWI.

This method requires two sequential acquisitions of identical images for a mean estimate of the signal intensity within a region-of-interest (ROI) and the calculation of the standard deviation of the signal intensity from the same ROI of a difference image (obtained from the subtraction of one image from the other). This was impractical for our acute stroke study given that we would have had to run one extra scan of each method (R=1, and mSENSE and GRAPPA R=2) following the first scan, thereby lengthening the duration of our protocol by 3 minutes. Nonetheless, any variations in SNR within the mSENSE and GRAPPA derived images did not impair lesion conspicuity even in the case of subtle lacunar infarcts in our patient cohort. It should be noted that the disparities between conventional and parallel imaging-based DWI can be more extensive when the image acquisition uses purely axial sections rather than obliques, a larger matrix and fields higher than 1.5T (Jaermann *et al* 2006).

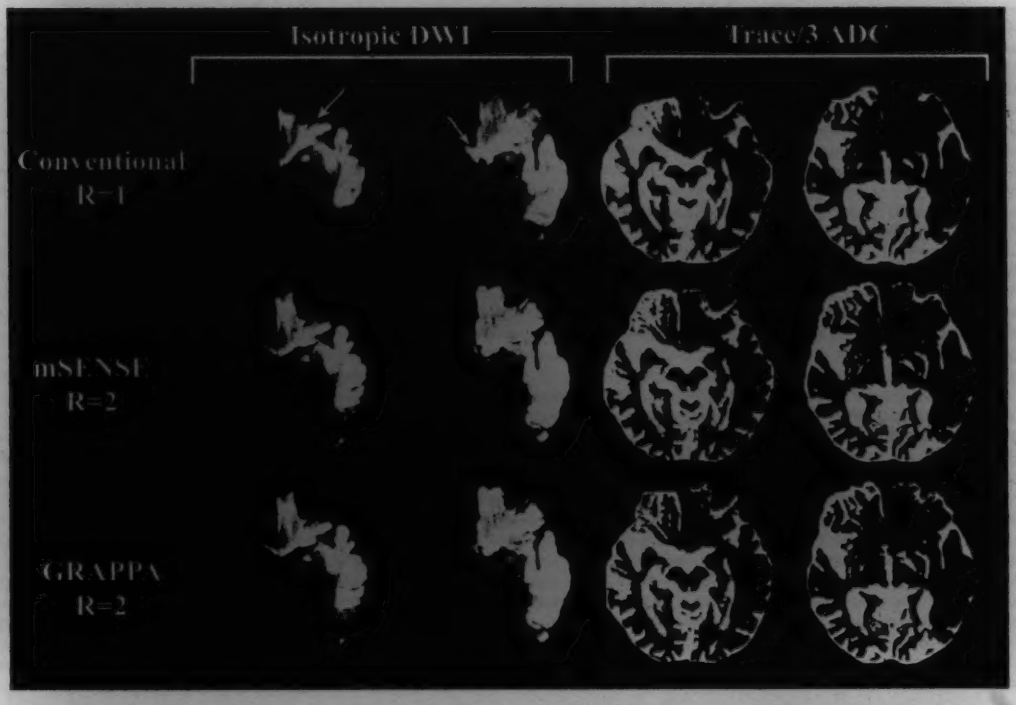

Figure 11-3: Two axial DWI (b=1000 s/mm^2) sections and corresponding Trace/3 ADC maps of an 85-year old subacute stroke patient within 26.5 hours of symptom onset for the conventional (R=1) and mSENSE and GRAPPA (R=2) DWI methods. As observed previously in Figure 11-2, in this case also images from the mSENSE and GRAPPA R=2 methods were more adept at handling the artifactually bright signals associated with the conventional acquisition at the base of the brain. The reduction of these off-resonance effects (arrows) led to an unaltered delineation of the patient's infarcts in the left ACA/MCA territories.

11.4 Conclusions and Future Directions

We have shown images and Trace/3 ADC maps of good quality with mSENSE and GRAPPA R=2 based DWI at 1.5T in acute stroke patients. A reduction of the susceptibility and off-resonance artifacts was primarily observed in basal regions of the brain. A significant visual improvement in lesion conspicuity on DW (b=1000 s/mm^2) images and lesion contrast on Trace/3 ADC maps of the GRAPPA and mSENSE R=2 methods was observed relative to the conventional R=1 method. Future work would entail a more extensive review of images from all patients by experienced neuroradiologists blinded to the method used and its acquisition parameters. The evaluation criteria would include image sharpness, level of artifacts and lesion conspicuity.

12

CONCLUSIONS

The research work presented in this thesis encompassed protocol optimization aspects as seen with the use of FLAIR (Chapter 7) and Parallel acquisition techniques (Chapters 9 and 11) in Diffusion Tensor Imaging (DTI) of the human brain. Furthermore, clinical applications of DTI to characterize diffusion anisotropy changes in the acute phases of stroke (Chapters 8 and 10) were also undertaken at 1.5T. This work has resulted in the advancement of DTI to produce high quality images and generate more precise and reliable measures of diffusion anisotropy. Below is a more detailed summary of the results from each project, their relative impact and implications for future work in these areas.

12.1 Cerebrospinal Fluid-Suppression in DTI and Aging

Our focus here was on quantifying the changes in diffusion anisotropy primarily in peripheral brain regions adjacent to the sulcal spaces that contain fast diffusing isotropic cerebrospinal fluid (CSF) (Chapter 7). By nulling the signal from CSF using the fluid attenuated inversion recovery (FLAIR) prepared method, we observed an apparent increase in fractional anisotropy (FA) of not only the peripheral subcortical white matter (WM) tracts, referred to as gyral WM, but also several central major WM tracts and cortical gray matter (GM) regions. The use of CSF-suppression and thinner slices aided in resolving partial volume averaging of CSF with brain tissue and improved the reliability and accuracy of FA measures of tissue microstructure. These changes have helped gather precise measures of normative anisotropy values in different brain regions for two distinct populations, a young group (21-25 years) and an elderly group (61-74 years). Our quantitative values can serve as an age-matched normative data set for evaluating future DTI studies of neurological diseases.

Although CSF-suppression in DTI provides more accurate measures of FA, particularly for brain regions adjacent to CSF-filled spaces, mainly in the elderly (Good *et al* 2001), FLAIR-DTI studies are impractical in most clinical settings owing to their lengthy acquisition times (8 minutes in our study). This may also be the reason for the paucity of FLAIR-based DTI studies in the literature. In our study, although we addressed partial volume effects of brain parenchyma with neighboring CSF by using thinner slices (3-mm

contiguous), adequate spatial resolution (2.3 x 1.7 mm^2 prior to zero-filling) and FLAIR, we did not rid our images of the partial voluming effects that occur between WM and GM in the periphery or particularly at the interfaces between the posterior limbs of the internal capsule and the thalamus or the basal ganglia and external capsule. A method best suited for obtaining a more precise anisotropy measure of one tissue (e.g. WM) by eliminating partial volume contamination between the other tissue (e.g. GM) and CSF would be double inversion recovery (DIR) based Diffusion imaging (Andrews *et al* 2006; Zacharopoulos and Narayana 1998). Future DTI studies incorporating DIR schemes may yield more precise diffusion measures of tissue microstructure.

Our study on aging went further than previous studies by measuring changes in diffusion anisotropy in 2 age groups in numerous distinct brain regions (26 in total) and we also evaluated the regional specific changes in the eigenvalues of the tensor to obtain a better insight into diffusion changes with aging. We noted significant increases in perpendicular diffusivities (λ_2, λ_3) coupled with a lack of change in parallel diffusivity (λ_1) that explained the observed widespread decreases in FA of WM tracts with aging. We also found a curious increase of 14% in FA of the putamen in the elderly group relative to the young group that has recently been reported by 2 other DTI studies of normal human aging (Abe *et al* 2006; Camara *et al* 2007). However the precise etiology of this change cannot be identified at present due to less than consistent results in the literature that show either increases or decreases in the volume of the putamen with age (Chapter 7, Section 7.5).

In the field of diffusion changes in human adult brain aging and to the best of our knowledge, there are no other studies that have evaluated the change in the eigenvalues to promote a better understanding of the changes in FA with age (Minati *et al* 2007). Future studies of normal human adult aging must focus on quantifying the changes in the eigenvalues to better account for the changes in diffusion anisotropy with age.

12.2 Diffusion Anisotropy in Acute Stroke

Patient recruitment for our studies on characterizing the trend of diffusion anisotropy in the early phases (≤34 hours) of stroke was achieved by fostering close ties with the Stroke program within the division of Neurology and the department of Radiology at the University of Alberta. In our first cross-sectional study on acute ischemic stroke patients (Chapter 8), we observed significant elevations in FA of ischemic major WM and subcortical WM tracts (defined by ≥30% decline in Trace/3 ADC relative to the contralateral hemisphere) of up to 25% in individual patients (6/9 patients) within 7 hours of symptom onset. Although the number of patients was small, the findings were consistent in that we did not observe increases in FA beyond the 7-hour time point post stroke onset. This helped establish a relationship between FA and the time of onset after stroke. The good quality FA maps and the improvements in image analysis compared to previous studies added another measure of confidence in our findings of elevated anisotropy in the hyperacute (≤7h) phase of stroke. The current interpretation for these findings of elevated FA in the hyperacute phase is that cellular swelling leads to greater

water restriction in the axoplasm environment and a more tortuous extracellular environment due to the decrease in space between the myelin fiber bundles (Sen and Basser 2005; Sotak 2002).

Our serial imaging study of 13 patients who were scanned within 7 hours post onset initially and underwent subsequent scanning between 21.5h and 29h post symptom onset showed significant increases of up to 16% in relative (r) FA values (in grouped patient data) of major WM, subcortical WM, deep GM and cortical GM lesions in 9/13 patients within 7 hours of onset. FA was then reduced (19% decrease) during the follow-up phase in the ischemic tissues in 11/13 patients. These results demonstrate increases in diffusion anisotropy are mainly associated with the hyperacute phase (≤7h) of stroke, with reductions in anisotropy more common in the subacute period (~24h). Furthermore, the follow-up phase data showing gross reductions in FA of ischemic regions corroborated with our cross-sectional data (Chapter 8) where we did not observe elevations in rFA after 8 hours of stroke onset. By showing that patients who demonstrate elevated FA within their ischemic brain regions in the initial phase (≤7h), and go on to show reduced FA at the subsequent time point of ~24 hours, we may be able to use DTI as a quantitative method for understanding changes in the microstructural status of brain tissue after stroke over time.

Although the role of anisotropy in the evaluation of acute (≤24h) ischemic lesions has yet to be firmly established, FA may serve as a potential marker for classifying symptom onset in the clinical realm. Patients presenting with an uncertain time of onset or those who wake up with stroke symptoms may be scanned with DTI to help elucidate any trends of FA. There are still considerable challenges in using FA for timing stroke onset, namely the heterogeneous nature of FA maps (compared to the homogeneous Trace/3 ADC maps) making the visualization of acute lesions difficult, and that rigorous (time consuming) quantitative measurements must be made on these maps for a firm assessment of any changes.

12.3 The Role of Parallel Acquisition Methods in Diffusion Imaging

The objectives of the study in chapter 9 were to compare the newer generation of self-calibrating parallel imaging techniques, the image domain based modified sensitivity encoding (mSENSE) and the k-space based Generalized autocalibrating partially parallel acquisitions (GRAPPA) methods with single-shot echo planar imaging (EPI) based DTI at 1.5T. Our results demonstrated that both GRAPPA and mSENSE with an acceleration factor of 2 yielded high quality images and Trace/3 ADC and FA maps relative to the conventional (R=1) DTI methods. Although, we noted decreases in signal-to-noise ratios with the parallel imaging methods, the quantitative parameters of Trace/3 ADC and FA were relatively robust and reproducible for all the brain regions evaluated. However, images acquired with higher acceleration factors (R=3, 4) were of poor quality and severely compromised by reconstruction artifacts such as aliasing and noise enhancement.

Due to the heightened interest and pursuit of high field (≥3.0T) clinical systems in the past 5-6 years in the MRI community, it is important to put our 1.5T results in perspective. Because the common EPI-related susceptibility artifacts and T2* blurring observed with our R=1 conventional images scale with field strength (Pruessmann 2004), incorporation of parallel imaging techniques with single-shot EPI at high fields would dramatically minimize these artifacts and lead to improved image quality. Along these lines several studies comparing SENSE to conventional diffusion-weighted imaging (DWI) (Kuhl *et al* 2005) or to conventional DTI (Jaermann *et al* 2004; Nagae-Poetscher *et al* 2004) and SENSE to GRAPPA for DTI (Ardekani *et al* 2006) and DWI at 3.0T (Skare *et al* 2007) have demonstrated enhancements in image quality with the parallel acquisition techniques.

Our parallel imaging based DWI studies in acute stroke patients have shown an over all improvement in image quality and lesion conspicuity with mSENSE and GRAPPA R=2 relative to conventional (R=1) DWI (chapter 11). Further detailed qualitative image evaluation by the neuroradiologists will reveal if one parallel imaging method is more outstanding than the other at resolving artifacts compared to the conventional DWI method. It is hoped that the method of choice will then be routinely used to scan acute stroke patients in the NMR facility within the University of Alberta hospital.

12.4 Summary

Diffusion Tensor Imaging (DTI) provides information on both the magnitude and directionality of water diffusion in the human brain, and therefore serves as a multi-purpose tool for evaluating neurological disorders. The quantitative parameters derived from DTI are extremely useful in understanding the changes in brain tissue in normal human aging and for monitoring tissue microstructural degradation in longitudinal studies of ischemic stroke. The technique has advanced our grasp of the age-related changes in the human brain. DTI may also provide a means of distinguishing the time of onset after stroke (especially in the early hours following stroke), however, there are analytical challenges and it has yet to obtain the imprimatur of clinicians for the diagnosis and prognosis of the acute stroke patient.

BIBLIOGRAPHY

Abe O, Aoki S, Hayashi N, Yamada H, Kunimatsu A, Mori H, Yoshikawa T, Okubo T, Ohtomo K (2002) Normal aging in the central nervous system: quantitative MR diffusion-tensor analysis. *Neurobiol Aging* 23:433-41.

Abe O, Yamasue H, Aoki S, Suga M, Yamada H, Kasai K, Masutani Y, Kato N, Kato N, Ohtomo K (2006) Aging in the CNS: Comparison of gray/white matter volume and diffusion tensor data. *Neurobiol Aging*.

Aboitiz F, Scheibel AB, Fisher RS, Zaidel E (1992) Fiber composition of the human corpus callosum. *Brain Res* 598:143-53.

Alexander AL, Tsuruda JS, Parker DL (1997) Elimination of eddy current artifacts in diffusion-weighted echo-planar images: the use of bipolar gradients. *Magn Reson Med* 38:1016-21.

Alexander AL, Hasan K, Kindlmann G, Parker DL, Tsuruda JS (2000) A geometric analysis of diffusion tensor measurements of the human brain. *Magn Reson Med* 44:283-91.

Alsop DC (1997) Phase insensitive preparation of single-shot RARE: application to diffusion imaging in humans. *Magn Reson Med* 38:527-33.

Andrews TJ, Osborne MT, Does MD (2006) Diffusion of myelin water. *Magn Reson Med* 56:381-5.

Arakawa S, Wright PM, Koga M, Phan TG, Reutens DC, Lim I, Gunawan MR, Ma H, Perera N, Ly J, Zavala J, Fitt G, Donnan GA (2006) Ischemic thresholds for gray and white matter: a diffusion and perfusion magnetic resonance study. *Stroke* 37:1211-6.

Ardekani S, Selva L, Sayre J, Sinha U (2006) Quantitative metrics for evaluating parallel acquisition techniques in diffusion tensor imaging at 3 Tesla. *Investigative radiology* 41:806-14.

Ardekani S, Kumar A, Bartzokis G, Sinha U (2007) Exploratory voxel-based analysis of diffusion indices and hemispheric asymmetry in normal aging. *Magn Reson Imaging* 25:154-67.

Assaf BA, Mohamed FB, Abou-Khaled KJ, Williams JM, Yazeji MS, Haselgrove J, Faro SH (2003) Diffusion tensor imaging of the hippocampal formation in temporal lobe epilepsy. *AJNR Am J Neuroradiol* 24:1857-62.

Aston-Jones G, Rogers J, Shaver RD, Dinan TG, Moss DE (1985) Age-impaired impulse flow from nucleus basalis to cortex. *Nature* 318:462-4.

Astrup J, Siesjo BK, Symon L (1981) Thresholds in cerebral ischemia - the ischemic penumbra. *Stroke* 12:723-5.

Auer RN, Siesjo BK (1988) Biological differences between ischemia, hypoglycemia, and epilepsy. *Ann Neurol* 24:699-707.

Augustin M, Fazekas F, Bammer R (2004) Fast patient workup in acute stroke using parallel imaging. *Top Magn Reson Imaging* 15:207-19.

Bammer R, Stollberger R, Augustin M, Simbrunner J, Offenbacher H, Kooijman H, Ropele S, Kapeller P, Wach P, Ebner F, Fazekas F (1999) Diffusion-weighted imaging with navigated interleaved echo-planar imaging and a conventional gradient system. *Radiology* 211:799-806.

Bammer R, Keeling SL, Augustin M, Pruessmann KP, Wolf R, Stollberger R, Hartung HP, Fazekas F (2001) Improved diffusion-weighted single-shot echo-planar imaging (EPI) in stroke using sensitivity encoding (SENSE). *Magn Reson Med* 46:548-54.

Bammer R, Auer M, Keeling SL, Augustin M, Stables LA, Prokesch RW, Stollberger R, Moseley ME, Fazekas F (2002) Diffusion tensor imaging using single-shot SENSE-EPI. *Magn Reson Med* 48:128-36.

Bammer R, Schoenberg SO (2004) Current concepts and advances in clinical parallel magnetic resonance imaging. *Top Magn Reson Imaging* 15:129-58.

Barber PA, Davis SM (2003) Limitations of current brain imaging modalities in stroke. In: *Magnetic Resonance Imaging in Stroke* (Davis SM, Fisher M, Warach S, eds), New York: Cambridge University Press, 15-30.

Basser P, Mattiello J, Le Bihan D (1994a) MR Diffusion tensor spectroscopy and imaging. *Biophys J* 66:259-67.

Basser P, Mattiello J, Le Bihan D (1994b) Estimation of the effective self-diffusion tensor from the NMR spin echo. *J Magn Reson B* 103:247-54.

Basser P (1995) Inferring microstructural features and the physiological state of tissues from diffusion-weighted images. *NMR Biomed* 8:333-44.

Basser P, Pierpaoli C (1996) Microstructural and physiological features of tissues elucidated by quantitative-diffusion-tensor MRI. *J Magn Reson B* 111:209-19.

Basser PJ, Pierpaoli C (1998) A simplified method to measure the diffusion tensor from seven MR images. *Magn Reson Med* 39:928-34.

Basser PJ, Pajevic S, Pierpaoli C, Duda J, Aldroubi A (2000) In vivo fiber tractography using DT-MRI data. *Magn Reson Med* 44:625-32.

Basser PJ, Jones DK (2002) Diffusion-tensor MRI: theory, experimental design and data analysis - a technical review. *NMR Biomed* 15:456-67.

Batchelor PG, Atkinson D, Hill DL, Calamante F, Connelly A (2003) Anisotropic noise propagation in diffusion tensor MRI sampling schemes. *Magn Reson Med* 49:1143-51.

Beatty J. (2001). *The Human Brain: Essentials of behavioral neuroscience.* Thousand Oaks: Sage Publications, Inc., 522pp.

Beaulieu C, Allen PS (1994) Determinants of anisotropic water diffusion in nerves. *Magn Reson Med* 31:394-400.

Beaulieu C, Does MD, Snyder RE, Allen PS (1996) Changes in water diffusion due to Wallerian degeneration in peripheral nerve. *Magn Reson Med* 36:627-31.

Beaulieu C, de Crespigny A, Tong D, Moseley M, Albers G, Marks M (1999) Longitudinal magnetic resonance imaging study of perfusion and diffusion in stroke: evolution of lesion volume and correlation with clinical outcome. *Ann Neurol* 46:568-78.

Beaulieu C (2002) The basis of anisotropic water diffusion in the nervous system- a technical review. *NMR Biomed* 15:435-55.

Blaimer M, Breuer F, Mueller M, Heidemann RM, Griswold MA, Jakob PM (2004) SMASH, SENSE, PILS, GRAPPA: how to choose the optimal method. *Top Magn Reson Imaging* 15:223-36.

Bloch F (1946) Nuclear Induction. *Phys Rev* 70:460-74.

Bloembergen N, Purcell EM, Pound RV (1948) Relaxation Effects in Nuclear Magnetic Resonance Absorption. *Phys Rev* 73:679-712.

Bockisch A, Beyer T, Antoch G, Freudenberg LS, Kuhl H, Debatin JF, Muller SP (2004) Positron emission tomography/computed tomography--imaging protocols, artifacts, and pitfalls. *Mol Imaging Biol* 6:188-99.

Boesch C, Gruetter R, Martin E (1991) Temporal and spatial analysis of fields generated by eddy currents in superconducting magnets: optimization of corrections and quantitative characterization of magnet/gradient systems. *Magn Reson Med* 20:268-84.

Brickman AM, Buchsbaum MS, Shihabuddin L, Hazlett EA, Borod JC, Mohs RC (2003) Striatal size, glucose metabolic rate, and verbal learning in normal aging. *Brain research* 17:106-16.

Bristow MS, Simon JE, Brown RA, Eliasziw M, Hill MD, Coutts SB, Frayne R, Demchuk AM, Mitchell JR (2005) MR perfusion and diffusion in acute ischemic stroke: human gray and white matter have different thresholds for infarction. *J Cereb Blood Flow Metab* 25:1280-7.

Broderick J, Connolly S, Feldmann E, Hanley D, Kase C, Krieger D, Mayberg M, Morgenstern L, Ogilvy CS, Vespa P, Zuccarello M (2007) Guidelines for the management of spontaneous intracerebral hemorrhage in adults: 2007 update: a guideline from the American Heart Association/American Stroke Association Stroke Council, High Blood Pressure Research Council, and the Quality of Care and Outcomes in Research Interdisciplinary Working Group. *Stroke* 38:2001-23.

Brott T, Adams HP, Jr., Olinger CP, Marler JR, Barsan WG, Biller J, Spilker J, Holleran R, Eberle R, Hertzberg V, et al. (1989) Measurements of acute cerebral infarction: a clinical examination scale. *Stroke* 20:864-70.

Buffon F, Molko N, Herve D, Porcher R, Denghien I, Pappata S, Le Bihan D, Bousser MG, Chabriat H (2005) Longitudinal diffusion changes in cerebral hemispheres after MCA infarcts. *J Cereb Blood Flow Metab* 25:641-50.

Bugiani O, Salvarani S, Perdelli F, Mancardi GL, Leonardi A (1978) Nerve cell loss with aging in the putamen. *Eur Neurol* 17:286-91.

Burdette JH, Elster AD, Ricci PE (1999) Acute cerebral infarction: quantification of spin-density and T2 shine-through phenomena on diffusion-weighted MR images. *Radiology* 212:333-9.

Butcher KS, Parsons M, MacGregor L, Barber PA, Chalk J, Bladin C, Levi C, Kimber T, Schultz D, Fink J, Tress B, Donnan G, Davis S (2005) Refining the perfusion-diffusion mismatch hypothesis. *Stroke* 36:1153-9.

Butts K, de Crespigny A, Pauly JM, Moseley M (1996) Diffusion-weighted interleaved echo-planar imaging with a pair of orthogonal navigator echoes. *Magn Reson Med* 35:763-70.

Butts K, Pauly J, de Crespigny A, Moseley M (1997) Isotropic diffusion-weighted and spiral-navigated interleaved EPI for routine imaging of acute stroke. *Magn Reson Med* 38:741-9.

Calamante F, Porter DA, Gadian DG, Connelly A (1999) Correction for eddy current induced Bo shifts in diffusion-weighted echo-planar imaging. *Magn Reson Med* 41:95-102.

Camara E, Bodammer N, Rodriguez-Fornells A, Tempelmann C (2007) Age-related water diffusion changes in human brain: a voxel-based approach. *Neuroimage* 34:1588-99.

Carano RA, Li F, Irie K, Helmer KG, Silva MD, Fisher M, Sotak CH (2000) Multispectral analysis of the temporal evolution of cerebral ischemia in the rat brain. *J Magn Reson Imaging* 12:842-58.

Carlson JW, Minemura T (1993) Imaging time reduction through multiple receiver coil data acquisition and image reconstruction. *Magn Reson Med* 29:681-7.

Chabriat H, Pappata S, Poupon C, Clark C, Vahedi K, Poupon F, Mangin J, Pachot-Clouard M, Jobert A, Le Bihan D, Bousser M-G (1999) Clinical severity in CADASIL related to ultrastructural damage in white matter- in vivo study with diffusion tensor MRI. *Stroke* 30:2637-43.

Chenevert TL, Brunberg JA, Pipe JG (1990) Anisotropic diffusion in human white matter: demonstration with MR techniques in vivo. *Radiology* 177:401-5.

Chou MC, Lin YR, Huang TY, Wang CY, Chung HW, Juan CJ, Chen CY (2005) FLAIR diffusion-tensor MR tractography: comparison of fiber tracking with conventional imaging. *AJNR Am J Neuroradiol* 26:591-7.

Cohen MS (1998) Theory of Echo-Planar Imaging. In: *Echo-Planar Imaging Theory, Technique and Application* (Schmitt F, Stehling MK, Turner R, eds), Berlin: Springer-Verlag, 11-30.

Collen D, Lijnen HR (2005) Thrombolytic agents. *Thromb Haemost* 93:627-30.

Concha L, Beaulieu C, Gross DW (2005a) Bilateral limbic diffusion abnormalities in unilateral temporal lobe epilepsy. *Ann Neurol* 57:188-96.

Concha L, Gross DW, Beaulieu C (2005b) Diffusion tensor tractography of the limbic system. *AJNR Am J Neuroradiol* 26:2267-74.

Concha L, Gross DW, Wheatley BM, Beaulieu C (2006) Diffusion tensor imaging of time-dependent axonal and myelin degradation after corpus callosotomy in epilepsy patients. *Neuroimage* 32:1090-9.

Copen WA, Schwamm LH, Gonzalez RG, Wu O, Harmath CB, Schaefer PW, Koroshetz WJ, Sorensen AG (2001) Ischemic stroke: effects of etiology and patient age on the time course of the core apparent diffusion coefficient. *Radiology* 221:27-34.

Copen WA, Sorensen AG (2003) Perfusion-weighted MRI in Stroke. In: *Magnetic Resonance Imaging in Stroke* (Davis S, Fisher M, Warach S, eds), New York: Cambridge University Press, 147-60.

Courchesne E, Chisum H, Townsend J, Cowles A, Covington J, Egaas B, Harwood M, Hinds S, Press G (2000) Normal brain development and aging: quantitative analysis at in vivo MR imaging in healthy volunteers. *Radiology* 216:672-82.

Crank J. (1975). *Mathematics of Diffusion*. Oxford: Oxford University Press.

Davis CP, McKinnon GC, Debatin JF, von Schulthess GK (1996) Ultra-high-speed MR imaging. *Eur Radiol* 6:297-311.

De Crespigny AJ, Wendland MF, Derugin N, Kozniewska E, Moseley ME (1992) Real-time observation of transient focal ischemia and hyperemia in cat brain. *Magn Reson Med* 27:391-7.

Demeter S, Ringo JL, Doty RW (1988) Morphometric analysis of the human corpus callosum and anterior commissure. *Hum Neurobiol* 6:219-26.

Dewar D, Underhill SM, Goldberg MP (2003) Oligodendrocytes and ischemic brain injury. *J Cereb Blood Flow Metab* 23:263-74.

Does MD, Gore JC (2000) Compartmental study of diffusion and relaxation measured in vivo in normal and ischemic rat brain and trigeminal nerve. *Magn Reson Med* 43:837-44.

Donnan GA, Wright PM, Markus R, Phan T, Reutens DC (2003) The ischemic penumbra: the evolution of a concept. In: *Magnetic Resonance Imaging in Stroke* (Davis SM, Fisher M, Warach S, eds), New York: Cambridge University Press, 191-206.

Doran M, Hajnal JV, Van Bruggen N, King MD, Young IR, Bydder GM (1990) Normal and abnormal white matter tracts shown by MR imaging using directional diffusion weighted sequences. *J Comput Assist Tomogr* 14:865-73.

Edelstein WA, Hutchison JM, Johnson G, Redpath T (1980) Spin warp NMR imaging and applications to human whole-body imaging. *Phys Med Biol* 25:751-6.

Einstein A. (1956). *Investigations on the Theory of Brownian Motion*. New York: Dover Publications Inc.

Eis M, Hoehn-Berlage M (1995) Correction of Gradient Crosstalk and Optimization of Measurement Parameters in-Diffusion MR-Imaging. *J Magn Reson Ser B* 107:222-34.

Engelter ST, Provenzale JM, Petrella JR, DeLong DM, MacFall JR (2000) The effect of aging on the apparent diffusion coefficient of normal-appearing white matter. *AJR Am J Roentgenol* 175:425-30.

Eriksson S, Rugg-Gunn F, Symms M, Barker G, Duncan J (2001) Diffusion tensor imaging in patients with epilepsy and malformations of cortical development. *Brain* 124:617-26.

Falcao AL, Reutens DC, Markus R, Koga M, Read SJ, Tochon-Danguy H, Sachinidis J, Howells DW, Donnan GA (2004) The resistance to ischemia of white and gray matter after stroke. *Ann Neurol* 56:695-701.

Falconer J, Narayana P (1997) Cerebrospinal fluid-suppressed high-resolution diffusion imaging of human brain. *Magn Reson Med* 37:119-23.

Fiebach JB, Jansen O, Schellinger PD, Heiland S, Hacke W, Sartor K (2002) Serial analysis of the apparent diffusion coefficient time course in human stroke. *Neuroradiology* 44:294-8.

Fiehler J, Knudsen K, Kucinski T, Kidwell CS, Alger JR, Thomalla G, Eckert B, Wittkugel O, Weiller C, Zeumer H, Rother J (2004) Predictors of apparent diffusion coefficient normalization in stroke patients. *Stroke* 35:514-9.

Filley C. (2001). *The Behavioral Neurology of White Matter*. New York: Oxford University Press.

Firbank MJ, Coulthard A, Harrison RM, Williams ED (1999) A comparison of two methods for measuring the signal to noise ratio on MR images. *Phys Med Biol* 44:N261-4.

Fischer H, Ladebeck R (1998) Echo-Planar Imaging Image Artifacts. In: *Echo-Planar Imaging Theory, Technique and Application* (Schmitt F, Stehling MK, Turner R, eds), Berlin: Springer-Verlag, 179-200.

Fiskum G, Murphy AN, Beal MF (1999) Mitochondria in neurodegeneration: acute ischemia and chronic neurodegenerative diseases. *J Cereb Blood Flow Metab* 19:351-69.

Forbes KP, Pipe JG, Karis JP, Heiserman JE (2002) Improved image quality and detection of acute cerebral infarction with PROPELLER diffusion-weighted MR imaging. *Radiology* 225:551-5.

Frank LR (2001) Anisotropy in high angular resolution diffusion-weighted MRI. *Magn Reson Med* 45:935-9.

Good CD, Johnsrude IS, Ashburner J, Henson RN, Friston KJ, Frackowiak RS (2001) A voxel-based morphometric study of ageing in 465 normal adult human brains. *Neuroimage* 14:21-36.

Green HA, Pena A, Price CJ, Warburton EA, Pickard JD, Carpenter TA, Gillard JH (2002) Increased anisotropy in acute stroke: a possible explanation. *Stroke* 33:1517-21.

Grieve SM, Williams LM, Paul RH, Clark CR, Gordon E (2007) Cognitive aging, executive function, and fractional anisotropy: a diffusion tensor MR imaging study. *AJNR Am J Neuroradiol* 28:226-35.

Griswold MA, Jakob PM, Heidemann RM, Nittka M, Jellus V, Wang J, Kiefer B, Haase A (2002) Generalized autocalibrating partially parallel acquisitions (GRAPPA). *Magn Reson Med* 47:1202-10.

Griswold MA, Kannengiesser S, Heidemann RM, Wang J, Jakob PM (2004) Field-of-view limitations in parallel imaging. *Magn Reson Med* 52:1118-26.

Griswold MA, Breuer F, Blaimer M, Kannengiesser S, Heidemann RM, Mueller M, Nittka M, Jellus V, Kiefer B, Jakob PM (2006) Autocalibrated coil sensitivity estimation for parallel imaging. *NMR Biomed* 19:316-24.

Guadagno JV, Donnan GA, Markus R, Gillard JH, Baron JC (2004) Imaging the ischaemic penumbra. *Curr Opin Neurol* 17:61-7.

Gudbjartsson H, Maier SE, Mulkern RV, Morocz IA, Patz S, Jolesz FA (1996) Line scan diffusion imaging. *Magn Reson Med* 36:509-19.

Gudbjartsson H, Maier SE, Jolesz FA (1997) Double line scan diffusion imaging. *Magn Reson Med* 38:101-9.

Gulani V, Webb AG, Duncan ID, Lauterbur PC (2001) Apparent diffusion tensor measurements in myelin-deficient rat spinal cords. *Magn Reson Med* 45:191-5.

Gunning-Dixon FM, Head D, McQuain J, Acker JD, Raz N (1998) Differential aging of the human striatum: a prospective MR imaging study. *AJNR Am J Neuroradiol* 19:1501-7.

Gupta RK, Saksena S, Hasan KM, Agarwal A, Haris M, Pandey CM, Narayana PA (2006) Focal Wallerian degeneration of the corpus callosum in large middle cerebral artery stroke: serial diffusion tensor imaging. *J Magn Reson Imaging* 24:549-55.

Guttmann CR, Jolesz FA, Kikinis R, Killiany RJ, Moss MB, Sandor T, Albert MS (1998) White matter changes with normal aging. *Neurology* 50:972-8.

Haacke EM, Brown RW, Thompson MR, Venkatesan R (eds) (1999). *Magnetic Resonance Imaging Physical Principles and Sequence Design*. New York: John Wiley & Sons, Inc., 914pp.

Hahn EL (1950) Spin Echoes. *Phys Rev* 77:746-.

Hahn EL (1953) Free nuclear induction. *Physics Today* 6:4-9.

Harris AD, Pereira RS, Mitchell JR, Hill MD, Sevick RJ, Frayne R (2004) A comparison of images generated from diffusion-weighted and diffusion-tensor imaging data in hyper-acute stroke. *J Magn Reson Imaging* 20:193-200.

Hasan KM, Alexander AL, Narayana PA (2004) Does fractional anisotropy have better noise immunity characteristics than relative anisotropy in diffusion tensor MRI? An analytical approach. *Magn Reson Med* 51:413-7.

Haselgrove JC, Moore JR (1996) Correction for distortion of echo-planar images used to calculate the apparent diffusion coefficient. *Magn Reson Med* 36:960-4.

Heart disease and stroke statistics- 2007 update. (2007): American Heart Association, p 43

Heidemann RM, Griswold MA, Haase A, Jakob PM (2001) VD-AUTO-SMASH imaging. *Magn Reson Med* 45:1066-74.

Heidemann RM, Ozsarlak O, Parizel PM, Michiels J, Kiefer B, Jellus V, Muller M, Breuer F, Blaimer M, Griswold MA, Jakob PM (2003) A brief review of parallel magnetic resonance imaging. *Eur Radiol* 13:2323-37.

Helenius J, Soinne L, Perkio J, Salonen O, Kangasmaki A, Kaste M, Carano R, Aronen H, Tatlisumak T (2002) Diffusion-weighted MR imaging in normal human brains in various age groups. *Am J Neuroradiol* 23:194-9.

Hennig J (1999) K-space sampling strategies. *Eur Radiol* 9:1020-31.

Heo JH, Han SW, Lee SK (2005) Free radicals as triggers of brain edema formation after stroke. *Free radical biology & medicine* 39:51-70.

Herve D, Molko N, Pappata S, Buffon F, LeBihan D, Bousser MG, Chabriat H (2005) Longitudinal thalamic diffusion changes after middle cerebral artery infarcts. *J Neurol Neurosurg Psychiatry* 76:200-5.

Hildebrand C, Remahl S, Persson H, Bjartmar C (1993) Myelinated nerve fibres in the CNS. *Prog Neurobiol* 40:319-84.

Hirsch J, Bock M, Essig M, Scahd L (1999) Comparison of diffusion anisotropy measurements in combination with the FLAIR-technique. *Magn Reson Imaging* 17:705-16.

Hjort N, Butcher K, Davis SM, Kidwell CS, Koroshetz WJ, Rother J, Schellinger PD, Warach S, Ostergaard L (2005) Magnetic resonance imaging criteria for thrombolysis in acute cerebral infarct. *Stroke* 36:388-97.

Hochachka PW, Buck LT, Doll CJ, Land SC (1996) Unifying theory of hypoxia tolerance: molecular/metabolic defense and rescue mechanisms for surviving oxygen lack. *Proc Natl Acad Sci U S A* 93:9493-8.

Horsfield M, Jones D (2002) Applications of diffusion-weighted and diffusion tensor MRI to white matter diseases - a review. *NMR Biomed* 15:570-7.

Howseman AM, Bowtell RW (1999) Functional magnetic resonance imaging: imaging techniques and contrast mechanisms. *Philos Trans R Soc Lond B Biol Sci* 354:1179-94.

Hunold P, Maderwald S, Ladd ME, Jellus V, Barkhausen J (2004) Parallel acquisition techniques in cardiac cine magnetic resonance imaging using TrueFISP sequences: comparison of image quality and artifacts. *J Magn Reson Imaging* 20:506-11.

Hunsche S, Moseley ME, Stoeter P, Hedehus M (2001) Diffusion-tensor MR imaging at 1.5 and 3.0 T: initial observations. *Radiology* 221:550-6.

Hutchinson M, Raff U (1988) Fast MRI data acquisition using multiple detectors. *Magn Reson Med* 6:87-91.

Iizuka H, Sakatani K, Young W (1989) Corticofugal axonal degeneration in rats after middle cerebral artery occlusion. *Stroke* 20:1396-402.

Jaermann T, Crelier G, Pruessmann KP, Golay X, Netsch T, van Muiswinkel AM, Mori S, van Zijl PC, Valavanis A, Kollias S, Boesiger P (2004) SENSE-DTI at 3 T. *Magn Reson Med* 51:230-6.

Jaermann T, Pruessmann KP, Valavanis A, Kollias S, Boesiger P (2006) Influence of SENSE on image properties in high-resolution single-shot echo-planar DTI. *Magn Reson Med* 55:335-42.

Jakob PM, Griswold MA, Edelman RR, Sodickson DK (1998) AUTO-SMASH: a self-calibrating technique for SMASH imaging. SiMultaneous Acquisition of Spatial Harmonics. *Magma* 7:42-54.

Jezzard P, Barnett AS, Pierpaoli C (1998) Characterization of and correction for eddy current artifacts in echo planar diffusion imaging. *Magn Reson Med* 39:801-12.

Johnson AC, Mc NA, Rossiter RJ (1950) Chemistry of wallerian degeneration; a review of recent studies. *Arch Neurol Psychiatry* 64:105-21.

Jones D, Lythgoe D, Horsfield M, Simmons A, Williams S, Markus H (1999a) Characterization of white matter damage in ischemic leukoaraiosis with diffusion tensor MRI. *Stroke* 30:393-7.

Jones D (2005) Fundamentals of Diffusion MR Imaging. In: *Clinical MR Neuroimaging Diffusion, Perfusion and Spectroscopy* (Gillard JH, Waldman AD, Barker PB, eds), New York: Cambridge University Press, 54-85.

Jones DK, Horsfield MA, Simmons A (1999b) Optimal strategies for measuring diffusion in anisotropic systems by magnetic resonance imaging. *Magn Reson Med* 42:515-25.

Jones DK, Simmons A, Williams SC, Horsfield MA (1999c) Non-invasive assessment of axonal fiber connectivity in the human brain via diffusion tensor MRI. *Magn Reson Med* 42:37-41.

Jones TH, Morawetz RB, Crowell RM, Marcoux FW, FitzGibbon SJ, DeGirolami U, Ojemann RG (1981) Thresholds of focal cerebral ischemia in awake monkeys. *J Neurosurg* 54:773-82.

Kandel ER, Schwartz JH, Jessell TM. (2000). *Principles of Neural Science*. Fourth edition ed. New York: McGraw-Hill Companies, 1414pp.

Karonen JO, Vanninen RL, Liu Y, Ostergaard L, Kuikka JT, Nuutinen J, Vanninen EJ, Partanen PL, Vainio PA, Korhonen K, Perkio J, Roivainen R, Sivenius J, Aronen HJ (1999) Combined diffusion and perfusion MRI with correlation to single-photon emission CT in acute ischemic stroke. Ischemic penumbra predicts infarct growth. *Stroke* 30:1583-90.

Keller PJ, Hunter WW, Jr., Schmalbrock P (1987) Multisection fat-water imaging with chemical shift selective presaturation. *Radiology* 164:539-41.

Kelly-Hayes M, Robertson JT, Broderick JP, Duncan PW, Hershey LA, Roth EJ, Thies WH, Trombly CA (1998) The American Heart Association Stroke Outcome Classification. *Stroke* 29:1274-80.

Kelton J, Mangin R, Wright S. (1989) An algorithm for rapid image acquisition using multiple receiver coils. In: *8th Annual Meeting of the Society for Magnetic Resonance in Medicine*, Amsterdam, p 1172

Kemper T (1994) Neuroanatomical and neuropathological changes during aging and dementia. In: *Clinical neurology of aging* (Albert M, Knoefel J, eds), New York: Oxford University Press, 3-18.

Kidwell CS, Saver JL, Mattiello J, Starkman S, Vinuela F, Duckwiler G, Gobin YP, Jahan R, Vespa P, Kalafut M, Alger JR (2000) Thrombolytic reversal of acute human cerebral ischemic injury shown by diffusion/perfusion magnetic resonance imaging. *Ann Neurol* 47:462-9.

Kingsley PB, Monahan WG (2005) Contrast-to-noise ratios of diffusion anisotropy indices. *Magn Reson Med* 53:911-8.

Kingsley PB (2006) Introduction to diffusion tensor imaging mathematics: Part II. Anisotropy, diffusion-weighting factors, and gradient encoding schemes. *Concept Magn Reson A* 28A:123-54.

Klatzo I (1987) Pathophysiological aspects of brain edema. *Acta neuropathologica* 72:236-9.

Koeppen AH (2004) Wallerian degeneration: history and clinical significance. *J Neurol Sci* 220:115-7.

Koga M, Reutens DC, Wright P, Phan T, Markus R, Pedreira B, Fitt G, Lim I, Donnan GA (2005) The existence and evolution of diffusion-perfusion mismatched tissue in white and gray matter after acute stroke. *Stroke* 36:2132-7.

Kuhl CK, Gieseke J, von Falkenhausen M, Textor J, Gernert S, Sonntag C, Schild HH (2005) Sensitivity encoding for diffusion-weighted MR imaging at 3.0 T: intraindividual comparative study. *Radiology* 234:517-26.

Kwong K, McKinstry R, Chien D, Crawley A, Pearlman J, Rosen B (1991) CSF-suppressed quantitative single-shot diffusion imaging. *Magn Reson Med* 21:157-63.

Lansberg MG, Albers GW, Beaulieu C, Marks MP (2000) Comparison of diffusion-weighted MRI and CT in acute stroke. *Neurology* 54:1557-61.

Larkman DJ, Atkinson D, Hajnal JV (2004) Artifact reduction using parallel imaging methods. *Top Magn Reson Imaging* 15:267-75.

Latour L, Warach S (2002) Cerebral spinal fluid contamination of the measurement of the apparent diffusion coefficient of water in acute stroke. *Magn Reson Med* 48:478-86.

Lauterbur PC (1973) Image Formation by Induced Local Interactions - Examples Employing Nuclear Magnetic-Resonance. *Nature* 242:190-1.

Le Bihan D, Breton E, Lallemand D, Grenier P, Cabanis E, Laval-Jeantet M (1986) MR imaging of intravoxel incoherent motions: application to diffusion and perfusion in neurologic disorders. *Radiology* 161:401-7.

Le Bihan D (1988) Intravoxel incoherent motion imaging using steady-state free precession. *Magn Reson Med* 7:346-51.

Le Bihan D, Delannoy J, Levin RL (1989) Temperature mapping with MR imaging of molecular diffusion: application to hyperthermia. *Radiology* 171:853-7.

Le Bihan D. (1995). *Diffusion and Perfusion Magnetic Resonance Imaging: Applications to Functional MRI*. New York: Raven Press, 374pp.

Le Bihan D, Mangin JF, Poupon C, Clark CA, Pappata S, Molko N, Chabriat H (2001) Diffusion tensor imaging: concepts and applications. *J Magn Reson Imaging* 13:534-46.

Lexa FJ, Grossman RI, Rosenquist AC (1994) Dyke Award paper. MR of wallerian degeneration in the feline visual system: characterization by magnetization transfer rate with histopathologic correlation. *AJNR Am J Neuroradiol* 15:201-12.

Leys D, Englund E, Del Ser T, Inzitari D, Fazekas F, Bornstein N, Erkinjuntti T, Bowler JV, Pantoni L, Parnetti L, De Reuck J, Ferro J, Bogousslavsky J (1999) White matter changes in stroke patients. Relationship with stroke subtype and outcome. *Eur Neurol* 42:67-75.

Liang Z-P, Lauterbur PC. (2000). *Principles of Magnetic Resonance Imaging, A signal processing perspective*. New York: Institute of Electrical and Electronics Engineers, Inc., 416pp.

Liddel U, Ramsey NF (1951) Temperature Dependent Magnetic Shielding in Ethyl Alcohol. *J Chem Phys* 19:1608-.

Liebeskind DS (2003) Collateral circulation. *Stroke* 34:2279-84.

Liebeskind DS (2005) Collaterals in acute stroke: beyond the clot. *Neuroimaging Clin N Am* 15:553-73, x.

Lim KO, Helpern JA (2002) Neuropsychiatric applications of DTI - a review. *NMR Biomed* 15:587-93.

Lin F, Yu C, Jiang T, Li K, Chan P (2007) Diffusion tensor tractography-based group mapping of the pyramidal tract in relapsing-remitting multiple sclerosis patients. *AJNR Am J Neuroradiol* 28:278-82.

Lipton P (1999) Ischemic cell death in brain neurons. *Physiological reviews* 79:1431-568.

Liu Y, D'Arceuil HE, Westmoreland S, He J, Duggan M, Gonzalez RG, Pryor J, de Crespigny AJ (2007) Serial diffusion tensor MRI after transient and permanent cerebral ischemia in nonhuman primates. *Stroke* 38:138-45.

Lowe MJ, Horenstein C, Hirsch JG, Marrie RA, Stone L, Bhattacharyya PK, Gass A, Phillips MD (2006) Functional pathway-defined MRI diffusion measures reveal increased transverse diffusivity of water in multiple sclerosis. *Neuroimage* 32:1127-33.

Luo L, O'Leary DD (2005) Axon retraction and degeneration in development and disease. *Annu Rev Neurosci* 28:127-56.

Ma X, Kadah YM, LaConte SM, Hu X (2004) Enhancing measured diffusion anisotropy in gray matter by eliminating CSF contamination with FLAIR. *Magn Reson Med* 51:423-7.

Malone MJ, Szoke MC (1985) Neurochemical changes in white matter. Aged human brain and Alzheimer's disease. *Arch Neurol* 42:1063-6.

Mansfield P, Grannell PK (1973) NMR Diffraction in Solids. *J Phys C Solid State* 6:L422-L6.

Mansfield P (1977) Multi-Planar Image-Formation Using NMR Spin Echoes. *J Phys C Solid State* 10:L55-L8.

Margosian P, Schmitt F, Purdy D (1986) Faster MR imaging: imaging with half the data. *Health Care Instruments* 1:195-7.

Marks MP, Tong DC, Beaulieu C, Albers GW, de Crespigny A, Moseley ME (1999) Evaluation of early reperfusion and i.v. tPA therapy using diffusion- and perfusion-weighted MRI. *Neurology* 52:1792-8.

Mattiello J, Basser PJ, Le Bihan D (1997) The b matrix in diffusion tensor echo-planar imaging. *Magn Reson Med* 37:292-300.

McDonald WM, Husain M, Doraiswamy PM, Figiel G, Boyko O, Krishnan KR (1991) A magnetic resonance image study of age-related changes in human putamen nuclei. *Neuroreport* 2:57-60.

McGibney G, Smith MR, Nichols ST, Crawley A (1993) Quantitative evaluation of several partial Fourier reconstruction algorithms used in MRI. *Magn Reson Med* 30:51-9.

Medina D, DeToledo-Morrell L, Urresta F, Gabrieli JD, Moseley M, Fleischman D, Bennett DA, Leurgans S, Turner DA, Stebbins GT (2006) White matter changes in mild cognitive impairment and AD: A diffusion tensor imaging study. *Neurobiol Aging* 27:663-72.

Meier-Ruge W, Ulrich J, Bruhlmann M, Meier E (1992) Age-related white matter atrophy in the human brain. *Ann N Y Acad Sci* 673:260-9.

Miller AK, Alston RL, Corsellis JA (1980) Variation with age in the volumes of grey and white matter in the cerebral hemispheres of man: measurements with an image analyser. *Neuropathol Appl Neurobiol* 6:119-32.

Minati L, Grisoli M, Bruzzone MG (2007) MR spectroscopy, functional MRI, and diffusion-tensor imaging in the aging brain: a conceptual review. *Journal of geriatric psychiatry and neurology* 20:3-21.

Mori S, van Zijl PC (2002) Fiber tracking: principles and strategies - a technical review. *NMR Biomed* 15:468-80.

Mori S, van Zijl P (2005) MR tractography using diffusion tensor MR imaging. In: *Clinical MR Neuroimaging Diffusion, Perfusion and Spectroscopy* (Gillard JH, Waldman AD, Barker PB, eds), New York: Cambridge University Press, 86-98.

Moseley M (2002) Diffusion tensor imaging and aging- a review. *NMR Biomed* 15:553-60.

Moseley ME, Cohen Y, Kucharczyk J, Mintorovitch J, Asgari HS, Wendland MF, Tsuruda J, Norman D (1990a) Diffusion-weighted MR imaging of anisotropic water diffusion in cat central nervous system. *Radiology* 176:439-45.

Moseley ME, Cohen Y, Mintorovitch J, Chileuitt L, Shimizu H, Kucharczyk J, Wendland MF, Weinstein PR (1990b) Early detection of regional cerebral ischemia in cats: comparison of diffusion- and T2-weighted MRI and spectroscopy. *Magn Reson Med* 14:330-46.

Moseley ME, Kucharczyk J, Mintorovitch J, Cohen Y, Kurhanewicz J, Derugin N, Asgari H, Norman D (1990c) Diffusion-weighted MR imaging of acute stroke: correlation with T2-weighted and magnetic susceptibility-enhanced MR imaging in cats. *AJNR Am J Neuroradiol* 11:423-9.

Mukherjee P, Bahn MM, McKinstry RC, Shimony JS, Cull TS, Akbudak E, Snyder AZ, Conturo TE (2000) Differences between gray matter and white matter water diffusion in stroke: diffusion-tensor MR imaging in 12 patients. *Radiology* 215:211-20.

Mukherjee P (2005) Diffusion tensor imaging and fiber tractography in acute stroke. *Neuroimaging Clin N Am* 15:655-65, xii.

Munoz Maniega S, Bastin ME, Armitage PA, Farrall AJ, Carpenter TK, Hand PJ, Cvoro V, Rivers CS, Wardlaw JM (2004) Temporal evolution of water diffusion parameters is different in grey and white matter in human ischaemic stroke. *J Neurol Neurosurg Psychiatry* 75:1714-8.

Nagae-Poetscher LM, Jiang H, Wakana S, Golay X, van Zijl PC, Mori S (2004) High-resolution diffusion tensor imaging of the brain stem at 3 T. *AJNR Am J Neuroradiol* 25:1325-30.

Nitz WR (2002) Fast and ultrafast non-echo-planar MR imaging techniques. *Eur Radiol* 12:2866-82.

Nunnemann S, Wohlschlager AM, Ilg R, Gaser C, Etgen T, Conrad B, Zimmer C, Muhlau M (2007) Accelerated aging of the putamen in men but not in women. *Neurobiol Aging*.

Nusbaum A, Cheuk Y, Buchsbaum M, Wei T, Atlas S (2001) Regional and global changes in cerebral diffusion with normal aging. *Am J Neuroradiol* 22:136-42.

O'Sullivan M, Jones D, Summers P, Morris R, Williams S, Markus H (2001) Evidence for cortical "disconnection" as a mechanism of age-related cognitive decline. *Neurology* 57:632-8.

O'Sullivan M, Morris RG, Huckstep B, Jones DK, Williams SC, Markus HS (2004) Diffusion tensor MRI correlates with executive dysfunction in patients with ischaemic leukoaraiosis. *J Neurol Neurosurg Psychiatry* 75:441-7.

Oberholzer K, Junginger T, Kreitner KF, Krummenauer F, Simiantonaki N, Trouet S, Thelen M (2005) Local staging of rectal carcinoma and assessment of the circumferential resection margin with high-resolution MRI using an integrated parallel acquisition technique. *J Magn Reson Imaging* 22:101-8.

Onal MZ, Fisher M, Bogousslavsky J (2001) Clinical evaluation of stroke. In: *Current review of cereborvascular disease* (Fisher M, Bogousslavsky J, eds), Philadelphia: Current Medicine, Inc., 102-14.

Ota M, Obata T, Akine Y, Ito H, Ikehira H, Asada T, Suhara T (2006) Age-related degeneration of corpus callosum measured with diffusion tensor imaging. *Neuroimage* 31:1445-52.

Ozsunar Y, Grant PE, Huisman TA, Schaefer PW, Wu O, Sorensen AG, Koroshetz WJ, Gonzalez RG (2004a) Evolution of water diffusion and anisotropy in hyperacute stroke: significant correlation between fractional anisotropy and T2. *AJNR Am J Neuroradiol* 25:699-705.

Ozsunar Y, Koseoglu K, Huisman TA, Koroshetz W, Sorensen AG (2004b) MRI measurements of water diffusion: impact of region of interest selection on ischemic quantification. *Eur J Radiol* 51:195-201.

Pajevic S, Pierpaoli C (1999) Color schemes to represent the orientation of anisotropic tissues from diffusion tensor data: application to white matter fiber tract mapping in the human brain. *Magn Reson Med* 42:526-40.

Pantoni L, Garcia JH, Gutierrez JA (1996) Cerebral white matter is highly vulnerable to ischemia. *Stroke* 27:1641-6; discussion 7.

Papadakis N, Martin K, Mustafa M, Wilkinson I, Griffiths P, Huang C-H, Woodruff P (2002) Study of the effect of CSF suppression on white matter diffusion anisotropy mapping in healthy human brain. *Magn Reson Med* 48:394-8.

Papadakis NG, Xing D, Houston GC, Smith JM, Smith MI, James MF, Parsons AA, Huang CL, Hall LD, Carpenter TA (1999) A study of rotationally invariant and symmetric indices of diffusion anisotropy. *Magn Reson Imaging* 17:881-92.

Pereira RS, Harris AD, Sevick RJ, Frayne R (2002) Effect of b value on contrast during diffusion-weighted magnetic resonance imaging assessment of acute ischemic stroke. *J Magn Reson Imaging* 15:591-6.

Persson J, Nyberg L, Lind J, Larsson A, Nilsson LG, Ingvar M, Buckner RL (2006) Structure-function correlates of cognitive decline in aging. *Cereb Cortex* 16:907-15.

Pesce C, Reale A (1987) Aging and the nerve cell population of the putamen: a morphometric study. *Clinical neuropathology* 6:16-8.

Petty MA, Wettstein JG (1999) White matter ischaemia. *Brain Res Brain Res Rev* 31:58-64.

Pfefferbaum A, Mathalon D, Sullivan E, Rawles J, Zipursky R, Lim K (1994) A quantitative magnetic resonance imaging study of changes in brain morphology from infancy to late adulthood. *Arch Neurol* 51:874-87.

Pfefferbaum A, Sullivan E, Hedehus M, Lim K, Adalsteinsson E, Moseley M (2000) Age-related decline in brain white matter anisotropy measured with spatially corrected echo-planar diffusion tensor imaging. *Magn Reson Med* 44:259-68.

Pfefferbaum A, Adalsteinsson E, Sullivan EV (2005) Frontal circuitry degradation marks healthy adult aging: Evidence from diffusion tensor imaging. *Neuroimage* 26:891-9.

Pfefferbaum A, Sullivan EV (2005) Diffusion MR imaging in neuropsychiatry and aging. In: *Clinical MR Neuroimaging Diffusion, Perfusion and Spectroscopy* (Gillard JH, Waldman AD, Barker PB, eds), New York: Cambridge University Press, 558-78.

Pierpaoli C, Basser PJ (1996) Toward a quantitative assessment of diffusion anisotropy. *Magn Reson Med* 36:893-906.

Pierpaoli C, Jezzard P, Basser P, Barnett A, Di Chiro G (1996) Diffusion tensor MR imaging of the human brain. *Radiology* 201:637-48.

Pierpaoli C, Barnett A, Pajevic S, Chen R, Penix LR, Virta A, Basser P (2001) Water diffusion changes in Wallerian degeneration and their dependence on white matter architecture. *Neuroimage* 13:1174-85.

Pipe JG, Farthing VG, Forbes KP (2002) Multishot diffusion-weighted FSE using PROPELLER MRI. *Magn Reson Med* 47:42-52.

Povlishock JT, Christman CW (1995) The pathobiology of traumatically induced axonal injury in animals and humans: a review of current thoughts. *J Neurotrauma* 12:555-64.

Prayer D, Roberts T, Barkovich AJ, Prayer L, Kucharczyk J, Moseley M, Arieff A (1997) Diffusion-weighted MRI of myelination in the rat brain following treatment with gonadal hormones. *Neuroradiology* 39:320-5.

Price RR, Axel L, Morgan T, Newman R, Perman W, Schneiders N, Selikson M, Wood M, Thomas SR (1990) Quality assurance methods and phantoms for magnetic resonance imaging: report of AAPM nuclear magnetic resonance Task Group No. 1. *Med Phys* 17:287-95.

Pruessmann KP, Weiger M, Scheidegger MB, Boesiger P (1999) SENSE: sensitivity encoding for fast MRI. *Magn Reson Med* 42:952-62.

Pruessmann KP (2004) Parallel imaging at high field strength: synergies and joint potential. *Top Magn Reson Imaging* 15:237-44.

Pugh KG, Lipsitz LA (2002) The microvascular frontal-subcortical syndrome of aging. *Neurobiol Aging* 23:421-31.

Purcell EM, Torrey HC, Pound RV (1946) Resonance Absorption by Nuclear Magnetic Moments in a Solid. *Phys Rev* 69:37-8.

Purves D, Augustine GJ, Fitzpatrick D, Katz LC, Mamantia A-S, McNamara JO, Williams SM. (2001). *Neuroscience*. Second edition ed. Sunderland: Sinauer Associates, Inc.

Ra JB, Rim CY (1993) Fast imaging using subencoding data sets from multiple detectors. *Magn Reson Med* 30:142-5.

Raz N, Rodrigue KM, Kennedy KM, Head D, Gunning-Dixon F, Acker JD (2003) Differential aging of the human striatum: longitudinal evidence. *AJNR Am J Neuroradiol* 24:1849-56.

Reeder SB, Wintersperger BJ, Dietrich O, Lanz T, Greiser A, Reiser MF, Glazer GM, Schoenberg SO (2005) Practical approaches to the evaluation of signal-to-noise ratio performance with parallel imaging: application with cardiac imaging and a 32-channel cardiac coil. *Magn Reson Med* 54:748-54.

Reese T, Heid O, Weiskoff R, Wedeen V (2003) Reduction of eddy-current-induced distortion in diffusion MRI using a twice-refocused spin echo. *Magn Reson Med* 49:177-82.

Roemer PB, Edelstein WA, Hayes CE, Souza SP, Mueller OM (1990) The NMR phased array. *Magn Reson Med* 16:192-225.

Rovaris M, Iannucci G, Cercignani M, Sormani MP, De Stefano N, Gerevini S, Comi G, Filippi M (2003) Age-related changes in conventional, magnetization transfer, and diffusion-tensor MR imaging findings: study with whole-brain tissue histogram analysis. *Radiology* 227:731-8.

Ruel L, Brugieres P, Luciani A, Breil S, Mathieu D, Rahmouni A (2004) Comparison of in vitro and in vivo MRI of the spine using parallel imaging. *AJR Am J Roentgenol* 182:749-55.

Sa de Camargo EC, Koroshetz WJ (2005) Neuroimaging of ischemia and infarction. *NeuroRx* 2:265-76.

Salat DH, Tuch DS, Greve DN, van der Kouwe AJ, Hevelone ND, Zaleta AK, Rosen BR, Fischl B, Corkin S, Rosas HD, Dale AM (2005) Age-related alterations in white matter microstructure measured by diffusion tensor imaging. *Neurobiol Aging* 26:1215-27.

Sarlls JE, Newbould RD, Altbach MI, Gmitro AF, Seeger J, Trouard TP (2005) Isotropic diffusion weighting in radial fast spin-echo magnetic resonance imaging. *Magn Reson Med* 53:1347-54.

Schaefer PW, Ozsunar Y, He J, Hamberg LM, Hunter GJ, Sorensen AG, Koroshetz WJ, Gonzalez RG (2003) Assessing tissue viability with MR diffusion and perfusion imaging. *AJNR Am J Neuroradiol* 24:436-43.

Schellinger PD, Fiebach JB, Mohr A, Ringleb PA, Jansen O, Hacke W (2001) Thrombolytic therapy for ischemic stroke--a review. Part II--Intra-arterial thrombolysis, vertebrobasilar stroke, phase IV trials, and stroke imaging. *Crit Care Med* 29:1819-25.

Schellinger PD, Jansen O, Hacke W (2003) Stroke MRI in Intracranial Hemorrhage. In: *Magnetic Resonance Imaging in Stroke* (Davis S, Fisher M, Warach S, eds), New York: Cambridge University Press, 103-12.

Schellinger PD, Kaste M, Hacke W (2004) An update on thrombolytic therapy for acute stroke. *Curr Opin Neurol* 17:69-77.

Schlaug G, Siewert B, Benfield A, Edelman RR, Warach S (1997) Time course of the apparent diffusion coefficient (ADC) abnormality in human stroke. *Neurology* 49:113-9.

Schlaug G, Benfield A, Baird AE, Siewert B, Lovblad KO, Parker RA, Edelman RR, Warach S (1999) The ischemic penumbra: operationally defined by diffusion and perfusion MRI. *Neurology* 53:1528-37.

Semelka RC, Armao DM, Elias J, Jr., Huda W (2007) Imaging strategies to reduce the risk of radiation in CT studies, including selective substitution with MRI. *J Magn Reson Imaging* 25:900-9.

Sen PN, Basser PJ (2005) A model for diffusion in white matter in the brain. *Biophys J* 89:2927-38.

Shen Q, Meng X, Fisher M, Sotak CH, Duong TQ (2003) Pixel-by-pixel spatiotemporal progression of focal ischemia derived using quantitative perfusion and diffusion imaging. *J Cereb Blood Flow Metab* 23:1479-88.

Shimony JS, McKinstry RC, Akbudak E, Aronovitz JA, Snyder AZ, Lori NF, Cull TS, Conturo TE (1999) Quantitative diffusion-tensor anisotropy brain MR imaging: normative human data and anatomic analysis. *Radiology* 212:770-84.

Skare S, Newbould RD, Clayton DB, Albers GW, Nagle S, Bammer R (2007) Clinical multishot DW-EPI through parallel imaging with considerations of susceptibility, motion, and noise. *Magn Reson Med* 57:881-90.

Sodickson DK, Manning WJ (1997) Simultaneous acquisition of spatial harmonics (SMASH): fast imaging with radiofrequency coil arrays. *Magn Reson Med* 38:591-603.

Sodickson DK, Griswold MA, Jakob PM (1999) SMASH imaging. *Magn Reson Imaging Clin N Am* 7:237-54, vii-viii.

Sodickson DK (2000) Spatial encoding using multiple rf coils: SMASH imaging and parallel imaging. In: *Methods in Biomedical Magnetic Resonance Imaging and Spectroscopy* (Young IR, ed), Vol. 1, New York: John Wiley and sons, 11.

Sodickson DK, McKenzie CA (2001) A generalized approach to parallel magnetic resonance imaging. *Med Phys* 28:1629-43.

Song SK, Sun SW, Ju WK, Lin SJ, Cross AH, Neufeld AH (2003) Diffusion tensor imaging detects and differentiates axon and myelin degeneration in mouse optic nerve after retinal ischemia. *Neuroimage* 20:1714-22.

Sorensen AG, Wu O, Copen WA, Davis TL, Gonzalez RG, Koroshetz WJ, Reese TG, Rosen BR, Wedeen VJ, Weisskoff RM (1999) Human acute cerebral ischemia: detection of changes in water diffusion anisotropy by using MR imaging. *Radiology* 212:785-92.

Sotak CH (2002) The role of diffusion tensor imaging in the evaluation of ischemic brain injury - a review. *NMR Biomed* 15:561-9.

Statistics & Background Information - Stroke Statistics. (2006), p http://ww2.heartandstroke.ca/

Stejskal EO, Tanner JE (1965) Spin Diffusion Measurements - Spin Echoes in Presence of a Time-Dependent Field Gradient. *J Chem Phys* 42:288-&.

Stys PK (2004) White matter injury mechanisms. *Curr Mol Med* 4:113-30.

Sullivan EV, Adalsteinsson E, Pfefferbaum A (2006) Selective age-related degradation of anterior callosal fiber bundles quantified in vivo with fiber tracking. *Cereb Cortex* 16:1030-9.

Sun SW, Liang HF, Le TQ, Armstrong RC, Cross AH, Song SK (2006) Differential sensitivity of in vivo and ex vivo diffusion tensor imaging to evolving optic nerve injury in mice with retinal ischemia. *Neuroimage* 32:1195-204.

Takahashi S, Yonezawa H, Takahashi J, Kudo M, Inoue T, Tohgi H (2002) Selective reduction of diffusion anisotropy in white matter of Alzheimer disease brains measured by 3.0 Tesla magnetic resonance imaging. *Neurosci Lett* 332:45-8.

Tamura H, Hatazawa J, Toyoshima H, Shimosegawa E, Okudera T (2002) Detection of deoxygenation-related signal change in acute ischemic stroke patients by T2*-weighted magnetic resonance imaging. *Stroke* 33:967-71.

Tang Y, Nyengaard J, Pakkenberg B, Gundersen H (1997) Age-induced white matter changes in the human brain: a stereological investigation. *Neurobiol Aging* 18:609-15.

Tello R, Crewson PE (2003) Hypothesis testing II: means. *Radiology* 227:1-4.

Thomalla G, Glauche V, Koch MA, Beaulieu C, Weiller C, Rother J (2004) Diffusion tensor imaging detects early Wallerian degeneration of the pyramidal tract after ischemic stroke. *Neuroimage* 22:1767-74.

Thomalla G, Glauche V, Weiller C, Rother J (2005) Time course of wallerian degeneration after ischaemic stroke revealed by diffusion tensor imaging. *J Neurol Neurosurg Psychiatry* 76:266-8.

Thomas DL, Lythgoe MF, Pell GS, Calamante F, Ordidge RJ (2000) The measurement of diffusion and perfusion in biological systems using magnetic resonance imaging. *Phys Med Biol* 45:R97-138.

Tissue plasminogen activator for acute ischemic stroke. The National Institute of Neurological Disorders and Stroke rt-PA Stroke Study Group (1995). *N Engl J Med* 333:1581-7.

Tomasch J (1954) Size, distribution, and number of fibres in the human corpus callosum. *Anat Rec* 119:119-35.

Torrey HC (1956) Bloch Equations with Diffusion Terms. *Phys Rev* 104:563-5.

Trapp BD, Peterson J, Ransohoff RM, Rudick R, Mork S, Bo L (1998) Axonal transection in the lesions of multiple sclerosis. *N Engl J Med* 338:278-85.

Tress BM (2003) Clinical use of standard MRI. In: *Magnetic Resonance Imaging in Stroke* (Davis S, Fisher M, Warach S, eds), New York: Cambridge University Press, 69-84.

Trouard TP, Theilmann RJ, Altbach MI, Gmitro AF (1999) High-resolution diffusion imaging with DIFRAD-FSE (diffusion-weighted radial acquisition of data with fast spin-echo) MRI. *Magn Reson Med* 42:11-8.

Tuch DS (2004) Q-ball imaging. *Magn Reson Med* 52:1358-72.

Turner R (1998) Diffusion Imaging with Echo-Planar Imaging. In: *Echo-Planar Imaging Theory, Technique and Application* (Schmitt F, Stehling MK, Turner R, eds), Berlin: Springer-Verlag, 311-24.

Vogt FM, Antoch G, Hunold P, Maderwald S, Ladd ME, Debatin JF, Ruehm SG (2005) Parallel acquisition techniques for accelerated volumetric interpolated breath-hold examination magnetic resonance imaging of the upper abdomen: assessment of image quality and lesion conspicuity. *J Magn Reson Imaging* 21:376-82.

Walhovd KB, Fjell AM, Reinvang I, Lundervold A, Dale AM, Eilertsen DE, Quinn BT, Salat D, Makris N, Fischl B (2005) Effects of age on volumes of cortex, white matter and subcortical structures. *Neurobiol Aging* 26:1261-70; discussion 75-8.

Wang J, Kluge T, Nittka M, Jellus V, Kuhn B, Kiefer B. (2001) Parallel acquisition techniques with modified SENSE reconstruction mSENSE. In: *Proceedings of the first Wurzburg workshop on parallel imaging basics and clinical applications*, Wurzburg, Germany, p 89

Warach S, Chien D, Li W, Ronthal M, Edelman RR (1992) Fast magnetic resonance diffusion-weighted imaging of acute human stroke. *Neurology* 42:1717-23.

Warach S, Gaa J, Siewert B, Wielopolski P, Edelman RR (1995) Acute human stroke studied by whole brain echo planar diffusion-weighted magnetic resonance imaging. *Ann Neurol* 37:231-41.

Warner J (2001) Sectional neuroanatomy. In: *Atlas of neuroanatomy*), Boston: Butterworth-Heinemann, 153-314.

Weber GF (1994) The pathophysiology of reactive oxygen intermediates in the central nervous system. *Med Hypotheses* 43:223-30.

Wedeen VJ, Hagmann P, Tseng WY, Reese TG, Weisskoff RM (2005) Mapping complex tissue architecture with diffusion spectrum magnetic resonance imaging. *Magn Reson Med* 54:1377-86.

Werring DJ, Toosy AT, Clark CA, Parker GJ, Barker GJ, Miller DH, Thompson AJ (2000) Diffusion tensor imaging can detect and quantify corticospinal tract degeneration after stroke. *J Neurol Neurosurg Psychiatry* 69:269-72.

Wielopolski PA, Schmitt F, Stehling MK (1998) Echo-Planar Imaging Pulse Sequences. In: *Echo-Planar Imaging Theory, Technique and Application* (Schmitt F, Stehling MK, Turner R, eds), Berlin: Springer-Verlag, 65-140.

Willinek WA, Gieseke J, von Falkenhausen M, Neuen B, Schild HH, Kuhl CK (2003) Sensitivity encoding for fast MR imaging of the brain in patients with stroke. *Radiology* 228:669-75.

Wimberger DM, Roberts TP, Barkovich AJ, Prayer LM, Moseley ME, Kucharczyk J (1995) Identification of "premyelination" by diffusion-weighted MRI. *J Comput Assist Tomogr* 19:28-33.

Wintermark M, Sesay M, Barbier E, Borbely K, Dillon WP, Eastwood JD, Glenn TC, Grandin CB, Pedraza S, Soustiel JF, Nariai T, Zaharchuk G, Caille JM, Dousset V, Yonas H (2005) Comparative overview of brain perfusion imaging techniques. *J Neuroradiol* 32:294-314.

Wu O, Ostergaard L, Sorensen AG (2005) Technical aspects of perfusion-weighted imaging. *Neuroimaging Clin N Am* 15:623-37, xi.

Xing D, Papadakis NG, Huang CL, Lee VM, Carpenter TA, Hall LD (1997) Optimised diffusion-weighting for measurement of apparent diffusion coefficient (ADC) in human brain. *Magn Reson Imaging* 15:771-84.

Yam PS, Dewar D, McCulloch J (1998) Axonal injury caused by focal cerebral ischemia in the rat. *J Neurotrauma* 15:441-50.

Yamada K, Kizu O, Mori S, Ito H, Nakamura H, Yuen S, Kubota T, Tanaka O, Akada W, Sasajima H, Mineura K, Nishimura T (2003) Brain fiber tracking with clinically feasible diffusion-tensor MR imaging: initial experience. *Radiology* 227:295-301.

Yang Q, Tress BM, Barber PA, Desmond PM, Darby DG, Gerraty RP, Li T, Davis SM (1999) Serial study of apparent diffusion coefficient and anisotropy in patients with acute stroke. *Stroke* 30:2382-90.

Zacharopoulos N, Narayana P (1998) Selective measurement of white matter and gray matter diffusion trace values in normal human brain. *Med Phys* 25:2237-41.

Zelaya F, Flood N, Chalk JB, Wang D, Doddrell DM, Strugnell W, Benson M, Ostergaard L, Semple J, Eagle S (1999) An evaluation of the time dependence of the anisotropy of the water diffusion tensor in acute human ischemia. *Magn Reson Imaging* 17:331-48.

Zhang K, Sejnowski TJ (2000) A universal scaling law between gray matter and white matter of cerebral cortex. *Proc Natl Acad Sci U S A* 97:5621-6.

Zhang Y, Schuff N, Jahng GH, Bayne W, Mori S, Schad L, Mueller S, Du AT, Kramer JH, Yaffe K, Chui H, Jagust WJ, Miller BL, Weiner MW (2007) Diffusion tensor imaging of cingulum fibers in mild cognitive impairment and Alzheimer disease. *Neurology* 68:13-9.

Zou KH, Fielding JR, Silverman SG, Tempany CM (2003) Hypothesis testing I: proportions. *Radiology* 226:609-13.

Appendix 1

MRVISION IMAGE PROCESSING COMMANDS

A1.1 To Generate Diffusion Tensor Indices

The 'macro' facility within the MRvision program (Winchester, MA) allows one to save a set of pre-defined image processing commands that can be executed in sequence. A set of commands from one such macro file, **tensor6drns.m**, are listed below. This macro file was used to generate diffusion tensor indices from a set of multislice diffusion weighted data, acquired with the Siemens twice-refocused spin echo EPI sequence (ep2d_diff). The steps below generated mean diffusion images (6-direction averaged), ADC maps with diffusion weighting along 6 noncollinear directions, and diffusion tensor indices such as maps of Trace/3 ADC, the eigenvalues (λ_1, λ_2, λ_3), components of the principal eigenvector (ε_1) corresponding to λ_1 (X_1, Y_1 and Z_1), and fractional anisotropy (FA) defined by 6 sets of gradient factors listed in the text file, 'sixdrns.txt'.

The variable, $mims is the number of images selected for the macro; $mims equals the number of slices. The macro assumes slices are arranged in 'slice order', i.e. all slices for 1st b=0 set and then all slices for b=1000 data sets. The text file, 'diff.bvals' contains the b values (low and high for a two-point fitting) used in the DWI acquisition. The program looks for this file in the directory according to the pathname specified. The sixdrns.txt file contains the direction vectors needed for the tensor calculations.

The MRVision IMV image file format consists of an ASCII header followed by binary image data.

```
autodis 0               # suppress auto image display
setvar A = $current     # b=0 image
setvar B = $A
setvar B + $mims        # set pointer to similar slice (b=1000) skipping
                          the number of slices listed
setvar C = $B
setvar C + $mims        # set pointer to the next image (same slice and
                          b value), but different direction

setvar D = $C
setvar D + $mims        # same as above, and continued onwards
setvar E = $D
```

```
setvar E + $mims
setvar F = $E
setvar F + $mims
setvar G = $F
setvar G + $mims
setvar H = $G

select $B $C $D $E $F $G          # select the 6 diffusion images where
                                    gradients have been applied in
                                    different directions

setvar R = $last                  # set pointer to last image G selected
setvar S = $mcount                # the operation will proceed for
                                    successive sets of diffusion images

mean $new                         # average image computed from the mean
                                    of the 6 diffusion images

setvar R + 1                      # set pointer to the new average
                                    diffusion image

select $R
save avgdiff.imv.$S3 IMV_FILE     # save average diffusion images

select $A $A $A $A $A $B $C $D $E $F $G   # select b=0 image and 6,
                                            b=1000 images for ADC
                                            maps
setvar J = $last - 6
setvar K = $J                     # set pointer to successive ADC maps
                                    being computed
setvar K + 1
setvar L = $K
setvar L + 1
setvar M = $L
setvar M + 1
setvar N = $M
setvar N + 1
setvar O = $N
setvar O + 1
setvar P = $O
setvar P + 1
setvar Q = $P

fit 2 1 1 diff.bvals 0.0000       # compute ADC maps with 0.000 for
                                    noise cutoff

select $K $L $M $N $O $P          # select a set of 6 ADC maps for
                                    computing tensor indices
setvar I = $last
setvar Z = $mcount

fit 22 1 1 sixdrns.txt 0.0000     # compute tensor indices with 0.000
                                    for noise cutoff

save adc.imv.$Z3 IMV_FILE         # save ADC maps
```

```
setvar I + 1
select $I
save trace.imv.$Z3 IMV_FILE        # save trace/3 ADC maps

setvar I + 1
select $I
save e1.imv.$Z3 IMV_FILE           # save 1st set of eigenvalue maps
                                     λ1 (mm^2/sec)

setvar I + 1
select $I
save e2.imv.$Z3 IMV_FILE           # save 2nd set of eigenvalue maps (λ2)

setvar I + 1
select $I
save e3.imv.$Z3 IMV_FILE           # save 3rd set of eigenvalue maps (λ3)

setvar I + 1
select $I
save x.imv.$Z3 IMV_FILE            # save x maps of principal eigenvector
                                     corresponding to λ1

setvar I + 1
select $I
save y.imv.$Z3 IMV_FILE            # save y maps of principal eigenvector
                                     corresponding to λ1

setvar I + 1
select $I
save z.imv.$Z3 IMV_FILE            # save z maps of principal eigenvector
                                     corresponding to λ1

setvar I + 1
select $I
save fa.imv.$Z3 IMV_FILE           # save fractional anisotropy maps

display $I                         # display the final output maps (FA
                                     maps)

autodis 1                          # reactivate auto image display
```

---

sixdrns.txt

```
1 0 1
-1 0 1
0 1 1
0 1 -1
1 1 0
-1 1 0
```

diff.bvals

```
0
1000
```

A1.2 To Generate Apparent Diffusion Coefficient Maps

Image processing commands from the macro file, **ADC_convDWI.m** are listed below for the MRVision program. This file computes apparent diffusion coefficient (ADC) maps for two-point datasets or b values (low and high) for trace-weighted diffusion images derived from Siemens 1.5T Sonata with a twice-refocused spin-echo EPI sequence. The file, 'diff.bvals' is a text file containing the b values 0 and 1000.

```
autodis 0               # turn auto display off
setvar A = $current     # set pointer to first b=0 image
setvar B = $A
setvar B + $mims        # set pointer to similar slice for b=1000
                          skipping the number of slices outlined
                          initially with the variable $mims

setvar C = $B

select $A $B            # Now select the b=0 image and corresponding
                          b=1000 image

setvar I = $last        # set pointer to the final b=1000 image thus far
setvar Z = $mcount      # The operation is meant to proceed for
                          successive sets of images using term $mcount

fit 2 1 1 diff.bvals 0.0000
# compute ADC maps using slice order and outputting new images (ADC
maps)with 0.000 for noise cutoff

setvar I + 1            # set pointer to the newly computed image (ADC
                          map) after the last diffusion image in series
                          (from 2 steps above)

select $I               # select the newly computed ADC map

save ADC.imv.$Z3 IMV_FILE
# save the newly computed ADC map assigning image number via the
variable $Z3 according to slice order

display $I              # display the ADC maps one at a time for a
                          single/multi slice dataset

autodis 1               # turn image display on
```

---

diff.bvals
0
1000